The University of Nottingham
UNITED KINGDOM · CHINA · MALAYSIA

Robinson, Kenneth Neil (2020) Investigating ionisation and material ejection in ultraviolet matrix-assisted laser desorption\ionisation mass spectrometry imaging. PhD thesis, University of Nottingham.

Access from the University of Nottingham repository:
http://eprints.nottingham.ac.uk/60562/2/ThesisFullTextNo3rdParty.pdf

Copyright and reuse:

The Nottingham ePrints service makes this work by researchers of the University of Nottingham available open access under the following conditions.

This article is made available under the University of Nottingham End User licence and may be reused according to the conditions of the licence. For more details see: http://eprints.nottingham.ac.uk/end_user_agreement.pdf

For more information, please contact eprints@nottingham.ac.uk

Investigating ionisation and material ejection in Ultraviolet Matrix-Assisted Laser Desorption\Ionisation Mass Spectrometry Imaging

Kenneth Neil Robinson

Thesis submitted to the University of Nottingham for the degree of Doctor of Philosophy

Abstract

Ultraviolet Matrix-Assisted Laser Desorption\Ionisation Mass Spectrometry (UV-MALDI MS) is a powerful analytical technique, allowing sensitive, unlabelled detection of a wide range of analytes. In recent decades this UV-MALDI has proven a highly successful Mass Spectrometry Imaging (MSI) modality, capable of imaging exogenous and endogenous compounds in complex biological tissues. Despite this, UV-MALDI MSI is hindered by incomplete knowledge regarding many aspects of desorption and ionisation. The researched presented in this thesis focuses on applying a quantitative metrological approach to investigate factors affecting desorption and ionisation in UV-MALDI MSI. The influence of analyte-to-matrix molar ratio and the use of the common additive trifluoroacetic acid (TFA) were explored for an array of matrices and analyte classes using multivariate analysis (MVA) techniques. A subset of these matrix-analyte systems was used to explore the relationship between ionisation, matrix optical absorption and laser fluence. UV-MALDI MSI laser sampling was investigated in detail us profilometry, quantifying material desorption and ion yield under MSI sampling conditions for the first time. Profilometry measurements were extended into tissue imaging, to probe the influence of tissue microenvironment on desorption and ionisation in a UV-MALDI imaging experiment. The first quantitative measurements of desorption, ion yield and ion suppression for MSI tissue data were achieved. MVA was used to identify probable causes of ion suppression, and to quantify tissue-region specific ion suppression, helping to inform and redefine data normalisation approaches.

Acknowledgements

I would first like to thank both my supervisors, Professor Josephine Bunch for providing mountains of advice, guidance and insightful perspective to help me discern when results were "a triumph" or "shat", and Professor David Barrett for all his invaluable support, help and useful advice. I could not have asked for two better people to guide me though this PhD.

I gratefully acknowledge the National Physical Laboratory (NPL) and ultimately the Department of Business, Energy, Innovation and Skills (BEIS) for providing the funding for this PhD as part of the AIMS HIGHER metrology programme.

A special thanks to all the NiCE-MSI group at NPL for welcoming me to the MSI field. In particular Dr Rory Steven for showing me the ropes of MALDI MSI and all things laser related, Dr Alan Race for his invaluable software packages used in all the MSI data processing, and for writing the instrument control scripts used in Chapter 4, and along with Dr Spencer Thomas and Dr Alexander Dexter for numerous discussions on the particulars of data analysis in MATLAB.

Further thanks to the Dimensional Metrology group at NPL for all their assistance in the use of the optical profilometry instruments, and in particular Dr Rob Hornby for providing the scripting tools required to process the CCI topography data for use in MATLAB in Chapter 5.

Finally, I would like to thank my partner Georgina Leung for her patience and support while I disappeared down the rabbit hole of lab work and writing, and my mother Charlotte Robinson who of all people this would never have been possible without.

Published works arising from this thesis

Robinson, K. N.; Steven, R. T.; Bunch, J. Matrix Optical Absorption in UV-MALDI MS. *J. Am. Soc. Mass Spectrom.* **2018**, 29 (3), 501–511. https://doi.org/10.1007/s13361-017-1843-4.

Robinson, K. N.; Steven, R. T.; Race, A. M.; Bunch, J. The Influence of MS Imaging Parameters on UV-MALDI Desorption and Ion Yield. *J. Am. Soc. Mass Spectrom.* **2019**, 30 (7), 1284–1293. https://doi.org/10.1007/s13361-019-02193-8.

Table of Contents

Abstract 2

Acknowledgements 3

Published works arising from this thesis 4

List of Figures 9

Table of Abbreviations 22

Chapter 1 - Introduction 24

1.1 - Matrix-assisted laser desorption/ionisation mass spectrometry (MALDI MS) 24

1.2 - Ultraviolet Matrix-Assisted Laser Desorption\Ionisation Mass Spectrometry Imaging (UV-MALDI MSI) 27

1.3 - Factors influencing UV-MALDI MSI 30

1.3.1 - Matrix physiochemical properties 30

1.3.1.1 - Optical properties 30

1.3.1.2 - Proton affinity and gas phase basicity 35

1.3.1.3 – Thermochemical and thermophysical properties 36

1.3.2 - Laser irradiation conditions 38

1.3.2.1 - Laser fluence and irradiated area 38

1.3.2.2 - Laser repetition rate 44

1.3.2.3 - Wavelength 46

1.3.2.4 - Pulse duration 49

1.3.2.5 - Beam profile 55

1.3.2.6 - Laser sampling modes in UV-MALDI MSI 58

1.3.2.7 - Irradiation geometry 60

1.3.3 - The influence of sample conditions in UV-MALDI MSI 61

1.3.3.1 - Analyte-to-matrix molar ratio 61

1.3.3.2 - Matrix deposition methods 63

1.3.3.3 – Ionisation additives 66

1.3.3.4 – Substrate effects 67

1.3.4 - Mechanisms of material ejection and ionisation in UV-MALDI MS 70

1.3.4.1 - UV-MALDI MS material ejection models 70

1.3.4.2 - Theoretical models UV-MALDI MS ionisation 74

1.4 - Applications of UV-MALDI MS and UV-MALDI MSI 80

1.4.1 - UV-MALDI MS 80

1.4.2 - UV-MALDI MSI 81

1.5 - Thesis overview 85

Chapter 2 - The influence of analyte-to-matrix molar ratio and TFA in UV-MALDI MS 88

2.1 - Introduction 88

2.2 - Materials 90

2.3 - Methods 91
2.3.1 - Matrix analyte molar ratio and TFA influence 91
2.3.2 - UV-MALDI MS 92
2.3.3 - Laser fluence measurement 93
2.3.4 – Data Processing 93
2.3.5 - t-distributed stochastic neighbour embedding (t-SNE) and Principal component analysis (PCA) 93

2.4 – Results 94
2.4.1 - UV-MALDI MS analyte average spectra 94
2.4.2 - Matrix-analyte molar ratio and addition of TFA 98
2.4.3 t-SNE 104
2.4.4 - PCA analysis 107

2.5 - Conclusions 120

Chapter 3 - Matrix optical absorption in UV-MALDI MS 122

3.1 - Introduction 122

3.2 - Materials 124

3.3 - Methods 125
3.3.1 - Matrix deposition for optical measurements – Home built sublimation system 125
3.3.2 - Matrix deposition for optical measurements – Edwards Evaporator 126
3.3.3 - UV-Vis spectroscopy of UV-MALDI matrix compounds 127
3.3.4 - Matrix film thickness measurement 128
3.3.5 – Matrix compound density 128
3.3.6 - UV-MALDI MS 129
3.3.6 - Laser fluence measurement 129
3.3.7 - Laser fluence variation experiments 129
3.3.8 - Data analysis 130

3.4 - Results and discussion 131
3.4.1 - Matrix compound solid phase optical absorption 131
3.4.2 - Desorption/Ionisation as a function of laser fluence for different matrix compounds and analytes 141
3.4.3 - Desorption/ionisation characteristics as a function of matrix optical absorption 150

3.5 - Conclusions 153

Chapter 4 - The influence of UV-MALDI MS imaging parameters on material ejection and ion yield 155

4.1 - Introduction **155**

4.2 - Materials **156**

4.3 - Methods **157**
4.3.1 - Sample preparation 157
4.3.2 - UV-MALDI MS 157
4.3.3 - Measurement of material ejection 159
4.3.4 - Data analysis 159
4.3.5- Calculation of ion transmission in MALDI Synapt G2-Si HDMS 160
4.3.6 - Determination of ion number 161

4.4 - Results **162**
4.4.1- Irradiation effects 162
4.4.2 - Characterising material ejection in UV-MALDI MSI 166
4.4.3 – Simulation of material removal in oversampling acquisition 173
4.4.4 - Ion yields in MSI 177

4.5 - Conclusions **186**

Chapter 5 - Characterising the influence of tissue microenvironment on desorption and ionisation in UV-MALDI MSI **189**

5.1 – Introduction **189**

5.2 - Materials **190**

5.3 - Methods **190**
5.3.1 - Experimental overview 190
5.3.2 - Tissue preparation 192
5.3.3 - Matrix and internal standard deposition 192
5.3.4 - Topographic imaging by Coherence Correlation Interferometry (CCI) 193
5.3.5 - UV-MALDI MSI optimisation 197
5.3.6 - UV-MALDI MSI 200
5.3.6 - Data processing 201
5.3.6.1 - UV-MALDI MSI 201
5.3.6.2 - CCI profilometry 202
5.3.6.3 - Image registration 202
5.3.7 - Calculation of number of ions generated and ion transmission 202

5.4 - Results **203**
5.4.1 - Tissue topography 203
5.4.2 - Matrix application homogeneity 206
5.4.3 - UV-MALDI MSI results 208
5.4.4 - Effects of tissue region on ion intensity 213
5.4.5 - Principal Component Analysis (PCA) of UV-MALDI MSI data 217
5.4.6 - Material removal in UV-MALDI MSI 220
5.4.7 - Ion yield in UV-MALDI MSI of tissue 222

5.5 - Conclusions **225**

Chapter 6 – Future Work **228**

References **236**

List of Figures

Figure 1.1. Schematic of the MALDI process **a)** a matrix analyte sample prior to absorption of the laser pulse and **b)** the resulting plume and ion formation after absorption of the laser pulse. 25

Figure 1.2. Development timeline of MALDI MS and MALDI MSI. Inset figures, in chronological order, adapted from Refs. 2, 7, 8, 9, 11, 14, 12, 13 and 15. . 26

Figure 1.3. Diagram of UV-MALDI MSI operating in microprobe mode. 27

Figure 1.4. Optical absorption spectra for five matrix compounds, 3-hydroxypicolinic acid (3-HPA), 2,4,6-trihydroxyacetophenone (THAP), 1,8-dihydroxy-10H-anthracen-9-one (Dithranol), 2-(4-hydroxyphenylazo) benzoic acid (HABA) and 6-aza-2-thiothymine (ATT), obtained in **a)** solution and **b)** solid phase. Figure adapted from Niehaus et al.[17] 31

Figure 1.5. UV-MALDI material ejection step as probed by photoacoustic analysis. PA signals were recorded as a function of laser fluence and rectangular flat top spot size from microcrystalline preparations of neat 2,5-DHB (DHB) and CHCA (HCCA) matrices (upper graphs). The bottom graphs display the same data set after normalization to the focal spot size. The coloured dashed lines depict a best fit of the quasi-thermal desorption model to the data, the red dash-dotted lines a best fit of the ln model and the black dotted lines a fit to the linear model. Figure and caption adapted from Niehaus et al[17]. 43

Figure 1.6. Ion intensity heat maps of different groups of species generated from two standard UV-MALDI matrixes (CHCA and 2,5-DHB) and five halogenated CHCA-derivatives, as a function of wavelength and laser pulse

energy. **a)** Summed $[A+H]^+$ intensities of five peptides. The laser penetration depth ($\alpha-1$) is shown as a white solid line. **b)** Yield of a-, b-, and y-fragments of the five peptides relative to the intensity sum of all analyte-derived ions. **c)** Total ion intensity of all matrix-derived ions generated from a neat matrix preparation. Figure and caption adapted from Soltwisch et al[22]..... 48

Figure 1.7. Snapshot of MD simulations, showing **a)** desorption and **b & c)** ablation material ejection regimes. Irritation parameters in **a & b)** correspond to thermal confinement conditions (τ_p = 150 ps) at **a)** low (34 J m^{-2}) **b)** high fluences (55 J m^{-2}). Conditions in **c)** correspond to stress confinement conditions (τ_p = 15 ps, 31 J m^{-2}). Figure reproduced from Zhigilei & Garrison.[86]..... 53

Figure 1.8. a) Plot showing concentration dependence of cluster- specific tissue extraction coefficients (TEC). Cluster images are shown on the right. Colour is required to interpret this plot. **b)** Single ion images of olanzapine $[M+H]^+$ (m/z 313.15), deposited by spraying, at 0, 77, 384, and 768 pmol/mm^2 calculated olanzapine density. Figure and caption adapted from Taylor et al.[144]..... 69

Figure 1.9. Detection of olanzapine and metabolite distribution at 2 h post-dose in a whole rat sagittal tissue section by MALDI MSI analysis. **a)** Optical image of a 2h post olanzapine dosed rat tissue section across four gold MALDI target plates. Organs outlined in red. **b)** MS/MS ion image of OLZ (m/z 256). **c)** MS/MS ion image of N-desmethyl metabolite (m/z 256). **d)** MS/MS ion

image of 2-hydroxymethyl metabolite (m/z 272). Bar, 1 cm. Figure reproduced from Khatib-Shahidi et al[177]. 82

Figure 1.10. UV-MALDI MS images of finger-marks simultaneously spiked with drugs and their metabolites at defined ratios to show the distribution of samples containing **a)** cocaine, BZE and EME in a 5:1:1 ratio; **b)** heroin, 6-MAM, morphine in a 5:1:1 ratio; **c)** amphetamine and MDA in a 1:1 ratio; and **d)** THC and THCA in a 1:1 ratio. Figure and caption adapted from Groeneveld et al[184]. 84

Figure 2.1. Molecular structures of the ten UV-MALDI matrix compounds selected for study. 90

Figure 2.2. Layout of the optical system used for laser delivery and monitoring during the UV-MALDI MS experiments detailed in this chapter. 92

Figure 2.3. Average UV-MALDI mass spectrum for Angiotensin II. The spectrum is the average of 45 spectra acquiring with 2,5-DHB in positive mode. Characteristic analyte and matrix peaks are tentatively assigned. 95

Figure 2.4. Average UV-MALDI mass spectrum for Haloperidol. The spectrum is the average of 45 spectra acquiring with 2,5-DHB in positive mode. Characteristic analyte peaks are tentatively assigned 96

Figure 2.5. Average UV-MALDI mass spectra for PC(34:1) lipid standard. The spectrum is the average of 45 spectra acquiring with 2,5-DHB in positive mode. Characteristic analyte peaks are tentatively assigned 97

Figure 2.6. Mean analyte $[M+H]^+$ intensities for ten matrix compounds and three analytes, across a range of matrix analyte ratios, with and without the addition of 0.1% v/v TFA. Data points represent mean values of 45 spectra.

Error bars describe the standard error. All mean intensities values <1 were considered as zero, for display purposes these values were set to 1..... 99

Figure 2.7. Mean analyte $[M+Na]^+$ intensities for ten matrix compounds and three analytes, across a range of analyte-to-matrix molar ratios, with and without the addition of 0.1% v/v TFA. Data points show mean values of 45 spectra. Error bars describe the expanded uncertainty (k=2). For display purposes mean intensities <1 were set to 1.....102

Figure 2.8. Mean analyte $[M+K]^+$ intensities for ten matrix compounds and three analytes, across a range of analyte-to-matrix molar ratios, with (dashed lines) and without (solid lines) the addition of 0.1% v/v TFA. Data points represent mean values of 45 spectra. Error bars describe the standard error. For display purposes mean intensities <1 were set to 1.....103

Figure 2.9. Cosine distance t-SNE plots of UV-MALDI-MS data for all the conditions studied in this chapter. t-SNE plots are colour-coded by **a)** analyte-to-matrix molar ratio **b)** matrix **c)** presence or absence of 0.1% TFA and **d)** analyte. A density map of the data points **e)** is included to aid interpretation of the t-SNE results.....106

Figure 2.10. a) Loadings spectrum of PC1 for 2,5-DHB, demonstrating the contamination issue. **b)** Mean spectra of 1,5-DAN matrix with PC (34:1) lipid standard. Common peaks between the two spectra are annotated.....108

Figure 2.11. a) PCA score plots showing the first three PCs for all collected mass spectra, grouped by matrix. Scores plots are colour coded by analyte-to-matrix molar ratio**. b)** Corresponding PCA loadings plots, grouped by

matrix. PCA was run on z-scored data to standardise the contributions of each peak in the spectra. 110

Figure 2.12. PCA score plots showing the first three PCs for all collected mass spectra, grouped by matrix. Scores plots are colour coded by analyte. PCA was run on z-scored data to standardise the contributions of each peak in the spectra..... 112

Figure 2.13. a) PCA score plots of the first three PCs for all collected mass spectra of Angiotensin II at 10^4 molar ratio. Scores plots are colour coded by the absence or addition of 0.1% v/v TFA. **b)** Corresponding PCA loadings plots. PCA was run on z-scored data to standardise the contributions of each peak in the spectra..... 114

Figure 2.14. a) PCA score plots of the first three PCs for all collected mass spectra of Haloperidol at 10^4 molar ratio Scores plots are colour coded by the absence or addition of 0.1% v/v TFA. **b)** Corresponding PCA loadings plots. PCA was run on z-scored data to standardise the contributions of each peak in the spectra..... 117

Figure 2.15. a) PCA score plots of the first three PCs for all collected mass spectra of PC(34:1) at 10^4 molar ratio . Scores plots are colour coded by the absence or addition of 0.1% v/v TFA. **b)** Corresponding PCA loadings plots. PCA was run on z-scored data to standardise the contributions of each peak in the spectra..... 119

Figure 3.1. Diagram of the two sublimation deposition approaches used to manufacture matrix thin films for absorption measurements. **a)** Homebuilt sublimation system **b)** Edwards Auto 306 evaporator..... 125

Figure 3.2. Solution and solid-state molar extinction coefficient (ε) spectra of 10 selected MALDI matrices. Solid state absorption values are scaled to the NUV maxima of the corresponding solution spectra. Dotted black lines at 337 and 355 nm mark the operating wavelengths of common UV-MALDI lasers. Spectra are the average of three measurements. 132

Figure 3.3. a) Mean thicknesses and expanded uncertainty (k=2) of the deposited matrix films used for absorption measurements. Values are the average step height measurements of AFM images acquired at four positions along a scratch in each film. **b)** Example of an AFM image used for film thickness determination, the matrix film is THAP. **c)** Height profile of THAP film shown in **b)** 135

Figure 3.4. a) Solid phase optical cross section (σ) spectra for the five studied UV-MALDI matrix compounds, as measured from sublimed thin films. Dotted line are the solution phase absorption spectra of the corresponding matrix (10 mmol L^{-1} in MeOH). The right axis shows the equivalent molar extinction coefficient (ε) scale. **b)** Corresponding solid phase spectra replotted as absorption coefficient (α). Dashed vertical lines mark the operating wavelengths of common UV-MALDI lasers. 137

Figure 3.5. Analyte $[M+H]^+$ intensity (IA) with varying laser fluence for the studied matrix analyte mixed systems. Data points are the mean IA taken from 45 spectra, x and y error bars show the expanded uncertainty (k =2). Solid line represents fitting of the data of equation 1, open data points signify the onset of reduction in IA due to fragmentation, this regime is not modelled by the equation and thus excluded in the fitting process..... 142

Figure 3.6. Threshold fluence regions of Figure 3.2 in linear scale demonstrating the variance in $Hthr\ A$ with analyte for the five studied matrix compounds. Error bars show the expanded uncertainty (k =2)..... 143

Figure 3.7. Calculated surface layer energy densities at observed threshold fluence for the studied matrix analyte combinations, as a function of matrix melting point..... 145

Figure 3.8. Analyte $[M+H]^+$ intensity (IA) with varying laser fluence for the studied matrix analyte mixed systems. Data points are the mean of 45 spectra, error bars show the expanded uncertainty (k =2). Solid lines represent fitting of the data of equation 3.1, open data points signify values excluded in the fitting process. 147

Figure 3.9. Derivative forms of the change in ion intensity with fluence produced by fitting of the data to equation 3.1, for each of the matrix analyte combinations..... 149

Figure 3.10. Relationship between matrix optical cross section at 355 nm ($\sigma 355$) and the analyte ion intensity curve parameters **(a)** $Hthr\ A$ **(b)** $Hk\ A$ **(c)** mA **(d)** RA and **(e)** IA**,** for the 15 studied matrix analyte combinations. Error bars represent the expanded uncertainty (k=2). Lines in the plots represent fitting of the data to **(a)** & **(b)** power, **(c)** 2nd order polynomial and **(d)** & **(e)** linear functions. 151

Figure 4.1. Change in laser spot area with pulse energy, as determined via fluorescent emission from CHCA matrix films. 158

Figure 4.2. Overview of the internal ion optics and ion path for the Synapt G2-Si HDMS. 160

Figure 4.3. Surface analysis techniques for characterising laser irradiation effects and material ejection in UV-MALDI MSI. **a)** SEM image **b)** AFM topography image with phase map overlay and **c)** CSLM topographic image of crater in CHCA film, resulting from spot mode acquisition, with a laser energy of 3.6 µJ and 500 Hz repetition rate. **d)** SEM images **e)** AFM topography image with phase map overlay and **f)** CSLM topography image of raster trench in 2,5-DHB film, resulting from 2 mm/s raster mode acquisition, with a laser energy 7.3 µJ and 500 Hz repetition rate. 164

Figure 4.4. Ionisation and material ejection from olanzapine + CHCA/2,5-DHB thin films in spot mode **a)** Averaged crater geometries (n=5) **b)** Cross sectional profiles of craters, at different pulse energies and repetition rates, obtained from CLSM measurements **c)** Corresponding olanzapine ion intensities (I_{OLZ}). Ion intensities are the summed values of H^+, Na^+ and K^+ adducts and all detected isotopic peaks **d)** calculated number of molecules removed at different pulse energies and repetition rates from CLSM crater volume measurements. All error bars represent the expanded uncertainty (k=2). 167

Figure 4.5. Change in crater area with pulse energy in spot mode for CHCA and 2,5-DHB at 500 Hz and 2000 Hz. Error bars show the expanded uncertainty (k=2). 169

Figure 4.6. a) Overview of sampling efficiency (S_{Eff}) concept and measurement. Diagrams on the left show a cross sectional view of how the full crater (top) and region of complete matrix ejection (bottom) volumes are determined, images on the right show the process with real crater data (CHCA, 500 Hz,

5.5 µJ). Change in S_{Eff} with laser pulse energy for CHCA and 2,5-DHB at 500 Hz and 2000 Hz, for **b)** spot mode, **c)** 2 mm s^{-1} raster **d)** 8 mm s^{-1} raster. 171

Figure 4.7. Illustration of spatial origin of ions under **a)** idealised oversampling conditions and **b)** oversampling with non-uniform laser beam profile. **c)** Simulation of material removal at different pixel sizes. Top: Surface topology of the matrix layer. Middle: Ion region, the total volume removed per pixel Bottom: Oversampled region, the volume removed at the current pixel location that comes from sample areas analysed in previous pixel. Crater data from CHCA 1.8 µJ, 2000 Hz data. 173

Figure 4.8. Heatmap showing the simulated degree of pixel oversampling at different pixel sizes, for CHCA and 2,5-DHB at different pulse energies and laser repetition rates. Contour lines marking different degrees of pixel oversampling are included to aid interpretation of the data..... 175

Figure 4.9. Ion yield of olanzapine (Y_{OLZ}) with increasing pulse energy under different imaging conditions. **a)** spot mode acquisition, **b)** 2 mm s^{-1} raster **c)** 8 mm s^{-1} raster. All raster data is normalised to pixel size. Error bars show the expanded uncertainty (k=2)..... 177

Figure 4.10. Total ion yield (Y_{TIC}) with increasing pulse energy under different imaging conditions. **a)** spot mode acquisition, **b)** 2 mm s^{-1} raster **c)** 8 mm s^{-1} raster. All raster data is normalised to pixel size. Error bars show the expanded uncertainty (k=2)..... 178

Figure 4.11. Change in number of removed molecules per pixel with 2,5-DHB and CHCA as a function of laser pulse energy and laser repetition rate at **a)**

2 mm s^{-1} and **b)** 8 mm s^{-1} raster speeds. Error bars show the expanded uncertainty (k=2). 181

Figure 4.12. Change in olanzapine ion yield (Y_{OLZ}) with pulse energy under equivalent irradiation conditions. Data shows raster mode acquisitions where the raster speed and laser repetition rate conditions resulted in four pulses delivered per µm of travel. 182

Figure 4.13. Change in total ion yield (Y_{TIC}) with pulse energy under equivalent irradiation conditions. Data show raster mode acquisition where the raster speed and laser repetition rate conditions resulted in four pulses delivered per µm of travel. All data is normalised to pixel size. 183

Figure 4.14. Simulated temperature rise from absorption of a single laser pulse (200 µm diameter, 3.6 µJ, 355 nm) in **a)** CHCA and **b)** 2,5-DHB matrix layers. Colour bars are scaled to the respective melting points of each matrix (CHCA: 250°C, 2,5-DHB: 205°C). Contour lines show the position of 50°C and the respective melting point of each matrix. 185

Figure 5.1. Sequence of sample preparation and analysis. CCI topography images are collected at each stage, allowing the tissue topography, as well as material changes from matrix deposition and UV-MALDI MSI analysis to be fully quantified. 191

Figure 5.2. Optimisation of CCI acquisition parameters. Cross sectional profile of an ablation crater in a CHCA thin film, **a)** acquired with four different microscope modes, **b)** in "XY" mode with the three different optimisation modes, **c)** example topography data in the default microscope mode and

d) acquired with the speed optimised "XY" mode that was selected for the remainder of the study. 195

Figure 5.3. Optimisation of uMALDI laser energy. **a)** on tissue summed lipid region (m/z 700-900) intensities and **b)** on-tissue TIC intensity as a function of laser pulse energy. Data were acquired in positive polarity and spot mode acquisition, from a mouse brain section coated with 700 nm CHCA. Laser repetition rate was 2500 Hz. Data points connected by solid lines were acquired using the fixed attenuator and data points connected by dash lines without. Error bars show the combined uncertainty (k=2). 198

Figure 5.4. Optimisation of uMALDI laser focus using CCI optical profilometry of ablation craters in 700 nm CHCA thin film. **a)** crater diameter **b)** crater volume **c)** crater area **d)** ratio of crater volume to area. A laser pulse energy of 0.7 µJ and repetition rate of 2500 Hz was used. Focus position is taken as the number of full micrometer turns from the end of the linear translation stage where the lens is closest to the sample region of the source. Datapoints are the averaged measurement of 25 craters; error bars show the combined uncertainty (k=2). 199

Figure 5.5. a) Height map of dehydrated mouse brain tissue section obtained by CCI microscopy. **b)** Corresponding brain region from Allen Mouse Brain Atlas. **c)** cross section height profile corresponding to the white dashed line in **a).** 204

Figure 5.6. Map of the thickness of deposited matrix over the sample. Inset images show tissue region specific changes in matrix thickness and morphology. 207

Figure 5.7. UV-MALDI MSI images of the mouse brain sample. **a)** Total ion current (TIC) **b)** Haloperidol $[M+H]^+$ **c)** CHCA $[M+H]^+$ **d)** PC (34:1) $[M+K]^+$ **e)** Cholesterol $[M-OH]^+$ **f)** PC (38:6) $[M+K]^+$.....209

Figure 5.8. Detected ion intensity for **a)** TIC and **b)** Haloperidol $[M+H]^+$as a function of tissue thickness at each on-tissue pixel location in the acquires MSI data.....211

Figure 5.9. Effect of tissue thickness on ion signal in MALDI MSI. **a)** Distribution of TIC pixel intensities before and after normalisation to tissue thickness at each pixel location **b)** Distribution of Haloperidol $[M+H]^+$ pixel intensities before and after normalisation to tissue thickness at each pixel location . All data comes from the on-tissue pixels. 212

Figure 5.10. a) TIC ion image and 2-Phase Graph cuts clustering segmentation of the MALDI MSI data. Colour coded clusters are grouped by the anatomical brain regions they represent, as identified from comparison to Allen Mouse Brain Atlas. **b)** Corresponding distributions of pixel TIC intensities within the different clusters. Median intensity values for each region are also reported.....214

Figure 5.11. a) Graph-cuts clustering segmentation of the MALDI MSI data. Colour coded clusters are group by the anatomical brain regions they represent, as identified from Allen Mouse Brain Atlas data. **b)** Corresponding distributions of pixel intensities for Haloperidol $[M+H]^+$within the different clusters. Median intensity values for each region are also reported. 215

Figure 5.12. PCA of the acquired brain UV-MALDI MSI data. **a)** PC1 image of the collected brain data. **b)** Corresponding PC1 spectral loadings. 217

Figure 5.13. a) Volume of removed material per pixel image and tissue regions segmented from the MSI data **b)** corresponding distributions Volume removed per pixel within the different tissue regions. Median Volume removed values for each region are also reported. 221

Figure 5.14. a) Total ion yield (Y_{TIC}) image of the tissue **b)** tissue regions segmented from the MSI data **v)** corresponding distribution of Y_{TIC} pixel values within the different tissue regions. Median Y_{TIC} values for each region are also reported. 223

Figure 5.15. a) Haloperidol $[M+H]^+$ ion yield (Y_{HALO}) image of the tissue **b)** tissue regions segmented from the MSI data **c)** corresponding distribution of Y_{HALO} pixel values within the different tissue regions. Median Y_{HALO} values for each region are also reported. 224

Table of Abbreviations

MALDI	Matrix-assisted laser desorption\ionisation
UV	Ultraviolet
MS	Mass spectrometry
MSI	Mass spectrometry imaging
m/z	mass-to-charge
Da	Dalton
TIC	Total ion current
LDI	Laser desorption ionisation
ESI	Electrospray ionisation
DESI	Desorption electrospray ionisation
FAB	Fast atom bombardment
SIMS	Secondary ion mass spectrometry
EI	Electron Ionisation
REIMS	Rapid evaporative ionisation mass spectrometry
LESA	Liquid extraction surface analysis
LC-MS	Liquid chromatography mass spectrometry
HPLC	High performance liquid chromatography
ToF	Time-of-flight
Qq-ToF	Quadrupole time-of-flight
FT-ICR	Fourier transform ion cyclotron resonance
ISD	In-source decay
NUV	Near ultraviolet
IR	Infrared
DPPS	Diode-pumped solid state
Nd:YAG	Neodymium-doped yttrium aluminium garnet
Er:YAG	Erbium-doped yttrium aluminium garnet
$Nd:YVO_4$	Neodymium-doped yttrium orthovanadate
OPO	Optical parametric oscillator
ADC	Analogue-to-digital converter
ITO	Indium tin oxide
FOV	Field of view
LOD	Limit of detection
DoE	Design of experiments
AP	Atmospheric pressure
DFT	Density functional theory
P_A	Proton Affinity
G_B	Gas Phase Basicity
MSE	Matrix suppression effect
ASE	Analyte suppression effect
t-SNE	t-distributed stochastic neighbour embedding
PCA	Principal component analysis
PVD	Physical vapour deposition
QCM	Quartz crystal microbalance
AFM	Atomic force microscopy

CLSM	Confocal laser scanning microscopy
SEM	Scanning electron microscopy
CCI	Coherence correlation interferometry
MRI	Magnetic resonance imaging
NMR	Nuclear magnetic resonance
PET	Positron electron tomography
LA-ICP MS	Laser-ablation inductively coupled plasma mass spectrometry
μ-XRF	Micro X-ray Fluorescence
GM	Grey matter
WM	White matter
TEC	Tissue extinction coefficient
PC	Phosphatidylcholine
PA	Phosphatidic acid
PE	Phosphatidylethanolamine
cPA	Cyclic phosphatidic acid
PGP	Glycerophosphoglycerophosphate
PE-NMe	Monomethyl phosphatidylethanolamine
PE-NMe2	Dimethyl phosphatidylethanolamine
THAP	2,4,6-trihydroxyacetophenone
2,5-DHAP	2,5-dihydroxyacetophenone
GAL	Galvinoxyl
MBT	2-mercaptobenzothiazole
DAN	1,5-diaminonapthalene
PNA	*para*- nitroaniline
DIT	Dithranol
CHCA	α-cyanohydroxycinnaminic acid
2,5-DHB	2,5-dihydroxybenzoic acid
FA	Ferulic acid
SA	Sinapinic acid
TFA	Trifluoracetic acid
MeOH	Methanol
ACN	Acetonitrile
THF	Tetrahydrofuran
DI	Deionised

Chapter 1 - Introduction

1.1 - Matrix-assisted laser desorption/ionisation mass spectrometry (MALDI MS)

A major driver of the development of mass spectrometry is to broaden the range of accessible analytes. To this end a variety of ionisation techniques have been developed with the goal of ionising increasingly massive, liable analytes of interest, such as peptides and proteins. By the mid 1980's techniques such as Secondary Ion Mass Spectrometry (SIMS) and Fast Atom Bombardment (FAB) were able to ionise analytes up to small peptides and proteins (few kDA) but suffered from poor limits of detection (LOD) and excessive fragmentation issues which limited analysis of high molecular mass compounds. At the same time Laser Desorption Ionisation (LDI) was being explored as a method for desorption of biomolecules but was restricted in analyte mass range due to severe fragmentation resulting from energy deposition of the laser.

Growing out of research in LDI, the concept of Matrix-Assisted Laser Desorption/Ionisation (MALDI) was first described in 1985 by Hillenkamp and Karas[1,2], who found that the addition of ultraviolet wavelength (UV) absorbing tryptophan to poorly absorbing alanine in LDI experiments allowed for the latter to be much more readily desorbed and ionised. The same workers would more fully describe the new technique the following year[3]. In 1988 Tanaka et al. extended the concept to molecules as large as 34 kDa, using 30 nm cobalt nanoparticles suspended in glycerol to promote analyte desorption and ionisation[4].

Tanaka's work on MALDI, along with Fenn's work on electrospray ionisation (ESI), would ultimately result in a shared award for 2002 Nobel Prize in Chemistry, in recognition of the role both techniques played in opening the possibility of routine MS analysis of liable biomacromolecules, and thus the widespread application mass spectrometry in biological sciences.

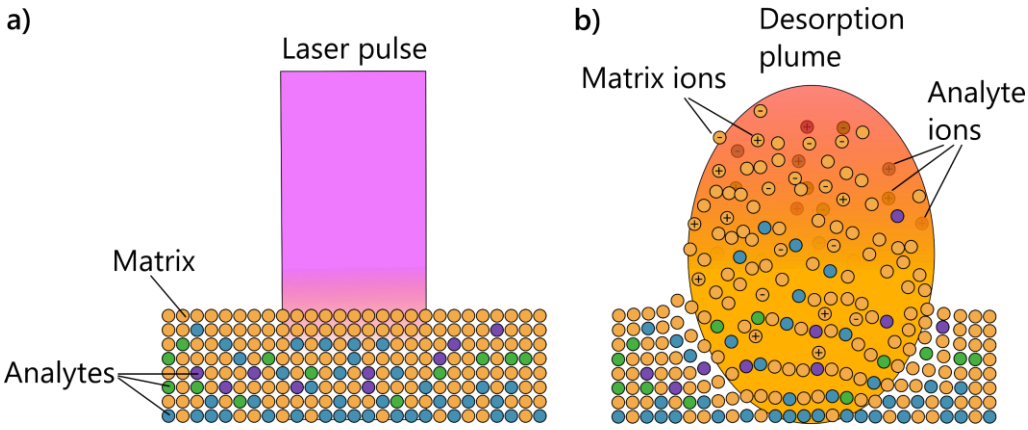


Figure 1.1. *Schematic of the MALDI process* ***a)*** *a matrix analyte sample prior to absorption of the laser pulse and* ***b)*** *the resulting plume and ion formation after absorption of the laser pulse.*

The MALDI process involves the application of a chemical additive, known as a "matrix", to a sample. When the sample is irradiated with a laser, the matrix absorbs this energy, ionising and desorbing from the sample surface, carrying molecules from the sample along with it (Figure 1.1). These molecules are then ionised in the desorbed matrix plume and detected by the mass spectrometer

The technique is typically described as "soft", in that it allows for the ionisation of large and/or fragile molecules intact. This is contrast to "hard" ionisation techniques such as SIMS or Electron Ionisation (EI), which typically result in extensive fragmentation. A MALDI mass spectrum is typically characterised by

the presence of singly charged, intact analyte ions, although multiply charged ions and fragments can occur depending on the experimental conditions.

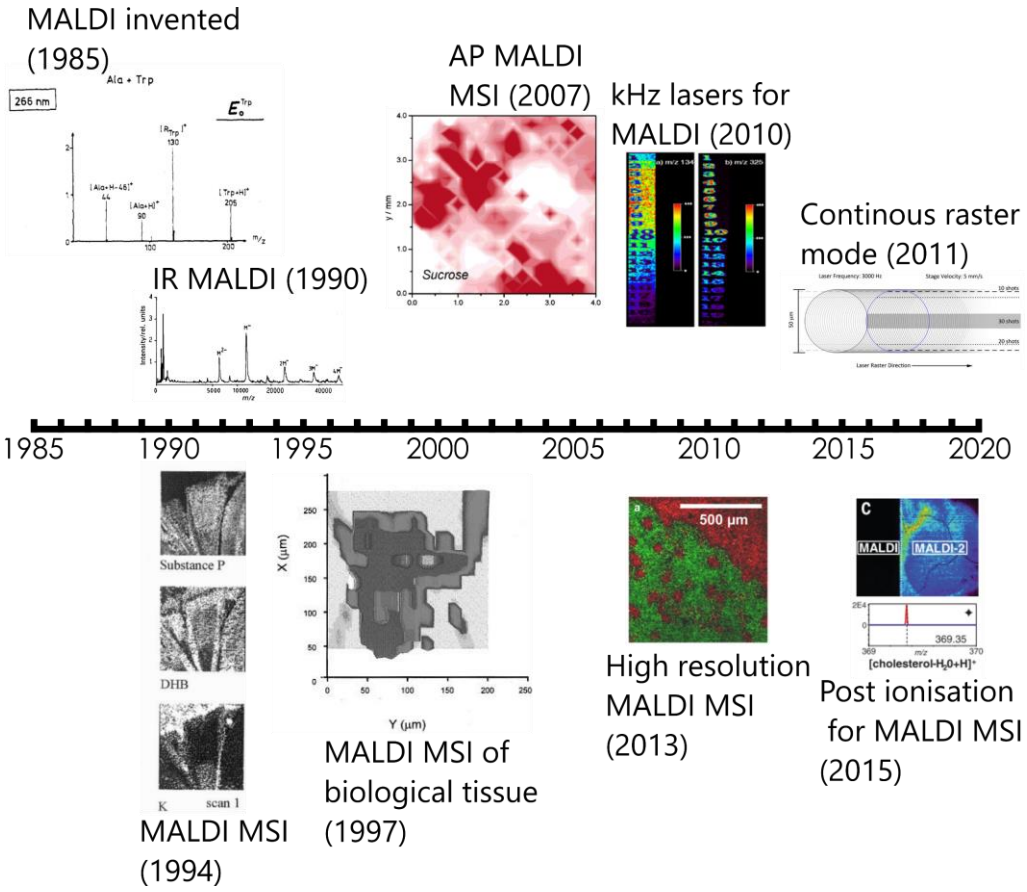


Figure 1.2. *Development timeline of MALDI MS and MALDI MSI. Inset figures, in chronological order, adapted from Refs. 2, 7, 8, 9, 11, 14, 12, 13 and 15.*

MALDI developed rapidly over the course of following decades (Figure 1.2), becoming routinely used for high mass analytes, particularly biomolecules. A wide variety of new matrix compounds were discovered, of which α-cyano-4-hydroxycinnamic acid (CHCA)[5] and 2,5-dihydroxybenzoic acid (2,5-DHB)[6] have become the most ubiquitous. The use of infrared wavelengths for MALDI (IR-MALDI) was also developed[7], although the majority MALDI research continues to use UV wavelength lasers; the technique will be referred to as UV-MALDI in this thesis unless specifically referring to MALDI at other wavelengths. UV-

MALDI has been coupled to a broad range of mass analysers enabling both high resolution and high throughput analysis of wide-ranging analytes.

1.2 - Ultraviolet Matrix-Assisted Laser Desorption\Ionisation Mass Spectrometry Imaging (UV-MALDI MSI)

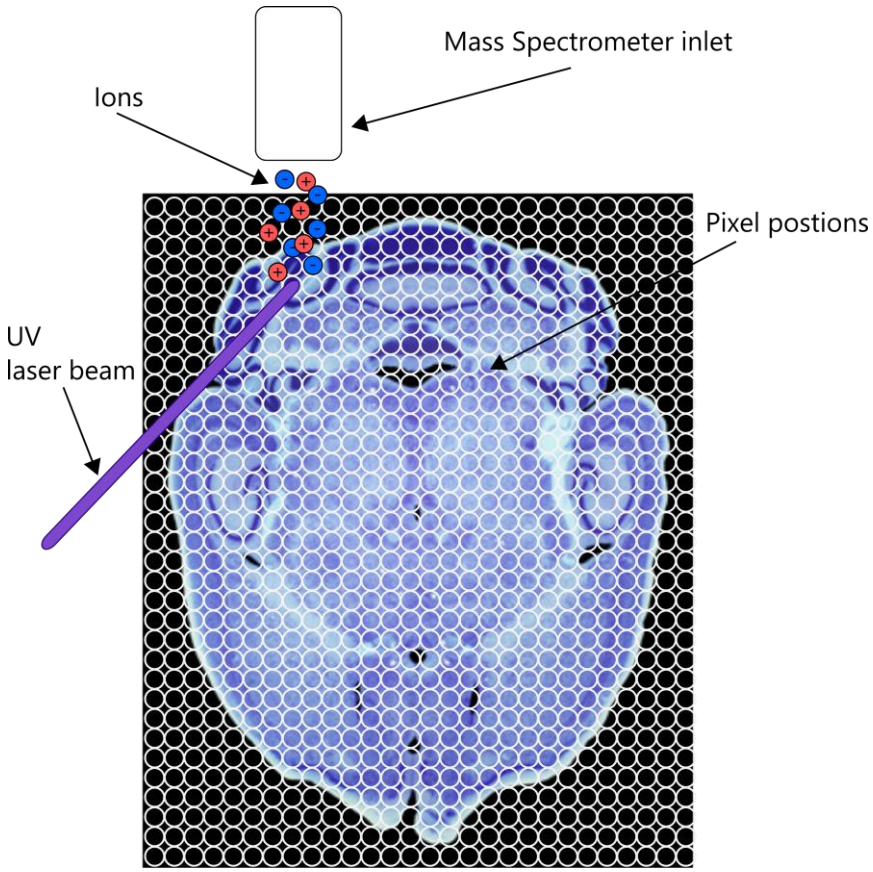


***Figure 1.3**. Diagram of UV-MALDI MSI operating in microprobe mode.*

Mass spectrometry imaging (MSI) is an application of mass spectrometry were mass spectra are collected in a spatially resolved manner from a sample surface (Figure 1.3). In doing so a multidimensional datacube is generated consisting of spatial coordinates (X, Y & occasionally Z), mass-to-charge values (*m/z*) and ion intensity. This datacube can be interrogated to determine the spatial distributions of detected ions, which correspond to molecular species within the sample.

There are two different configurations of UV-MALDI MSI, microprobe and microscope mode. The oldest, and by far the most common, is microprobe mode, whereby the laser is focused to a small area and used to interrogate the sample surface in a point to point wise fashion, where every analysed point represents a pixel in the resulting image. In microscope mode the laser is defocused extensively to irradiate the whole sample at once, ions are produced simultaneously across the sample surface and focused onto a position sensitive detector within the mass spectrometer.

UV-MALDI MSI was first demonstrated in a research poster by Spengler in 1994, to show the distribution of analytes within matrix crystals and distribution of metal ions in biological tissues[8]. In 1997 that Caprioli et al. demonstrated UV-MALDI MSI of biomolecules in biological tissues for the first time[9], albeit with very basic images that were more akin to profiling experiments. It wasn't until 2001 that Stoeckli et al. published the first UV-MALDI MS images of biological tissues as they are known today[10]. Further developments included atmospheric pressure MALDI MSI (AP-MALDI MSI), as well as the use of an infrared (IR) laser, both introduced by Li et al[11]. While both AP-MALDI MSI and the use of IR lasers bring many advantages, such as eliminating the need for samples to be held at vacuum and the ability to use water ice as a matrix, only a handful of commercial ion sources have been developed, with their application typically limited to custom-built system housed in a small number of research labs.

Significant increases in spatial resolution have occurred since the instruction of UV-MALDI MSI, with attainable pixel sizes for typical UV-MALDI MSI systems

around 30-50 µm and 5 µm in high spatial resolution instruments, sub-micron pixel sizes have even demonstrated on specialised systems[12]. The demands of high spatial resolution MSI has also driven increases in throughput through the adoption of continuous raster mode sampling[13] and high repetition rate lasers[14]. Similarly the smaller sampling volumes associated with the decreased pixel sizes and general low ionisation efficiency of UV-MALDI MSI has led to increasing efforts to improve limits of detection (LOD) and sensitivity through post-ionisation strategies involving lasers[15] or plasma[16]. Due to the large number of mass spectra that need to be acquired in an imaging experiment, which can typical range from anywhere between 10^4 to 10^6, UV-MALDI MSI is typically coupled to time-of-flight (ToF) or quadrupole time-of-flight (Qq-ToF) mass analysers, which have sufficiently high acquisition rates (>10Hz) to keep image acquisition times to acceptable levels. High mass resolution and mass accuracy analysers, for example ion traps such as the Orbitrap or those based on Fourier-Transform Ion Cyclotron Resonance (FT-ICR), are however being increasing used in UV-MALDI MSI. Compared to ToF based instruments these mass analysers can better discriminate between molecular species of similar mass and provide greater confidence to mass-based assignment of peak identities, making them superior for the identification of species in complex samples such as biological tissue. The primary drawback of these mass analysers is the low rate of data acquisition, typically a few Hz at best, which significantly increases imaging times.

1.3 - Factors influencing UV-MALDI MSI

1.3.1 - Matrix physiochemical properties

Due to its role in coupling the laser energy to the sample and generation of analyte ions, the properties of the matrix compound are of great importance in UV-MALDI MSI. Table 1.1 shows the some of the matrix physicochemical properties that are believed to be pertinent to the UV-MALDI process.

Table 1.1. *Primary matrix physicochemical properties relevant to UV-MALDI MS.*

Physicochemical property	**Relevance**
Optical absorption	Determines the uptake of laser energy by the matrix. All known UV-MALDI matrix compounds exhibit strong absorption bands in the near-UV (NUV) wavelength range (200-400 nm).
Photoluminescence	Photoluminescence processes limit the proportion of absorbed energy that is available for desorption and ionisation. Fluorescence is believed to be the most important process in UV-MALDI due to the ns timescales of the processes involved.
Proton affinity and gas phase basicity	Governs the extent of proton exchange between the matrix and analyte. A large difference in between matrix and analyte will favour protonation/deprotonation of the analyte. A similar importance is found for affinities for other cations (Na, K) and anions (Cl) typically observed in UV-MALDI.
Ionisation potential	Considered important in UV-MALDI ionisation theories that involve matrix ions as the primary source of ionisation
Heat capacity	Heat capacity governs the extent of heating in them matrix upon laser irradiation, as such it is one of the main thermodynamic properties governing material ejection in UV-MALDI.

1.3.1.1 - Optical properties

The interplay between matrix optical properties and the laser strongly determines UV-MALDI MS performance. The importance of matrix optical

properties has been acknowledged from the very first UV-MALDI experiments, and consequently numerous studies have been carried out to investigate these properties.

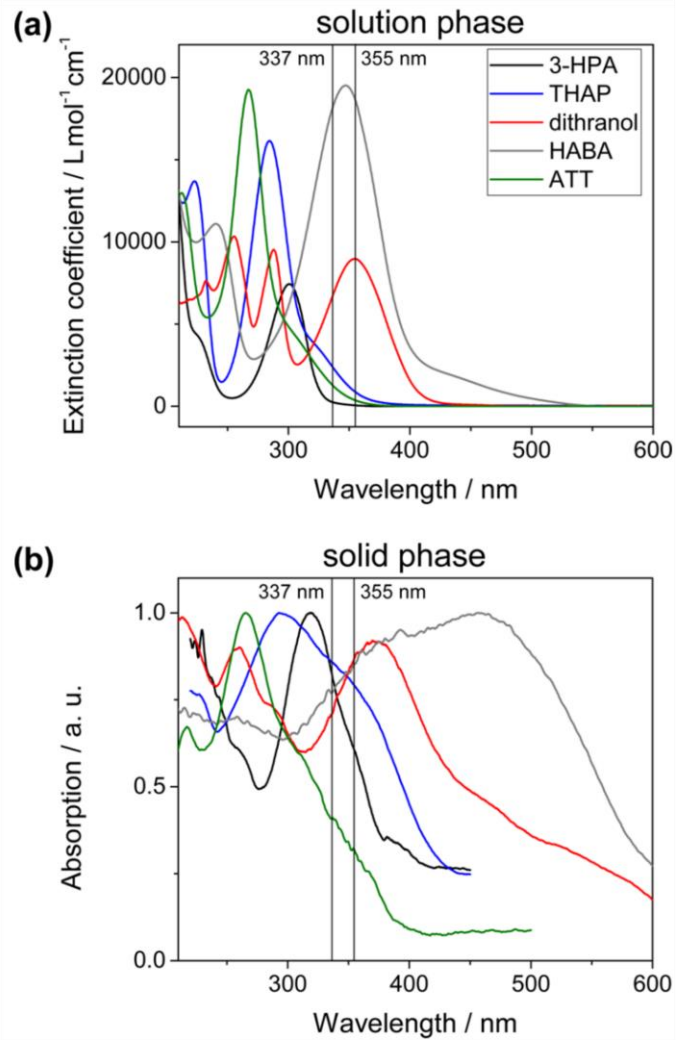


Figure 1.4. *Optical absorption spectra for five matrix compounds, 3-hydroxypicolinic acid (3-HPA), 2,4,6-trihydroxyacetophenone (THAP), 1,8-dihydroxy-10H-anthracen-9-one (Dithranol), 2-(4-hydroxyphenylazo) benzoic acid (HABA) and 6-aza-2-thiothymine (ATT), obtained in* ***a)*** *solution and* ***b)*** *solid phase. Figure adapted from Niehaus et al.*[17]

The optical absorption spectra for UV-MALDI matrix compounds can show extensive differences between solution and solid phase spectra (Figure 1.4). Typically these include a broadening and bathochromic shift of the absorption bands toward longer wavelengths[18–24]. These spectral effects have used to explain why certain compounds, e.g. 3-HPA (Figure 1.4b), are able to function as matrix despite having solution phase absorption peaks some distance from the standard UV-MALDI laser wavelengths. The appearance of new absorption bands, suggested as a result of dimer formation, has also been observed for some matrix compounds, such as CHCA and Coumarin 120[20].

The need for solid phase optical absorption spectra to properly describe UV MALDI matrix compounds has limited quantitative investigations into the role this property has in determining UV-MALDI results. Typically, quantitative measurements of optical absorption are acquired from solutions[2,6,25–29], which hinders comparability to usually crystalline UV-MALDI matrix compounds. Additionally, many reported solid phase spectra have been recorded using spectrophotometers operating with diffuse reflection geometry. These measurements can only show the relative changes in absorption across wavelengths for given a sample[22–24], limiting comparison between different matrix compounds. Normalisation of non-quantitative solid phase measurements to quantitative solution phase data has been used in the past[21], but due to the differences between solid and solution spectra the accuracy of such an approach is limited[20]. Fully quantitative solid phase optical absorption data for the UV-MALDI matrices CHCA, FA, 2,5-DHB and SA were reported by Allwood et al.[20]. To date quantitative solid phase data have been reported for

eleven matrix compounds in total [19,20,30], of which only 2,5-dihydroxybenzoic acid (2,5-DHB), sinapinic acid (SA) and CHCA remain widely in use today.

Comparison of matrix optical absorption to UV-MALDI MS results was reported by Allwood et al. who investigated four structurally similar benzoic acid derivates, 3,4,5-trihydroxybenzoic acid (THB) , 2,3-dihydroxybenzoic acid (2,3-DHB), 2,4-DHB and 2,5-DHB, comparing matrix absorption coefficient (α) with qualitative assessments of matrix performance[21]. A correlation between a higher matrix α at the wavelength of the laser used (337 nm) and better performance was found. Additionally, it was shown that significant improvement in matrix performance could be gained from better matching of the laser wavelength to the matrix absorption spectrum, as demonstrated by utilising a XeCl excimer laser (308nm) to strongly enhance the performance of the matrix TBH. Chen et al. [31] investigated generation of polypeptide ions with the matrix compounds CHCA, SA and β-indole acrylic acid across a range of near UV (NUV) wavelengths, finding that polypeptide ions were only detectable where the matrix α was >6 x10^4 cm^{-1}, and when the average absorbed energy per volume in the surface layer of the matrix of exceeded 8 kJ cm^{-3}.

The relationship between ion intensity, material ejection and ion yield, and matrix solid phase absorption profiles, was investigated in a series of studies from the Dreisewerd group[17,22–24]. Material ejection was found to closely follow the absorption profile of the matrices, suggesting UV-MALDI desorption is by and large determined by the total energy deposited in the surface layers of the matrix. Similarly, the total number of ions detected also closely tracked the

matrix absorption profiles, with optimal conditions for ionisation found near the absorption maxima of the matrices.

Radiative decay processes, particularly photoluminescence, are another important property of UV-MALDI matrices. This is because energy re-emitted as photons via photoluminescence will not take part in the UV-MALDI process, acting as a limiter on the available energy in the system for desorption and ionisation. Due to the nanosecond time scales over which the MALDI process occurs, the most significant photoluminescent process is generally agreed to be fluorescence[32].

An early study by Ehring and Sundqvist studied luminescence in ferulic acid (FA) and 2,5-DHB matrices, finding low quantum yields (<0.2) implying majority of absorbed laser energy is consumed by thermal and ionisation processes. The observed increase of fluorescent quantum yield at low temperatures (77K) was also used to explain the increase in threshold fluence with decreasing temperature[33]. Allwood et al. quantitatively measured the fluorescent properties of a set of five matrices, FA, SA, 2,5-DHB, CHCA and coumarin 120[32]. The fluorescent quantum efficiencies determined from the fluorescence measurements were used to determine the upper limits on energy available for heating of the matrix lattice, and consequently desorption. It was found that all matrix compounds had upper limits of >50% on the proportion of energy available for lattice heating, with 2,5-DHB evidencing the lowest (54%) and CHCA the highest limits (94%). These findings agreed with observed behaviours of these matrices in UV-MALDI MS experiments, with threshold fluences for

CHCA significantly lower than that of 2,5-DHB. The measurement of various radiative decay processes such as fluorescence is also particularly useful for determining the lifetime of photo-excited states of matrix molecules[34–36], which feature heavily in many of the proposed UV-MALDI ionisation models.

1.3.1.2 - Proton affinity and gas phase basicity

The tendency for formation of protonated and deprotonated ions in UV-MALDI naturally led to proton affinities being considered an important matrix property. Proton affinity (P_A) and gas phase basicity (G_B) are closely related properties describing the addition or removal of a proton to a molecule (M) in the reactions

$$M + H^+ \rightarrow [M + H]^+$$

$$M \rightarrow [M - H]^- + H^+$$

The G_B and P_A describing the negative change in free energy ($-\Delta G^o$) and negative change in enthalpy ($-\Delta H^o$), respectively. The two properties can be related using equation 1.1.

$$\Delta G = \Delta H - T\Delta S \qquad (1.1)$$

Where T is the temperature and ΔS is the change in entropy. As can be seen from the equation, the difference between P_A and G_B is that the latter also takes into consideration and changes in entropy to the molecule. The change in entropy is typically negligible for protonation reactions, unless large changes in molecular conformational or rotational symmetry numbers occur[37].

A number of studies have sought to measure P_A and G_B of UV-MALDI matrix compounds, either experimentally using kinetic[38], thermo-kinetic[39] or bracketing methods[37,40,41], or computationally using Density Functional Theory

(DFT) calculations[42–44]. The typical range of values for matrix P_A is 750- 950 kJ mol^{-1} and 800 – 910 kJ mol^{-1} for G_B. The manipulation of P_A and G_B was used by Jaskolla et al. as strategy to guide development of a series of rationally designed matrices[22,45,46]. The authors used the addition of halogen atoms, F and Cl, to decrease the P_A of CHCA based matrix derivatives. While only moderate success was achieved with fluorinated CHCA derivatives, a chlorinated CHCA derivative, 4-chloro-α-cyanocinnamic acid (Cl-CHCA) was found to possess substantially enhanced sensitivity and limits of detection when compared to CHCA, on account of its particularly low P_A (823 kJ mol^{-1}). Using Cl-CHCA the authors were able to demonstrate a tenfold improvement in sequence coverage (48%) from a 1 fmol bovine serum albumen (BSA) tryptic digest solution.

1.3.1.3 – Thermochemical and thermophysical properties

Due to the transition of solid to gas phase required in the UV-MALDI process, the sublimation properties of matrices have long been considered important. Price et al.[47] measured the sublimation properties of six DHB isomers using thermogravimetry, but did not find any correlation between sublimation enthalpy of the DHB isomer and performance as an effective UV-MALDI matrix. A more recent paper by Monte et al. studied the same set of compounds to provide more accurate measurements of sublimation properties[48]. While they found a different ordering of the compounds, similarly there was no discernible relationship with matrix performance. It is clear from these findings that the sublimation properties alone are not the main determinant for a compounds ability to act as successful matrix. That said the there are some practical considerations linked to matrix sublimation properties. The wide variety of

atmospheric conditions found in UV-MALDI ions sources, ranging from high vacuum (10^{-8} mbar) to ambient pressure, mean the absolute magnitude of matrix sublimation properties have a significant impact on the practicality of using a given matrix in an ion source. While many common matrices, such as CHCA, are stable even at high vacuum, matrices such as *para*-nitroaniline (PNA) and nor-Harmane will rapidly sublimate at room temperature under such conditions. These matrices are thus limited, particularly for imaging applications where acquisition times is in the order of hours, to use in AP-MALDI or intermediate pressure sources[49].

The intense laser radiation present in typical UV-MALDI conditions leads to significant heating of the matrix, therefore the thermal stability of a matrix is an important factor to consider. Laser induced degradation of the matrix has long been suspected of causing an experimental feature of UV-MALDI MS termed the "shot effect", wherein the analyte ion signal from a sample region at the threshold fluence rapidly decays with successive laser pulses but can be recovered by irradiation with a higher laser fluence. This shot effect is highly matrix dependant, with common matrices CHCA and SA evidencing it[50,51]. The shot effect has also been suggested as the origin of various non-linear behaviours observed UV-MALDI MSI experiments using kHz repetition rate lasers in conjunction with continuous raster mode[52].

Tarzi et al. [53] investigated the effects of temperature on the stability of the UV-MALDI matrices CHCA ,2,5-DHB, 2,4,6-Trihydroxyacetophenone (THAP), SA, nor-Harmane and Harmane. Of the matrices studied, both CHCA and SA showed

evidence of decomposition upon heating. The authors used H^1NMR and ESI MS techniques to unambiguously characterise the decay products of the two matrices, identifying that purely thermal rather than photochemical processes were behind the shot effect. Further investigations of the thermal stability of dihydroxyacetophenone (DHAP) isomers, 2,4-DHAP, 2,5-DHAP, 2,6-DHAP and 2,5-DHAP, found that all matrices were stable after heating above their melting points.[54]

1.3.2 - Laser irradiation conditions

1.3.2.1 - Laser fluence and irradiated area

Perhaps one of the most important laser parameters in UV-MALDI is the delivered energy per unit area, known as laser fluence. Fluence is typically defined in units of J m^{-2}, although J cm^{-2} is also sometimes used. The importance of fluence as the key laser energy parameter was established in the early years of UV-MALDI through experiments comparing of UV-MALDI at different laser pulse durations[55,56], where it was found that the rate of energy deposition (irradiance) had minimal influence on ionisation efficiencies. A further modification of the relevance of fluence in UV-MALDI was recently provided by Knochenmuss[57], who applied his Coupled Physical and Chemical Dynamics (CPCD) theoretical UV-MALDI ionisation model to explain experimental results on the wavelength and fluence dependency of ion intensity reported by Soltswich et al[24,58]. Knochenmuss proposed that the total photon number per unit area was the actual relevant parameter, although as UV-MALDI is almost universally conducted at a few fixed, closely matched wavelengths, the use of fluence is still appropriate in most instances. For example, the difference in

photon number per unit area at fixed fluence between the two most prevalent UV-MALDI laser wavelengths, 337 nm and 355 nm, is only ~5%.

One of the most striking features associated with fluence in the context of UV-MALDI is the effect on the evolution of ion intensity, particularly the sudden onset of ion production once a certain fluence is reached. This feature is termed the "threshold fluence", or sometimes "ionisation threshold", and has been the focus of significant interest since the beginning of UV-MALDI. The existence of a physical threshold for ion generation has been called into question by Westmacott et al., who used an axial ToF instrument configured with either pulse-counting or analogue ion detection methods, and an orthogonal Qq-ToF using pulse-counting methods[59]. The differences in observed threshold fluences found with the different instrumental configurations led the authors to conclude that the ionisation thresholds were more a feature of instrumental limits of detection and ion transmission efficiencies than a true physical event. Post ionisation studies have revealed that the threshold for desorption of neutral species from a sample is significantly lower than that observed for the detection of ions[60,61], which when considered alongside the low ionisation efficiencies (10^{-7} – 10^{-9} for matrix, 10^{-3} – 10^{-8} for analytes) observed for UV-MALDI, could support the view of ionisation threshold being a primarily a feature of instrumentation.

Beyond the threshold fluence detected ion intensity increases exponentially, before ultimate saturating at a higher fluence, sometimes termed the "plateau region". Overall the relationship between laser fluence and ion intensity takes a characteristic "s" shape, approximating the form of a logistic function.

Traditionally the relationship between ion intensity (I) and laser fluence (H) was described in terms of a simple power law (Equation 1.2)

$$I \propto H^m \qquad (1.2)$$

Where the m factor is often considered characteristic of certain experimental conditions, although no connection any physical meaning has been ever determined[62]. m values in the literature range from 1 – 10, and have been shown to be strongly influenced by the matrix[63] and the laser spot size[60,63], as well as to a lesser extent instrumental configuration[59,64].

More recently Soltwisch et al. proposed a more comprehensive model (Equation 1.3) of the relationship[24,58], taking into account the plateau region seen at high fluences.

$$I = \hat{I}\frac{(H-H_{thr})^m}{(H_k-H_{thr})^m+(H-H_{thr})^m} \qquad (1.3)$$

This function makes use of three additional fitting factors as approximations for important characteristics of the ion intensity curve. H_{thr} describes the threshold fluence and $\hat{I}$ the maximum ion intensity of the curve. The H_k parameter corresponds to the fluence at which the highest ion yield, and thus experimental sensitivity may be obtained[24]. m in equation 1.3 retains a similar function to that in equation 1.2, but is typically a factor of 0.75 smaller due to the influence of the other parameters[24].

The effects of laser fluence on spectral quality in UV-MALDI is highly dependent on the type of instrument used. Prior to the introduction of delayed extraction methods, laser fluences were limited to around the threshold fluence for UV-MALDI on axial ToF instruments. On these instruments higher laser fluences

were found to result in serve reductions in mass resolution and mass accuracy, and increased levels of fragmentation. This was due to multiple factors, including the broader ion velocity distributions, increased variation in the position of ion origins, and increased collision with desorbed neutrals found at higher laser fluences[65]. For UV-MALDI on other mass spectrometers, such as orthogonal Qq-ToF and ion traps the laser fluence is less of a concern, as conditions during ion production are effectively decoupled from the mass analyser measurement; although as a general rule, excessively high laser fluences are associated with increased analyte fragmentation and lower signal to noise with all mass spectrometers[66,67].

A notable feature of UV-MALDI MS is the strong dependence of the ionisation threshold fluence, and by extension the full laser fluence ion intensity curve, on the total size of the area irradiated by the matrix. Typically termed the "spot size effect", this is evidenced by an inverse relationship between total irradiated area and ionisation threshold, whereby as the spot size decreases the ionisation threshold fluence increases. Dreisewerd et al. carried out a detailed study of the spot size effect, using a flat top beam profile laser and different apertures to investigate detected ion intensities in UV-MALDI MS with spot sizes from 10 - 200 μm. This study also made use of a second laser for post-ionisation of desorbed neutral molecules from the sample, allowing desorption processes to be studied in isolation from ionisation[63]. They observed that threshold fluences for ionisation spanned over an order of magnitude from the smallest to the largest laser spots used, and that the slope of the ion intensity/laser fluence curve became shallower as spot size decreased. Interestingly they found that

the change in threshold fluence for ion detection with area followed a cubic rather than linear relationship, the latter being what would be expected if the effect was just the result of more of the sample being irradiated at larger spot sizes. Unlike the directly formed ions, the post-ionised desorbed neutrals were found to have a quadratic relationship with the spot area. The authors postulated that the non-linear relationship between spot size and detected ions/desorbed neutrals arose because, for a similar number of particles desorbed from smaller areas more of the material would have to come from deeper within the matrix, a process which may hindered by the layers above.

The cubic nature of the spot size effect on ion detection was confirmed in a subsequent study by Qiao et al., who also observed that the dependence became linear for fluences around the plateau region for the curves[60]. They also observed that the ion yield per unit area, here meaning the number of ions detected per unit area, was highest for the smallest spot sizes, suggesting that smaller spot sizes resulted in better limits of detection and sensitivity.

A recent study by Niehaus and Soltwisch used a combination of photoacoustic and laser post-ionisation measurements to explore the mechanisms behind material ejection at different spot diameters, spanning 7-200 μm[61]. The photoacoustic measurements revealed that material ejection was only dependant on fluence, with no spot size influence observed once the data was normalised to laser spot area (Figure 1.5). They also observed that, because of different optimal fluences required at different spots sizes, that material ejection from the smaller laser spot sizes was primarily though ablation while desorption

was dominant at large spot sizes. The relatively cooler material ejection caused by ablation processes dominant at small spot sizes was also found to result in reduced analyte fragmentation.

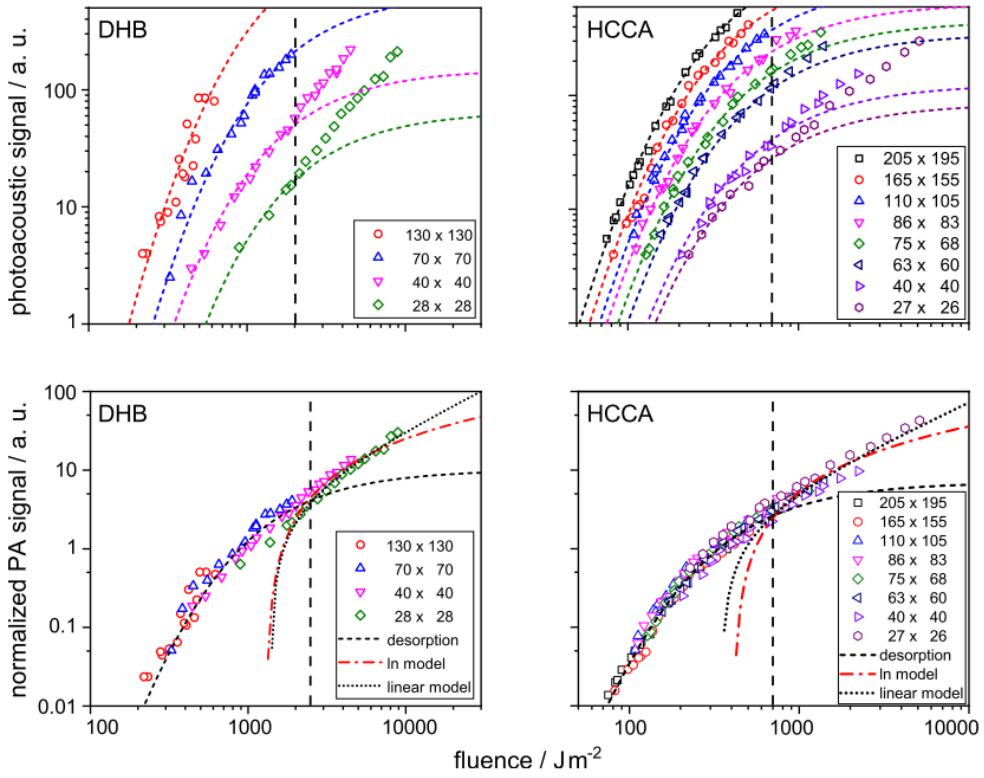


Figure 1.5. *UV-MALDI material ejection step as probed by photoacoustic analysis. PA signals were recorded as a function of laser fluence and rectangular flat top spot size from microcrystalline preparations of neat 2,5-DHB (DHB) and CHCA (HCCA) matrices (upper graphs). The bottom graphs display the same data set after normalization to the focal spot size. The coloured dashed lines depict a best fit of the quasi-thermal desorption model to the data, the red dash-dotted lines a best fit of the ln model and the black dotted lines a fit to the linear model. Figure and caption adapted from Niehaus et al*[17].

In contrast to the photoacoustic measurements they found that the optimal desorption fluences for post-ionisation showed a strong dependence on laser spot size. To explain this discrepancy, the authors proposed that the spot size effect arises from thermodynamic development of the plume and is related the relative speed at which desorption plumes from different spot sizes can dissipate their internal energy. They demonstrated theoretically that for small laser spot sizes, the resulting plume can rapidly lose its internal energy, therefore higher laser fluences are needed to restore favourable thermodynamic conditions for ionisation.

A limited number of studies have looked at the effect of spot size in UV-MALDI MSI have been reported[67,68]. For the most part the same trends seen in UV-MALDI MS are found in imaging experiments, although some interesting phenomena have been reported. Wiegelmann et al. investigated the influence of laser spot size in UV-MALDI MSI operating in oversampling mode[68]. They found that at a fixed pixel size of 20 µm, increasing laser spot size above 50 µm resulted in a gradual decrease in spatial resolution, overestimating the width of imaged tissue structures (~50 µm) by up to two-fold. The influence of spot size was found to vary with tissue region, this was considered likely as a result of tissue region specific variation in threshold fluence also identified by the authors, and previously by Steven et al.[67]

1.3.2.2 - Laser repetition rate

Repetition refers to the frequency of emitted pulses from a pulsed laser source. For UV-MALDI the importance of repetition rate is related to analytical

throughput, as the more pulses that can be delivered to the sample surface, the less time is needed per acquisition.

Originally UV-MALDI MS was conducted using relatively low repetition rate (10-30 Hz) N_2 lasers. This was because at the time such lasers were relatively inexpensive and able to deliver higher pulse energies than contemporary higher repetition rate lasers. With advancements in laser technology, particularly the spread of low cost diode-pumped solid state (DPSS) lasers, high repetition rate (>100 Hz) lasers began to be more frequently used for high throughput UV-MALDI MS[69,70], and are today the most common laser type found in UV-MALDI MS.

Given the large amount of data typical in UV-MALDI MSI, imaging studies were particularly well suited to take advantage of the introduction of high repetition rate lasers. The first application of a high repetition rate laser for UV-MALDI MSI was demonstrated by Trim et al. who used a Nd:YVO_4 DPPS laser capable of operating up 20 kHz[71], coupled to a orthogonal Qq-ToF mass spectrometer. The authors were able to evidence a significant reduction in the time required for image acquisition compared to the instruments N_2 laser. An optimum repetition rate was found at around 5-10 kHz, although this was attributed to the energy characteristics of laser used, rather than any inherent changes in desorption or ionisation process. The dependence of ion intensity with repetition rate was briefly explored by Spraggins et al. in a study demonstrating the use of a prototype UV-MALDI MSI instrument for imaging applications[13]. It was reported that, for a fixed number of delivered pulses, the ion intensity reduced in an

approximately linear fashion with increasing repetition rate. This was attributed to the increasing degree of overlap between the pulses as the repetition rate increases, the authors proposed a limit of < 50 pulses/unit area as a rule for maintaining good experimental results.

1.3.2.3 - Wavelength

For most of the history of UV-MALDI MS the deciding factor on which wavelengths are used has been for the most part driven by considerations other than the analytical suitability. The very earliest UV-MALDI MS experimentation was conducted at wavelengths of 355 nm and 266 nm, obtained using the third and fourth harmonics of Nd:YAG lasers. This was then rapidly replaced by a standard operating wavelength of 337 nm, due to the availability of cheaper and higher powered N_2 lasers. Later on, and continuing to the present day, the proliferation of DPPS laser has moved the standard operating wavelengths back to 355 nm of the Nd:YAG laser, or the closely located 349 nm obtained from Nd:YVO_4 based lasers. During these developments various researchers have demonstrated MALDI at wavelengths outside the UV region. IR MALDI was first demonstrated by Overberg et al. who used Er:YAG laser operating at 2.94 μm[7]. The use of this wavelength is particularly interesting for MALDI MSI of biological sample as it enables access to OH vibrational absorption bands, allowing endogenous water, or an ice layer on frozen tissue, to act as a matrix[72]. Visible wavelengths for MALDI have also been explored in numerous studies[73–76], but despite some notable advantages, namely less fragmentation than UV and less sample consumption than IR, this approach has been only moderately successful compared to the other wavelength regimes.

As described earlier in this thesis introduction, the effect of wavelength in UV-MALDI is closely tied to the absorption characteristics of the matrix being used, with a strong dependence of detected ion intensities to the matrix absorption at the wavelength being employed being reported in numerous studies[22,24,31]. Aside from this, the other important consideration regarding UV-MALDI at different wavelengths is the relative energies of the photons being delivered to the sample, as photon energy increase inversely to the wavelength of the laser. While it may be tempting to invoke single photon ionisation processes, this is unlikely given that typical ionisation potentials (IP) for UV-MALDI matrices are in the range of 7.5-10 eV[77,78], which corresponds to single photon energies at wavelengths between 123-165 nm, well outside the range of wavelengths explored for use in MALDI (193 nm -10.6 μm). While single photon ionisation is not a realistic prospect, proposed energy pooling matrix ionisation process[79], which requires the pooling of energy from at least 3 photons, would almost certainly be affected. For example, taking the typical matrix IP range of 7.5-10 eV, the cross over to ionisation from the pooled energy of two photons would occur between 300-330 nm, tentative evidence of this crossover behaviour was recently observed by Neihaus et al.[17]

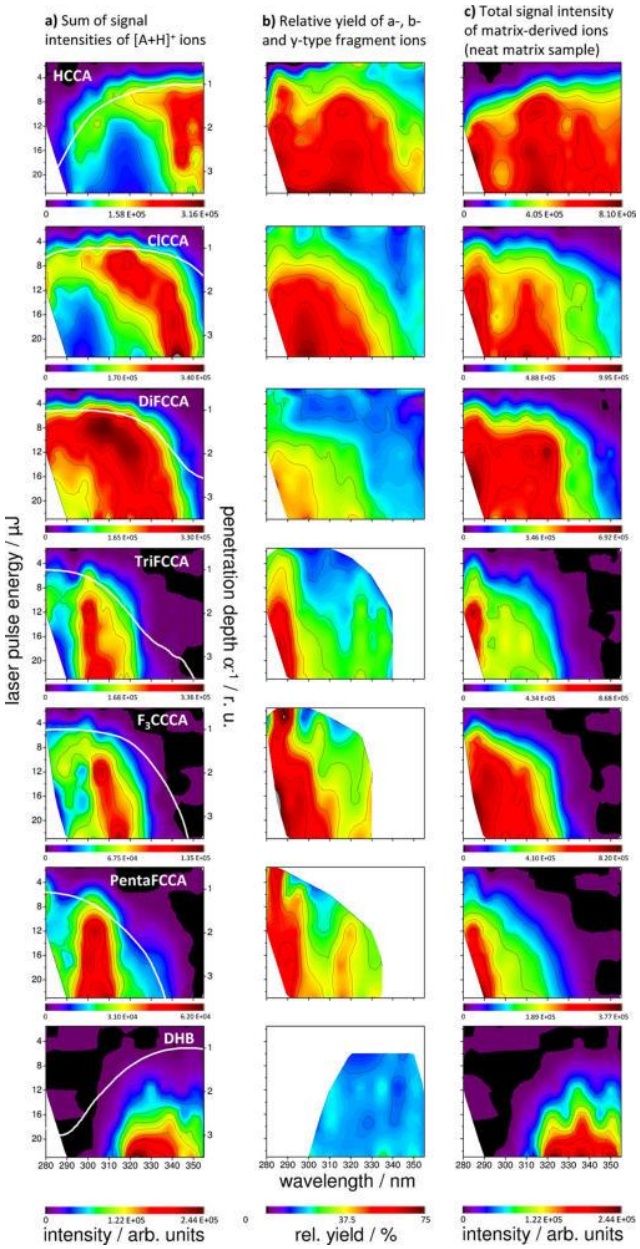


Figure 1.6. *Ion intensity heat maps of different groups of species generated from two standard UV-MALDI matrixes (CHCA and 2,5-DHB) and five halogenated CHCA-derivatives, as a function of wavelength and laser pulse energy.* ***a)*** *Summed $[A+H]^+$ intensities of five peptides. The laser penetration depth ($\alpha-1$) is shown as a white solid line.* ***b)*** *Yield of a-, b-, and y-fragments of the five peptides relative to the intensity sum of all analyte-derived ions.* ***c)*** *Total ion intensity of all matrix-derived ions generated from a neat matrix preparation. Figure and caption adapted from Soltwisch et al*[22].

Another factor arising from the changing photon energy with wavelength is the degree of photochemical interactions in the sample. Increased levels of matrix adduct formation have been observed at shorter wavelengths, with Horneffer et al. finding enchantment of such effects at 308 and 266 nm in comparison to 337 and 355 nm, and 2.94 μm[21]. Fragmentation arising from the higher photon energies found at shorter wavelengths can also be a concern, as shown by Soltwisch et al. (Figure 1.6) who observed reduced intact ion intensities and increased degrees of fragmentation for both analyte and matrix, at wavelengths below the absorption maxima of various matrices[22,24]. Although Knochenmuss suggests this may be partly affected by the reduction in number of delivered photons, for the same pulse energy, that would occur at shorter wavelengths[57].

Moving to wavelengths above the typical UV-MALDI range has been shown to increase the formation of multiply charged ions[31,80], something not typically seen in UV-MALDI, and which has potential benefits for the analysis of peptides, proteins and other large molecules that would be otherwise inaccessible to instruments with limited mass ranges. Potential evidence for changing ionisation mechanisms was observed by Niehaus et al., who noted significant drop off in ion signal at visible wavelengths even in the presence of sizable matrix optical absorption[17].

1.3.2.4 - Pulse duration

It is well understood from laser ablation studies that pulse duration (τ_p) can have a significant effect on the desorption of material, coming about due to changes in ejection mechanism brought on though the irradiated material volumes

operating in the thermal and stress confinement regimes[81]. Thermal confinement conditions arise when the pulse duration is shorter than the thermal relaxation time of the irradiated material, while under stress confinement conditions the pulse duration is comparable or shorter than the materials mechanical relaxation time[82]. The precise time domains where each regime operates are governed by the properties of the interacting material, and the wavelength of the laser. For UV-MALDI matrices irradiated with lasers operating at UV wavelengths of 337 nm or 355 nm, as is typical of the majority of UV-MALDI MS experiments, thermal confinement occurs for pulse durations between ~10 ns and ~50 ps, below which stress confinement conditions begin to apply[62].

Typical pulse durations in UV-MALDI MS range from 0.5-10 ns, placing the vast majority of UV-MALDI experimentation in the thermal confinement regime. Excimer lasers, occasionally used in UV-MALDI studies, can have pulse durations up to 25 ns, putting them above the thermal confinement regime, but typically these lasers operate at shorter wavelengths (100-300 nm) than standard in UV-MALDI. In this wavelength region most organic compounds exhibit intense absorption bands, which may act as a counterbalance to the effect of longer pulse duration, due to the strong influence of optical penetration on thermal relaxation time.

Experimentally there has been a few studies looking at the effects of pulse duration outside of the typical UV-MALDI range. Demirev et al. investigated the effects of ultrashort pulse duration in UV MALDI MS with an excimer laser

operating at 248 nm and 496 nm, with a pulse duration of 560 fs. In the study they compared the use this laser to a standard ns N_2 laser for the desorption and ionisation of insulin, myoglobin and trypsin in the matrix ferulic acid (FA). It was found that compared to the ns laser, fs pulse durations resulted in lower analyte ion intensities and evidenced greater fragmentation; additionally, while all the analytes were successfully detected using the ns laser, the fs laser was only successful at producing ions of one of the analytes (insulin). One particularly important observation from the study was that the threshold energy for ionisation was similar between the two lasers, this was used to support the conclusion that ionisation in UV-MALDI MS is dependent on the amount of laser energy deposited into the sample (fluence), rather than the rate it is deposited (irradiance).[55]

A similar study by Wichmann et al. employed a Ti-Sapphire laser (60 fs, 400 nm and 800 nm), finding increased fragmentation and reduced intact molecular ion intensities for the peptide angiotensin II when compared to a N_2 laser (337nm, 3 ns)[83]. Interestingly, the use of fs pulses enabled the collection of spectra at a wavelength (800 nm) where the employed matrix system (CHCA/SA mixture) showed no measurable absorption. This effect was explained as arising from multiphoton absorption, which is known to become significant at the photon densities typical of ultrashort laser pulses. A follow up study by the same authors used the control of laser pulse chirp to investigate the same sample system across a range of pulse durations spanning 120 fs to 6 ps, confirming the role of multiphoton ionisation. Furthermore, the ratio of analyte cationization to

protonation was also observed to show a modest increase with decreasing pulse duration. [84]

The effects of pulse durations across the typical UV-MALDI range has been investigated by Dreisewerd et al., who made use of two N_2 lasers with pulse durations of 3 ns and 500 ps with a range of matrices and anayltes[56]. It was found the response of ion signal to increasing laser fluence, as well as the obtained spectra, were identical at both pulse durations. This result further supported the conclusions of Demirev et al. regarding the importance of laser fluence in UV-MALDI.[55], by resolving ambiguities regarding the effect of laser wavelength present in the earlier study. A more recent study by Liang et al. looked at a similar range of pulse durations (150 ps – 1 ns) with CHCA, 2,5-DHB and SA. Similar to the Dreisewerd study, spectra remained unchanged across the range of pulse durations, additionally the ion yield and velocity distribution of desorbed neutral molecules were similarly unaffected[85].

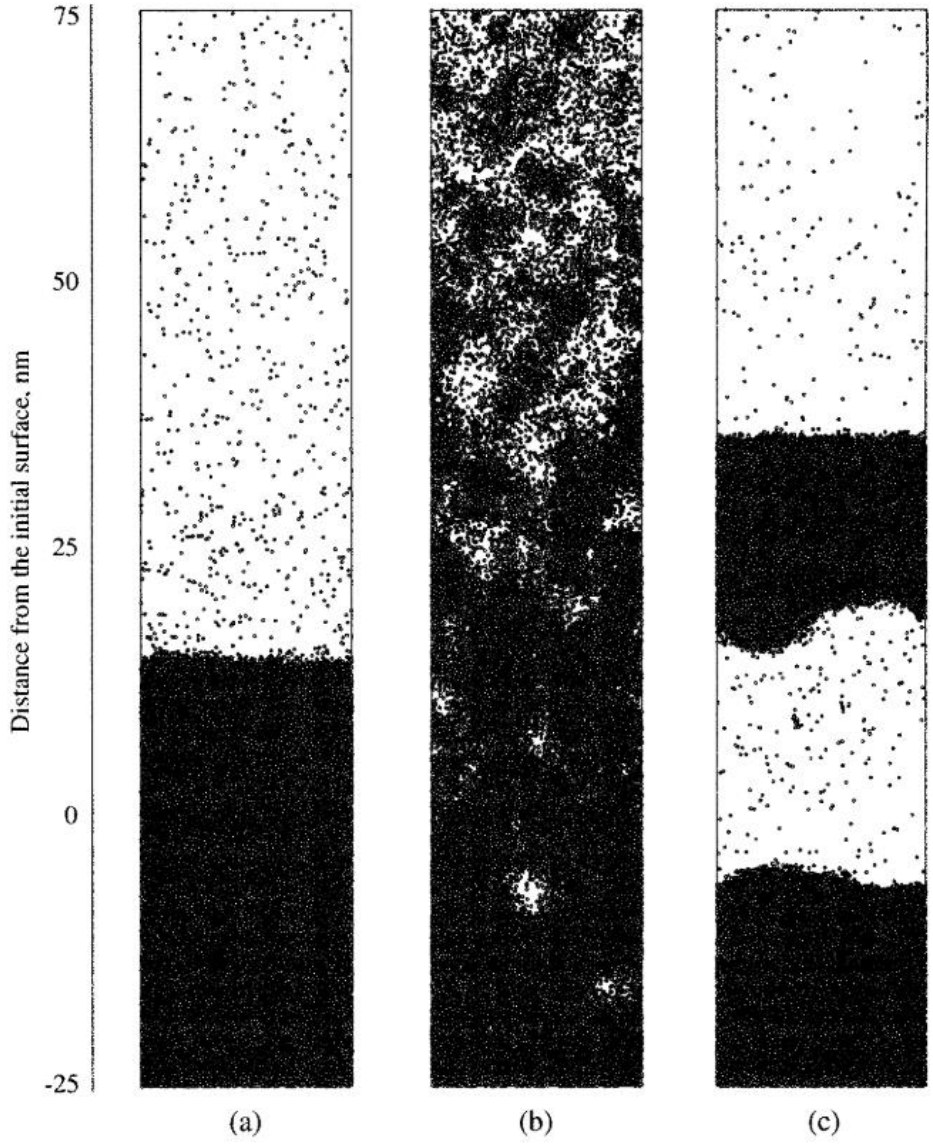


Figure 1.7. *Snapshot of MD simulations, showing* ***a)*** *desorption and* ***b & c)*** *ablation material ejection regimes. Irritation parameters in* ***a & b)*** *correspond to thermal confinement conditions (τ_p = 150 ps) at* ***a)*** *low (34 J m^{-2})* ***b)*** *high fluences (55 J m^{-2}). Conditions in* ***c)*** *correspond to stress confinement conditions (τ_p = 15 ps, 31 J m^{-2}). Figure reproduced from Zhigilei & Garrison.*[86]

In a series of molecular dynamics (MD) studies carried out by Garrison, Zhigilei and co-workers explored the effects of pulse duration (τ_p = 15 ps , 150 ps, 1 ns) on desorption in UV-MALDI like systems[82,86–88]. Two distinct regimes of material

ejection regimes were found to exist, depending on whether the process was occurring under thermal or stress confinement conditions (Figure 1.7). Material ejection under stress confinement conditions, found at the shortest pulse durations (15 ps), was driven by the formation of significant cavitation within the irradiated volume, leading to an ablative like process characterised by spallation of large, energetically "cool" fragments from the surface (Figure 1.7c). Under thermal confinement conditions (τ_p =150 ps & 1 ns) the material ejection process was found to occur either through thermal desorption at low laser fluence (<35 J m^{-2})., or ablative, phase explosion mechanism at higher fluence (>40 J m^{-2}). It was also observed that the threshold for the onset of ablative material ejection was approximately 20% higher under thermal confinement conditions.

A further MD study carried out by Knockenmuss and Zhigilei combined the previous models of material ejection with CPCD ionisation theory to provide a comprehensive simulation of influence of pulse duration and fluence on primary and secondary ionisation processes[89]. Shorter pulse durations (35 ps & 360 ps) were found to generate an initial ion concentration up a 6-fold higher compared to longer pulse durations (3 ns), but the differences rapidly equalised across nanosecond timescales due to ion recombination, consequently ion yield was found to be only weakly dependant on pulse duration over the ranges studied.

1.3.2.5 - Beam profile

Despite being just an important to the generation of ions as the more well studied parameters of laser fluence and spot size, the distribution of energy within the laser spot is an often-overlooked aspect of UV-MALDI MS. Holle et al. were the first to explore the effects of beam profile in UV-MALDI MS, seeking to understand reason behind the inferior performance of Nd:YAG lasers, at the time, when compared to N_2 lasers[90]. A spatial light modulator was used to generate structured beam profile with a Nd:YAG laser. The performance of these structured profiles was then compared against the native Gaussian profile of the laser, as well as a N_2 laser, with its native structured beam profile. It was found that the use of the Nd:YAG with a Gaussian profile resulted in lower ion intensities, poorer mass resolution and lower sensitivity when compared to the other laser setups. The Nd:YAG structured beam profiles were found to be as good, and in many instances superior to the N_2 laser. The authors concluded that structured beam profiles were superior for most UV-MALDI MS applications, including imaging. Further beam profile manipulation experiments were carried out by Qaio et al. who used 2 m and 10 m long optical fibres to homogenise the beam profiles of Nd:YAG and N_2 lasers for UV-MALDI MS experiments[60]. It was found that improved beam homogenisation, achieved using either longer fibre lengths (30 m) and/or mechanical twisting of the fibres, significantly improved UV-MALDI MS sensitivity.

The use of Gaussian laser beam profile was investigated by Zavalin et al. for high resolution UV-MALDI MSI of proteins, using a commercial UV-MALDI ToF instrument originally designed to produce a structed laser beam spot down to

20 µm diameter [91]. They compared the structured beam for imaging of tissue at a range of pixel sizes. It was found that while structured beam profile of the instrument provided better imaging performance at larger spot sizes (>20 um), when the laser spot approached diameters nearing that of the structured beam features (5-15um), the Gaussian beam profile proved superior. A different paper by the same authors also showed how the applications of a pinhole to spatially filter out the extra spatial modes of a Gaussian beam could be used to further improve UV-MALDI MSI the focusing of the laser, enabling improvements to spatial resolution[92].

A particularly interesting use of beam profile manipulation was demonstrated by Sherrod et al. who explored the use of dynamic spatial modulation of beam profiles via a digital micromirror device (DMD) to increase spatial resolution and reduce acquisition times in UV-MALDI MSI[93]. This DMD consisted of a 1024×768 array of individually addressable 13x13 µm micro-mirrors, enabling the generation of arbitrary beam profiles based on a digital image input. Using the DMD system the authors demonstrated the ability to individually address peptide microarray spots for UV-MALDI MS analysis, without the need to move the sample stage. Unfortunately, the application of the DMD system for UV-MALDI MSI was seemingly never continued, which in this authors opinion represents as missed chance, given the obvious benefits such an approach could have for various imaging applications.

The overall shape of the laser beam profile is a particularly important characteristic in UV-MALDI MSI studies. This is because the chemical

information collected from the irradiated region is ultimately represented as square pixel in an image, thus significant deviation of laser beam shape from this could lead to distortions of the resulting chemical species distributions in the MSI data. This property is especially relevant where the laser is operating in oversampling or continuous raster mode, as the beam shape will have a large influence on many factors, not limited to, number of delivered pulses per unit area, spatial resolution and limits of detection.

A comparison of square and round beam shapes was conducted by Steven et al, who used optical fibres of different geometries for the analysis for thin film systems and tissue imaging[67]. Interestingly they found that for the same beam size, round fibres resulted in a lower threshold fluence for ionisation than square, on both thin film at tissue. Which was attributed to the larger average feature sizes of the laser intensity speckle pattern within the beam profile produced by the round fibres.

The same threshold fluence relationship was observed in a comparison of square flat top and round Gaussian beam profiles generated by a fundamental beam shaper (FSB) in a recent imaging study by Wiegelmann et al[68]. They reported that, compared to the Gaussian beam, a square flat-top beam profile resulted in a better signal-to-noise ratio in oversampling spot mode, but had no obvious effect in continuous raster mode acquisition. Although in this authors opinion their raster imaging data does indeed show an enchantment, albeit to a lesser extent than the oversampling spot mode data.

1.3.2.6 - Laser sampling modes in UV-MALDI MSI

The method by which the laser interrogates the sample highly important in UV-MALDI MS, particularly for imaging experiments, which is either in the form of discrete sampling of fixed points on the sample, or continuous raster sampling of the surface. The discrete sample mode, commonly referred to as "spot" mode, usually involves the delivery of a fixed number of laser pulses to a position, generating a mass spectrum, before the sample stage is moved to the next position and the process repeated; spot mode is the predominant sampling mode in classical UV-MALDI MS.

When spot mode sampling is used in an imaging context, the pitch between the different sampling positions defines the pixel size of the image. If the pixel size is larger than the diameter of the laser beam the imaging acquisition is said to be under sampling. Conversely when the pixel size is smaller than the beam diameter there will be an overlap of regions irradiated by the laser, a concept known as oversampling[94]. Oversampling is used widely in UV-MALDI MSI as it allows the imaging of features smaller that laser beam, effectively increasing the achievable spatial resolution without the need for alteration of the laser optics. A caveat associated with oversampling is that complete removal of the matrix from the current position must be achieved before the next position is sampled. This is to prevent residual matrix from analysed pixel positions interfering with subsequent pixels, which would lead to a reduction of spatial resolution of the final image. That said, the Gaussian beam profile found in most lasers used for MALDI MSI makes this effect almost impossible to eliminate completely. Oversampling can also be used to conduct different mass spectrometry

experiments at similar positions on the same, a good example of which was demonstrated by Hansen et al. who used a spiralled oversampling mode to carry out up 9 different mass spectrometry experiments from the same pixel position[95]. They used this approach to image a maize leaf at 10 µm pixel size, simultaneously collecting mass spectra with two different mass ranges, each with associated data dependent MS/MS spectra, at every pixel position in the image.

Compared to spot mode, the use of continuous raster mode acquisition has some significant advantages for imaging applications[13,52,68,96–98]. In continuous raster mode the instrument stage is constantly moving while the laser is firing, resulting a quasi-continuous stream of ions into the mass spectrometer. The pixel size is then defined by the rate at which the mass spectrometer collects spectra, the speed of the stage movement and the vertical pitch of the raster lines. The most immediate benefit of continuous raster mode is the significant increase in rate of data acquisition, with improvements of up to 10-fold commonly reported[13,97]. Improvements to sensitivity are possible, as the rastering beam more efficiently samples the matrix when compared to discrete sampling methods[68].

Despite the benefits, there are some experimental complexities associated with the use of raster mode. As continuous raster mode is, in-effect, an extreme example of oversampling, when combined with Gaussian beams, a degree of spectral interference between adjacent pixel is to be expected, which may result in a reduced spatial resolution. Additionally, the use of circular beam shapes will

resulting in different regions across the height of the beam experiencing different numbers of laser shots[13]. The use of flat-top laser beam profiles, and square beam shapes have been demonstrated to address these issues[68], but as of yet remain rarely used. Significant changes in the optimal fluences for ionisation, as well as complex interactions with laser repetition rate have also been observed with changing to raster speed, pointing to as of yet unidentified mechanisms may be occurring under raster conditions.[52]

1.3.2.7 - Irradiation geometry

Irradiation geometry in UV-MALDI MS refers the method of laser delivery to the sample and is particularly important for imaging applications. This can either be through reflection geometry, where the beam impinges on the sample surface on the same side as the inlet to the mass spectrometer, or transmission geometry, were the laser irradiated the sample from the opposite side of the sample.

Most UV-MALDI MS experiments, either on commercial instrumentation or custom-built sources, operate in reflection geometry. The primary consideration for irradiation geometry in this configuration is the incident angle of the laser on the sample surface. The importance of this parameter is mostly related to the resulting geometry of the laser spot on the surface, as increasingly shallow angles of incidence will lead to elongation of the laser spot along one axis; this is particularly undesirable for imaging applications where it is preferable to keep spot dimensions similar to the pixel size of the acquisition. Other than this modification of spot dimension, it has been found that, at least within a certain

range of angles (30°-60°), the angle of incidence has no effect on UV-MALDI MS results[99].

With increasing demand for high spatial resolution UV-MALDI MSI, use of transmission geometry has become more common in recent years[16,98,100,101]. This is due to the fact that transmission geometries can easily accommodate the final focusing optics significantly closer to the sample surface without obstructing the desorption plume from the sample. This enables the use of short focal length, high numerical aperture (N.A.) focusing lens typically required to produce diffraction limited spot sizes. Despite the significant differences in the absorption of the laser energy, the consensus is that transmission and reflection geometries produce broadly similar results. Schürenberg et al. compared the two geometries for simple matrix-analyte mixtures, finding only minor differences in threshold fluences, and identical spectra[100]. For tissue imaging one can expect a greater difference between the two geometries, but despite there being numerous studies using transmission geometry for tissue imaging[16,98,101–103] a detailed study into mechanistic differences is still pending.

1.3.3 - The influence of sample conditions in UV-MALDI MSI

1.3.3.1 - Analyte-to-matrix molar ratio

The ratio between the molar concentrations of matrix and analyte has a strong influence on the quality of spectra obtained in UV-MALDI MS. Molar ratios can vary considerably depending on the analyte being studied, with readily ionisable compounds, such as phosphatidylcholine lipids or basic peptides, detectable at analyte-to-matrix ratios as high as $1:10^9$. Conversely poorly ionisable analytes,

such polymers and many small molecule pharmaceuticals, can required ratios as low as 1.[104]

One of the most notable effects when varying the analyte-to-matrix ratio is the complete suppression of matrix peaks seen at fluences near the ionisation threshold and low ratios[105]. Dubbed the "matrix suppression effect" (MSE), this results in an essentially ideal UV-MALDI MS spectrum, consisting solely of peaks related to the analyte(s). The origin of this effect has been explored extensively in the context of the CPCD ionisation theory proposed by Knockenmuss[79,105–107], as it is held as evidence of the secondary ionisation reactions integral to the proposed ionisation mechanism. The MSE is believed to occur when the number of available matrix ions in the plume is insufficient to fully ionise all accessible analyte molecules, under these conditions all the matrix ions will lose their charge during the secondary ionisation reactions with the analytes. The related "analyte suppression effect" (ASE), where the presence of one analyte will supress the ionisation of another, is also believed to be influenced by analyte-to-matrix ratio via competition for primary matrix ions[108].

In UV-MALDI MSI the influence of analyte-to-matrix ratio is particularly complicated by the presence of large numbers of unknown molecular species at unknown concentrations. Indeed, this issue is one of the primary reasons that the application of UV-MALDI MSI as a quantitative technique is limited to investigation of single analytes under highly controlled conditions and with appropriate internal standards[109]. Typical approaches to circumvent this problem involve ensuring that enough matrix is present on the sample to ensure

that there is no competition for charge between analytes, and that all optimal analyte-to-matrix ratios are included. Although given the enormous range of optimal ratios seen in the literature, the extent to which this is a successful strategy is still up for debate.

1.3.3.2 - Matrix deposition methods

Unsurprisingly the nature of matrix application is of great importance in any UV-MALDI MS experiment, but there are some significantly different requirements between classical UV-MALDI MS and UV-MALDI MSI. For UV-MALDI MS analysis the two most important factors are incorporation of the analyte, necessary to ensure the best sensitivity and LODs are achieved, and matrix homogeneity, essential for reducing variation of the MS data. The typical sample format for classical UV-MALDI MS analysis consist of spotting mixtures of the sample and matrix onto a substrate. This has led to a wide variety of deposition routines, ranging from simple two layer[110], sandwich[111] and matrix crushing[112] methods, to more complex approaches involving electrowetting[113] or manipulation of fluidic convection within the droplet[114]. For the detection of analytes that are insoluble in common matrix solvents "dry" preparations have been developed[115–118], where the matrix and analytes are mixed together as a fine powder, an approach that has proven particularly popular for the analysis of polymers.

In UV-MALDI MSI, the application of the matrix is particularly important given the spatial nature of the mass spectral data acquired. Generally, application of the matrix needs fulfils a set of requirements for success in an imaging context.

Firstly, the matrix must be uniform across the imaging area and have sufficient incorporation of analytes to ensure the resulting imaging data is representative of the sample. Secondly, analyte delocalisation and matrix crystal sizes must be minimal, or at least on scales smaller than the pixel size of the acquisition. At the smallest pixel sizes used in UV-MALDI MSI (<10 μm) the matrix crystal size and analyte delocalisation become particularly important to the collection of meaningful imaging data.

"Wet" deposition techniques, where the matrix is applied as a solution in a suitable solvent. are the most ubiquitous method of matrix deposition for imaging studies. A wide variety of different devices are used, of which the most common are robotic nebulising sprayers, such as the TM Sprayer (HTX, USA) and ImagePrep (Bruker, Germany) systems, where the matrix is sprayed over the sample area, fully coating it. Typically these devices operate using either heated capillary[119] or vibrational capillary[120] based sprayer configurations. Electrospray based deposition can offer some significant advantages over nebulising sprayers, with respects to uniformity of the deposited matrix layer and minimising matrix crystals sizes[121,122]. On the other hand, the additional instrumental complexity required to generate the electrospray has limited the use of such approaches to home-built devices in individual laboratories,

Targeted spotter devices such as acoustic multi-spotters[123] and inkjet printers[124], were the matrix is deposited at discrete spots, are sometimes used, but are normally limited to relatively large pixel sixes due to the size of the deposited spots. One particular advantage of this type of spotted deposition this that

multiple matrices can be deposited on the sample with no interference between each other, allowing the optimal matrix selection for multiple analyses on a single sample[124,125].

The continuing reduction of achievable pixels sizes in UV-MALDI MSI has increased the requirements on analyte delocalisation and matrix crystal size below the capabilities of most "wet" matrix application methods. "Dry" or "solvent free" matrix deposition methods, where a matrix is deposited onto the sample surface using sublimation[126–128] or powder dusting[129,130], without the need it to be in a solution phase, have seen a significant uptake in recent years to meet these challenges. By far the most common solvent-free method is sublimation deposition, introduced by Hankin et al. in 2007[126]. In this method the sample and matrix are placed in a chamber that is pumped down to a partial vacuum, typically ~$5x10^{-2}$ mBar, the matrix is then heated to the point it begins to sublime/vaporise, the matrix vapour produced then condenses on the surface of the sample, which is usually cooled via attachment to a cold finger or water cooled surface. The resulting matrix films are normally highly uniform across the sample surface, with matrix crystal sizes in the sub-micron range. While it has been shown that some molecular species, such as lipids and fatty acids, will readily migrate into the matrix layer unassisted[131], others like metabolites, peptides and proteins are poorly incorporated. In these cases recrystallisation of the matrix film is carried out by exposing the sample to an atmosphere saturated with a suitable solvent vapour[132–134]. This process is believed to partially re-dissolve the matrix on a microscopic level, providing analyte extraction similar to that achieved in "wet" deposition methods. Superficially the

recrystallisation process is said to preserve the uniformity and small crystal sizes of the sublimed film, although as of yet there have been no studies investigating the degree of analyte migration that may be occurring,

1.3.3.3 – Ionisation additives

The use of additives to enhance the detection of analytes is a long-standing practice in UV-MALDI MS and MSI, with many of the most common additives being imported from the field of chromatography. The most frequent rational behind the use of additives in UV-MALDI MS is to favour the formation of certain analyte adducts over others. Forcing the formation of a specific analyte adduct has two beneficial effects, firstly simplification of the resulting mass spectrum is achieved as other molecular adducts (e.g. Na^+, K^+, Cl^-) are ideally removed or strongly suppressed. Secondly, improvement to limits of detection and sensitivity are obtained, as the analytes of interest are now present as a single species in the mass spectrum. The enhancement of analyte protonation for positive mode MS is perhaps the most common use of additives in UV-MALDI MS. Typically this involved the use simple acids, such as trifluoracetic acid (TFA), phosphoric acid (PA) and formic acid (FA), to manipulate the pH of the matrix solution to favour analyte protonation[135]. A similar forcing of protonation can be achieved through the application of surfactants[136] or chelating agents[137] to sequester cations and anions in the sample, although this approach is much less commonly used. Most common matrix additives for protonation were adopted in the early years of UV-MALDI MS, when the analytes of interest were primarily peptides and proteins. Despite this, many continue to be routinely used today for analysis of analyte classes, and in tissue imaging experiments, with little

evidence for their suitability to the experiment being conducted. The use of additives to favour the formation of other adducts, for example Na^+ or Cl^-, is also frequently found in the literature, with most common approaches to achieving this is through the use of metal or halide salts to provide excesses of the desired cation or anion[138,139].

1.3.3.4 – Substrate effects

A wide variety of sample substrates are used UV-MALDI MS, with the most common being bare or gold coated stainless steel, glass or indium tin oxide (ITO) conductive glass slide, the latter two being most often used in UV-MALDI MSI due to compatibility with standard microscopy-based imaging methods. The influence of substrate in UV-MALDI MS on ionisation has been briefly investigated in the literature, with the focus on metal substrates. Frankevich et al. showed that the use of bare stainless steel reduced positive ion yields in dried droplet samples up to 2 orders of magnitude compared to non-conductive substrates[140]. Conversely, McCombie et al. showed that very thin samples produced by electrospray deposition have enhanced ionisation on conductive surfaces (stainless steel and gold), with the effect seemingly being related to interactions between the matrix electronic states and the metal conduction band lowering the ionisation potential for the matrix[141,142].

UV-MALDI MSI studies of biological samples, where tissue thicknesses are generally 5-10 µm or more, the tissue itself is considered the substrate, and contributions from any supporting substrate are believed to be minimal in most instances. The influence of the underlying tissue on ionisation efficiencies has

been an active topic of interest in recent years. It has been observed in numerous studies that the suppression or enhancement for a given molecular species can vary significantly between different tissues[143], or even from different regions within the same tissue[109,144]. This variation in ionisation makes extracting meaningful quantitative information regarding the amount of a detected substance at a given location exceedingly difficult and can even complicate qualitative analyses by distorting the resulting ion distribution images.

The exact mechanisms behind this tissue substrate effect have yet to be determined, although the reported evidence so far suggests some convolution of both changes to material ejection and analyte-analyte suppression may be occurring. A significant increase in the ionisation threshold fluence of the endogenous membrane lipid PC (34:1) in brain tissue, compared the same compound in matrix thin films, was observed by Steven et al., who also found evidence of variation in the ionisation threshold fluence between different tissue regions[67]. Similar observations were made by Wiegelmann et al. in mouse brain, who noted that removal of alkali salts by tissue washing helped reduced the effect; they also noted different matrix crystallisation behaviours between different tissue regions[68].

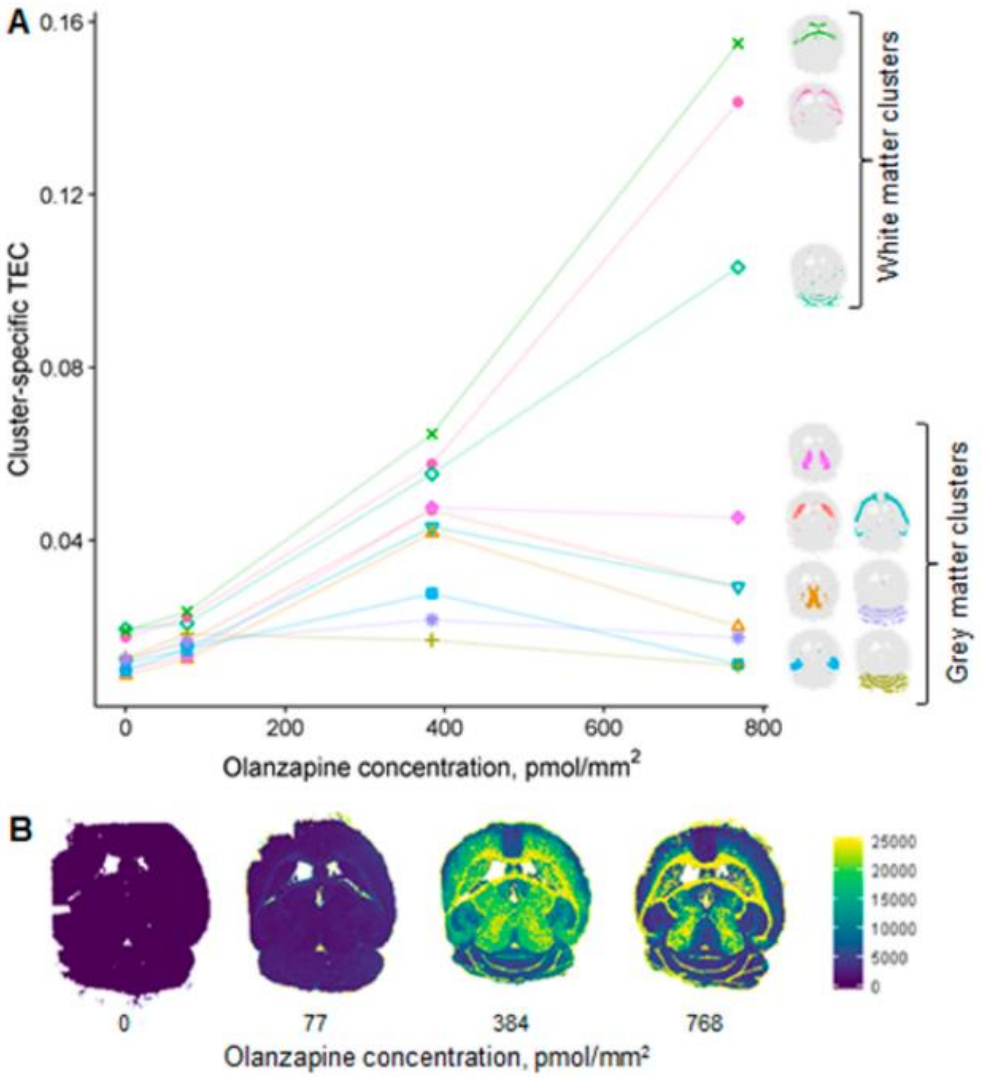


Figure 1.8. a) *Plot showing concentration dependence of cluster- specific tissue extraction coefficients (TEC). Cluster images are shown on the right. Colour is required to interpret this plot.* ***b)*** *Single ion images of olanzapine $[M+H]^+$ (m/z 313.15), deposited by spraying, at 0, 77, 384, and 768 pmol/mm^2 calculated olanzapine density. Figure and caption adapted from Taylor et al.*[144]

The magnitude of the tissue substrate effect has been quantified through comparison of the detected ion intensity of a uniformly distributed internal standard between on and off tissue regions[109,143], being used to inform corrective Tissue Extinction Coefficients (TEC) for use in obtaining quantitative

measurements of single analyte concentrations in UV-MALDI MSI tissue imaging. The concept of TECs was extended to heterogenous tissues by Taylor et al.[144], who found that different subregions within mouse brain showed large variation in ion suppression of a uniformly deposited analyte (olanzapine), with detected analyte intensities ranging anywhere from 1% to 20% that seen on the substrate (Figure 1.8).

1.3.4 - Mechanisms of material ejection and ionisation in UV-MALDI MS

1.3.4.1 - UV-MALDI MS material ejection models

Material ejection in UV-MALDI MS is intimately linked to analyte detection and sensitivity, as ultimately no detection of an ionised analyte in the mass spectrometer can occur if it is not first transferred into the gas phase. As such determining the exact mechanism involved has been the focus of a numerous studies[62]. Currently there are two primary mechanisms proposed as applicable under typical UV-MALDI conditions, quasi-thermal desorption and volume ablation or phase explosion.

In the quasi-thermal desorption model[24,62,63], heat generated from absorption of a laser pulse causes evaporation of the surface layers of the matrix. Depending on the properties of the matrix this can either be through a melting and evaporation process, or sublimation directly into the gas phase. The desorbing matrix molecules then carry entrained analyte molecules into the gas phase, with the desorbed molecules having an internal energy dependant on the maximum temperature of the matrix surface. Materia ejection follows an Arrhenius-like dependence on the temperature within the surface layers of the

matrix, and the number of desorbed molecules (N_{Des}) can be described by equation 1.4.[24]

$$N_{Des} \propto exp^{\left(\frac{-E_a}{k_b(T_0+\eta H)}\right)} \qquad (1.4)$$

Where E_a is the activation energy requires to disrupt the lattice structure of the matrix, k_b is Boltzmann's constant and H is laser fluence. η is a factor representing the conversion of photon energy to heat, and can be described, to the first order, by equation 1.5

$$\eta = \frac{\alpha}{\rho c} \qquad (1.5)$$

Where α is the optical absorption coefficient of the matrix, ρ is the density and c specific heat capacity. Further refinement of this factor can be achieved by accounting for additional energy loss pathways such as reflection from the surface and radiative decay processes like fluorescence.[62]

In the ablation, or phase explosion model, material ejection occurs though a volume ablation process, whereby the matrix is superheated to beyond its melting/sublimation temperature, eventually reaching a point where spinodal decomposition of the whole irradiated volume occurs[145]. A simple equation (Equation 1.6) for the number of ejected molecules (N_{Ab}) with fluence (H) was proposed by Zhigilei et al. through the application molecular dynamics simulations of ablation in UV-MALDI-like conditions.[82,86]

$$N_{Ab} = \rho_n \delta \ln\left(\frac{H}{\delta(E_v^* - cT_0)}\right) \qquad (1.6)$$

Where ρ_n is the number density of the material, δ is the penetration depth of the laser pulse into the material, which is the reciprocal of the materials absorption coefficient ($\delta = \alpha^{-1}$), E_V^* is the critical energy density of the material,

above which it is ablated, c is the specific heat capacity and T_0 is the initial sample temperature. A characteristic feature of the phase explosion model is the ejection of very large clusters consisting of 1000's of molecules, as opposed to the solely uni/oligomeric desorption of the quasi-thermal model. These clusters are expected to have significantly lower kinetic energy than single molecule ejecta, leading to "slow" and "fast" components of the resulting plume.[82].

Evidence suggesting that both mechanisms occur common UV-MALDI conditions can be found with the literature. The existence of clusters within UV-MALDI material ejection plumes, suggesting a volume ablation process, has been well documented. Handschuh et al. used cold plate trapping of plume ejecta from 2,5-DHB/PEG 3000 films to study particle ejection in UV-MALDI MS experiments. Atomic force microscopy (AFM) analysis of the trapping plates revealed submicron clusters of 2,5-DHB and 2,5-DHB/PEG 3000, as well as a uniform molecular film of PEG 3000. It was also observed that proportion of material ejected as clusters decreased towards higher fluences [146]. Dynamic light scattering (DLS) was used by Jackson et al. to characterise aerosolised particles from ablation of multiple UV-MALDI matrix compounds. Mean particle sizes of approximately 700 nm were observed at 500 Jm^{-2} laser fluence for all matrices. Evidence of a threshold for the onset of particle generation was found, as well as decreasing particle size with increasing fluence[147]. A similar study by Musapelo and Murray used scanning mobility particle sizing (SMPS) to investigate particle production in reflection and transmission geometry laser irradiation of a range of matrices. Two populations of particle sizes were

observed in reflection geometry ablation, with the increasing fluence tending to favour smaller particles[148].

The existence of fast and slow plume components was also observed by Puretsky et al. via laser-induced fluorescence (LIF) imaging of plumes generated from 3-HPA matrix. The plumes were found to consist of a fast (0.1 cm/μs) and slow (0.05 cm/μs) components, with the latter mostly consisting of intact 3-HPA.

Despite the extensive evidence for ablation like processes occurring under typical UV-MALDI MS conditions, most studies directly measuring material ejection have found quasi-thermal desorption as the most applicable model. Schürenberg et al. used laser post ionisation of neutrals in the UV-MALDI plume to study material ejection at a range of sample temperatures. The evolution of neutral desorption with fluence was found to be well described by the quasi-thermal model. Additionally, a linear relationship between sample temperature and onset of material ejection was cited as evidence of quasi-thermal processes were in effect[149]. An extensive set of experiments by Soltwisch et al. used photo-acoustic methods to measure material ejection across a range of laser wavelengths and fluences also found that material ejection best explained by quasi-thermal desorption [24].

In recent years this somewhat disparate picture of UV-MALDI material ejection mechanisms has become clearer. Increasingly it has been proposed that both quasi-thermal desorption and volume ablation via phase explosion can occur within the range of typical UV MALDI conditions. In this framework quasi-thermal desorption is the principal mechanism at low fluences, while volume

ablation appears to dominate at higher fluences. A series of MD simulations carried out by Zhigilei and Garrison predicted the existence of an energy threshold for phase explosion processes, below which quasi-thermal desorption dominates The authors suggested that this threshold is the same as that at which ions are detected in UV-MALDI MS[82,86]. Experimental evidence somewhat supporting these predictions was reported Rolhfing et al. who used laser post-ionisation, fast flash imaging and photo-acoustic analysis to investigate material ejection processes of the liquid matrix 3-nitrobenzyl alcohol (3-NBA). They found evidence for two distinct desorption regimes, with the low fluence regime best described by quasi-thermal desorption and the high fluence regime ablation processes. Notably the onset of sizable analyte ion generation occurred at the threshold between the two regimes[150]. A recent study by Niehaus and Soltwisch made use of laser post ionisation and photoacoustic measurements to explore the effects of laser fluence and spot size on material ejection in UV-MALDI MS. Photoacoustic measurements of desorption were found to be well described by quasi-thermal desorption up to a threshold energy, beyond which ablation models provided better description of the data[61].

1.3.4.2 - Theoretical models UV-MALDI MS ionisation

Not long after the advent of UV-MALDI Ms it was determined that, due to the photon densities typically used, direct photo-ionisation could not feasibly be the mechanism by which analyte ions were formed[151]. At present there is still no agreement upon an ion formation mechanism for the technique, with three primary models proposed.

Coupled Physical and Chemical Dynamics (CPDC)

Sometimes referred to as the "Two-step" or "Gas phase" model, the Coupled Physical and Chemical Dynamics (CPDC) model was developed primarily by Knochenmuss and co-workers[79,107,108,152,153]. In the CPCD model the matrix acts as the source of primary ions, with analytes being ionised through secondary gas phase reactions in the plume. As photon energies at common UV-MALDI wavelengths (337 nm & 355 nm) are not sufficient for resonant single photon ionisation to occur, and photon densities are also too low for multiphoton ionisation to be an efficient pathway. The CPCD theory proposes that a multistep photoexcitation process, in which the energy of multiple photoexcitation events is concentrated in a single matrix molecule via process known as exciton pooling, provides energy for ionisation. The pooling process that generate primary matrix ions ($[m]^+$) can be generalised by the following reaction schemes

$$S_0 + hv \rightarrow S_1$$

$$S_1 + S_1 \rightarrow S_0 + S_n$$

$$S_n + S_1 \rightarrow [m]^+ + e^-$$

Where S_0 is a matrix molecule in the ground state, S_1 is a matrix molecule in the first excited state, and S_n is a higher excited state. Negative matrix ions ($[m]^-$) are then formed through capture of the resulting free electron by another matrix molecule (m).

$$e^- + m \rightarrow [m]^-$$

The matrix ions formed by this electron transfer process ($[m]^+$ & $[m]^-$) can then also interact via a reversable proton transfer reaction to form protonated and deprotonated pairs.

$$[m]^+ + [m]^- \leftrightarrow [m+H]^+ + [m-H]^-$$

Evidence for exciton pooling in UV-MALDI primarily comes from optical emission experiments, where the quenching of fluorescence emission under high excitation densities has been observed for a range of UV-MALDI matrices[34,36,154]. The effect on ionisation was directly studied by Setz et al. using 2,5-DHB matrix doped with the fluorophore 4-(dicyanomethylene)-2-methyl-6-(4-dimethylaminostyryl)-4H-pyran (DCM). As predicted, the DCM molecules acted as traps for the mobile excitons, quenching the pooling process and resulting in significantly reduced ion yields[154].

Analytes ionisation is proposed to occur though secondary reactions with the matrix ions in the expanding plume. These reactions depend on the physicochemical properties of the matrix and analyte, with proton affinity and cation affinity being particularly relevant. Example reaction schemes for analyte protonation and deprotonation, typically the most prevalently detected ions in UV-MALDI MS, are shown below.

$$[m+H]^+ + A \rightarrow m + [A+H]^+$$

$$[m-H]^- + A \rightarrow m + [A-H]^-$$

$$[A+H]^+ + B \leftrightarrow A + [B+H]^+$$

Where m is the matrix and A and B are analytes. Various experimental observations in UV-MALDI MS have been proposed as evidence for secondary ionisation reactions in the plume. The most important of these is the matrix suppression effect (MSE), whereby increasing the analyte-to-matrix molar ratio can result in the complete elimination of the matrix derived peaks from mass spectra. The existence of the MSE is held as evidence of secondary ionisation processes, as the effect is attributed to the complete depletion of matrix ions through secondary reactions with the analyte[105]. Similar to the MSE, the analyte suppression effect (ASE) is also routinely observed in UV-MALDI MS, whereby the presence of certain analytes in a mixture can supress the ionisation of other analyte components. Controlled studies using mixed matrix-analyte systems[106] as well as the observations of positive to negative analyte ionisation ratios[155] and hydrogen-deuterium exchange (HDX) experiments[44] have all pointed to the importance of secondary ionisation reactions in generation the majority of observed analytes ions in UV-MALDI MS.

Material ejection in CPCD model comes from the non-radiative decay of S_1 and S_n excited states, converting the electronic energy into thermal-vibration of the crystal lattice. MD simulations using the CPCD model show that material ejection is primarily an ablation process, with significant ejection of particle and large chunks of matrix[89,156]. The model has been shown to predict many features of material ejection in UV-MALDI, such as experimentally observed fast and slow plume components[89,157] and the dependence of ion intensity on spot size[79,158] and initial sample temperature[159]. Of all the UV-MALDI theoretical models the CPCD is arguable the most complete, as it integrates both the material ejection

and ionisation processes. As such it is the only model that can provide quantitative predictions for the entire UV-MALDI MS process.

The Unified MALDI model

The Unified MALDI model[160] is the most recent iteration of series of models proposed by Hillenkamp, Karas and coworkers[161,162], being a combination of the "Cluster" or "Lucky Survivor" model with the CPCD model. The Unified MALDI model proposes that analytes are incorporated into the matrix crystals as preformed ions paired with a counter ion; the analyte maintaining the charge state obtained while in solution. Evidence of pre-charged ions with matrix has been found through the use of pH indicator dyes[163], as well as the manipulation of adduct formation using strong acid dopants in the preceding matrix-analyte solution[164]. Upon irradiation with the laser, a similar matrix desorption and ionisation process as proposed in the CPCD model (exciton pooling) occurs, with the resulting plume containing the analytes embedded within matrix clusters. Due to a net equivalency of charge most of these clusters dissociate completely into neutral molecules and so are ultimately not detected. In some cases, a cluster has a net excess of charge, originating from matrix ions in the cluster. As the cluster dissociates, the analyte is ionised though neutralisation of its associated counterion or deprotonation, these analyte molecules are termed the "lucky survivors". The importance of clusters to ionisation in UV-MALDI has long been suspected. Evidence from material ejection studies have shown that the ejection of large matrix clusters, associated with the crossover to ablation mechanisms, is concomitant to the onset of significant ion detection[82,87,150].

Moreover, the existence of ambient ionisation techniques such as matrix-assisted ionisation (MAI)[165,166], wherein analyte ionisation occurs from desorbed matrix without the need for a laser, show that the matrix cluster desolvation is a valid mechanism for analyte ionisation. This lucky survivor mechanism, and the CPCD gas phase secondary ionisation mechanism are both proposed to occur in the plume, with the former favoured by low laser fluences, higher matrix proton affinity and larger analyte mass, and the latter by high laser fluences, lower matrix proton affinity and smaller analyte mass[160].

Thermal proton transfer model

In recent years a new model of UV-MALDI ionisation has been proposed by workers form the Kim and Ni groups. The thermal proton transfer (TPT) model[167,168] proposes an ionisation mechanism that relies purely on thermal input rather than photoexcitation or preformed ions. In the TPT model ions are generated through thermally mediated proton transfer reactions in the dense, high temperature early stage of the desorption plume. In this state the plume is described as a thermal polar fluid, allowing proton transfer reactions analogous to those observed in polar solutions. For the generation of positive analyte ions, typical reactions are of the from.

$$[m+H]^+ + A \leftrightarrow m + [A+H]^+$$

$$m + A \leftrightarrow [m-H]^- + [A+H]^+$$

Gas phase reactions in the later plume are believed to be limited due to rapid expansion, so ionisation is governed primary by conditions in the early polar fluid environment. The TPT model has been used to make quantitative

predictions of ion yields for analytes and matrice[169]. These results, and the associated measurements to validate them, proved somewhat contentious as they showed ion yields significantly lower (10^{-7} – 10^{-9} for matrix and 10^{-3} – 10^{-8} for analytes) than those assumed by the other main UV-MALDI models (10^{-1} – 10^{-3} for all ions)[168–170].

1.4 - Applications of UV-MALDI MS and UV-MALDI MSI

1.4.1 - UV-MALDI MS

The relative ease of use and simple sample preparation coupled with high sensitivity and low limits of detection have ensured UV-MALDI MS has become an invaluable tool for chemical analysis in wide variety of fields. The technique has seen significant application for high throughput screening experiments, partially in the biological sciences where the soft nature of ionisation in UV-MALDI allows the routine analysis of large and liable biomolecules. In biological sciences UV-MALDI MS has been applied to a wide range of analytical problems such as metabolite dynamics[171], biomarker discovery[172], genotyping[173] studies.

One field that has been revolutionised by the application of UV-MALDI MS has been microbiological diagnostics; the identification, classification and characterisation of microorganisms[174]. Typically, this is achieved through matching characteristic ribosomal protein profiles of a microorganism to a reference database. The popularity of UV-MALDI MS for microbiological diagnostics is primary due to the minimal required sample volume, high sensitivity, relative cost effectiveness and speed of analysis when compared to pre-existing analytical techniques such as phenotyping or gene sequencing[175].

The application of UV-MALDI MS in the field of microbiological diagnostics has resulted in integration of the technique into clinical settings, with dedicated commercial systems such as the Bruker Biotyper and Vitek MS available, representing the perhaps first instance of a routine clinical application for the technique.

1.4.2 - UV-MALDI MSI

With its powerful analytical capabilities, amenability to imaging and relative simplicity UV-MALDI MSI has become the most prevalent mass spectrometry imaging technique in life sciences. Within this field UV-MALDI MSI is most commonly applied in the analysis of pharmaceuticals, peptides and proteins, lipids, small molecule metabolites, and carbohydrates. A prevalent and long-standing application of UV-MALDI MSI is imaging of pharmaceutical and metabolite distributions for drug development studies[176]. Khatib-Shahidi et al used UV-MALDI MSI to image whole body sections of rats dosed with olanzapine to study the temporal changes in drug and drug metabolites (Figure 1.9), and correlate to previous whole body autoradiography (WBA) studies[177].

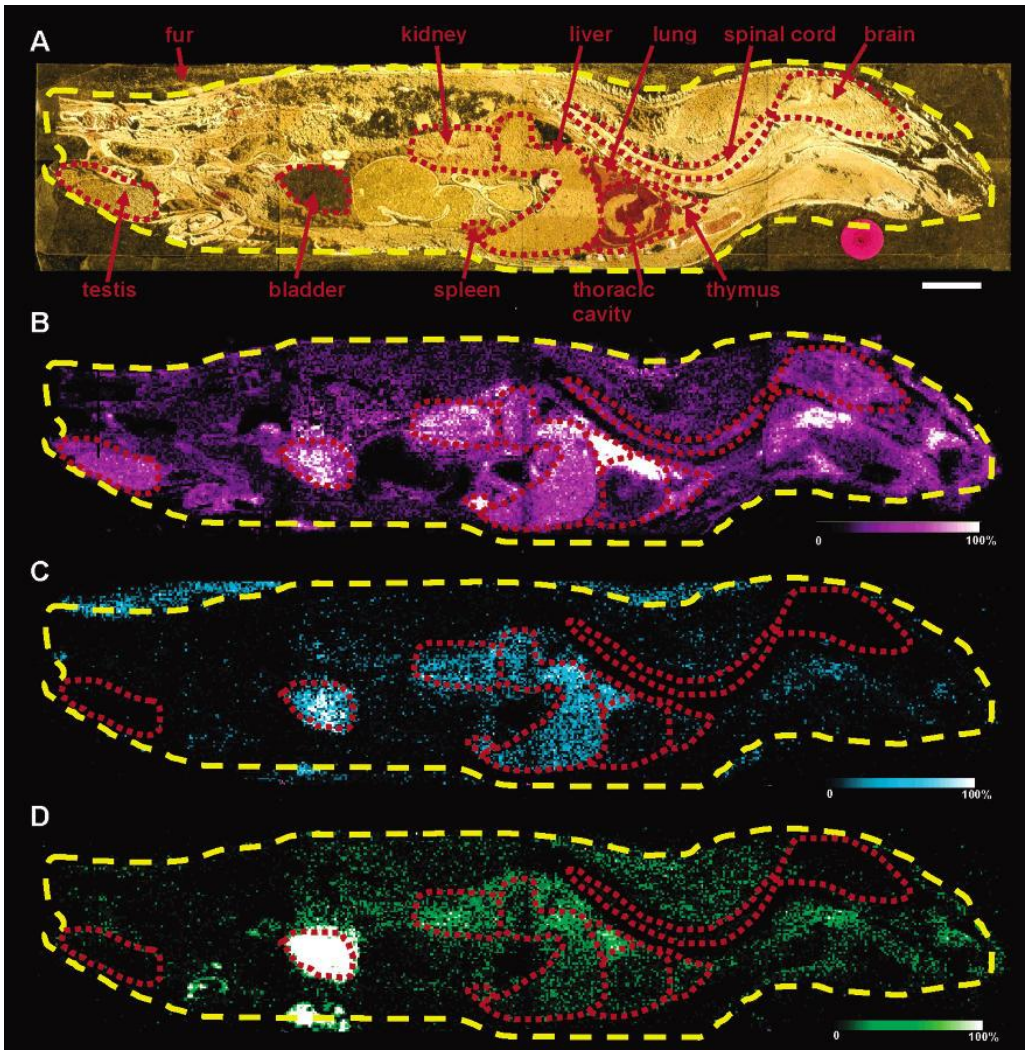


Figure 1.9. *Detection of olanzapine and metabolite distribution at 2 h post-dose in a whole rat sagittal tissue section by MALDI MSI analysis.* ***a)*** *Optical image of a 2h post olanzapine dosed rat tissue section across four gold MALDI target plates. Organs outlined in red.* ***b)*** *MS/MS ion image of OLZ (m/z 256).* ***c)*** *MS/MS ion image of N-desmethyl metabolite (m/z 256).* ***d)*** *MS/MS ion image of 2-hydroxymethyl metabolite (m/z 272). Bar, 1 cm. Figure reproduced from Khatib-Shahidi et al*[177].

The amenability of UV-MALDI MSI to the detection of endogenous species such as proteins, peptides, lipids and makes the technique a powerful tool for the study of disease and cancer. Rauser et al. applied UV-MALDI MSI to classify

human epidermal growth factor receptor 2 (HER2) status in breast tumour tissues, identifying specific peptides and proteins associated with HER2 overexpression[178]. While in another stud by Mirnezami et al, UV-MALDI MSI was used to observe lipodomic changes in colorectal cancer, revealing biochemical differentiation between healthy tissues related to tumour proximity, providing insight into the role of lipids in field canceristion[179]. With appropriate sample preparation, UV-MALDI MSI has also been shown to be compatible with-fixed paraffin embedded (FFPE) tissue samples, a particularly important capability given that FFPE is the primary sample format of biobank tissue archives[180]. Outside of cancer research UV-MALDI MSI has helped provide insights into the molecular biology of other common diseases, such as investigating amyloid-β pathology in Alzheimer's disease mouse models[181], or identifying biomarkers associated with Autosomal recessive polycystic kidney disease (ARPKD)[182].

One of the more unique applications of UV-MALDI MSI can be found in the field of forensics, where it has been used in imaging of fingerprints, allowing determination of fingerprint ridge patterns, as per classical finger print analysis, as well providing detailed chemical information[183].

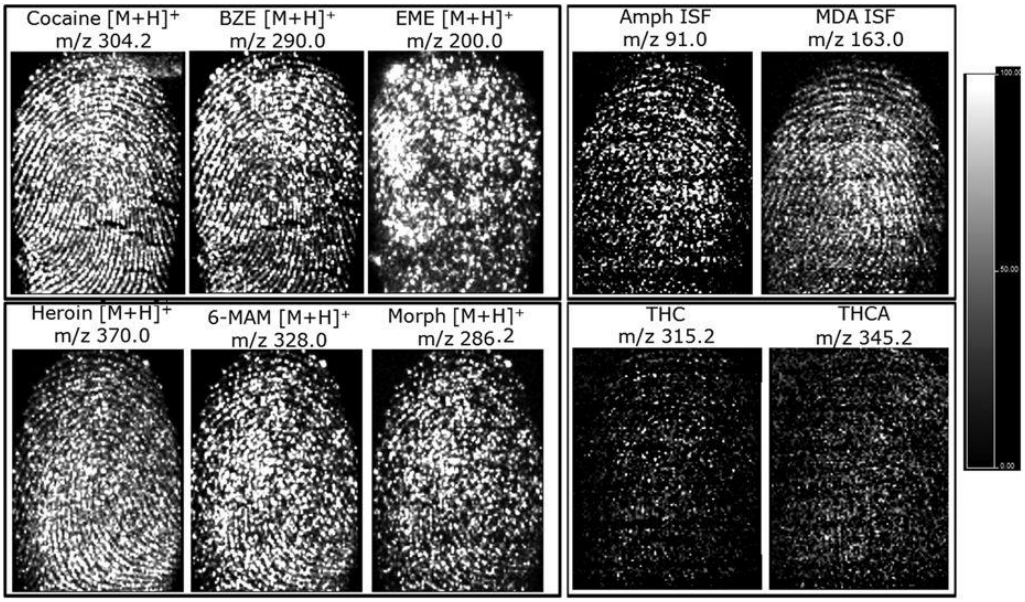


Figure 1.10. *UV-MALDI MS images of finger-marks simultaneously spiked with drugs and their metabolites at defined ratios to show the distribution of samples containing* ***a)*** *cocaine, BZE and EME in a 5:1:1 ratio;* ***b)*** *heroin, 6-MAM, morphine in a 5:1:1 ratio;* ***c)*** *amphetamine and MDA in a 1:1 ratio; and* ***d)*** *THC and THCA in a 1:1 ratio. Figure and caption adapted from Groeneveld et al*[184].

UV-MALDI MSI has been successfully demonstrated for the detection of narcotics and their metabolites from finger-marks (Figure 1.10), the latter proving particularly powerful as it allows differentiation between contact with or ingestion of a narcotic[184,185]. Direct imaging of protein and peptides within finger-marks, coupled with multivariate spectral models has also been shown to enable determination of the sex of the person with an 85% accuracy[186]. The strength of UV-MALDI MSI for the forensic analysis of finger-marks has led to the technique entering pseudo-operational and operational trials with police forces, potentially paving the way for eventual adoption of the technique as a recommended technology for forensic analysis[187].

Increasingly UV-MALDI MSI has been used in conjunction with other techniques in multimodal studies to provide complementary information on a sample. Many other MSI techniques have been combined with UV MALDI to take advantage of each technique's relative strengths. For example, SIMS, an MSI technique with superior (sub-micron) spatial resolution but comparatively poor chemical information has been demonstrated[188,189]. Similarly, solvent based MSI techniques such as desorption electrospray mass spectrometry (DESI)[190,191] or liquid extraction surface analysis (LESA)[192,193] have been used in combination with UV-MALDI MSI to provide enhanced coverage of analytes. The combination of UV-MALDI MSI with orthogonal imaging techniques have been demonstrated successfully in many studies[191], with some examples including: Whole Body Autoradiography (WBA)[71], Magnetic Resonance Imaging (MRI)[194], Fourier-transform Infrared (FTIR) spectroscopy and Positron Emission Tomography (PET)[195].

1.5 - Thesis overview

This thesis investigates the influence of various experimental conditions on material ejection and ionisation in UV-MALDI MS and MSI. In particular, a focus is given to the quantification of effects arising from conditions relating to the sample, matrix, laser and sampling mode.

Chapter 2 explores the influence of analyte-to-matrix molar ratio and the use of common ion enhancement agent TFA, on UV-MALDI MS results. A range of ten matrix compounds and three representative compounds of common UV-MALDI MS analyte classes, are investigated.

In Chapter 3 the optical absorption properties of the ten matrix compounds from Chapter 2 are characterised in both solution and solid phase. A subset of these matrix compounds are selected for fully quantitative measurements of solid phase optical absorption. These matrix compounds are then investigated in laser fluence variation experiments with the three analytes from Chapter 2 to explore and characterise the relationship between matrix optical absorption, laser fluence and ionisation in UV-MALDI MSI.

Chapter 4 explores the influence of common UV-MALDI MSI laser and sampling conditions on material ejection and ionisation efficiency in detail using a suite of surface analysis techniques. Highly uniform and well characterised thin film model systems consisting of olanzapine and either CHCA or 2,5-DHB are analysed under different UV-MALDI MSI sampling conditions, enabling quantitative measurements of material ejection and ion yield to be made. Comparison of spot and raster mode, as well as the effects of laser pulse energy, laser repetition rate and raster speed are explored in a systematic manner to study the effect of these common UV-MALDI MSI parameters on material ejection and ion yield. Simulations of material ejection in oversampling imaging mode, using acquired ablation crater data, are also used to explore the implications of non-uniform sampling typical of Gaussian laser beam profiles commonly used in UV-MALDI MSI.

In Chapter 5 the methodology used to characterise material ejection and ion yield demonstrated in the previous chapter are extended to MSI experiments on tissue. Using optical profilometry and precisely controlled deposition of CHCA

and haloperidol internal standard, the origins regional ion suppression in heterogeneous tissue are explored. The influence of features of tissue microenvironment, such as local thickness and anatomical structures, on matrix deposition, material ejection and ionisation are quantitatively characterised.

Finally, in Chapter 6, the conclusions of the previous chapters are reiterated and recommendations for promising future studies is proposed.

Chapter 2 - The influence of analyte-to-matrix molar ratio and TFA in UV-MALDI MS

2.1 - Introduction

The ratio between the molar concentrations of matrix and analyte has a strong influence on the quality of spectra obtained in UV-MALDI MS. Optimal molar ratios in vary considerably depending on the analyte being studied, ranging from analyte-to-matrix ratios as high as $1:10^9$ for readily ionisable compounds, to as low as 1 for weakly ionisable analytes[104]. In UV-MALDI MSI this picture is complicated by the presence of large numbers of unknown molecular species at unknown concentrations, resulting in many optimal analyte-to-matrix ratios, that may be very different. This is the main reason quantitation in UV-MALDI MSI is limited to investigation of single analytes and with appropriate internal standards[109]. Typical approaches to circumvent this problem involve ensuring and that all optimal analyte-to-matrix ratios are included through excess of matrix. Although given the enormous range of optimal ratios seen in the literature, the extent to which this is a successful strategy is not known. Furthermore, investigations addressing the influence of analyte-to-matrix ratios have mainly focused on the matrix suppression effect (MSE) and its implications for UV-MALDI MS ionisation theories. As MSE only occurs under specific molar ratio and laser fluence conditions, therefore it is useful to explore the effect of analyte-to-matrix ratio for conditions more in line general UV-MALDI MSI experimentation.

The use of additives to improve ion intensities in UV-MALDI is a well-established practice. Among these additives trifluoroacetic acid (TFA) the most commonly used for the generation of positive, protonated ions. Being a common additive in liquid chromatography-mass spectrometry (LC-MS), where it was used to aid the solvation of basic analytes, and as an ion paring agent, TFA was naturally employed from the beginning of UV-MALDI experimentation to enhance co-crystallisation of the matrix and analyte, and provide additional protons for ion formation[196]. Today, despite of the many changes the UV-MALDI MS technique has undergone, many experimenters will still include TFA in standard sample preparation, irrespective of the matrix or analyte being studied. Moreover, the use of TFA has fallen out of favour in LC-MS, as it has been found that its ability to form strong ion-pairs with analytes interferes with subsequent ionisation pathways, leading to significant suppression of analyte ion signals[197]. It is therefore important to fully investigate if the addition of this additive is as universally applicable as generally presumed.

A range of UV-MALDI matrix compounds was selected from the literature (Figure 2.1). α-cyano-4-hydroxycinnamic acid (CHCA)[5] and 2,5-dihydroxybenzoic acid (2,5-DHB)[6] were chosen due to their widespread and longstanding use in MALDI. Along a similar line *para*-nitroaniline (PNA)[198], 1,5-diaminonaphthalene (DAN)[199], 2-mercaptobenzothiazole (MBT)[200] and Dithranol (DIT)[201] were included as novel matrix compounds that have been discovered in recent years. To provide some insight into the effects of molecular structural features on matrix compound performance in UV-MALDI MS, structurally similar matrix compounds, 2,4,6-trihydroxyacetophenone (THAP)[202] and 2,5-

dihydroxyacetophenone (2,5-DHAP)[203], as well as the DHB isomer 2,6-dihydroxybenzoic acid (2,6-DHB)[204] were also included. The free radical Galvinoxyl (GAL) was also selected, as an example of a matrix previously identified though rational selection methods[205]. Three compounds, Haloperidol, Angiotensin II and PC (34:1) lipid standard, were selected as representatives of common analyte classes analysed by UV-MALDI MS.

2.2 - Materials

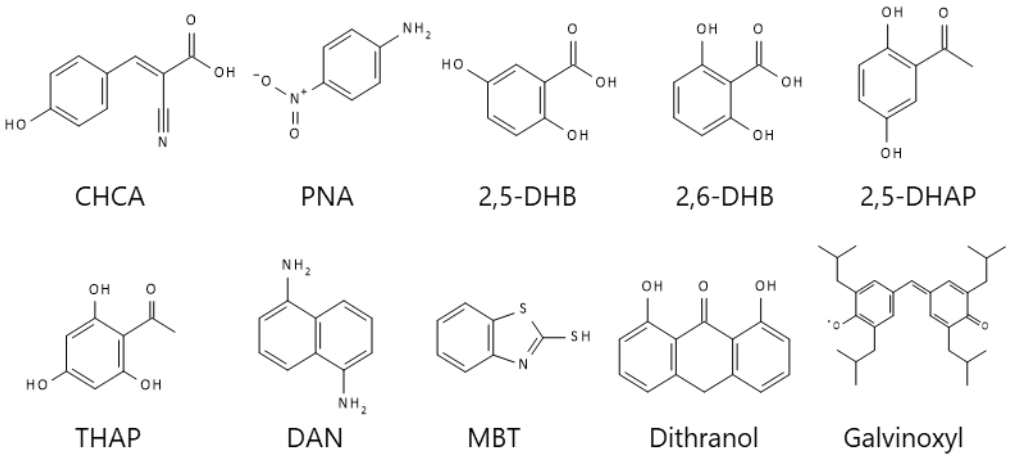


Figure 2.1. *Molecular structures of the ten UV-MALDI matrix compounds selected for study.*

CHCA, 2,6-DHB, PNA, 2,5-DHAP, THAP, DAN and MBT, Haloperidol, Angiotensin II Human, TFA, acetonitrile (ACN) and tetrahydrofuran (THF) were purchased from Sigma Aldrich (UK). 2,5-DHB, GAL and DIT were purchased from Alfa Aesar (UK). PC(34:1) lipid standard was purchased from Avanti Polar Lipids (USA). HPLC grade methanol (MeOH) was obtained from Fisher Scientific (UK). Unless stated otherwise all water was deionised (ρ=15 MΩcm^{-1}) and generated using an Elga

Purelab system (Elga, UK). Stainless steel MALDI target plates were obtained from Sciex (UK).

2.3 - Methods

2.3.1 - Matrix analyte molar ratio and TFA influence

Solutions of the different analytes were made to a concentration of 10 nmol/mL. The matrix solutions were made up at molar concentrations of 100 nmol/mL, 1 µmol/mL, 10 µmol/mL and 100 µmol/mL, with and without the addition of 0.2% v/v TFA. Solutions of matrix and analyte were made up in a solvent system consisting of THF:MeOH:H_2O in a 1:1:1 ratio, which was found to have good solvation qualities for the majority of matrices and analytes, across the concentration range, as well as retaining sufficient water content to allow for the formation of stable droplets while spotting on the MALDI plates. Due to solubility issues DIT and GAL solutions had to be made up in pure THF.

Equal volumes (5 µL) of analyte and matrix solutions were pipetted into Eppendorf tubes and vortexed for 30 seconds to ensure thorough mixing. This way individual combinations of each matrix and analyte, at matrix analyte ratios of 10:1, 100:1, 1000:1 and 10000:1, with and without 0.1% v/v TFA, were made up. A 10 x 10 spot stainless steel MALDI target plate was cleaned via sonication in a 1:1 v/v mixture of acetonitrile and DI water for 15 minutes and dried under a nitrogen stream. The individual matrix analyte combinations were manually deposited via the dried droplet method. 0.3 µL of each matrix analyte combination were pipetted out in triplicate into individual spots and allowed to dry under ambient conditions in a fume cupboard.

2.3.2 - UV-MALDI MS

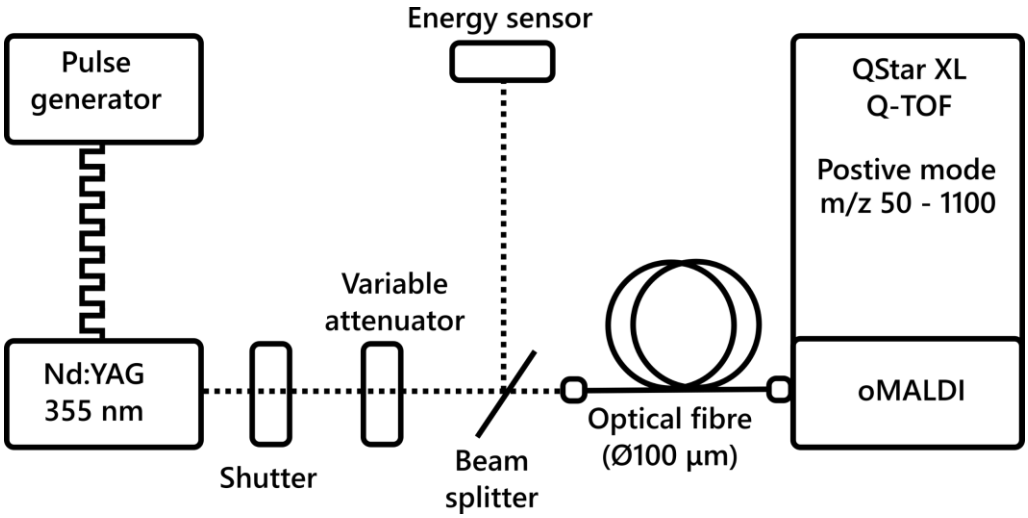


Figure 2.2. *Layout of the optical system used for laser delivery and monitoring during the UV-MALDI MS experiments detailed in this chapter.*

UV-MALDI MS data were collected over a mass range of 50-1100 *m/z* in positive mode using a QSTAR XL Qq-ToF mass spectrometer fitted with a oMALDI2 source (Sciex, UK), coupled via 100 µm round optical fibre (Fiberguide Industries, USA) to a 355 nm Nd:YAG DPPS laser (FQS-100-1-Y-355, Elforlight, UK), operating at 1kHz with a pulse width of <4 ns. The laser was triggered with a square wave signal by a function generator (TG2000 20 MHz DDS, TTi, UK). A shutter system, previously described by Steven et al.[206], was used to aid pulse energy stability during experiments (Figure 2.2). Data collection were controlled via the Analyst QS 1.1 and oMALDI server 5.1 software packages (Sciex, UK).

For the matrix analyte ratio experiments, UV-MALDI MS data was obtained at a laser fluence of 127 J/m^2 and 1 kHz repetition rate. Data were acquired using the instruments quasi-spot mode, where the laser beam is rastered across the dried droplet in a pattern designed to sample the whole spot area. Data were acquired for 15 seconds per spot, resulting in 15 spectra per spot.

2.3.3 - Laser fluence measurement

Pulse energy was monitored by sampling the beam with a partially reflecting mirror (BSF-10-UV, Thorlabs, UK) prior to entry into the fibre, and diverting it towards a photodiode sensor (PD10-C, Ophir Photonics, Germany). Delivered pulse energy was determined through calibration to post experiment end of fibre measurements, corrected for known losses (13%) from the delivery optics of the instrument. The laser incidence angle was approximately 65°, forming an elliptical spot 111 µm x 235 µm at the sample, as determined via the fluorometric method[207] from CHCA thin films using ImageJ[208] . Variation in delivered laser fluence was achieved via a Brewster angle variable attenuator (Watt Pilot, Altechna, Lithuania).

2.3.4 – Data Processing

Unless stated otherwise all data were processed in MATLAB (R2018b, Mathworks, UK). MS data were converted to .mzML using AB MS Data Converter (v 1.3, Sciex, UK) and then into .imzML using imzMLConverter[209], and imported into MATLAB using SpectralAnalysis[210] for further processing and analysis. A gradient based peak picking process was carried out on the data, selecting all the peaks with intensity greater than 5 counts from the base peak spectra of the combined datasets, and integrating the area under the peak.

2.3.5 - t-distributed stochastic neighbour embedding (t-SNE) and Principal component analysis (PCA)

t-SNE was carried out using MATLAB's built-in tsne function, based on the algorithm developed van der Maaten and Hinton[211]. Before t-SNE, a scaling

process was applied to the data to allow for equal weighting of all the peaks in the spectra. This was done by applying a z-score function to the peak intensity data, which mean centred and scaled to the standard deviation for each peak. The data were reduced by t-SNE to two dimensions, using the Barnes-Hut implementation with a cosine distance metric, a perplexity setting of 20 and 5000 maximum iteration limit. The t-SNE parameter settings were optimised based on recommendations by Belinka et al[212].

PCA was carried out on using MATLABs in-built PCA function. Similar to the t-SNE analysis, the MS data were scaled using a z-score function for equal weighting of all the peaks in the spectra.

2.4 – Results

2.4.1 - UV-MALDI MS analyte average spectra

The use of multiple analytes provides the opportunity to probe differences that can arise in UV-MALDI MS analyses, particularly imaging experiments where multiple classes of analyte are being ionised. For the MS experiments, Haloperidol; a common antipsychotic drug previously used in UV-MALDI MS studies[213,214], Angiotensin II; a small peptide hormone used in many UV-MALDI MS studies and PC(16:0-18:1), referred to in this work as PC(34:1); a phosphatidylcholine lipid prevalent in cell membranes and widely used in many biophysical experiments, serve as representatives of common analyte classes encountered in UV-MALDI MS. To provide some context on the spectral features associated with the analytes in UV-MALDI MS, mean mass spectra for each analyte, collected with 2,5-DHB, are shown below (Figures 2.3 - 2.5).

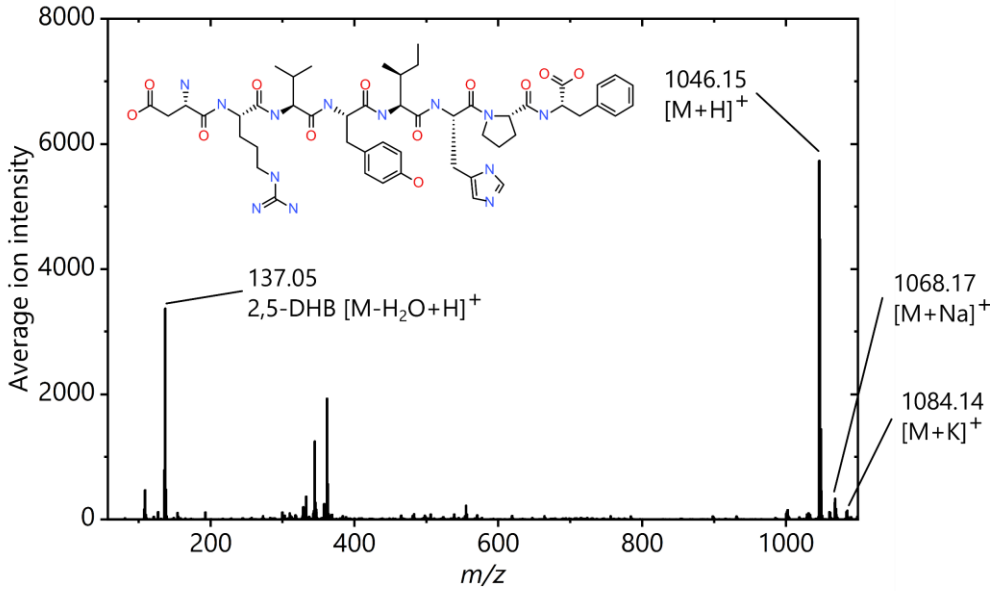


Figure 2.3. *Average UV-MALDI mass spectrum for Angiotensin II. The spectrum is the average of 45 spectra acquiring with 2,5-DHB in positive mode. Characteristic analyte and matrix peaks are tentatively assigned.*

Figure 2.3 shows the average spectrum of Angiotensin II. The intense peak at *m/z* 137. corresponds to 2,5-DHB $[M\text{-}H_2O+H]^+$ fragment ion , which is typically the most abundant 2,5-DHB ion observed in positive mode UV-MALDI MS. The peaks at *m/z* 1046.15, *m/z* 1068.16 and *m/z* 1084.14 correspond to the $[M+H]^+$, $[M+Na]^+$ and $[M+K]^+$ adducts of Angiotensin II. Peptides can undergo complex fragmentation, resulting in characteristic ions which are commonly identified using the nomenclature system proposed by Roepstorff and Fohlman[215] and later modified by Biemann[216]. In this instance the relative abundances of such fragment ions were low, due to "soft" nature of the 2,5-DHB matrix and moderate laser fluence used. The theoretical *m/z* values of common Angiotensin II positive fragment ions are shown in Table 2.1.

Table 2.1. *Theoretical Angiotensin II fragment ions.*

Fragment ion (*m/z*)							
Order	**a**	**b**	**c**	**x**	**y**	**z**	**Order (+1)**
1	88.039	116.03	133.06	-	1046.54	1029.50	**8**
2	244.14	272.14	289.16	957.49	931.52	914.49	**7**
3	343.21	371.20	388.23	801.39	775.41	758.39	**6**
4	506.27	534.27	551.29	702.33	676.35	659.32	**5**
5	619.36	647.35	664.38	539.26	513.28	496.26	**4**
6	756.42	784.41	801.44	426.18	400.20	383.17	**3**
7	853.47	881.46	898.49	289.12	263.14	246.11	**2**
8	1000.54	1028.53	-	192.07	166.09	149.06	**1**

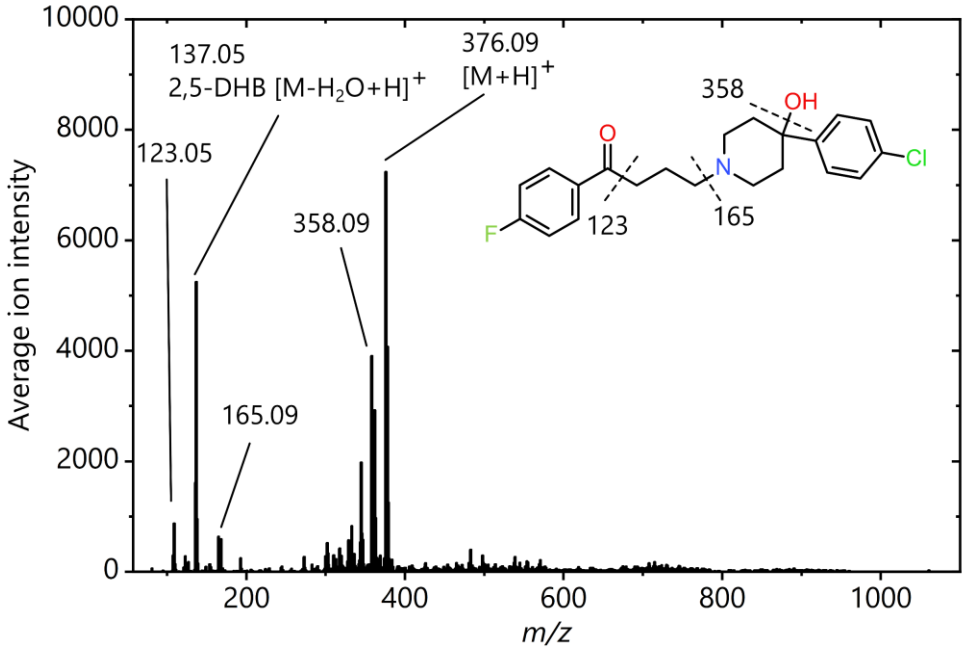


Figure 2.4. *Average UV-MALDI mass spectrum for Haloperidol. The spectrum is the average of 45 spectra acquiring with 2,5-DHB in positive mode. Characteristic analyte peaks are tentatively assigned.*

Figure 2.4 shows the average spectrum of Haloperidol with 2,5-DHB as the matrix. The peak at *m/z* 376.09 corresponds to Haloperidol $[M+H]^+$ adduct, no other adducts were detected. Characteristic fragments of the analyte, previously

identified from the literature[217], at *m/z* 358.09, *m/z* 165.09 and *m/z* 123.05 are also highlighted.

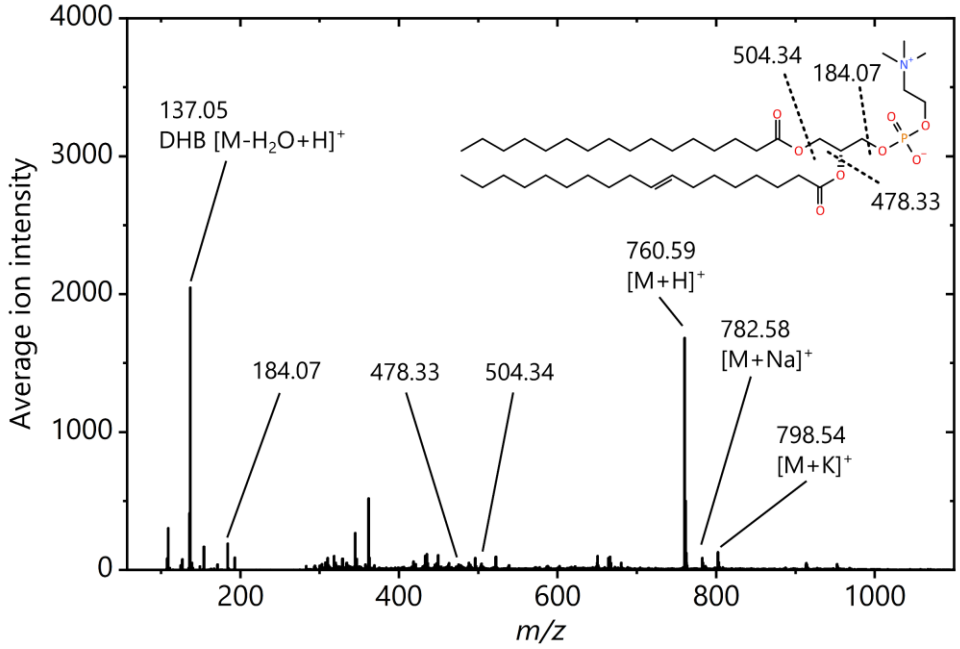


Figure 2.5. *Average UV-MALDI mass spectra for PC(34:1) lipid standard. The spectrum is the average of 45 spectra acquiring with 2,5-DHB in positive mode. Characteristic analyte peaks are tentatively assigned.*

Figure 2.5 shows the average spectrum of PC (34:1) with 2,5-DHB as the matrix. The peaks at *m/z* 760.38, *m/z* 782.36 and *m/z* 798.34 correspond to the $[M+H]^+$, $[M+Na]^+$ and $[M+K]^+$ adducts of PC(34:1). Characteristic fragments of the analyte, previously identified from the literature[218,219], including the lipid head group (*m/z* 184.08), as well as two fragments corresponding to loss of each acyl chain (*m/z* 504.12 and *m/z* 478.33).

2.4.2 - Matrix-analyte molar ratio and addition of TFA

Some effects arising from variation in matrix-analyte molar ratio, such as the matrix suppression effect (MSE), are well studied in UV-MALDI MS. That said, there remains a lot of uncertainty with regards to the influence of this parameter beyond the narrow set of conditions used to study effects like MSE. This becomes particularly important for imaging studies, where the matrix-analyte molar ratio can vary dramatically between the different components in a sample. Additionally, it is useful to also assess the benefit of using the common matrix additive TFA to understand the appropriateness of its application in modern UV-MALDI MS analyses. To this end the effects of matrix analyte ratio and TFA were investigated for a selection of 10 matrices and three analytes. The protonated molecular ion intensity for each combination of matrix and analyte are shown below in Figure 2.6.

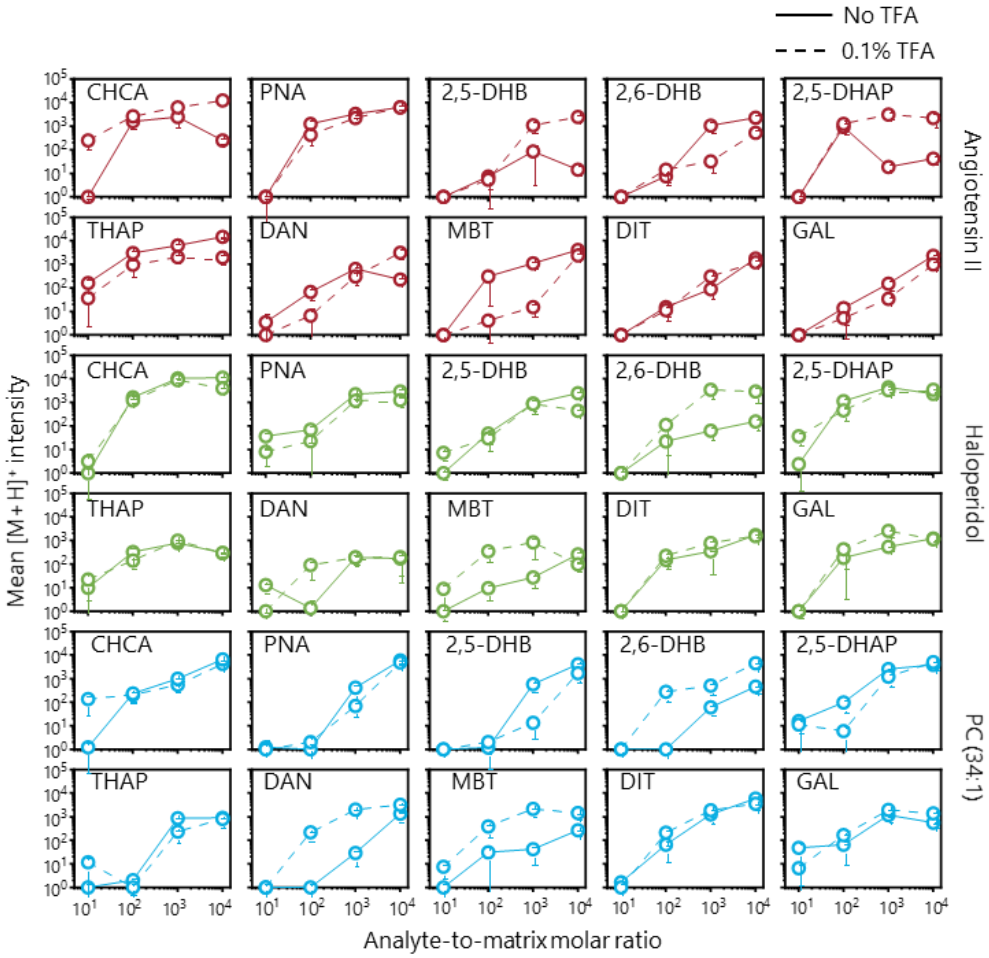


Figure 2.6. *Mean analyte $[M+H]^+$ intensities for ten matrix compounds and three analytes, across a range of matrix analyte ratios, with and without the addition of 0.1% v/v TFA. Data points represent mean values of 45 spectra. Error bars describe the standard error. All mean intensities values <1 were considered as zero, for display purposes these values were set to 1.*

The analyte $[M+H]^+$ intensity results (Figure 2.6) reveal that, in general, a larger matrix analyte molar ratio resulted in a higher analyte $[M+H]^+$ intensity, although CHCA, 2,5-DHAP and DAN were notable exceptions to this trend, evidencing reduction at higher molar ratios. For DAN this is not entirely unexpected, as this particular matrix was first applied as a reducing matrix for

peptide sequencing [199], therefore it stands to reason that higher concentrations of this matrix may lead to greater analyte fragmentation, and consequently a lower analyte $[M+H]^+$ signal. A similar effect may be happening with 2,5-DHAP, as this matrix has been previously shown useful for the generation of in-source decay (ISD) fragmentation of oligosaccharides[220]. The CHCA results are somewhat confusing, as this matrix is routinely used for peptide analysis, and so would be expected to effectively ionise angiotensin II at high molar ratios. Although the relatively "hot" nature of this matrix may be also causing reductions in analyte $[M+H]^+$ due to fragmentation.

The effect of TFA on analyte $[M+H]^+$ intensities varied between matrix compounds, and between analytes for the same matrix. For angiotensin II, addition of TFA resulted in increased $[M+H]^+$ intensities when CHCA, 2,5-DHB and 2,5-DHAP were the matrix, and reduced $[M+H]^+$ intensities when 2,6-DHB, THAP, DAN, MBT and GAL were used; $[M+H]^+$ intensities obtained with PNA and DIT remained relatively unaffected. Addition of TFA increased Haloperidol $[M+H]^+$ intensities when 2,6-DHB, MBT and GAL were used as the matrix, and reduced when PNA was used, with remaining matrices relatively unaffected. For PC(34:1) $[M+H]^+$ intensities were enhanced by TFA when 2,6-DHB, DAN, MBT and GAL were used as the matrix, but reduced with 2,5-DHB and 2,5-DHAP, with remaining matrices relatively unaffected. An interesting observation from the data is that even for the basic peptide Angiotensin II, the analyte most likely to see an enhancement from TFA, there were many matrices where suppression of $[M+H]^+$ intensity occurred. It was also notable that TFA served to counteracted the reductions in analyte $[M+H]^+$ intensity seen at high analyte-matrix molar

ratios for CHCA, 2,5-DHAP and DAN, either through enhancement of analyte ionisation efficiency, or in the case of DAN, supressing the reducing properties of the matrix.

Ultimately, no single matrix or analyte universally benefited or suffered from the addition of TFA. Of all the matrices and analytes studied here, DIT showed the least effect, suggesting that for applications involving this matrix, TFA is not a suitable additive.

In addition to analyte $[M+H]^+$, it is also useful to understand how matrix-analyte molar ratio and TFA can affect cation adducts as well. This is particularly important for UV-MALDI MS and MSI of biological samples, as $[M+Na]^+$ and $[M+K]^+$ adducts are typically the dominant molecular species observed in mass spectra obtained from such samples. With this in mind the effect of molar ratio and TFA on these adducts, for the different matrix analyte systems are shown in Figures 2.7 and 2.8 below.

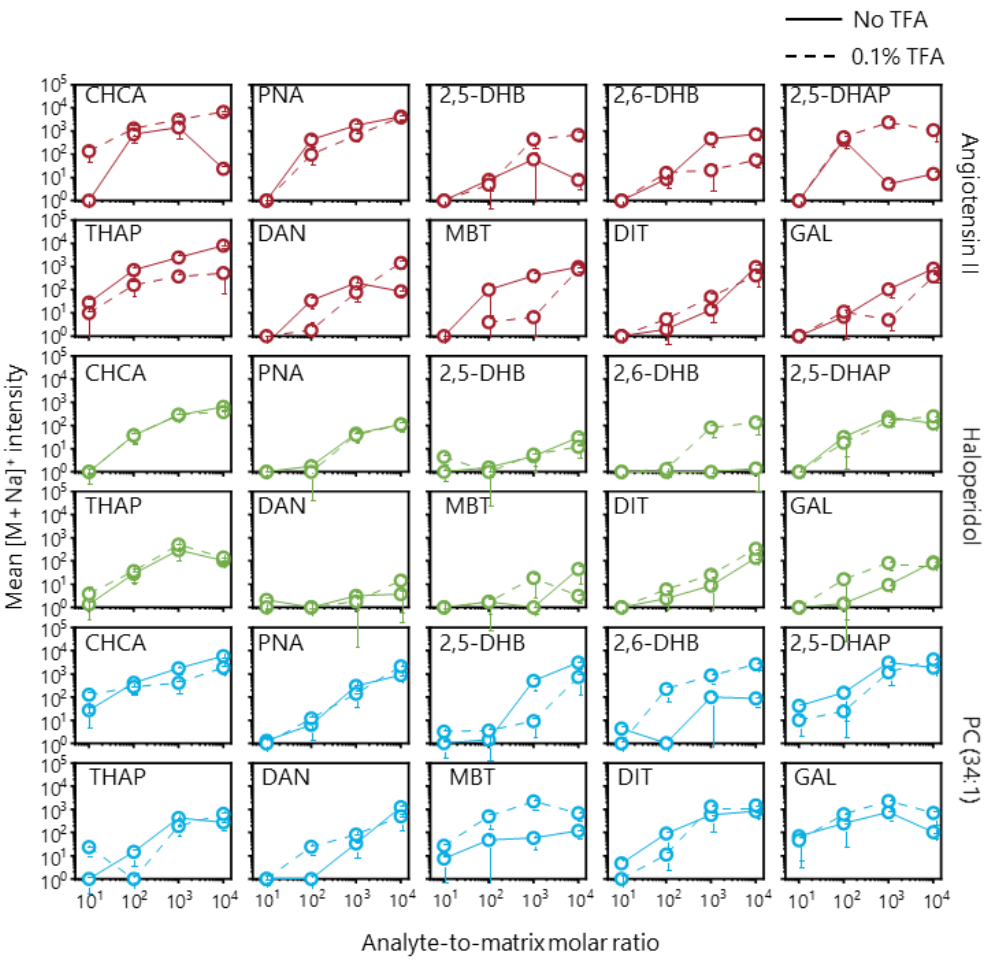


Figure 2.7. *Mean analyte $[M+Na]^+$ intensities for ten matrix compounds and three analytes, across a range of analyte-to-matrix molar ratios, with and without the addition of 0.1% v/v TFA. Data points show mean values of 45 spectra. Error bars describe the expanded uncertainty (k=2). For display purposes mean intensities < 1 were set to 1.*

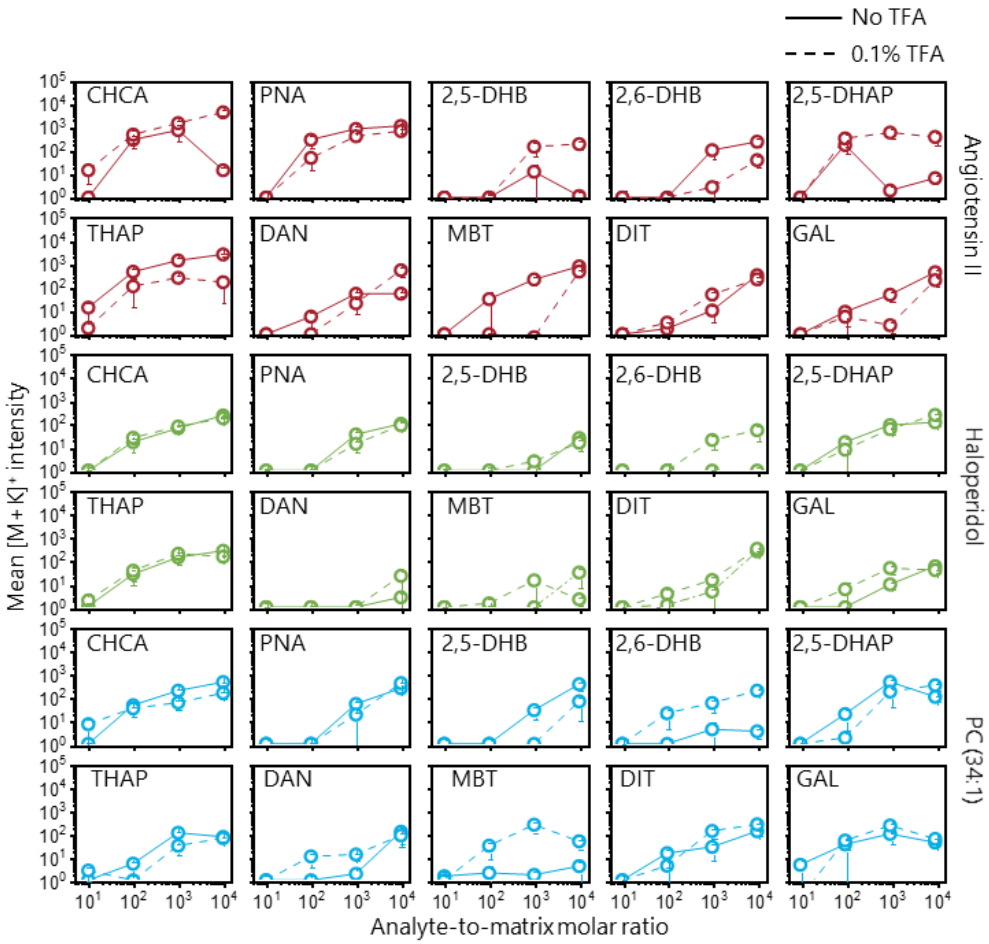


Figure 2.8. *Mean analyte $[M+K]^+$ intensities for ten matrix compounds and three analytes, across a range of analyte-to-matrix molar ratios, with (dashed lines) and without (solid lines) the addition of 0.1% v/v TFA. Data points represent mean values of 45 spectra. Error bars describe the standard error. For display purposes mean intensities <1 were set to 1.*

From the cation adduct ion intensity data it can be seen that in the majority of matrix analyte combinations, the effect of molar ratio and TFA addition mirrored what was seen in the $[M+H]^+$ data. There was some evidence of cation adduct suppression as a result of TFA addition in certain combinations, with the most clear example being PC(34:1) when CHCA was used as the matrix (Figures 2.7 &

2.8). Additionally, for matrix analyte combinations where TFA showed enhancement in analyte $[M+H]^+$ intensities (Figure 2.6), the effect on cation adduct intensities was much less pronounced, for example PC (34:1) with DAN and haloperidol with MBT.

These findings show that the assumption of TFA as a universally applicable additive for positive mode UV-MALDI MS is untrue for many matrix compounds and highlights the need for more careful consideration of additive inclusion in MALDI sample preparation protocols. The utmost caution should be used when applying TFA to tissue imaging, as its potential suppression effects make it unsuitable for most untargeted MS imaging experiments.

2.4.3 t-SNE

Due to the acquired data being highly complex, with many different variables being present, it was decided that further analyses would benefit from application of multivariate analysis approaches. With this in mind, two commonly used dimensionally reduction algorithms, t-distributed stochastic neighbour embedding (t-SNE) and Principal component analysis (PCA), were selected to apply to the data.

Introduce by van der Maaten and Hinton, t-SNE is a non-linear dimensionality reduction technique that is frequently applied in the visualisation of complex, multidimensional data[211]. While detailed discussion of the operating principles of t-SNE is outside the scope of this work, a short explanation of the application and interpretation of t-SNE for use on MS data is pertinent.

Dimensionality reduction in t-SNE works in such a way that similar data is clustered together in the reduced space, in the context of t-SNE applied to MS data this results in the clustering of similar mass spectra. It is important to note that because t-SNE is a non-linear technique, distances between clusters in the reduced t-SNE space are not reflective of those in the original data. This non-linear quality, along with the stochastic nature of the algorithm, means that inferences taken from distances between clusters, and their relative placement, cannot be used to describe relationships in the original data. Additionally, this means t-SNE cannot provide information about what *m/z* values may be driving the clustering of spectra.

The results of t-SNE applied to the all the UV-MALDI MS data collected for the different studied conditions, is shown in Figure 2.9. The cosine distance metric was used in the t-SNE so as to ensure that spectral data was equally weighted and absolute intensities did not skew the results.

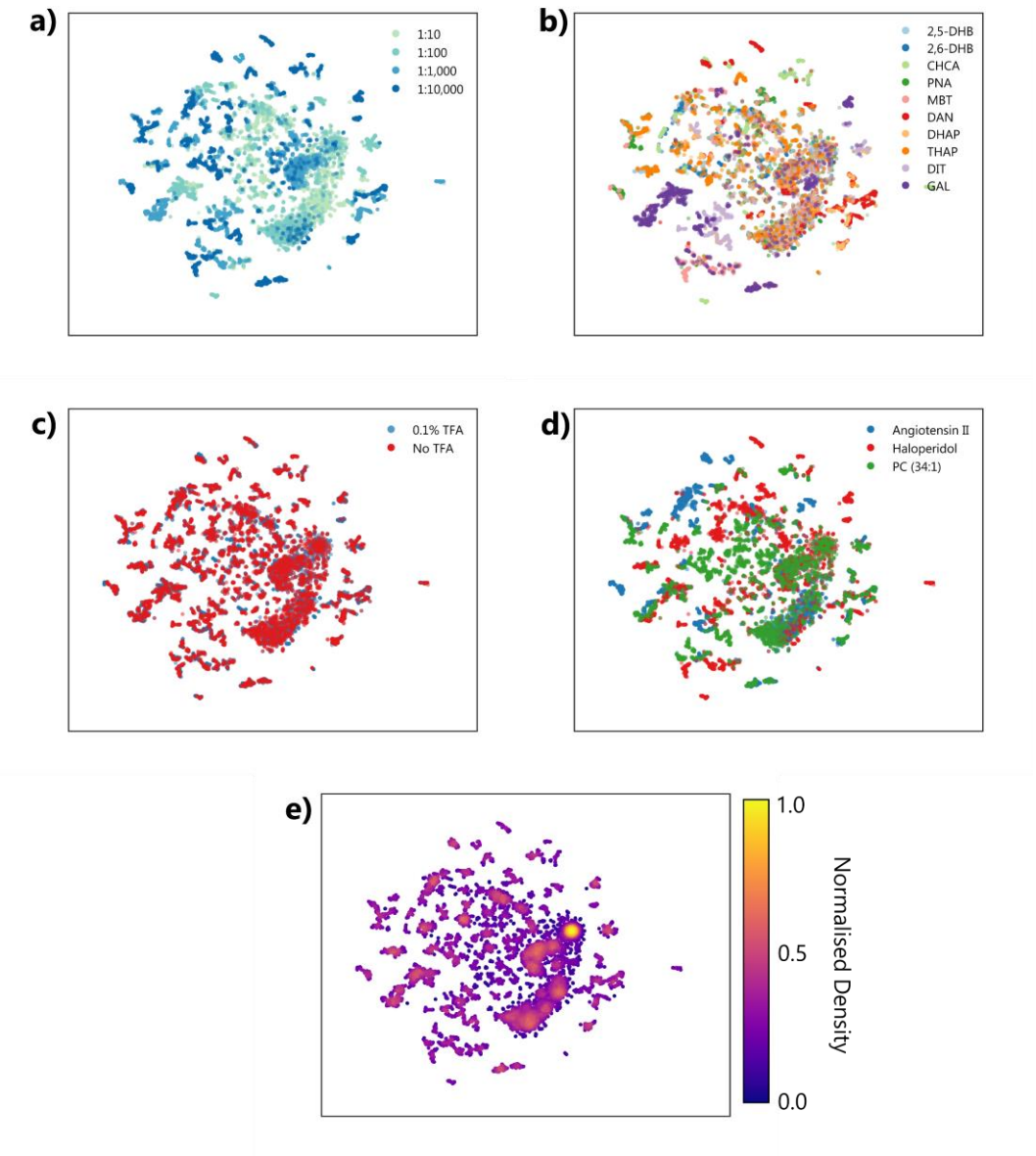


Figure 2.9. *Cosine distance t-SNE plots of UV-MALDI-MS data for all the conditions studied in this chapter. t-SNE plots are colour-coded by* ***a)*** *analyte-to-matrix molar ratio* ***b)*** *matrix* ***c)*** *presence or absence of 0.1% TFA and* ***d)*** *analyte. A density map of the data points* ***e)*** *is included to aid interpretation of the t-SNE results.*

The t-SNE plots of all collected MS data shows evidence for numerous clear clustering by certain conditions. From the results it can be seen that that broadly

speaking molar ratio (Figure 2.9d) was the biggest driver of similarity between the spectra, with low ratios resulting in diffuse clustering irrespective of the other variables such as matrix (Figure 2.9a) or analyte (Figure 2.9b). Generally, the spectra only begin to cluster at molar ratios in excess of 10^3, at which point clustering by both matrix and analyte becomes evident. That said, some matrix analyte combinations can be distinguished at matrix-analyte molar ratios of 10^2, such as angiotensin with CHCA, and DIT and GAL with all the analytes. Although in for the latter two matrices it is clear that matrix is the main driver of the clustering at this ratio (Figure 2.9a & 2.9b).

When looking at the data as a whole it is also clear that TFA had the least effect of all the variables studied (Figure 2.9c). This is perhaps not surprising, given that any global effect of that addition of TFA may have on the spectra must be significantly less than either the matrix or the analyte.

2.4.4 - PCA analysis

While the t-SNE results provided a general overview of the structure of the data, they are not able to provide information about the spectral changes that matrix-analyte molar ratio and TFA addition may be inducing. With this in mind, PCA was applied to the spectral data associated with each matrix compound. PCA is a linear dimensionality reduction method, therefore can provide information on the spectral features driving differences between the different experimental conditions. As with t-SNE, normalisation of the data was required to ensure equal weighting of each peak in the spectra. It is pertinent to note that unlike t-SNE, which reduced the data based on similarity, PCA described the variation in

the data. This is particularly important when interpreting the loadings results, as a high positive or negative loading on a peak is a descriptive of its variation in the data and is not a correlation to intensity.

Initial inspection of the PCA loadings for the different conditions revealed a consistent set of peaks that dominated the variation found in the data, apart from DIT and GAL these peaks were the main drivers of variation in PC1 for all matrix systems. An example of this is shown in Figure 2.10 and the dominant peaks listed in Table 2.2.

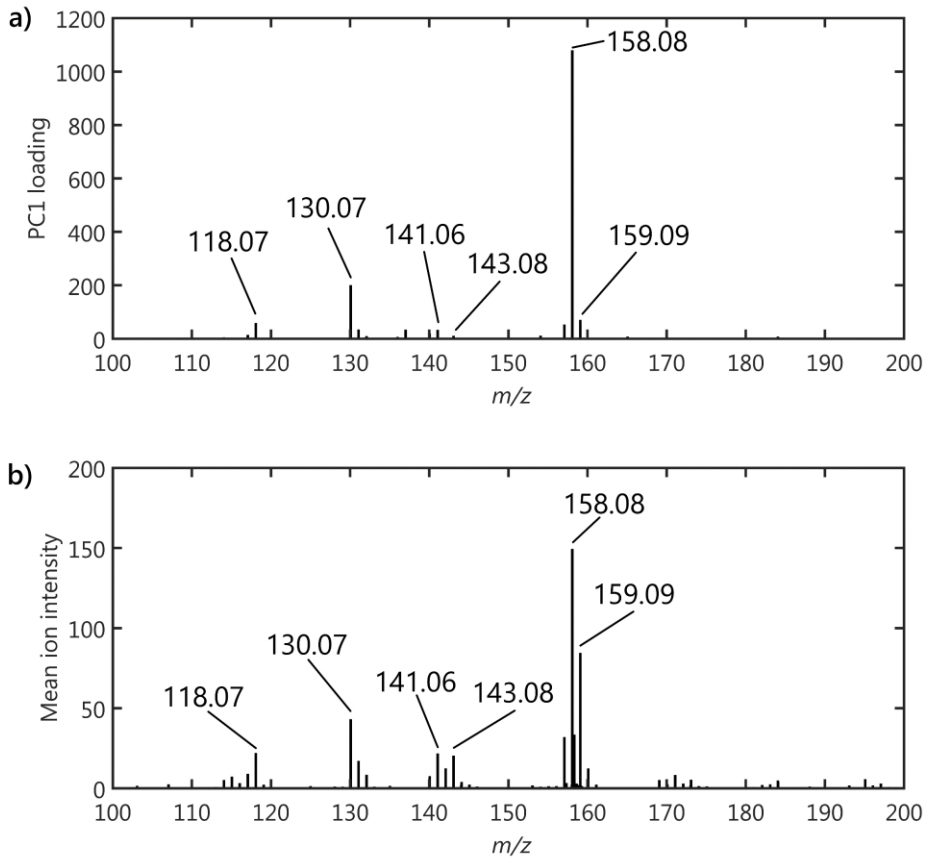


Figure 2.10. a) *Loadings spectrum of PC1 for 2,5-DHB, demonstrating the contamination issue.* ***b)*** *Mean spectra of 1,5-DAN matrix with PC (34:1) lipid standard. Common peaks between the two spectra are annotated.*

Table 2.2. *List of identified contaminating peaks, with assignments. Molecular species (M) has been tentatively assigned as DAN matrix.*

m/z	**Formula mass**	**Tentative assignment**
159.09	$C_{10}H_{11}N_2$	$[M+H]^+$
158.08	$C_{10}H_{10}N_2$	$[M]^+$
143.08	$C_{10}H_9N$	$[M-NH_2]^+$
141.06	$C_{10}H_7N$	Unknown fragment
130.07	C_9H_8N	$[M-HNC]^+$
118.07	C_9H_{10}	Unknown fragment

Inspection of the *m/z* values revealed that these peaks were most likely related to the matrix DAN (Figure 2.10). This conclusion was further supported by the fact that the PCA loadings results for matrices that used a unique solvent system (pure THF), DIT and GAL, were less affected by the contamination. To remove the influence of this contamination, the peaks identified from the PCA results were removed for all matrices other than DAN, and PCA run again in the resulting spectra (Figure 2.11).

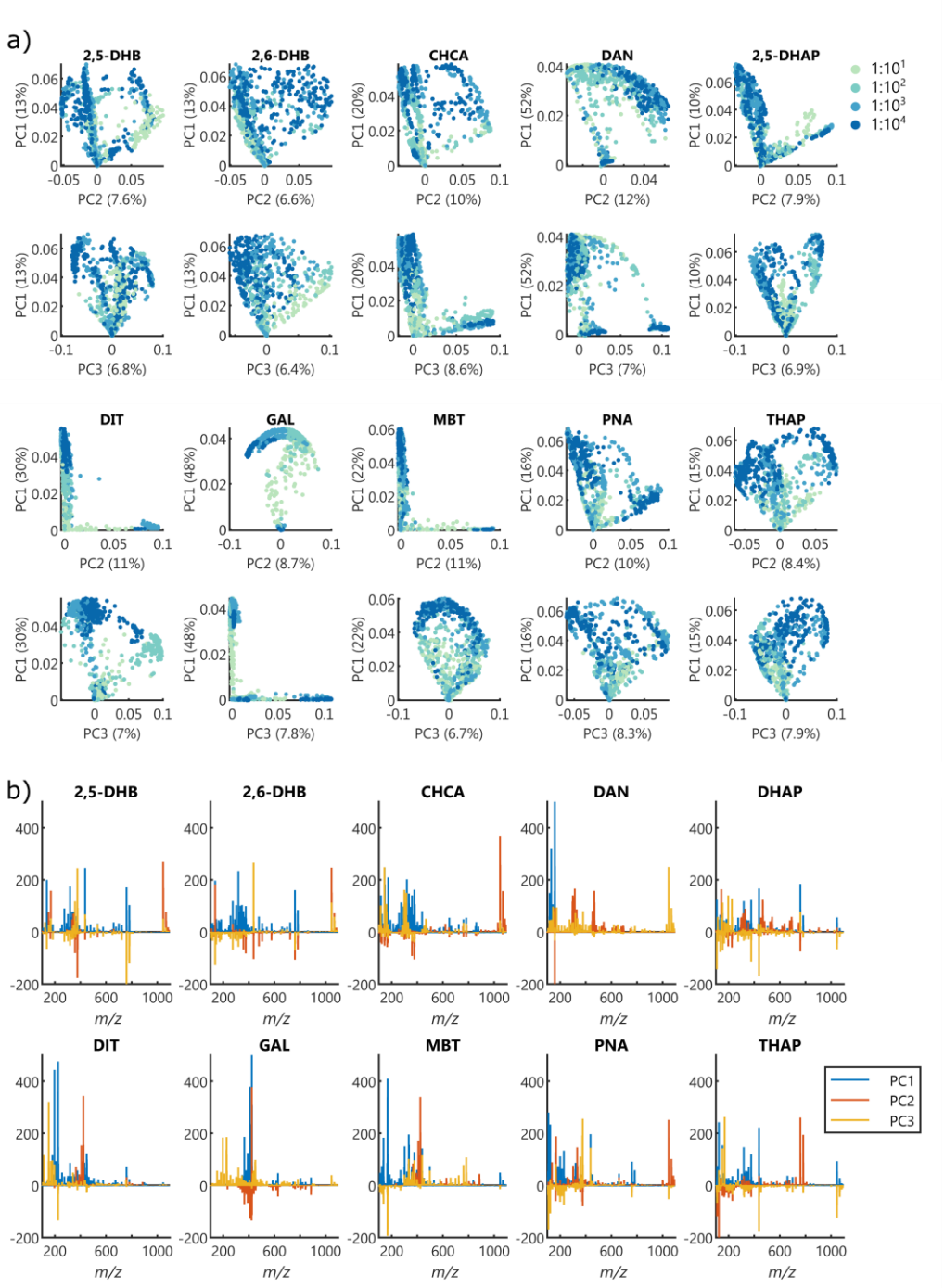


Figure 2.11. a) *PCA score plots showing the first three PCs for all collected mass spectra, grouped by matrix. Scores plots are colour coded by analyte-to-matrix molar ratio.* ***b)*** *Corresponding PCA loadings plots, grouped by matrix. PCA was run on z-scored data to standardise the contributions of each peak in the spectra.*

From the PCA scores plots it can be seen that generally the spectral variation in data was reflective of changes in the analyte-to-matrix molar ratio (Figure 2.11a), with the different ratios grouping together along PC 1 and PC 2, and to a lesser extent PC3, for most matrices. The matrices DAN, DIT, GAL and MBT evidenced particularly strong grouping by ratio, suggesting that spectra obtained with these matrices change noticeably. Conversely some matrices (e.g. 2,5-DHAP) show a relatively weak clustering by molar ratio, suggesting the spectra obtained from these matrices were relatively stable to changes in this parameter. Inspection of the corresponding PC loading plots (Figure 2.11b) suggested that one of the main contributors to the variance associated with molar ratio were matrix related peaks. For example, the DHB isomers showed a strong contribution from *m/z* 137.01 (Figure 2.11b), which corresponds to the $[M\text{-}OH]^+$ fragment, commonly the most abundant peak for DHB. Such a result makes sense for the systems studied here, as the amount of analyte was fixed, thus increases in molar ratio beyond a certain point would only lead to an increase in matrix related ions.

Unsurprisingly given the nature of the samples systems studied, the analytes also had a significant influence on the variance in the data, as clearly shown in Figure 2.12.

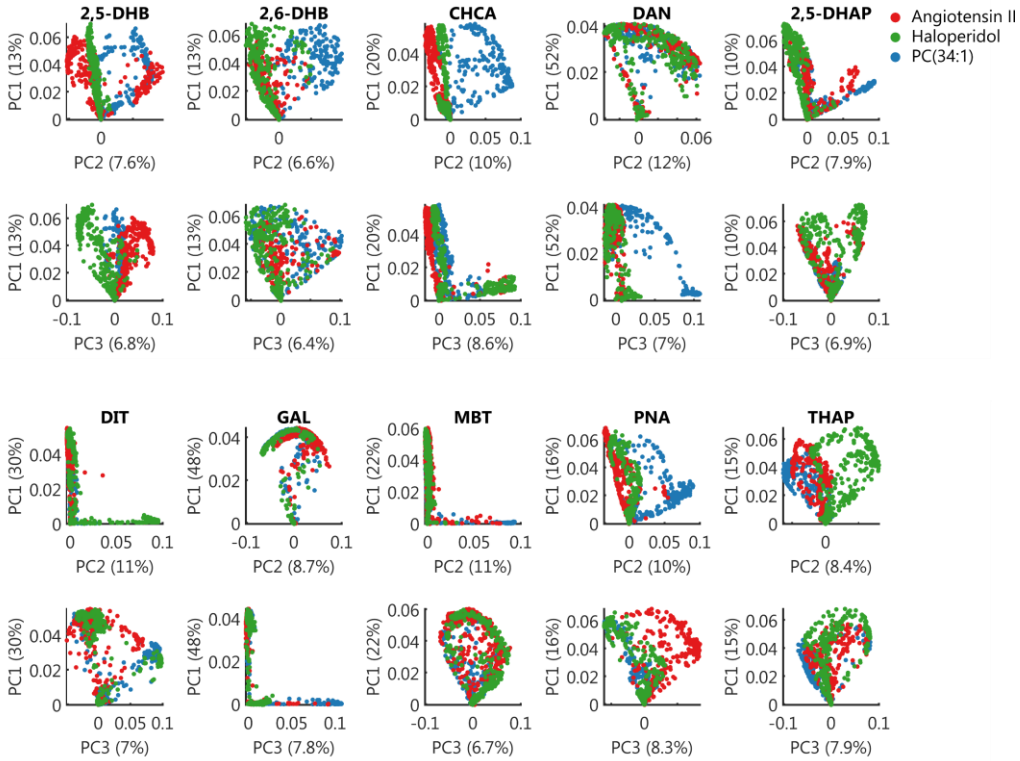


Figure 2.12. *PCA score plots showing the first three PCs for all collected mass spectra, grouped by matrix. Scores plots are colour coded by analyte. PCA was run on z-scored data to standardise the contributions of each peak in the spectra.*

When inspecting the PCA scores plots coloured by analyte, there is a clear clustering of the spectral data along PC2 and PC 3 axes. This behaviour is most clearly expressed for CHCA, 2,6-DHB, PNA, DAN and THAP. It's also interesting to note the interaction of analyte and molar ratio occurring in some instances, for example with 2,5-DHB matrix the analytes are clearly separated along PC2 (Figure 2.12), with the exception of Angiotensin II which is split between low and molar ratios (Figure 2.11a).

From the scores plots there is also a clear pattern to differentiation between the analytes, with Angiotensin II and Haloperidol grouping together more frequently, most evident in the data associate with CHCA, DAN, PNA and GAL. This suggests that for theses matrices, Angiotensin II and Haloperidol had similar behaviour over range of experimental parameters studied.

An interesting feature of note is that the relative loadings for some of the analyte adduct peak varied for the different matrices (Figure 2.11b). In particular, CHCA, MTB and GAL showed that PC(34:1) $[M+Na]^+$ had a greater variation over the whole data than the $[M+H]^+$, perhaps reflecting that for these matrix compounds, the formation of $[M+Na]^+$ is somehow affected by the molar ratio or addition of TFA. Likely sources for the variance associated with these experimental parameters may be either the suppression of cation adduct formation arising from the TFA, or a dilution effect brought on by the increasing amount of matrix content in the samples.

To isolate the effect of TFA from the other experimental variables, PCA was rerun on reduced datasets consisting individual matrix-analyte combinations at a single molar ratio of 10^4 (Figure 2.13).

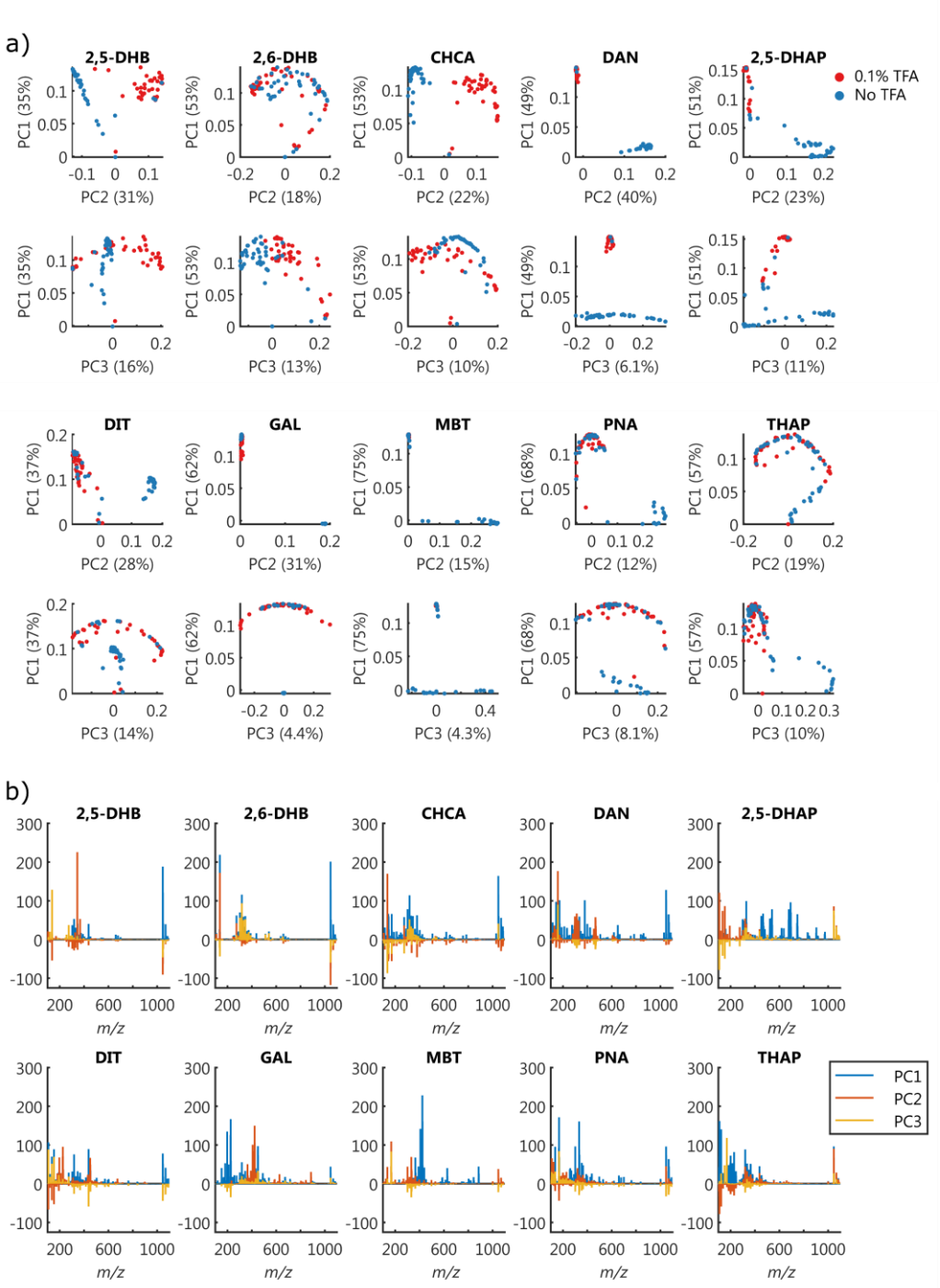


Figure 2.13. a) *PCA score plots of the first three PCs for all collected mass spectra of Angiotensin II at 10^4 molar ratio. Scores plots are colour coded by the absence or addition of 0.1% v/v TFA.* ***b)*** *Corresponding PCA loadings plots. PCA was run on z-scored data to standardise the contributions of each peak in the spectra.*

The PCA scores plots of the reduced dataset for Angiotensin II show clear separation between the presence and absence of TFA for some of the matrices (Figure 2.13a). With the exception of THAP and PNA, all the matrix compounds showed a greater or lesser degree of separation along one of the first three PCs. DIT and GAL showed some evidence of a TFA related effect, but with clear evidence of a strong unidentified source of variation as well.

The corresponding loadings plots for the angiotensin II data showed the largest source of variation for most matrices was either the matrix molecular peaks ($[M+H]^+$ or $[M]^+$) and the Angiotensin II $[M+H]^+$ peak (Figure 2.13b). Some matrices showed evidence of alterations between the analyte adducts, for example the $[M+Na]^+$ adduct (*m/z* 1068) with PNA and DAN. Evidence of changes to analyte fragmentation induced by the TFA can also be found in the loadings data. For example, *m/z* 619.3, *m/z* 647.3 *m/z* 756.4 and *m/z* 784.4 ions appear in the loadings plots of CHCA, DAN and PNA, can be tentatively matched to the a_5, b_5, a_6 and b_6 fragment ions of the peptide.

All the matrixes appeared to show a strong PC1 or PC2 contributions from various ions in the *m/z* 300-400 range, these were likely related to the formation of matrix clusters as they were common throughout the different analytes for a given matrix. 2,5-DHAP showed a particularly strong set of peaks across its loading mass spectrum for PC1, although no obvious identity for these species could be determined, they were likely related to Angiotensin II as they were not evident in the loading spectra for the other analytes. 2,5-DHAP has been previously used to enhance ISD of oligosaccharides, so the addition of TFA may

be related to enhanced ISD with this matrix[220]. As whole the addition of TFA appeared to be associated with changes in analyte ionisation, including alterations in adducts for some matrices. Changes in degrees of fragmentation and matrix cluster formation also appear to be a feature.

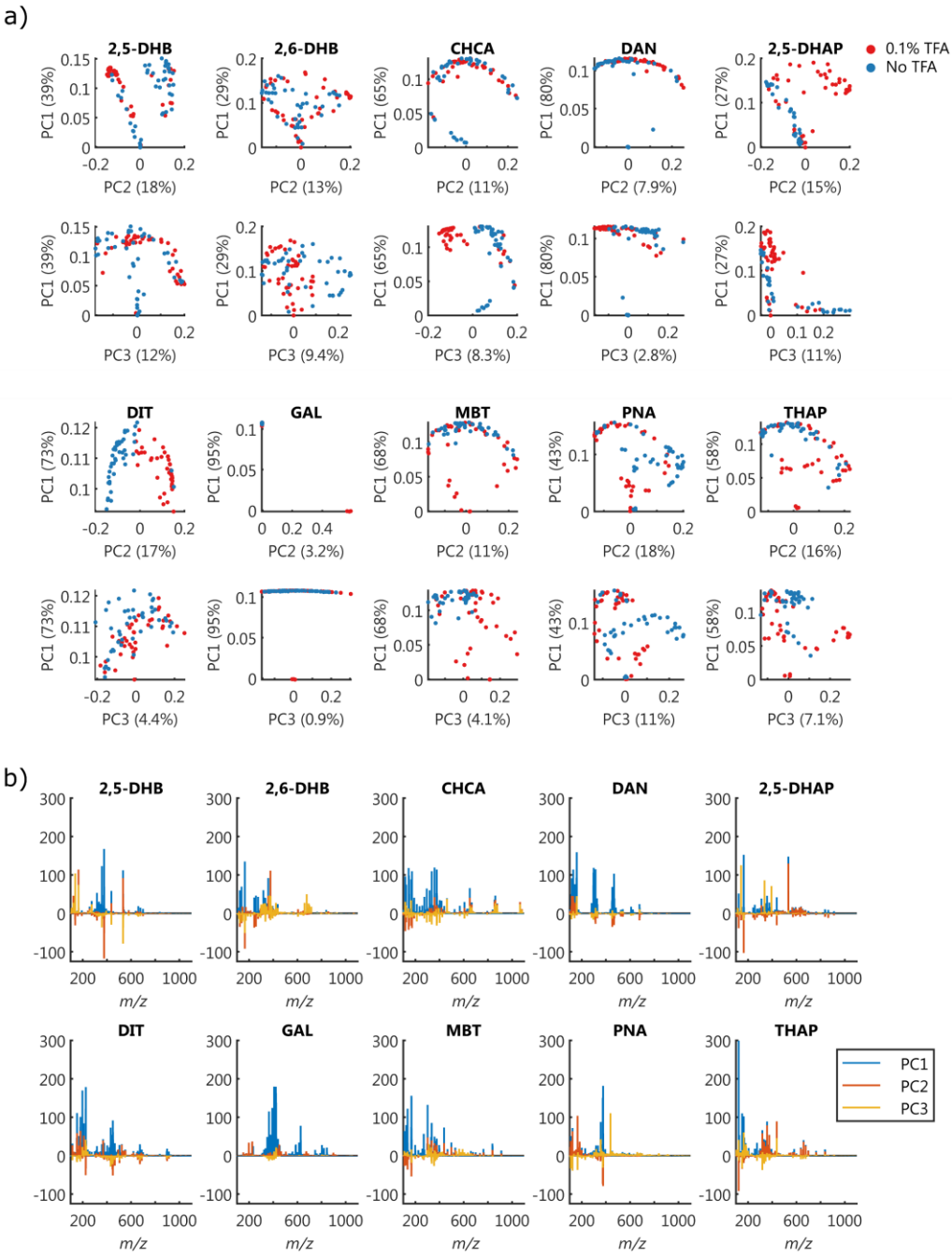


Figure 2.14. a) *PCA score plots of the first three PCs for all collected mass spectra of Haloperidol at 10^4 molar ratio Scores plots are colour coded by the absence or addition of 0.1% v/v TFA.* ***b)*** *Corresponding PCA loadings plots. PCA was run on z-scored data to standardise the contributions of each peak in the spectra.*

PCA scores plots for Haloperidol show that with most of the matrix compounds the addition of TFA had very little influence on the resulting spectra (Figure 2.14a). Of the matrix compounds, CHCA, 2,5-DHAP, DIT and GAL showed some evidence of TFA influence. The correspond loadings spectra show that Haloperidol $[M+H]^+$ and its characteristic fragments were the main driver of variation for the majority of matrices (Figure 2.14b), although as the scores results showed TFA had little influence, some other factor is likely at play. For DAN, DIT and GAL the loadings spectra were dominated by change to matrix related peaks. As with Angiotensin II some degree of variation in Haloperidol fragmentation was associated with the addition of TFA, with 2,5-DHAP showing significant variation in the *m/z* 123 and *m/z* 165 fragments.

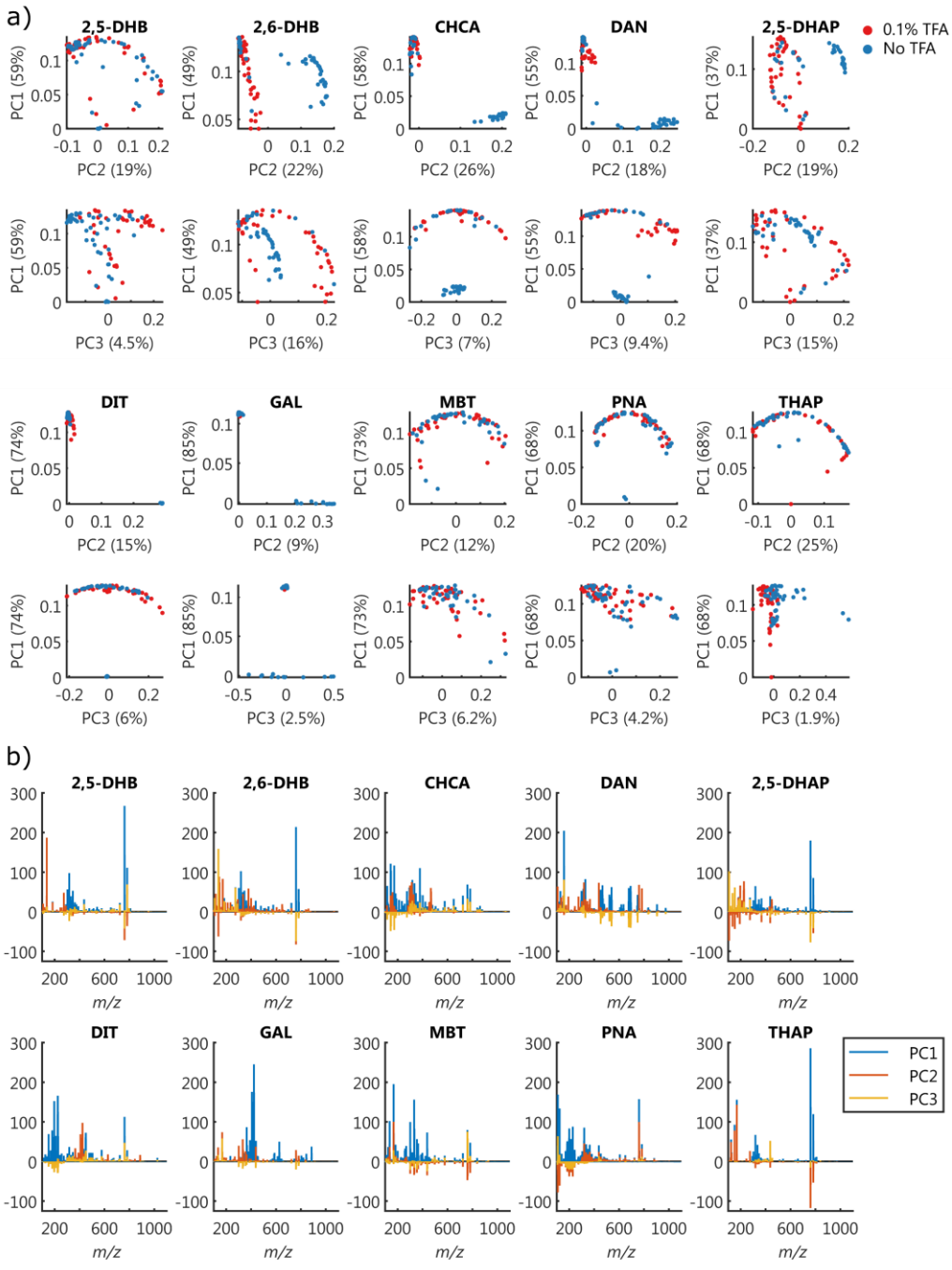


Figure 2.15. a) *PCA score plots of the first three PCs for all collected mass spectra of PC(34:1) at 10^4 molar ratio . Scores plots are colour coded by the absence or addition of 0.1% v/v TFA.* ***b)*** *Corresponding PCA loadings plots. PCA was run on z-scored data to standardise the contributions of each peak in the spectra.*

The PCA scores plot for the first three components of the spectra associated PC(34:1) lipid standard showed clear separation resulting from TFA for 2,6-DHB, CHCA, DAN and 2,5-DHAP, and to a lesser degree 2,5-DHB and THAP (Figure 2.15a). Similar to what was observed with angiotensin II, DIT and GAL showed strong influence an unidentified source of variance.

Inspection of the corresponding spectra loadings plots (Figure 2.15b) reveal that the PC(34:1) $[M+H]^+$ and cation adducts were one of major sources of variation for both the DHB isomers, 2,5-DHAP, DIT, PNA and THAP. CHCA also showed a relatively similar loading for both the protonated and sodiated PC(34:1) species, suggesting that for this matrix TFA did not significantly alter adduct ratios.

As whole the addition of TFA appeared to be associated with changes in analyte ionisation, including alterations in adducts for some matrices. Changes in degrees of fragmentation and matrix cluster formation also appeared to be a feature. It is clear from the results that the blanket application of TFA in positive mode UV-MALDI MS, irrespective of the matrix used or analyte studied, is problematic. In particular the data showed here shows that its use with Haloperidol was for the most part unnecessary.

2.5 - Conclusions

The effects of two common UV-MALDI MS sample preparation parameters, analyte-matrix molar ratio and use of TFA, were investigated using a range of 10 matrices and three analytes. Analyte-to-matrix molar ratio ranging from 10 to 10^4. A positive correlation between ratio and analyte molecular ion intensities was observed for the majority of system, although some matrices (CHCA, 2,5-

DHAP and DAN) evidenced reductions at higher ratios. While this implies that higher ratios are almost always preferable for UV-MALDI MS, the associated increase in matrix related peaks suggests that a trade-off between better analyte sensitivity and increased spectral complexity exists in many cases.

The application of TFA as an additive to enhance analyte ionisation was found to be highly specific to only a few matrix analyte combinations, with none of the matrix systems studied showing an enactment for all three analytes, and many showing significant ion suppression. TFA was found to be associated with variation in matrix cluster formation, analyte fragmentation and levels of cation adduct. These findings show that the assumption of TFA as a universally applicable additive for positive mode UV-MALDI MS is untrue and highlights the need for more careful consideration of additive inclusion in sample preparation protocols. The utmost caution should be used when applying TFA to tissue imaging, as its notable suppression effects make it unsuitable for most untargeted MS imaging experiments.

In the course of the experiments it was found that variation in quality of samples could be quite high. In particular the differences in crystallisation behaviours between the various matrix compounds, exacerbated by the dried droplet deposition method used here, were substantial, and may have had an impact on the eventual results. With this in mind, these experiments could be repeated with a more reliable and consistent sample preparation method in future.

Chapter 3 - Matrix optical absorption in UV-MALDI MS

Work presented in this chapter has been published in the following journal article.

Robinson, K. N.; Steven, R.T.; Bunch, J. Matrix Optical Absorption in UV-MALDI MS. *J. Am. Soc. Mass Spectrom.* **2018**, 29 (3), 501–511. https://doi.org/10.1007/s13361-017-1843-4.

3.1 - Introduction

The interaction between matrix optical absorption and the wavelength and pulse energy of the incident laser radiation strongly influences UV-MALDI mass spectra. Consequently these parameters have been investigated in numerous studies seeking to determine their relative influences[23,24,67]. Additionally, significant debate continues regarding the nature of ion formation in UV-MALDI MS, with the principal proposed models all considering optical absorption one of the primary matrix physicochemical properties involved in ion formation and desorption [79,107,152,160–162,167–169].

Previous studies have shown that higher matrix optical absorption corresponds to improved spectral quality [221], as well as higher analyte ion intensities and ion yields [17,22,24]. MALDI MS studies using tuneable wavelength lasers have also suggested the existence of a minimum matrix optical absorption required for detection of analyte ions[31]. Despite the obvious benefits to optimisation of UV-MALDI MS experimentation and development of ionisation theories, available data on matrix optical absorption is minimal. This is in part the result of well know differences between absorption in solids, the form most matrices are

present as in UV-MALDI MS, and solutions, the typical sample type for optical absorption measurements. To date only a handful matrix compounds have semi-quantitative[22–24] or quantitative[19,20,30] solid phase absorption data available.

The number of photons per unit area has been determined as the principal laser parameter determining desorption and ionisation in UV-MALDI MS[57]. At fixed wavelengths typical of UV-MALDI MS this is equivalent the energy delivered per unit area, or fluence. Traditionally the relationship between fluence (H) and ion intensity (I) in UV-MALDI MS has been characterised via the function $H \propto I^m$ [62], with m describing the increase of ion intensity. Recently a more a comprehensive model has been published (Equation. 3.1)[24].

$$I = \hat{I}\frac{(H-H_{thr})^m}{(H_k-H_{thr})^m+(H-H_{thr})^m} \qquad (3.1)$$

This function makes use of three additional factors as approximations for important characteristics of the ion intensity curve. H_{thr} describes the threshold fluence and $\hat{I}$ the maximum ion intensity of the curve. The H_k parameter corresponds to the fluence at which the highest ion yield, and thus experimental sensitivity may be obtained[24].

In many previous fluence studies in UV-MALDI MS the analytes studied are, by and large, confined to a small range of peptides and proteins. A few investigations into laser energy effects have made use of different classes of analyte[17,170,222], although few have measured laser fluence[17,67]. A systematic study of the relationship between matrix optical absorption, laser fluence and

detected ion intensity in UV-MALDI MS across a range of analyte classes and matrix compounds is therefore of clear interest.

3.2 - Materials

CHCA, PNA, 2,6-DHB, 2,5-DHAP, DAN, MBT, THAP, Galvinoxyl, Haloperidol, Angiotensin II and acetonitrile (ACN) were purchased from Sigma Aldrich (UK). 2,5-DHB and Dithranol were purchased from Alfa Aesar (UK). PC(34:1) lipid standard was purchased from Avanti Polar Lipids (USA). HPLC grade methanol (MeOH) and tetrahydrofuran (THF) were purchased from Fisher Scientific (UK). Unless stated otherwise all water was deionised (ρ=15 MΩcm^{-1}) and generated using a Purelab system (Elga, UK)

Stainless steel MALDI target plates were purchased from Sciex (UK). 25 mm x 25 mm quartz substrates were purchased from Agar Scientific (UK). Quartz cuvettes (path length = 10 mm) were purchased from Hellma (UK). Silicon wafer (110, 20 nm SiO_2) was obtained from University Wafer (USA)

3.3 - Methods

3.3.1 - Matrix deposition for optical measurements – Home built sublimation system

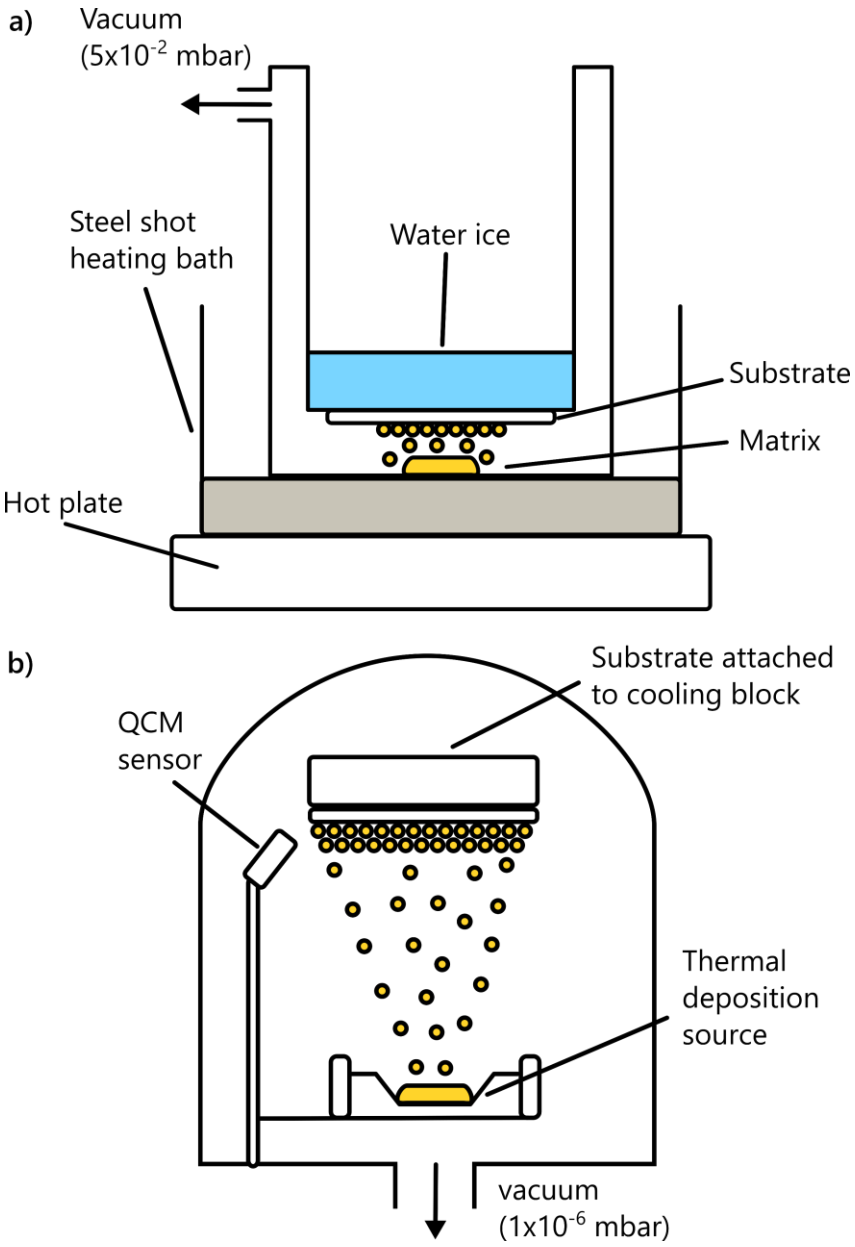


***Figure 3.1**. Diagram of the two sublimation deposition approaches used to manufacture matrix thin films for absorption measurements. **a)** Homebuilt sublimation system **b)** Edwards Auto 306 evaporator.*

Matrix thin films for optical characterisation were prepared used two different sublimation deposition approaches (Figure 3.1). For the initial set of absorption measurements for the 10 matrix compounds a glass sublimation chamber (Ace Glass, USA) coupled to a homemade vacuum system was utilised (Figure 3.1a). The vacuum system consisted of a vacuum pump (EM2, Edwards, UK) connected via a cold finger to the sublimation chamber. The pressure within the vacuum system was monitored using a Priani gauge (APG100-XM, Edwards, UK) connected to an instrument controller (TIC Instrument Controller 3 Head, Edwards, UK) to enable readout from the gauge. Pressure within the vacuum system was controlled via a manual needle valve (LV10K, Edward, UK) coupled to the lab nitrogen supply, allowing controlled admittance of gas into the vacuum system.

Matrix was placed on the bottom of the sublimation chamber in an even layer, and a quartz substrate was attached to the bottom face of the condenser section of the chamber using thermally conductive tape (3M, UK). The chamber was pumped down and the pressure regulated to 5.0×10^{-2} mbar and placed in a heating bath filled with steel shot. A water-ice mix was then placed in the condenser to keep the substrate cool during deposition. Deposition was controlled by varying the amount of time the chamber was heated for and the temperature of the heating bath.

3.3.2 - Matrix deposition for optical measurements – Edwards Evaporator

Matrix thin films were deposited on quartz substrates using an Auto 306 Thermal Evaporator (Edwards, Eastbourne, UK) under intermediate vacuum

conditions (~10^{-4} mbar) (Figure 3.1b). Along with the quartz substrate a silicon wafer (10 x 10 mm) was simultaneously coated for deposited film thickness determination measurements. Both substrates were attached to a chilled (~5°C) block of copper with thermal conductive tape (3M, UK) to ensure deposition of the matrix compounds. Deposition was carried out by placing 100 mg of matrix in a homebuilt tantalum resistive boat. The boat was fitted with perforated lid to prevent ejection of large particles from the matrix powder during deposition. The sample boat was then connected to two electrodes and the chamber pumped down to vacuum. Once the correct pressure range was reached a current was applied across the boat, resulting in resistive heating of the sample and sublimation. The deposition rate was monitored via the evaporator's quartz crystal microbalance (QCM) sensor.

3.3.3 - UV-Vis spectroscopy of UV-MALDI matrix compounds

All absorption spectra were acquired using a UV-Vis spectrophotometer (Lambda 850, Perkin Elmer, UK). Solid phase absorption measurements were obtained from three different positions on the matrix thin films to account for any macroscopic variations in film thickness. Inclusion of another quartz substrate in the reference beam of the instrument meant that losses from reflection were primarily a result of differences in refractive index (*n*) between the matrix and substrate. From calculations using reported *n* values for cinnamaldehyde[223] and nitrobenzene[224] acting as analogues of the matrix compounds, reflection losses (at normal incidence) were estimated to be no greater than 3%. For the films produced using the Edwards Evaporator, optical scattering effects, which can lead to erroneous measurement of absorption by

deflecting light away from the detector of spectrophotometer, were assumed to be negligible due to the high transparency and uniformity of the matrix films produced. Solution phase measurements were taken from 10 mmol L^{-1} solutions of matrix compound in MeOH or THF. 700 µL of matrix solution was pipetted into a quartz cuvette for analysis. Another quartz cuvette filled with matching pure solvent was used in the reference beam on the instrument.

3.3.4 - Matrix film thickness measurement

Deposited matrix film thickness was determined by Atomic force microscopy (AFM: Cypher S, Asylum Research, UK) measurements of the co-deposited Si wafers samples. A pair of fine tipped tweezers were used to manually score the films. AFM measurements were taken at four points along the scratches, and typically extended 20 µm from the edge of the trench to ensure any material ploughing effects did not affect the height measurement. The substrate flatness in the AFM images served as a quality check that no damage had occurred and that the matrix layer had been effectively removed.

3.3.5 – Matrix compound density

Matrix compound density was determined using an AccuPyc 1340 gas pyknometer (Micromeritics, UK). Samples of matrix powder were placed in a desiccator for five days prior to the analysis to minimise the effects of absorbed atmospheric water on the measurements. A minimum of five measurements were performed at 21°C, using helium as the displacement medium.

3.3.6 - UV-MALDI MS

UV-MALDI MS data were collected over a mass range of *m/z* 50-1100 in positive mode using a QSTAR XL Qq-ToF mass spectrometer fitted with a oMALDI2 source (Sciex, UK), coupled via 100 µm round optical fibre (Fiberguide Industries, USA) to a 355 nm Nd:YAG DPPS laser (FQS-100-1-Y-355, Elforlight, UK), operating at 1kHz with a pulse width of <4 ns. The laser was triggered with a square wave signal by a function generator (TG2000 20 MHz DDS, TTi, UK). A shutter system, previously described by Steven et al.[206], was used to aid pulse energy stability during experiments. Data collection were controlled via the Analyst QS 1.1 and oMALDI server 5.1 software packages (Sciex, UK).

3.3.6 - Laser fluence measurement

Pulse energy was monitored by sampling the beam with a partially reflecting mirror (BSF-10-UV, Thorlabs, UK) prior to entry into the fibre, and diverting it towards a photodiode sensor (PD10-C, Ophir Photonics, Germany). Delivered pulse energy was determined through calibration to post experiment end of fibre measurements, corrected for known losses (13%) from the delivery optics of the instrument. The laser incidence angle was approximately 65°, forming an elliptical spot 111 µm x 235 µm at the sample, as determined via the fluorometric method[207] from CHCA thin films using ImageJ[208]. Variation in delivered laser fluence was achieved via a Brewster angle variable attenuator (Watt Pilot, Altechna, Lithuania).

3.3.7 - Laser fluence variation experiments

Stainless steel MALDI imaging plates were cleaned with a 50:50 ACN:H_2O solution in a sonicator for 15 minutes to remove any contamination.

Combinations of each matrix compound and analyte were dissolved in 80:20 MeOH:H_2O at 10000:1 molar ratio and deposited onto the imaging plates using a pneumatic sprayer (TM Sprayer, HTX Imaging, USA). The nominal deposited surface concentrations of the matrix and analyte were 9.55 x 10^{-9} mol mm^{-2} and 9.55 x 10^{-13} mol mm^{-2} respectively. UV-MALDI MS data were collected as individual raster lines in continuous raster mode over a range of laser fluences (5 to 360 J m^{-2}) at 0.2 mm s^{-1} raster speed, with a horizontal pixel size of 200 µm, resulting in 1000 laser shots per acquired spectra. The raster lines were vertically separated by 800 µm to ensure no oversampling of previous raster lines.

3.3.8 - Data analysis

Unless stated otherwise all data were processed in MATLAB (R2016b, Mathworks, UK). AFM data were processed in SPIP (v6.6.3, Image Metrology, Denmark), film thicknesses were determined via histogram analysis using the Step Height function. MS data were converted to .mzML using AB MS Data Converter (v 1.3, Sciex, UK) and then into .imzML using imzMLConverter[209], and imported into MATLAB using SpectralAnalysis[210] for further processing and analysis. Spectral data underwent a zero-filling process before peak intensities, taken as the integrated area at full width half maximum (FWHM), were extracted. Data fitting was carried out in OriginPro 2016 (OriginLab, USA) using the Levenberg-Marquardt algorithm.

3.4 - Results and discussion

3.4.1 - Matrix compound solid phase optical absorption

In UV-MALDI MS the uptake of laser energy, and thus energy available for desorption and ion formation, is governed primarily by the absorption of the matrix[24]. It is therefore useful to characterise a matrix compounds absorption profile to inform suitability of a matrix to the particular wavelength of laser utilised (e.g. 337 nm or 355 nm), or if seeking to understand the relative differences in observed performance between matrix compounds. Additionally while it is commonplace to measure the optical absorption of a compound in solution, it has been previously observed that there are significant differences between these spectra and that of the corresponding solid[20,24,30]. As most matrix compounds are present in MALDI experiments as solids, it is therefore preferable to measure matrix compound optical absorption in the solid phase.

The solid phase absorption spectra for the ten matrix compounds from the Chapter 1 were collected from thin film samples made via sublimation deposition using the home-built deposition system (Figure 3.1a). This approach was used as films deposited using a solvent sprayer-based approach proved highly scattering, preventing meaningful measurements from being obtained. To provide an quantitative estimation of optical absorption the solid phase spectra were normalised to the near-UV (NUV) maxima of the corresponding solution phase measurements, as previously described by Allwood et al[20].

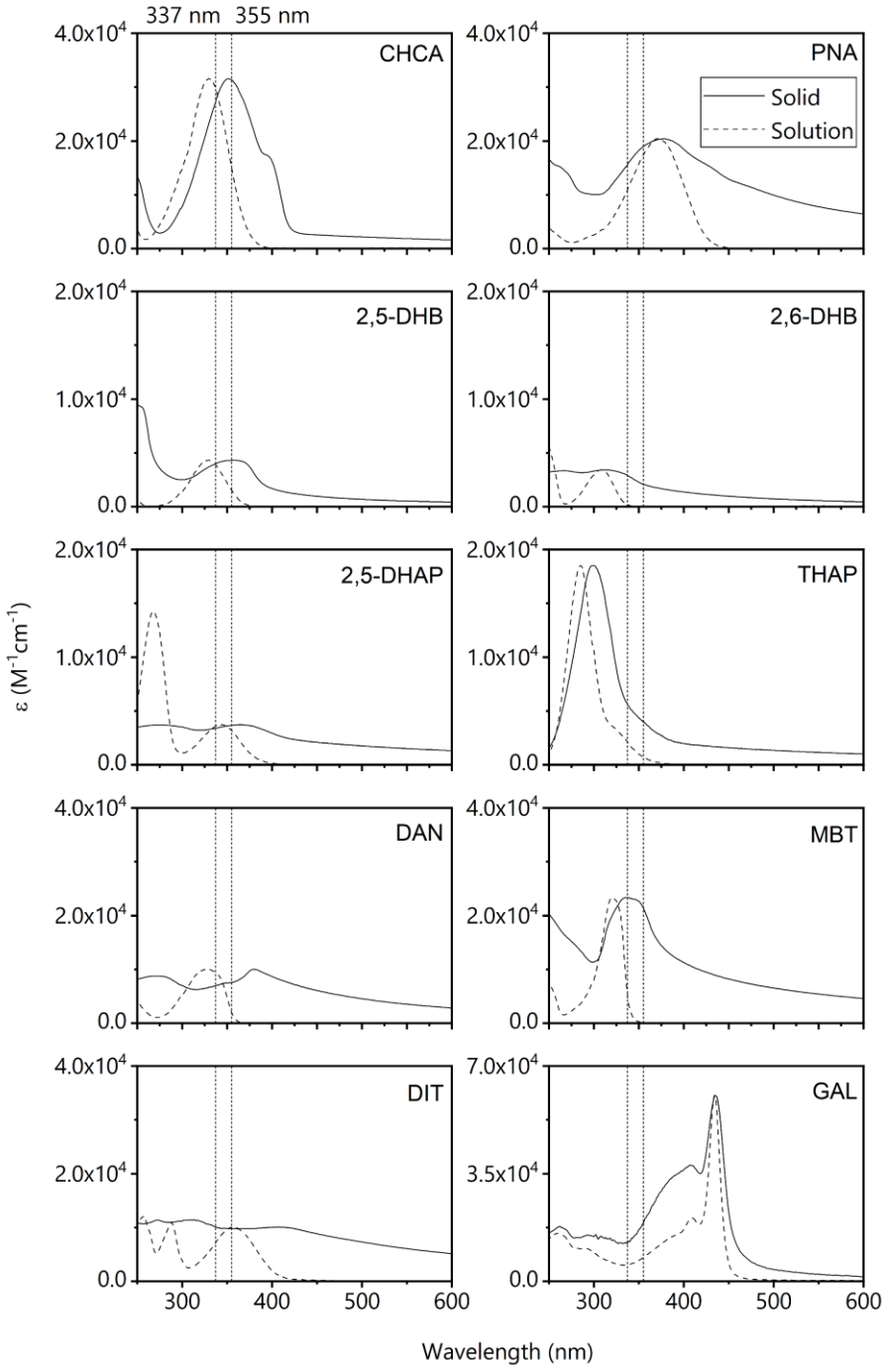


Figure 3.2. *Solution and solid-state molar extinction coefficient (ε) spectra of 10 selected MALDI matrices. Solid state absorption values are scaled to the NUV maxima of the corresponding solution spectra. Dotted black lines at 337 and 355 nm mark the operating wavelengths of common UV-MALDI lasers. Spectra are the average of three measurements.*

As previously observed with UV-MALDI matrix compounds [19,21,22,24,30], significant differences between solid phase and solution spectra were evident, with broader absorption bands observed for all matrix compounds (Figure 3.2). Absorption band broadening in organic molecular solids is characteristic of the existence of excitonic bands within the crystal structure, which arise due to the interaction of photo-excited states with neighbouring molecules and with the crystal lattice structure as a whole[225]. This absorption band broadening also accounts for the hypochromic shift of solid phase spectra observed for all the matrix compounds, due to the population of excited states being divided among a greater number of energy levels.

Relative to the data collected from solution, a typical bathochromic shift in the absorption spectra of up to 30 nm was observed for the solid phase (Figure 3.2), although Dithranol exhibited a shift of nearly 75 nm. This effect is termed the "solvent shift" and arises from intermolecular interactions, such as Van der Waals bonding[225]. Hypsochromic shifts in absorption spectra can arise from solvent dipole-dipole interactions and H-bonding on molecular electronic transition energies[226]. The solvents used here were either methanol or THF, both polar solvents, therefore the observed bathochromic shift in the solid phase spectra is likely the result of a relative reduction in dipole-dipole interactions and H-bonding and increase in Van der Waals bonding.

New absorption bands were observed for CHCA, MBT, DAN and PNA and to a lesser extent 2,5-DHB (Figure 3.2). In molecular solids this behaviour is characteristic of Davydov splitting, whereby interactions between molecules

within the crystal unit cell leads to a splitting of a given molecular electronic transition into *n* bands, where *n* is the number of differently oriented molecules within the unit cell[225]. Davydov splitting has been previously reported for some of the matrix compounds studied here[18,30,227,228].

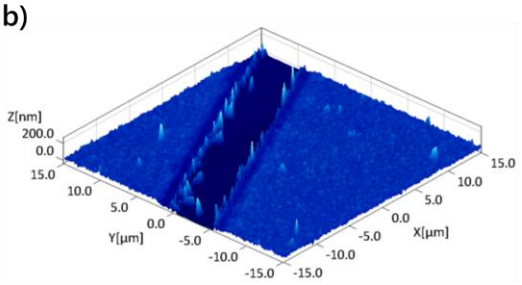
Due to the rudimentary nature of the deposition system some of the matrix films exhibited relatively high degrees of scattering (e.g. 2,5-DHAP and DIT) resulting from surface roughness of the films. Additionally, the small distance from the substrates to the matrix resulted in visible film heterogeneity across the substrate in many instances, most likely due to local variations heating and in the distribution of matrix powder across the base of the sublimation chamber.

For these reasons matrix thin film samples produced from the homebuilt sublimation system were not characterised beyond their relative optical absorptions, thus a direct quantitative measure of their absorption was not possible. To address this a subset of five matrix compounds (CHCA, PNA, 2,5-DHB, MBT and THAP) were selected for further characterisation using samples made with the commercial vacuum coater system (Figure 3.1b). This system allowed for a more uniform and controlled deposition of the matrices (Figure 3.3); the greater distance from the matrix to the substrate and point-like

deposition source minimising any potential for variation arising from localised variations in the heating material distribution of the matrix compounds.

a)

Matrix	Film Thickness (nm)	
	Mean	U
CHCA	33.90	1.01
PNA	151.70	4.41
MBT	39.69	4.26
DHB	101.54	5.47
THAP	57.92	3.36



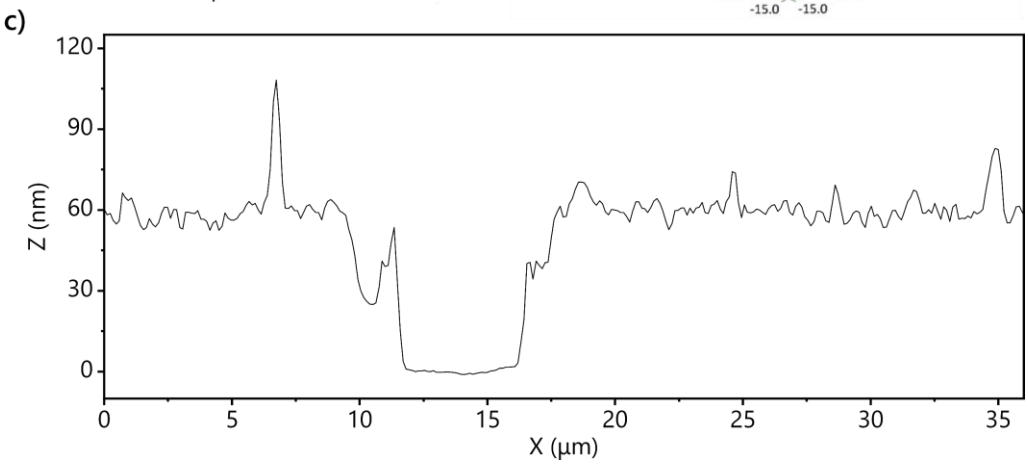


Figure 3.3. a) *Mean thicknesses and expanded uncertainty (k=2) of the deposited matrix films used for absorption measurements. Values are the average step height measurements of AFM images acquired at four positions along a scratch in each film.* ***b)*** *Example of an AFM image used for film thickness determination, the matrix film is THAP.* ***c)*** *Height profile of THAP film shown in* ***b)***

The most commonly metrics for quantitative measurements of optical absorption in solids are the absorption coefficient (α) and optical cross section (σ). These metrics are measures of different aspects of absorption, with α describing the absorption per unit volume and σ the absorption per molecule. They can be calculated using equations 3.2 and 3.3.

$$\alpha = \frac{A_e}{l} \qquad (3.2)$$

$$\sigma = \frac{\alpha}{n} \qquad (3.3)$$

Where A_e = Napierian absorption, l = path length and n = number density.

l was determined via AFM measurements of scratches in the matrix thin films, showing that the deposited matrix films ranged from 34-152 nm in thickness (Figure 3.3a). n was calculated from measured densities for the studied matrix compounds (Table 3.1).

Quantitative data on matrix optical properties, from solid state measurements most applicable to UV-MALDI MS experimental conditions, are essential for investigating the role of the matrix in ion formation. Solid phase σ and α data for the five matrices; with the corresponding solution phase σ data for comparison, are shown in Figure 3.4.

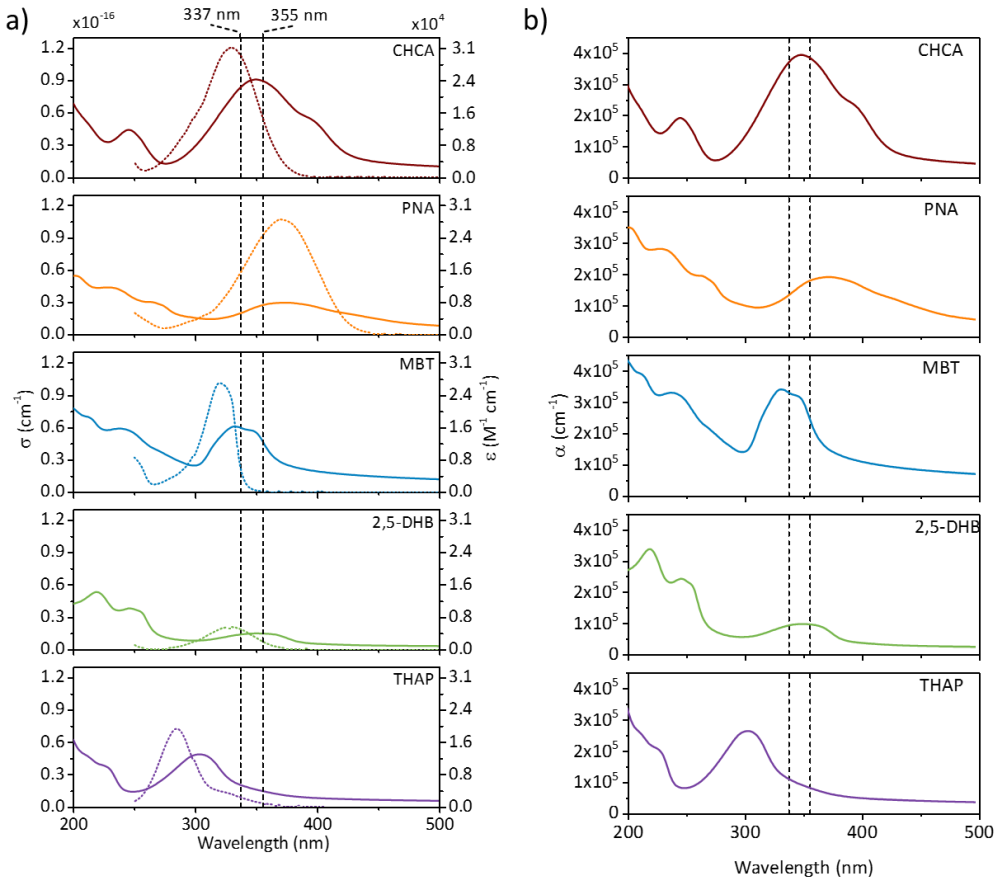


Figure 3.4. a) *Solid phase optical cross section (σ) spectra for the five studied UV-MALDI matrix compounds, as measured from sublimed thin films. Dotted line are the solution phase absorption spectra of the corresponding matrix (10 mmol L^{-1} in MeOH). The right axis shows the equivalent molar extinction coefficient (ε) scale.* ***b)*** *Corresponding solid phase spectra replotted as absorption coefficient (α). Dashed vertical lines mark the operating wavelengths of common UV-MALDI lasers.*

Along with the previously observed differences between solution and solid phase optical absorption spectra (Figure 3.2), was a notable hypochromic shift of solid phase spectra observed for all the matrix compounds (Figure 3.5). This

is likely linked to the absorption band broadening due to the population of excited states being divided among a greater number of energy levels.

For practical use of these qualitative optical absorption data it is convenient to present the values at wavelengths of common UV-MALDI MS lasers (Table 3.1). Additionally, in light of the demonstration of tuneable-wavelength laser systems for UV-MALDI MS[22–24,31] and previous recommendations for optimal wavelength ranges[21], the λ_{max} of the matrix compounds in the near-UV region (300-400 nm) are also included.

Table 3.1. *Densities and solid state α and σ of the selected UV-MALDI matrix compounds. Values corresponding to the common laser wavelengths employed in UV-MALDI (337 & 355 nm) and the NUV λ_{max} are reported, as well as the position of the NUV λ_{max}. The expanded uncertainty (k=2) is reported, for density measurements these were typically <0.001 g cm^{-3} so are not reported.*

Matrix	ρ (g cm^{-3})	NUV λ_{max} (nm)	α (10^5 cm^{-1})			σ (10^{-17} cm^{-2})		
			α_{337}	α_{355}	$\alpha_{NUV\ \lambda max}$	σ_{337}	σ_{355}	$\sigma_{NUV\ \lambda max}$
CHCA	1.44	350	3.82 ± 0.46	4.12 ± 0.51	4.18 ± 0.51	8.31 ± 1.00	8.98 ± 1.17	9.09 ± 1.11
PNA	1.43	374	1.21 ± 0.15	1.68 ± 0.20	1.83 ± 0.22	1.94 ± 0.23	2.70 ± 0.32	2.95 ± 0.36
MBT	1.51	333	3.25 ± 0.90	2.60 ± 0.73	3.30 ± 0.91	5.96 ± 1.65	4.76 ± 1.34	6.06 ± 1.68
2,5-DHB	1.57	351	0.81 ± 0.14	0.87 ± 0.15	0.91 ± 0.15	1.32 ± 0.23	1.42 ± 0.24	1.43 ± 0.24
THAP	1.48	304	1.05 ± 0.19	0.74 ± 0.13	2.54 ± 0.45	1.98 ± 0.35	1.40 ± 0.25	4.80 ± 0.85

Having a quantitative measurement of matrix optical absorption allows direct comparison between the compounds. It also allows validation of using quantitative solution measurements as representative of solid phase data[20,21].

Here the ratio of $\sigma_{NUV\ \lambda max}$ in solid phase to that in solution ranged from 1.4 for CHCA to 3.3 for THAP (Figure 3.4a), suggesting estimations of solid phase absorption from data acquired from solutions are reliable to within a factor of 3. This represented a reduction in the accuracy of such an approach, previously around a factor of 2[20], and demonstrates that solution optical absorption measurements should be used with caution for estimating matrix solid phase optical absorption. For example, scaling to solution absorption suggests that at 355 nm PNA had similar optical absorption to MBT (Figure 3.2), but direct solid phase measurement reveals it is in fact approximately half (Figure 3.4).

For the matrix compounds studied α values were typically of the order of 10^5 cm^{-1}, and σ of the order of 10^{-17} cm^{-2}. α values are of the same order as those reported by Allwood et al., who measured an α_{337} of 2.18 x10^5 cm^{-1} and 0.80 x10^5 cm^{-1} for CHCA and 2,5-DHB sublimed thin films respectively[20]. While the findings for 2,5-DHB are in good agreement with their data, their α_{337} for CHCA is significantly smaller (43%) than our measurements (Figure 3.4b). It should be noted that the observed NUV λ_{max} for CHCA in that work occurred at ~370 nm, noticeably different from that found here (Table 3.1). Back calculations of the Allwood data yields a CHCA $\alpha_{NUV\ \lambda max}$ only 13% smaller than the finding here. This suggests that the differences in NUV λ_{max} position is likely responsible for the discrepancy between in CHCA α_{337}. The reason for this difference is not known, although other reported NUV λ_{max} for CHCA are in agreement with the findings presented here[22].

The molar attenuation coefficient (ε) for 2,5-DHB spin coated films has been previously reported by Heise and Yeung as $2.80x10^3$ $M^{-1}cm^{-1}$ at 337 nm [19], this corresponds to a σ_{337} of $1.07x10^{-17}$ cm^{-2} and is 19% smaller than the value obtained here (Table 3.1). The difference between the two results may be due to the alternate methods of deposition employed, or that film thickness and matrix compound density were not directly measured in that work. Similarly, σ values reported by Allwood et al. for CHCA and 2,5-DHB used an assumed matrix density of 1.1 gcm^{-3}, recalculation using the new density values reported here yields $\sigma_{NUV\ \lambda max}$ that are 13% and 3% smaller than the measurements for CHCA and 2,5-DHB respectively, in good agreement with the findings here.

Comparison of the σ values at the wavelength of the laser used in this study (355 nm) showed that CHCA was by far the most strongly absorbing matrix (Table 3.1). The σ_{355} of the remaining matrix compounds MBT, PNA 2,5-DHB and THAP, were 53%, 30%, 16% and 16% of the CHCA σ_{355} respectively. The σ_{337} and σ_{355} values showed a correlation with widely used characterisations of the matrix compounds with relation to analyte fragmentation, with the traditionally "hot" matrix compound CHCA[229] having the largest σ and "cold" matrix compounds 2,5-DHB and THAP[229,230] demonstrating the smallest.

Ion yields within UV-MALDI MS have been reported as highest around the λ_{max} of the matrix employed [22,24], thus the solid phase spectra presented here (Figure 3.4) can be used to identify optimal laser wavelengths for UV-MALDI MS experimentation with these matrix compounds. Comparison of the $\sigma_{337,}$ σ_{355} and $\sigma_{NUV\ \lambda max}$ values (Table 3.1) shows that most of the compounds are already well

suited to standard UV-MALDI MS lasers, not surprising given the untargeted nature of MALDI matrix discovery. The one exception was THAP, which has σ_{337} and σ_{355} only 41% and 29% that of its $\sigma_{NUV\ \lambda max}$. The use of XeCl excimer (308 nm) lasers may be beneficial for this matrix. Alternatively, wavelength-tuneable lasers, previously demonstrated in UV-MALDI MS [22–24,31], enabling direct matching of laser wavelength to the matrix λ_{max}.

3.4.2 - Desorption/Ionisation as a function of laser fluence for different matrix compounds and analytes

A complex interaction of factors is believed to contribute to ionisation and desorption in UV-MALDI MS, reflecting the multistep nature of the technique. Each step of the UV-MALDI process will have its own requirements with regards to matrix properties, with absorption and photoemission, thermo-physical properties and gas phase chemistry among those considered critical to the desorption and ionisation of analytes. To investigate the influence of matrix optical absorption on UV-MALDI MS results, data were acquired at a range of laser fluences, with a range of analytes (Figure 3.5). The compounds selected here were Haloperidol, Angiotensin II and PC (34:1). The use of multiple analytes provides the opportunity to probe differences that can arise in UV-MALDI MS analyses, particularly imaging experiments where multiple classes of analyte are being ionised. It was also useful to control other experimental parameters, such as analyte-to-matrix molar ratio, as these are rarely controlled in fluence variation experiments. The recently proposed sigmoidal function (Equation 3.1)[24] was used to fit the data, allowing more experimentally pertinent features of the fluence-ion intensity data to be described.

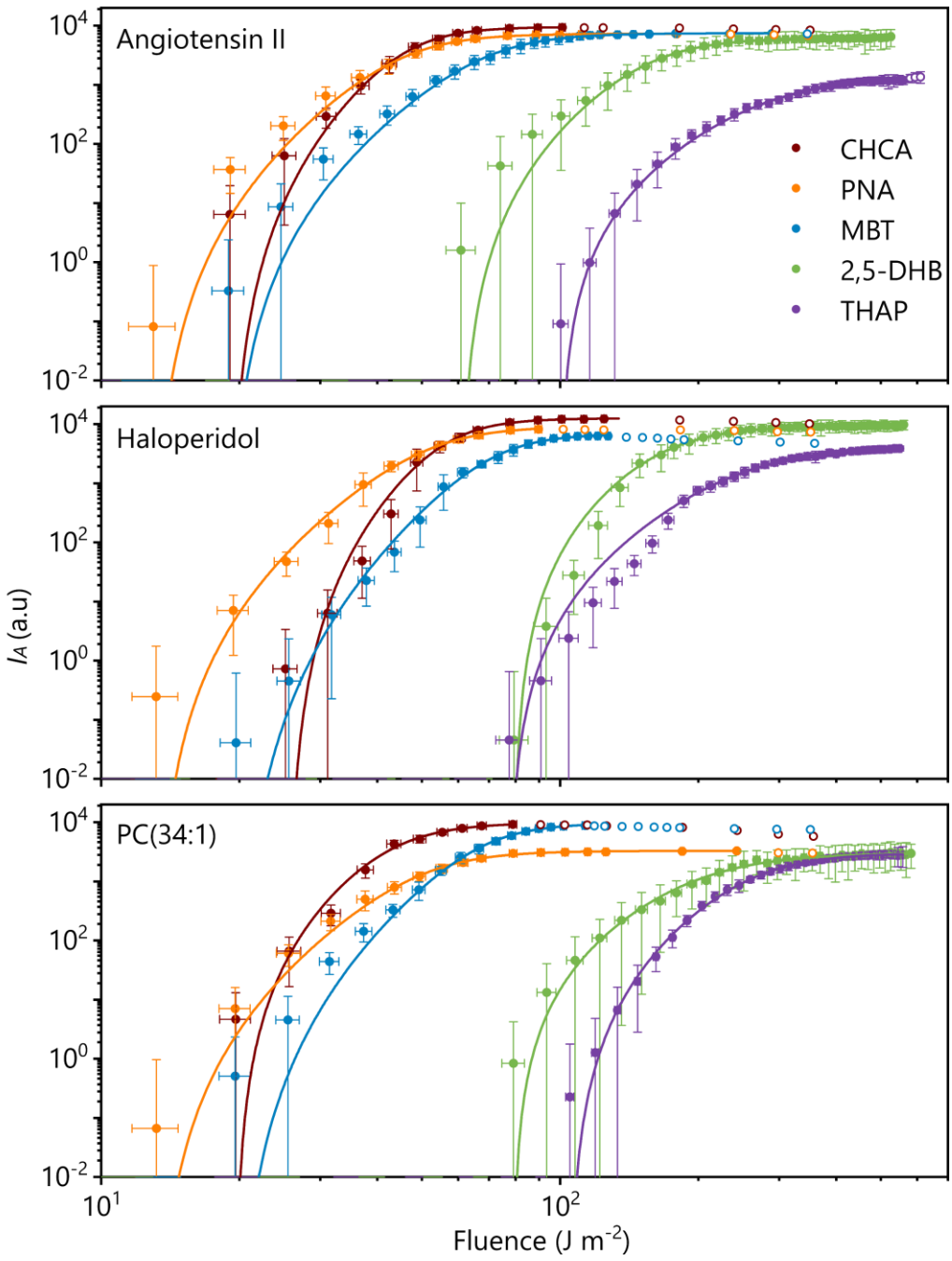


***Figure 3.5**. Analyte [M+H]$^+$ intensity (I_A) with varying laser fluence for the studied matrix analyte mixed systems. Data points are the mean I_A taken from 45 spectra, x and y error bars show the expanded uncertainty (k =2). Solid line represents fitting of the data of equation 1, open data points signify the onset of reduction in I_A due to fragmentation, this regime is not modelled by the equation and thus excluded in the fitting process.*

In line with previous observations[62], threshold fluences for the analytes ($H_{thr\,A}$) were strongly matrix dependent, with the matrix compounds falling into two distinct groups (Figure 3.6). With $H_{thr\,A}$ for 2,5-DHB and THAP much higher those found for CHCA, PNA and MBT, this relative ordering is broadly in line with previous observations[24,59,60,63,68,158,231]. Due to the strong influence laser spot size has on H_{thr}[60,63,68,158], direct comparison with reported values is difficult, although previous work using the same UV-MALDI MS set up reported H_{thr} for CHCA in good agreement with the values shown here[67]. The ordering of $H_{thr\,A}$ by matrix compound generally reflects their relative absorptions at the wavelength of the laser used (Table 3.1), with the exception of PNA which deviated from the trend. This is in agreement with previous findings that H_{thr} has some correlation with the absorption spectrum of the matrix[24], although as UV-MALDI is a complex process other variables are expected to contribute to the observed result.

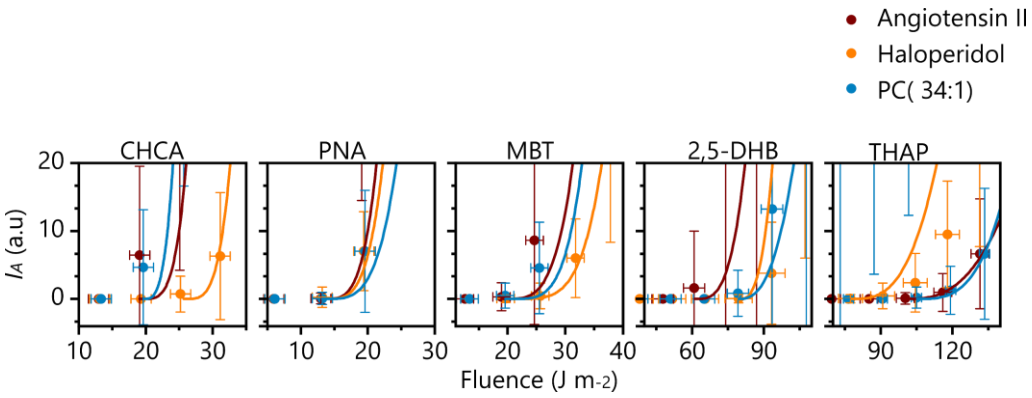


Figure 3.6. *Threshold fluence regions of Figure 3.2 in linear scale demonstrating the variance in $H_{thr\,A}$ with analyte for the five studied matrix compounds. Error bars show the expanded uncertainty (k =2)*

$H_{thr\,A}$ appears to exhibit a small dependence on the analyte in question as well as the matrix used in some instances (Figure 3.7), for example Haloperidol demonstrated a $H_{thr\,A}$ 30% higher for CHCA but 30% lower for THAP compared to the other analytes. Matrix crystal morphology has been previously reported as having an effect on threshold fluences in UV-MALDI MS[232]. Inspection of the samples under a microscope showed differences in the morphology of deposited CHCA when Haloperidol was the analyte, potentially explaining the different $H_{thr\,A}$. On the other hand, THAP appeared visually identical for all the analytes. $H_{thr\,A}$ has been previously suggested as dependent on analyte molecular mass[99]. Whilst no trend of this nature was evident in the data, the fact that the mass range of the analytes investigated here (375 - 1045 Da) was much smaller than that examined in that study (5.7 - 66 kDa) may explain this discrepancy.

Using the previously measured absorption coefficient data for the matrix compounds, the energy per unit volume (E_V) in the surface layers of the samples upon irradiation, ignoring losses due to reflection, can be calculated via equation 3.4[62].

$$E_V = \alpha H_0 \qquad (3.4)$$

Where H_0 = incident laser fluence. E_V at the observed threshold fluence ranged from 0.2-1 kJ cm^{-3} for the matrix compounds studied, which is significantly lower than the 8 kJ cm^{-3} determined by Chen at al.[31], although Dreisewerd suggests[62] this is anomalously high and most reported values are in the order of 1 kJ cm^{-3}, in agreement with the findings here. Typical energy densities at the observed threshold fluences were 43 kJ mol^{-1}, 128 kJ mol^{-1}, 166 kJ mol^{-1}, 188 kJ mol^{-1} and

215 kJ mol^{-1} for PNA, MBT, 2,5-DHB, THAP and CHCA respectively. While these values represent approximately the amount of energy absorbed by the matrix compounds at the observed threshold fluence, it should be noted that they will not fully describe the energy available for UV-MALDI desorption/ionisation processes due to the existence of other energy decay mechanisms. Fluorescence in particular has been reported to account for a significant proportion of absorbed energy in some matrix compounds[33], although there is still large uncertainty in the exact values[32]. The large difference in energy densities between matrix compounds with similar H_{thr}, CHCA, MBT and PNA, is striking, revealing the influence of additional matrix compound physicochemical properties.

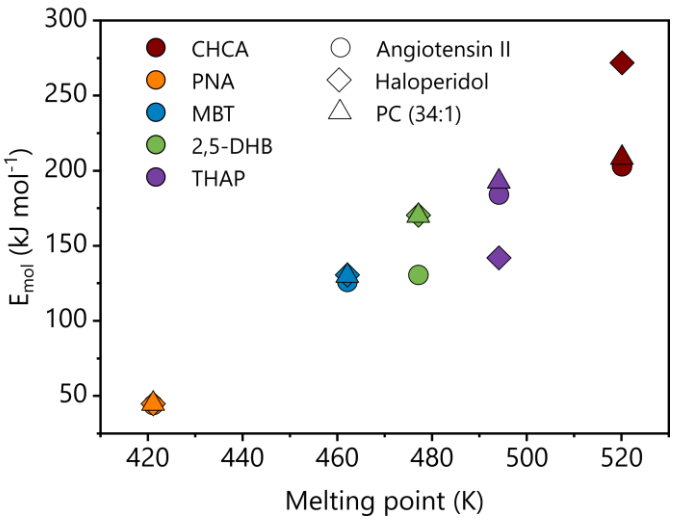


Figure 3.7*. Calculated surface layer energy densities at observed threshold fluence for the studied matrix analyte combinations, as a function of matrix melting point.*

Sublimation enthalpies have been reported for some of the matrices studied here[47,233], although, in agreement with previous investigations[47,234], no correlation is observed. Similarly, no correlation with matrix proton affinity could

be found. Interestingly a correlation with the melting point of the matrix is evident (Figure 3.7), which suggests that other thermodynamic properties may be playing a role. This may somewhat explain why PNA, a matrix known to readily sublimate at room temperature in vacuum[49,235], had a similar observed $H_{thr\,A}$ to CHCA despite having a significantly smaller σ_{355}. Further studies to characterise such properties are therefore clearly of interest.

H_k describes the inflection point of the ion intensity-fluence curve, and has been proposed as the optimal fluence for UV-MALDI analyses [24]. $H_{k\,A}$ demonstrated a similar dependency on matrix as $H_{thr\,A}$ (Figure 3.5). $H_{k\,A}$ values for CHCA, PNA, MBT, 2,5-DHB and THAP were approximately 50 J m^{-1}, 50 J m^{-1}, 73 J m^{-1}, 200 J m^{-1} and 300 J m^{-1} respectively, although the variance in data is large. $H_{k\,A}$ was also somewhat analyte dependent (Figure 3.8). With CHCA, Haloperidol resulted in a 20% higher $H_{k\,A}$ compared to the other analytes. Both PNA and MBT showed relatively little variation arising from different analytes. With respect to the other analytes, PC(34:1) demonstrated ~30% higher $H_{k\,A}$ when 2,5-DHB was the matrix and Angiotensin II ~10% higher with THAP. Overall, as with $H_{thr\,A}$, there was no discernible trend to the variation.

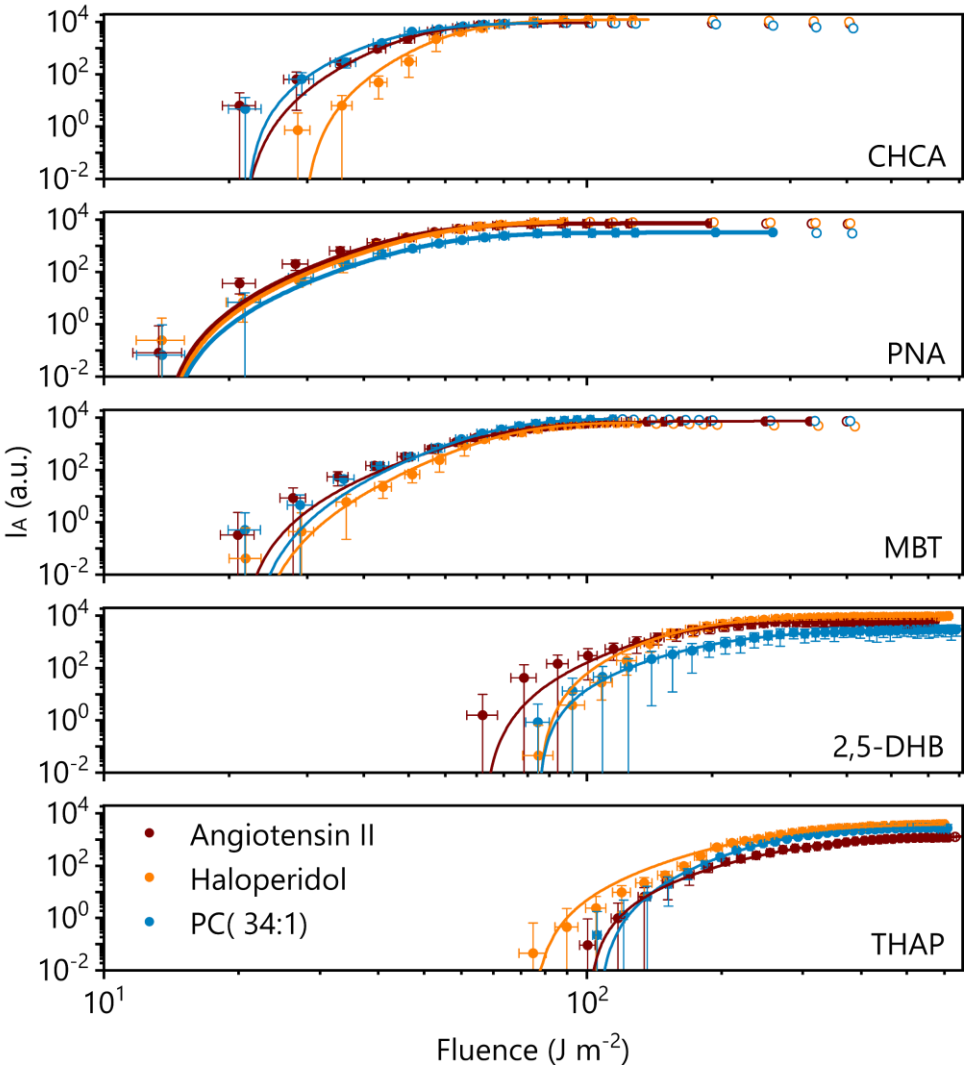


***Figure 3.8**. Analyte $[M+H]^+$ intensity (I_A) with varying laser fluence for the studied matrix analyte mixed systems. Data points are the mean of 45 spectra, error bars show the expanded uncertainty (k =2). Solid lines represent fitting of the data of equation 3.1, open data points signify values excluded in the fitting process.*

The maximum observed analyte $[M+H]^+$ intensity ($\hat{I}_A$) also varied considerably depending on the matrix compound used (Figure 3.6). For all the analytes studied, CHCA consistently produced the highest $\hat{I}_A$ values, ranging from 4-30%

higher than next highest $\hat{I}_A$. Due to limitations in the accessible experimental fluence range, $\hat{I}_A$ values for 2,5-DHB and THAP were obtained from projection of the fitting curve, and as such some caution should be taken with their interpretation.

$\hat{I}_A$ also varied with analyte for a given matrix (Figure 3.9). Haloperidol produced the highest $\hat{I}_A$ for all the matrix compounds with the exception of MBT, ranging from 20-300% higher than the other analytes. As molar concentrations of matrix and analyte were constant for all experiments, these findings can be taken as approximately indicative of matrix ionisation efficiency towards the individual analytes, under the conditions studied. With this in mind it is clear that CHCA is the most efficient matrix for the analytes studied, and that with the exception of MBT, Haloperidol was the most readily ionised of the analytes.

The parameter m has been previously described as matrix dependent[24], in this study values for m for the analyte ion intensity (m_A) was found to be typically lower for 2,5-DHB (2.7 – 3.4) and THAP (2.7- 3.2) and larger for CHCA (3.4 - 4.2), PNA (3.8 - 4.0) and MBT (3.9 - 4.8), loosely reflecting the division observed in previously discussed properties such as σ_{355} and "hot" and "cold" matrices . The effect of analyte on m_A values was seemingly uncorrelated with known properties, with variation of the order of ±1.

The ion intensity-laser fluence relationship can be alternatively visualised by plotting derivatives of the ion intensity curves (Figure 3.10). This approach provides a more intuitive extraction and understanding of some experimental features and trends. The fluences at which both H_{thr} and $\hat{I}$ occur are located at

the two x-intercepts, and H_k, can be easily identified as corresponding to the locations of the derivative curve maxima on the x -axis.

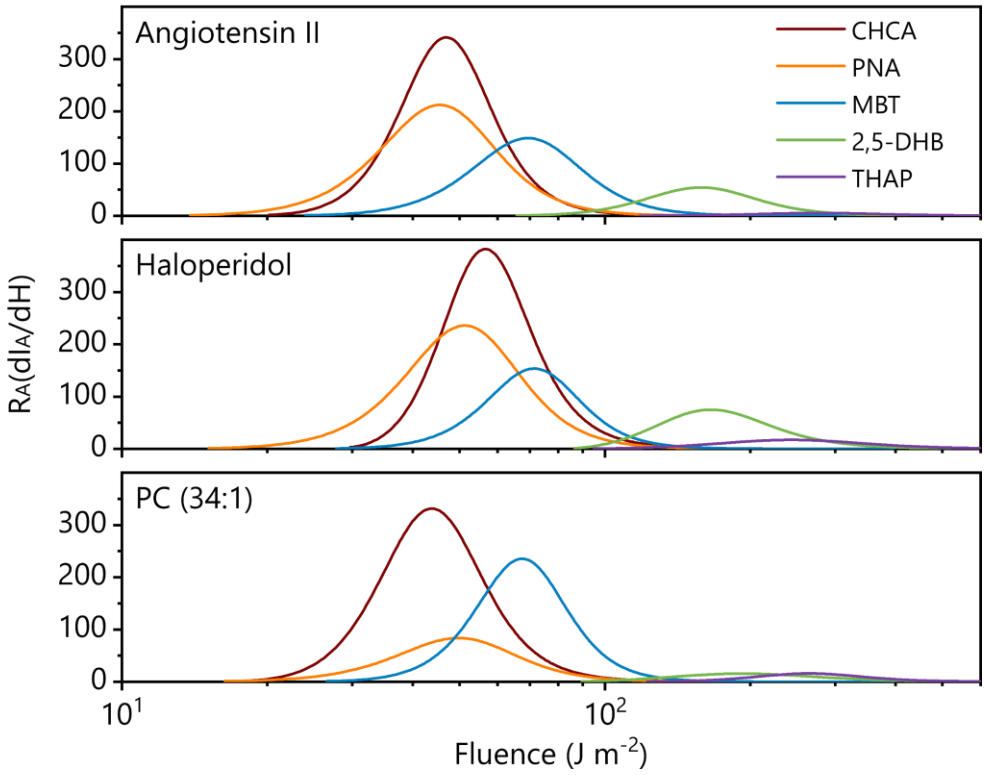


Figure 3.9. *Derivative forms of the change in ion intensity with fluence produced by fitting of the data to equation 3.1, for each of the matrix analyte combinations.*

By taking the height of the derivative of equation 1 it is possible to determine the maximum rate of change in ion intensity with laser fluence. This new metric, R, can be thought of as a more intuitive alternative to the m parameter, which also describes the increase in ion intensity. As with m_A, the maximum rate of change in I_A (R_A) was influenced by matrix utilised (Figure 3.10), with CHCA producing the highest R_A (340-380) of all the matrix compounds, for all analytes. R_A values with PNA (84-235) and MBT (149-235) were approximately grouped together, while the lowest R_A values were obtained with 2,5-DHB (16-75) and THAP (5-17). The grouping of R_A is somewhat reflective of the matrix compound

optical absorption, although the scatter in values for PNA and 2,5-DHB indicate other factors are having a strong influence. Unlike m_A there was a noticeable trend in R_A with respect to the analyte used (Figure 3.10), with Haloperidol giving the largest $R_{A,}$ for all matrix compounds with the exception of MBT.

3.4.3 - Desorption/ionisation characteristics as a function of matrix optical absorption

Defining the relationships between the various physicochemical properties of a matrix compound and its desorption/ionisation characteristics is a long-standing goal in UV-MALDI research. Such knowledge would benefit ionisation mechanism investigations but could also guide rational development of new matrix compounds for improving UV-MALDI MS analyses. Keeping in mind that optical absorption is only one of many properties that has been identified as critical in UV-MALDI MS, the matrix σ_{355} was compared with the parameters obtained from the fluence variation experiments, to further explore the relationship between this specific matrix property and analyte desorption/ionisation (Figure 3.10).

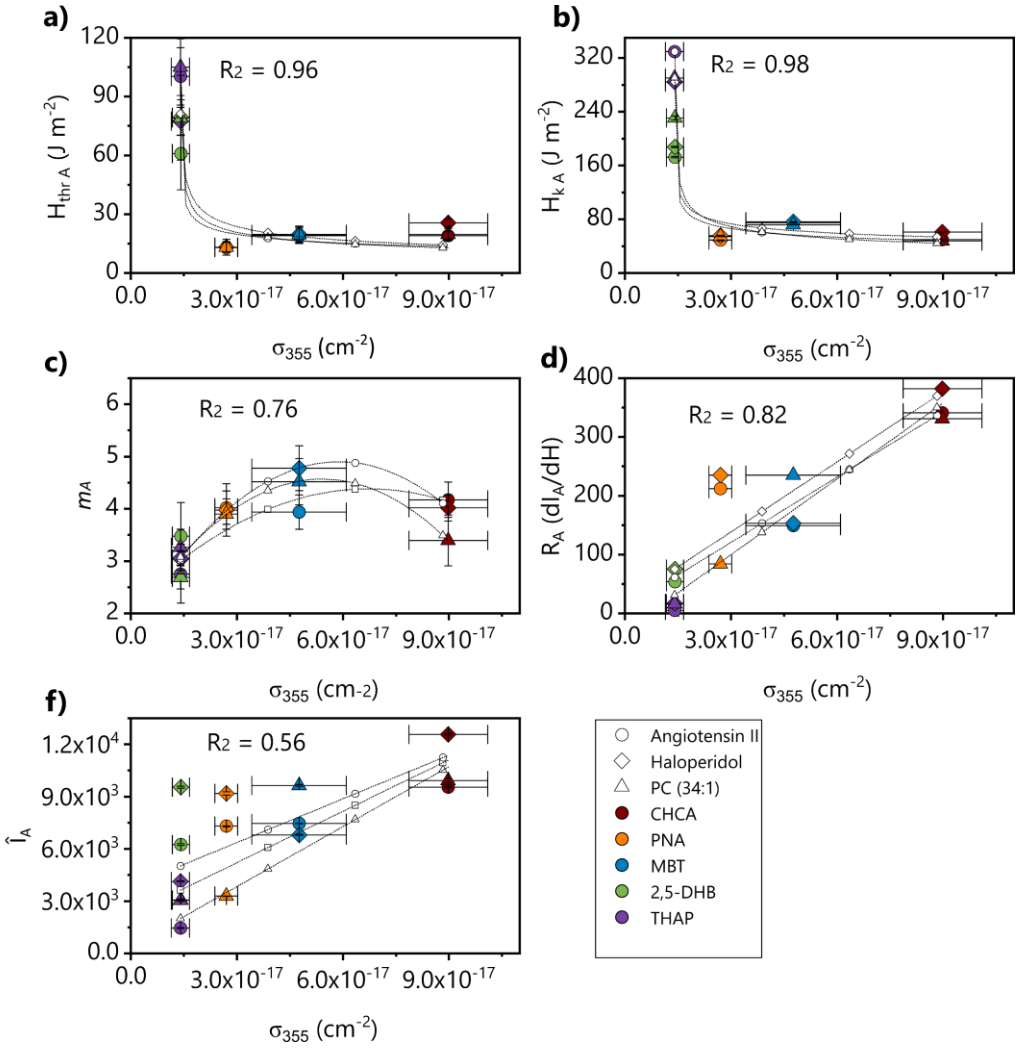


***Figure 3.10**. Relationship between matrix optical cross section at 355 nm (σ_{355}) and the analyte ion intensity curve parameters **(a)** $H_{thr\,A}$ **(b)** $H_{k\,A}$ **(c)** m_A **(d)** R_A and **(e)** $\hat{I}_A$, for the 15 studied matrix analyte combinations. Error bars represent the expanded uncertainty (k=2). Lines in the plots represent fitting of the data to **(a)** & **(b)** power, **(c)** 2nd order polynomial and **(d)** & **(e)** linear functions.*

Both $H_{thr\,A}$ and $H_{k\,A}$ can be modelled with a power law relationship (Figure 3.11a & 11b) of the form.

$$H_{(thr,K)} = n(\sigma - \sigma_{min})^{-p} \qquad (3.5)$$

Where n and p are fitting parameters. p for both $H_{thr\,A}$ and $H_{k\,A}$, had similar values, ranging from 0.26 to 0.44. n was slightly larger for $H_{k\,A}$ (2.0×10^{-5} to 3.1×10^{-3}) than $H_{thr\,A}$ (1.0×10^{-6} to 1.1×10^{-4}). Both parameters varied with analyte, although with no obvious correlation. σ_{min}, which describes the point on the x-axis where the curve tends to infinity, ranged from 1.28×10^{-17} - 1.39×10^{-17} cm^{-2}, and appeared to scale inversely with analyte molecular mass. For the matrix compounds studied this corresponds to an α of $6\text{-}8 \times 10^{4}$ cm^{-1} which is close to the 6×10^{4} cm^{-1} observed by Chen et al. as the minimum α required for detection of analytes[31]. The wavelengths at which the α of CHCA and 2,5-DHB falls below this minimum also correspond closely to those observed by Soltwisch et al. at which significant drops in observed analyte ion intensities for these matrix compounds occurred[24]. Data for THAP from a recent work from the same group also showed signs of this effect[17]. σ_{min} could therefore, tentatively, be thought of as describing the minimum σ required for a compound to function as an effective matrix in UV-MALDI MS, although further studies with additional matrix compounds and laser wavelengths would be necessary to confirm this.

From the relationship (Figure 3.11a & 11b) it can be seen that decreasing matrix cross section below 2×10^{-17} cm^{-2} resulted in rapid increasing $H_{thr\,A}$ and $H_{k\,A}$. Such information can be useful in guiding identification of novel matrix compounds, if for example one was seeking to create matrix compounds that

are optimised for low fluences to minimise analyte fragmentation or extend laser lifetimes.

Both m_A and $\hat{I}_A$ showed only weak correlations to σ (Figure 3.5c & 5e). $\hat{I}_A$ has been reported as wavelength dependant[24] and therefore would be expected to show some relation to matrix σ, the discrepancy may be due to the uncertainty in determining $\hat{I}_A$ in this study. R_A showed a strong linear relationship with matrix σ (Figure 3.11d), highlighting another benefit of using this metric over m.

3.5 - Conclusions

Quantitative solid phase optical absorption spectra were acquired for a selection of common UV-MALDI matrix compounds. These data were employed, in conjunction with MS experiments using multiple analytes across a range of laser fluences, to investigate the influence of matrix optical absorption on desorption/ionisation characteristics in UV-MALDI MS. We report the solid phase optical absorption and densities for the selected matrix compounds, most for the first time. While no significant alterations to current UV-MALDI ionisation models are expected, incorporation of this new physicochemical data presented here can improve the quality of theoretical predictions, as well as aid the extension of the existing models to a broader range of matrix compounds.

The desorption/ionisation of analytes was found to be determined, in part, by matrix optical absorption, with the influence of other factors also apparent. Correlation of estimated threshold fluence energy densities within the matrix with melting point suggests further characterisation of matrix compounds, such as thermos-physical or photo-emissive properties, could provide additional

insight on energy uptake in UV-MALDI MS. The variances observed in the desorption/ionisation characteristics of the different analytes has important implications with regards to experimental optimisation. Careful consideration of matrix choice and laser energy is required, particularly in MSI studies were multiple analytes are being detected simultaneously, to ensure the validity of conclusions drawn from resulting data.

The alternative visualisation of the ion intensity data provided useful information. In particular, enabling extraction of the R metric, displayed a stronger correlation with matrix σ, than the commonly employed m factor.

Finally, identified constraints on matrix σ required for detection of analyte ions, in line with previous findings[31], point to an aspect of ion generation in UV-MALDI MS that warrants investigation in future studies.

Chapter 4 - The influence of UV-MALDI MS imaging parameters on material ejection and ion yield

Work presented in this chapter has been published in the following journal article.

Robinson, K. N.; Steven, R.T.; Race, A. M.; Bunch, J. The Influence of MS Imaging Parameters on UV-MALDI Desorption and Ion Yield. *J. Am. Soc. Mass Spectrom.* **2019**, 1284–1293. https://doi.org/10.1007/s13361-019-02193-8.

4.1 - Introduction

The ejection of material, resulting from the interaction between the matrix, sample and the laser, is one of the key steps of the UV-MALDI process, and as such will have a strong influence on UV-MALDI MSI data. Widely described as "desorption" in literature, the material ejection in a typical UV-MALDI MS experiment can, in fact, involve either a steady release of molecules from the matrix into the gas phase (desorption) or a rapid disintegration into clusters and free molecules (ablation), or a combination of the two[61,62].

Material ejection in UV-MALDI MS has been extensively studied[62], with two primary mechanisms, phase explosion[89] and quasi-thermal desorption[24], proposed to describe the ablation and desorption processes respectively. Under typical UV-MALDI MS conditions both mechanisms are expected to occur[81], with a recent study by Niehaus et al. showing evidence that quasi-thermal desorption occurs at low laser fluences until a certain threshold is reached, above which ablative processes like phase explosion dominate[61]. Despite the widespread use of volumetric measurements in laser ablation studies[81], there has been

surprisingly few examples of such measurements related to UV-MALDI MS, with only two measurement of crater volumes, via profilometry[236] and confocal laser scanning microscopy (CLSM)[12] being reported.

The topic of ion yields, the ratio of formed ions to total number of ejected molecules, in UV-MALDI MS has received significant attention recent years. A lively debate has arisen between the proponents of the CPCD[79,237,238] and Thermal ionisation theories [153,167–170,237,239–242], with significant focus on the magnitude of ion yield in MALDI and its relevance to the respective proposed ionisation mechanism. Investigations into the influence experimental conditions on ion yield have been typically focused on basic parameters such as laser fluence/energy, analyte molar ratios and choice of matrix compound. Parameters relevant UV-MALDI MSI, such as laser repetition rate, spot size, sampling mode and raster speed, have received significant attention in recent years[13,14,17,52,68]. But thus far investigations have been limited to detected ion intensities, therefore a study into how common imaging acquisition parameters can affect material ejection and absolute ion yields is clearly of interest.

4.2 - Materials

CHCA was purchased from Sigma Aldrich (UK). 2,5-DHB and Olanzapine (312.4 g mol^{-1}) were purchased from Alfa Aesar (UK). Superfrost microscope slides for deposition substrates and HPLC grade methanol (MeOH) were purchased from Fischer Scientific (UK). AFM tips were purchased from NuNano (UK). Deionised (DI) water (ρ= 15 MΩcm^{-1}) was generated by an Elga Purelab system (UK).

4.3 - Methods

4.3.1 - Sample preparation

Substrates were cleaned via 10 minutes sonication in MeOH followed by DI water, and finally 15 minutes in a UV ozone cleaner (T10X10/OES, UVOCS, USA).

Deposition of the analyte and matrix layers was carried out in an Auto 306 thermal evaporator (Edwards, UK), operating at ~$6x10^{-6}$ mbar. A chilled block of copper (~ 5°C) was used to cool the substrates, ensuring deposition of the compounds. 3 nm layers of Olanzapine were deposited onto the substrates, followed by either CHCA (360 nm) or 2,5-DHB (136 nm) layers. Resulting analyte-to-matrix ratios in the samples were 1:221 (CHCA) and 1:107 (2,5-DHB). Deposition was monitored via the evaporator's in-built quartz crystal microbalance (QCM) sensor.

4.3.2 - UV-MALDI MS

UV-MALDI MS data were acquired with a Synapt G2-Si Qq-ToF mass spectrometer (Waters, UK), using the WREnS scripting tool (Waters, UK) to automate variation of the sampling conditions during data collection. Positive mode MS data (*m/z* 50 - 1500) were acquired using the instruments "Resolution" mode, in both spot and raster mode, at five laser energies, two repetition rates and two raster speeds. MS data were collected with a fixed scan time of 0.085 s, for the 500 Hz at 2000 Hz laser repetition rates used here, corresponding to ~42 and ~212 pulses per spectra respectively. Laser pulse energy was monitored during the experiment by using partially reflecting mirror (BSF-10-UV, Thorlabs, UK) to sample a portion of the beam and direct it towards a pyro-electric sensor

(PD10-C, Ophir Photonics, USA). Post experiment measurements of the full beam energy were used to calibrate the experimental measurements. As the instruments laser (Nd:YAG DPPS, 355 nm, <1.1 ns) had a Gaussian beam profile, laser spot size ranged from a minimum of 119 x 130 μm to maximum of 194 x 246 μm depending on pulse energy used, as measured from CHCA thin film via the fluorescence method[207]. The change in spot area with pulse energy is shown in Figure 4.1.

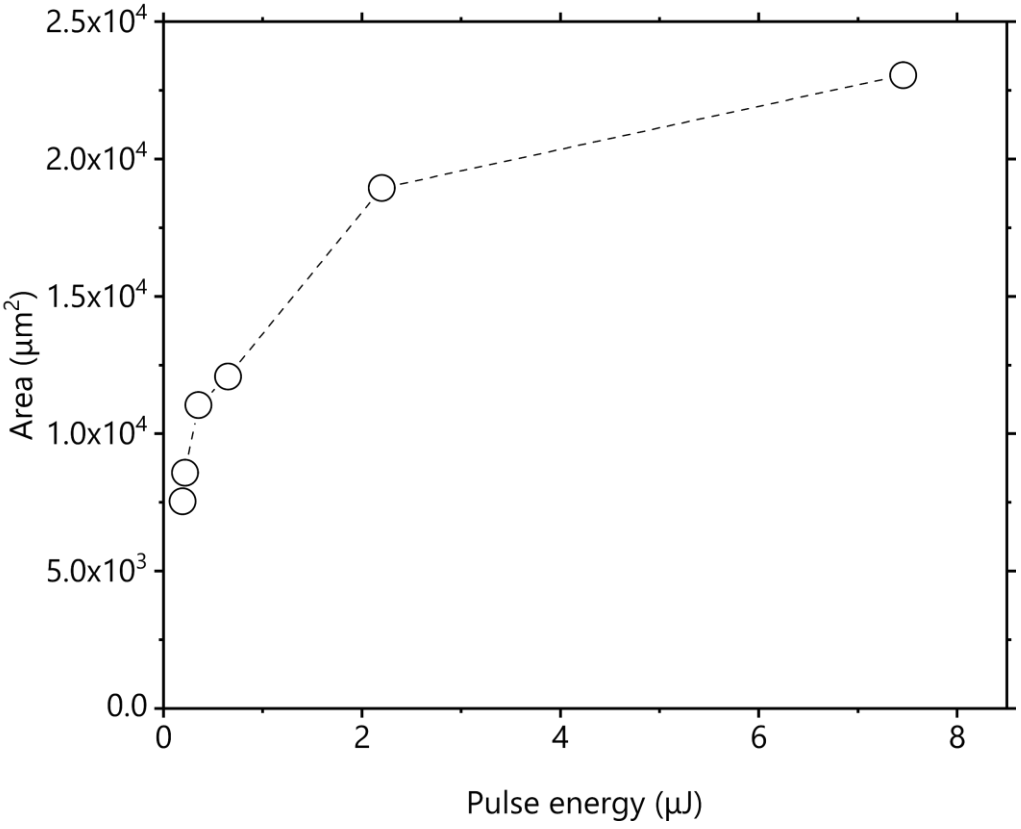


Figure 4.1. *Change in laser spot area with pulse energy, as determined via fluorescent emission from CHCA matrix films.*

4.3.3 - Measurement of material ejection

AFM measurements were carried out using an MFP-3D-SA AFM (Asylum Research, UK) operating in alternating contact (AC) mode.

CLSM imaging was carried out using a LEXT OLS4100 CLSM (Olympus, UK). A x50 objective (MPLAPON50XLEXT, Olympus, UK) was used resulting in a 256 µm x 256 µm square field of view. This objective was used with a laser power setting of 36, to achieve the best obtainable depth resolution whilst preventing sample damage from the microscope's UV laser. For imaging features that were larger than the field of view three stepped images were acquired for later tiling.

Electron microscopy images was acquired using a Supra 40 FE-SEM (Zeiss, UK) at 3 keV with a 20 µm aperture and 14.3 mm working distance. Samples were coated with layer of Au (approx. 2 nm) using a Q150T S sputter coater (Quorum Technologies, UK) to reduce charging effects during imaging.

4.3.4 - Data analysis

Unless stated otherwise all data were processed in MATLAB (R2017a, Mathworks, USA) and OriginPro 2019b (OriginLab, USA).

AFM and CLSM data were processed in SPIP (v6.6.3, Image Metrology, Denmark). Determination of crater boundaries were obtained with the software's Particle and Pore Analysis tool, using the Advanced Thresholding setting (Pore RMS factor = -1). Stitching of CLSM images was carried out in Gwyddion 2.48 [243].

MS data were converted to into .imzML using imzMLConverter[209], and imported into MATLAB using SpectralAnalysis[210] for further processing and analysis.

Spectral data underwent an interpolation re-binning process (bin size = *m/z* 0.002) before peak intensities, taken as the integrated peak area at full width half maximum (FWHM), were extracted. MS data for olanzapine ion yield calculations were taken from the summed intensities of the $[M+H]^+$, $[M+Na]^+$ and $[M+K]^+$ ions, including all detected isotopic peaks.

4.3.5- Calculation of ion transmission in MALDI Synapt G2-Si HDMS

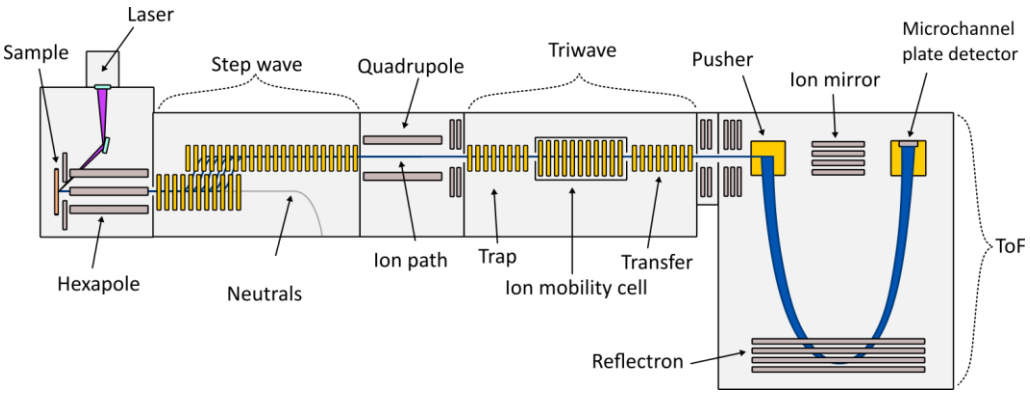


***Figure 4.2**. Overview of the internal ion optics and ion path for the Synapt G2-Si HDMS.*

The Synapt G2-Si has two modes of ToF configuration, "V" & "W", which refer to the path ions take through the ToF. In "V" mode ion packets are sent from the pusher and reflected once off the reflectron before entering the detection system. In "W" mode ion packets are reflected off the reflectron towards an ion mirror and then back to the reflectron before finally entering the detection system (Figure 4.2).

Here the instrument was operated using the predefined "Resolution" option from the control software. The option makes use of the "V" mode ToF configuration, which has an ion transmission efficiency of 43%. Further ion losses

occur in the ion transfer optics from the UV-MALDI source to the ToF, which for the "Resolution" mode used here was 30%.

As the Synapt G2-Si is an orthogonal Qq-ToF instrument, it has a pusher that injects the ions coming though the ion transfer optics into the ToF. The duty cycle refers to the percentage of available ions that are injected orthogonally into the ToF by the pusher. The maximum duty cycle for the Synapt G2-Si HDMS is 22.5%. Duty cycle is dependent on the upper limit of the mass range (m/z_{max}) studied and the mass of the ion of interest (m/z_{i},), and can be calculated using equation 4.1

$$Duty\ Cycle = 22.5\sqrt{\frac{m/z_i}{m/z_{max}}} \qquad (4.1)$$

Combining all the above sources of ion loss allows us to calculate ion transmission of the instrument (Equation 4.2)

$$Ion\ transmission\ (\%) = \%\ T_{transfer\ optics} \times \%\ duty\ cycle \times\ \%\ T_{TOF} \qquad (4.2)$$

Using the above values and equations the ion transmission for the analyte (*m/z* 313.14) was calculated as 1.33%.

4.3.6 - Determination of ion number

The instrument reports ion signal as an "intensity" which has to be related to the actual number of ions hitting the detector. This can be done through a stored system parameter, called the "single ion intensity", that relates the analogue signal from the detector to the 8-bit digital output of the instruments analogue to digital converter (ADC). Specifically, this value is the average area under the intensity curve generated by a single ion impacting the detector.

The instrument has an automated electrospray routine for determining this parameter, which involves monitoring changes in detected intensities of Leucine Enkephalin $[M+H]^+$ (*m/z* 556.27) under a series of different conditions, for the experiments here the single ion intensity was 24. It should be noted that this value is technically specific to Leucine Enkephalin $[M+H]^+$, but from discussions with technical experts from the instrument manufacturer, it was determined the difference for the analyte used here would be negligible.

The ion number can then be determined by dividing the reported ion intensity by the single ion intensity. This can then be combined with the transmission to estimate the total number of ions generated from the sample

$$number\ of\ ions\ generated = ion\ transmission * \frac{ion\ intensity}{24} \qquad (4.3)$$

4.4 - Results

4.4.1- Irradiation effects

When seeking to determine the surface effects resulting from laser sampling in UV-MALDI a variety of parameters are useful to measure. Firstly, knowledge of the initial matrix conditions, are evidently important. Additionally, aspects of crater geometry (size, shape, volume) resulting from UV-MALDI MSI analysis can prove highly informative in determining factors influencing limits of detection and spatial resolution. Finally, chemical and physical modification of UV-MALDI matrices during laser irradiation has long been suspected to have an experimental impact, therefore is it also advantageous to distinguish any changes to the matrix, be it to morphological or other properties.

Table 4.1. *Summary of the surface analysis techniques used*

	AFM	**SEM**	**CLSM**
UV-MALDI relevant information	Crystal morphology & size Surface topography Surface mechanical properties	Crystal morphology & size Surface feature dimensions (2D)	Crystal morphology & size Surface topography
Resolution	Angstrom scale Susceptible to tip shape effects	Down to 1 nm	Lateral @ x 50 - 250 nm Depth @ x 50 - 10 nm
Sample preparation	None	Deposition of conductive layer typically required for imaging insulating materials	None
Measurement environment	Ambient	High vacuum (~10^{-8} mbar)	Ambient
Sample damage	Negligible	Negligible	Possible with strongly absorbing materials. Dependant on magnification and laser power
Field of View	Up to 90 µm x 90 µm	Up to cm range, but with trade-off in resolution	Defined by objective lens, trade-off with spatial resolution. 256 µm x 256 µm @ x50
Measurement speed	Typically, 40 minutes for large areas	> 20 mins for high resolution images	1 minute
Data processing required	Removal of image artefacts. Difficult to get consistent results	None	Removal of image artefacts. Removal consistent for a given objective lens.
Image stitching	Yes, but complicated by data processing required	Yes	Yes

AFM, SEM and CLSM, were used to characterise laser irradiation effects from the UV-MALDI MSI experiments (Figure 4.3), a summary of each technique can be

found in Table 4.1. This overview is specific to instrumentation used here and is not a comment on the capabilities of the techniques as a whole.

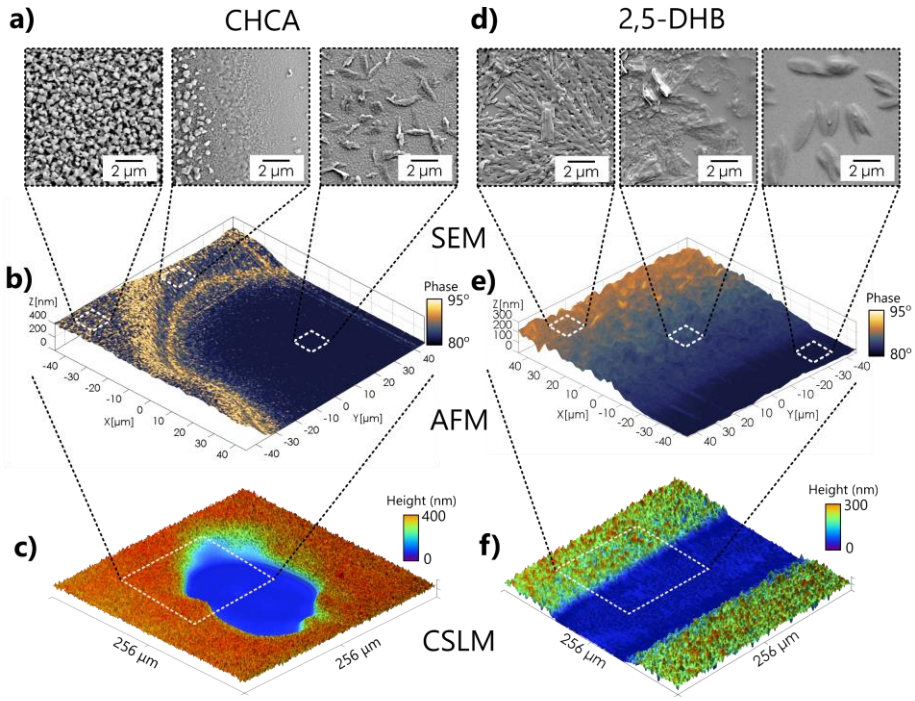


Figure 4.3. *Surface analysis techniques for characterising laser irradiation effects and material ejection in UV-MALDI MSI.* ***a)*** *SEM image* ***b)*** *AFM topography image with phase map overlay and* ***c)*** *CSLM topographic image of crater in CHCA film, resulting from spot mode acquisition, with a laser energy of 3.6 µJ and 500 Hz repetition rate.* ***d)*** *SEM images* ***e)*** *AFM topography image with phase map overlay and* ***f)*** *CSLM topography image of raster trench in 2,5-DHB film, resulting from 2 mm/s raster mode acquisition, with a laser energy 7.3 µJ and 500 Hz repetition rate.*

SEM imaging of the pristine matrix films revealed significant differences in crystal shape between the matrix compounds (Figures 3a & d). Matching previous reports for sublimed films of the matrix compounds, CHCA films

consisted of sub-micron sized angular crystals whereas the 2,5-DHB films consisted of few micron long branched crystals.

Post laser irradiation, 2,5-DHB showed a smoothing of crystal edges, becoming more apparent moving towards the centre of the crater/raster trench, caused either through melting or sublimation (Figures 4.3d). Cone-like and ripple structures have been previously observed occurring after irradiation of large 2,5-DHB crystal surfaces[236,244], although this was not evident here, mostly likely due to differences in sample studied. Craters in the CHCA film exhibited distinct morphological zones, with the angular matrix crystals gradually giving way to an amorphous porous surface, possibly evidencing a melting effect (Figure 4.3a). AFM images collected across these regions revealed distinct bands in the obtained phase map data (Figure 4.3b). AFM phase images, which shows changes in energy dissipation experienced by the AFM tip, act as is an indicator of adhesion, viscoelasticity and other material properties of a surface[245]. The bands, which correspond roughly to the zones observed in SEM (Figure 4.3a), therefore may represent areas where the matrix has undergone modification by the laser. Phase maps for 2,5-DHB revealed a gradual change (Figure 4.3e), also reflecting the SEM data for that matrix (Figure 4.3d).

Unidentified crystalline material, which was morphologically different from pristine matrix, was observed in the central regions of 2,5-DHB craters/raster trenches (Figure 4.3d & f). Due to surrounding regions being completely clear, re-deposition was presumed to be an unlikely source for this material. A similar effect was observed for CHCA (Figure 4.3a & c), although the uniform coverage

of the remaining material suggest re-deposition could be a source in this case. For both matrices there was no obvious visible evidence of redeposited material on the surrounding matrix film areas.

Due to the large number of measurements required, and limitations of the SEM and AFM instruments (Table 4.1), CLSM was employed as the primary surface analysis technique to characterise material ejection resulting from the different studied UV-MALDI MSI experimental parameters.

4.4.2 - Characterising material ejection in UV-MALDI MSI

Characterising material ejection from a sample can provide valuable insight into many aspects of UV-MALDI MSI as it impacts both limits of detection and spatial resolution of UV-MALDI MSI analyses. CLSM was used to characterise material ejection from model systems, consisting of a thin film of olanzapine with an over layer of CHCA or 2,5-DHB. The uniform nature of the samples enabled the craters/trenches formed under different UV-MALDI MSI sampling conditions to be accurately characterised. Figure 4.4 shows the changes in crater depth and size, material ejection and olanzapine ion intensity over a range of laser pulse energies and repetition rates. The previously measured matrix density values from Chapter 2 enabled material ejection, defined by the total number of molecules removed, to be estimated.

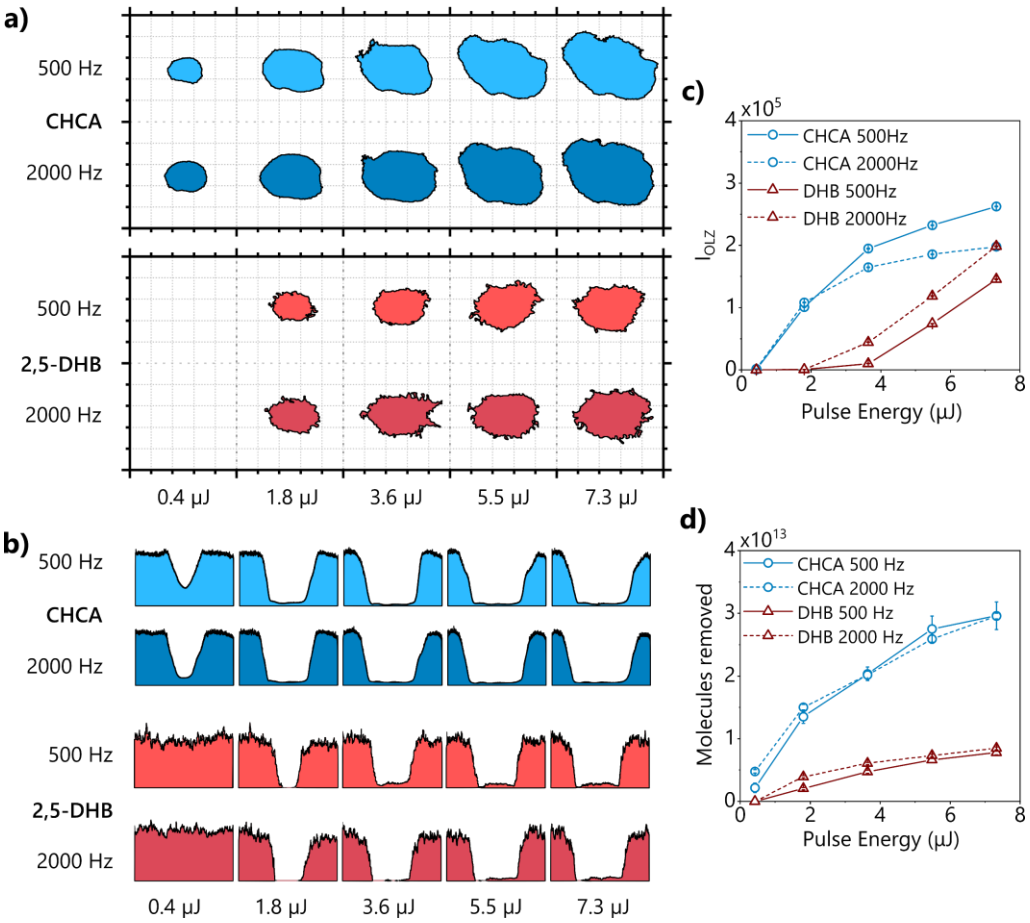


Figure 4.4. *Ionisation and material ejection from olanzapine + CHCA/2,5-DHB thin films in spot mode* ***a)*** *Averaged crater geometries (n=5)* ***b)*** *Cross sectional profiles of craters, at different pulse energies and repetition rates, obtained from CLSM measurements* ***c)*** *Corresponding olanzapine ion intensities (I_{OLZ}). Ion intensities are the summed values of H^+, Na^+ and K^+ adducts and all detected isotopic peaks* ***d)*** *calculated number of molecules removed at different pulse energies and repetition rates from CLSM crater volume measurements. All error bars represent the expanded uncertainty (k=2).*

The intensity of olanzapine (I_{OLZ}) increased with pulse energy (Figure 4.4c), reflecting the familiar relationship seen in UV-MALDI MS[59,60,67,246]. In contrast to the ion intensity data, the change in material ejection with pulse energy (Figure

4.4d) was much less pronounced, which is in agreement with previous reports showing significant deviations between material ejection and detected ion intensities[24,236]. One distinguishing feature between desorption and ablation models in UV-MALDI is the relationship between laser energy and material ejection, with quasi-thermal desorption predicting an exponential relationship, and ablation either logarithmic or linear [62]. The evolution of material ejection with pulse energy (Figure 4.4d) appears to follow a logarithmic trend, suggesting that the ablation type processes are dominant. This agrees with previous studies that have placed this transition to ablation-like ejection mechanisms as coincident with the onset of significant ion generation[82,147,150]. On the other hand, photoacoustic measurements reported by the Dreisewerd group have shown that quasi-thermal desorption best describes material ejection at the laser energy range and spot size used here [24,61]. The reason for this discrepancy is unknown but may be due the relatively short pulse width (≤1.1 ns) and higher repetition rates (500 Hz & 2500 Hz) used here, which are both likely to favour ablation-like mechanisms.

The influence of laser repetition rate on I_{OLZ} was more complex, with the higher repetition rate increasing I_{OLZ} at all pulse energies for 2,5-DHB, but for CHCA a crossover is evident above 1.8 μJ pulse energy (Figure 4.4c). Comparison with the number of molecules desorbed (Figure 4.4d) suggests greater material ejection may explain some of the observed I_{OLZ} increase in 2,5-DHB, whereas for CHCA other effects are clearly occurring. Given the layered nature of the samples a depth-of-sampling effect is possibly also influencing the data in some

instances, especially at the lower pulse energies where full penetration of the matrix layer is not achieved (Figure 4.4b).

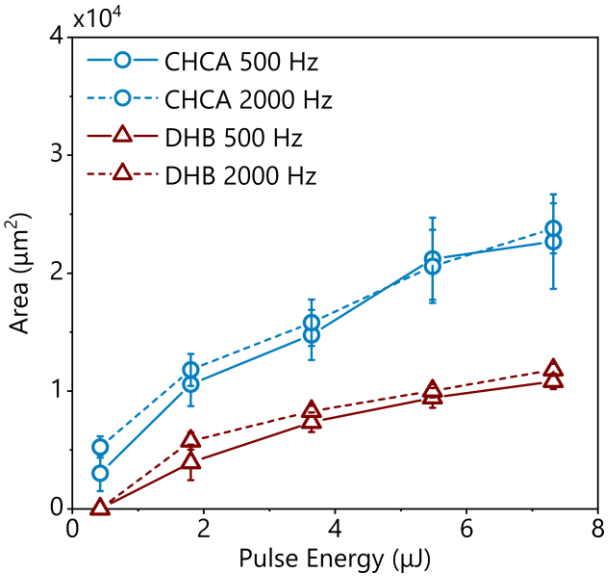


Figure 4.5. *Change in crater area with pulse energy in spot mode for CHCA and 2,5-DHB at 500 Hz and 2000 Hz. Error bars show the expanded uncertainty (k=2).*

Changes to crater geometry is an important factor to consider for UV-MALDI MSI experiments, particularly if an oversampling or continuous raster acquisition mode is employed. CLSM measurements were used to determine the crater geometries under different pulse energies and repetition rates for both matrix compounds (Figure 4.4a). Differences between the matrix compounds, arising from their physiochemical properties, can be observed. For the same delivered pulse energy 2,5-DHB exhibited craters areas approximately 50% smaller than CHCA (Figure 4.5). This is likely due to 2,5-DHB having significantly weaker absorption at the wavelength of the laser (355 nm)[246], thus having less energy available to drive material ejection. The change in crater size with pulse energy was less pronounced for 2,5-DHB (Figure 4.4a). Overall crater shape remained

somewhat symmetrical for this matrix, unlike CHCA which evidenced significant elongation along the axis of the incident laser beam at higher pulse energies (Figure 4.4a). This suggests that 2,5-DHB is more robust to the variations in energy distribution within the laser spot and changes in pulse energy, and so less likely to suffer from spatial resolution issues associated with Gaussian beam profiles. Although 2,5-DHB is well known to form larger crystals than CHCA, which may serve to counteract this effect in many experiments, particularly those using solvent spray-based matrix depositions. Alternatively the use of homogeneous beam profiles[68] could be used to by and large negate these effects.

Despite noticeable differences I_{OLZ} between the two laser repetition rates (Figure 4.4b), the impact on crater geometry was far less pronounced, with crater areas effectively the same for both repetition rates (Figure 4.5). A small increase in material ejection at the higher repetition rate with 2,5-DHB (Figure 4.5) might explain the differences in I_{OLZ} for this matrix, pointing to sampling effects. This also suggests that variation in laser repetition rate is less of a concern for spatial resolution but can have an influence on limits of detection.

For lasers with a Gaussian energy distribution, typically used in UV-MALDI MSI, heterogeneous ejection of material is to be expected within the irradiated sample area. The collected crater topography data allows us to quantify this effect under the conditions studied.

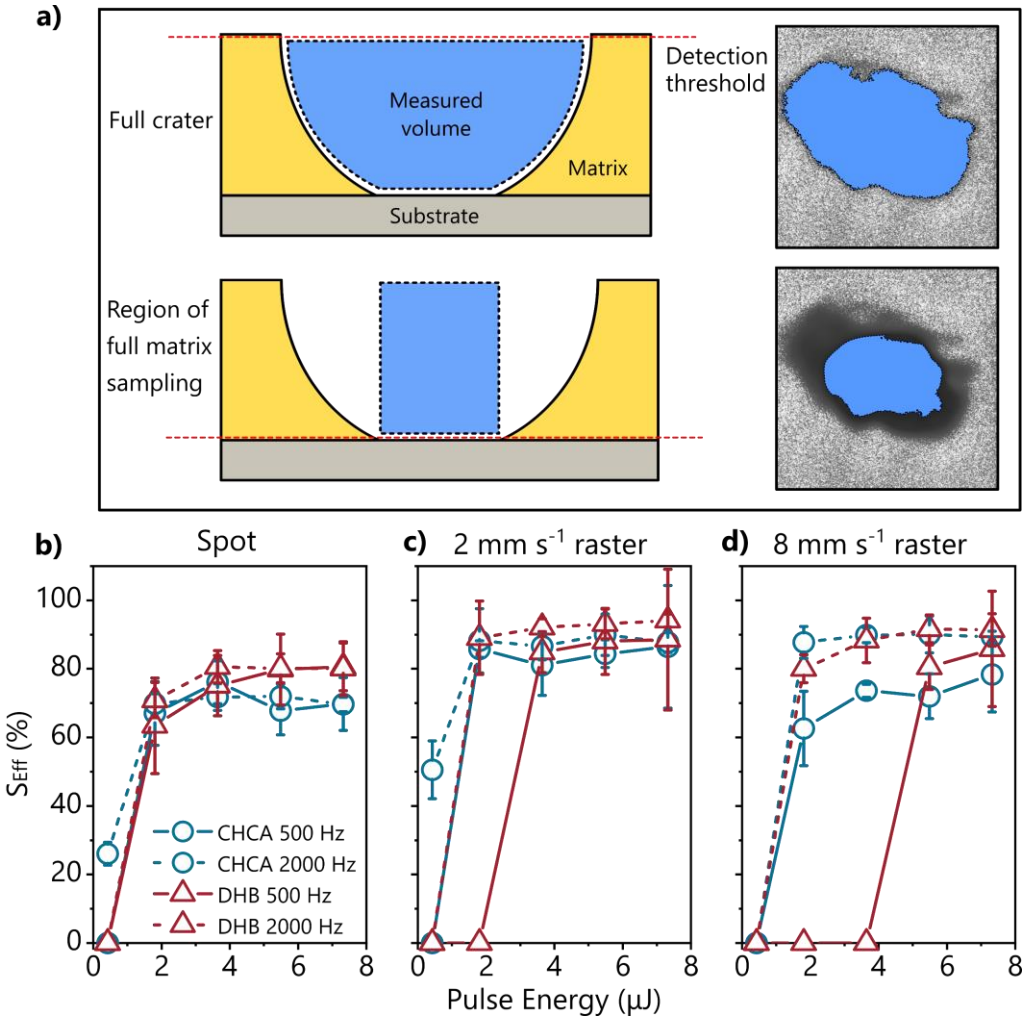


Figure 4.6. a) *Overview of sampling efficiency (S_{Eff}) concept and measurement. Diagrams on the left show a cross sectional view of how the full crater (top) and region of complete matrix ejection (bottom) volumes are determined, images on the right show the process with real crater data (CHCA, 500 Hz, 5.5 µJ). Change in S_{Eff} with laser pulse energy for CHCA and 2,5-DHB at 500 Hz and 2000 Hz, for* ***b)*** *spot mode,* ***c)*** *2 mm s^{-1} raster* ***d)*** *8 mm s^{-1} raster.*

Using knowledge of the matrix layer thickness, the threshold height for the crater edge detection algorithm was adjusted to be just above the substrate, allowing the region within a crater where the matrix layer was completely ejected to be identified (Figure 4.6a). By taking the ratio of crater volume

bounded by this region to that of the full crater volume an estimate of the efficiency of sampling (S_{Eff}) under the studied conditions (Figure 4.6b-d) can be provided. Within the limits imposed by UV-MALDI MS ionisation dynamics and analyte extraction into the matrix layer, this metric describes the degree to which the ejected matrix is reflective of the underlying sample region, with a S_{Eff} of 100 % corresponding to complete measurement. As such S_{Eff} should have a direct impact to both the limits of detection of UV-MALDI analyses and on spatial resolution.

In spot mode, S_{Eff} increased with pulse energy, reaching a maximum of 80% for 2,5-DHB and 70% for CHCA (Figure 4.6b). Based purely on material ejection 2,5-DHB could be seen a superior matrix for lower limits of detection and higher spatial resolution with Gaussian profile beams, as its higher achievable S_{Eff} ensures maximal consumption of analyte within the matrix layer for given irradiated region. Although as previously noted, this matrix has a tendency to form large crystals, potentially counteracting any benefit in spatial resolution.

A S_{Eff} of up to ~90% was observed in raster mode, with higher laser pulse energy and repetition rate improving S_{Eff}, and increased raster speed reducing it (Figure 4.6c & d). This was likely due to effective material ejection requiring sufficient laser energy and/or number of pulses per unit area. The higher S_{Eff} in raster mode compared to spot mode may be due to the shorter duration a specific area is irradiated, minimising material ejection in the low energy fringes of the laser spot material. These results suggest that on top of evident improvements

in acquisition time, modest gains in limits of detection and spatial resolution can be made from adopting raster mode sampling over spot mode.

4.4.3 – Simulation of material removal in oversampling acquisition

To further understand the effect the crater shape can have on spatial resolution, the crater topography data was used as the basis to simulate matrix removal during a MALDI MS image acquisition experiment. As for continuous raster mode there was no way of knowing the exact shape of the volume removed per pixel, a spot mode acquisition with increasing degrees of oversampling was simulated (Figure 4.7).

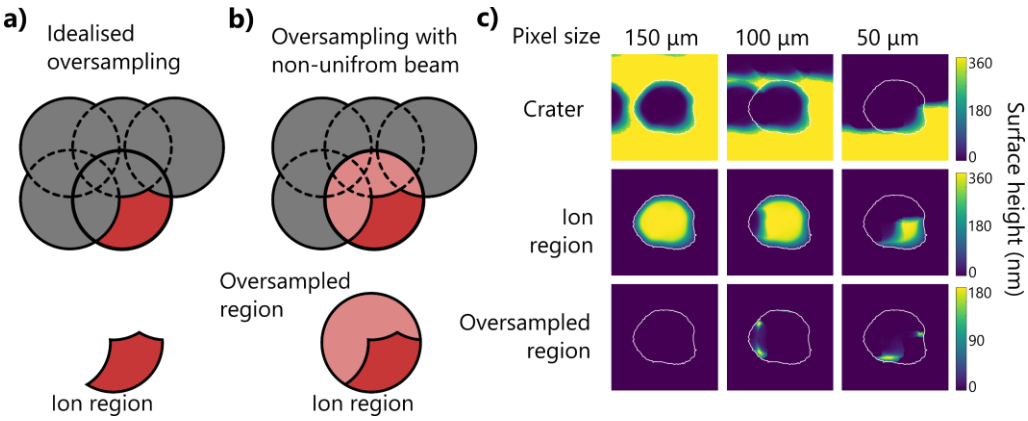


***Figure 4.7**. Illustration of spatial origin of ions under **a)** idealised oversampling conditions and **b)** oversampling with non-uniform laser beam profile. **c)** Simulation of material removal at different pixel sizes. Top: Surface topology of the matrix layer. Middle: Ion region, the total volume removed per pixel Bottom: Oversampled region, the volume removed at the current pixel location that comes from sample areas analysed in previous pixel. Crater data from CHCA 1.8 µJ, 2000 Hz data.*

Oversampling acquisition works on the principle that for each pixel location, complete matrix removal is achieved within the region irradiated by the laser (Figure 4.7a)[94]. In practice, due to the non-uniform removal of material within the irradiated region associated with Gaussian beam profiles, in many instances there will appreciable amounts of matrix remaining that can contribute to subsequent pixels (Figure 4.7b). Using the simulated oversampling acquisition, the volumes of removed matrix associated with the ion region, the origin of all ions in the corresponding mass spectrum, and the oversampled region, the region that has contributed ions to previous pixel spectra, can be determined for a range of pixel sizes (Figure 4.7c).

The ions arising from the oversampled region will contribute to an error the spatial resolution of the resulting image, as the region of the sample they originate from will have been sampled in multiple pixels. To understand the potential magnitude of this effect, the ratio of the oversampled region to the ion region volumes was used to provide an estimate of the proportion of matrix removed at a given pixel location that corresponds to regions of the sample previously analysed. This metric was then estimated for a range of pixel sizes for both matrices, at all the pulse energies and repetition rates studied in this chapter (Figure 4.8).

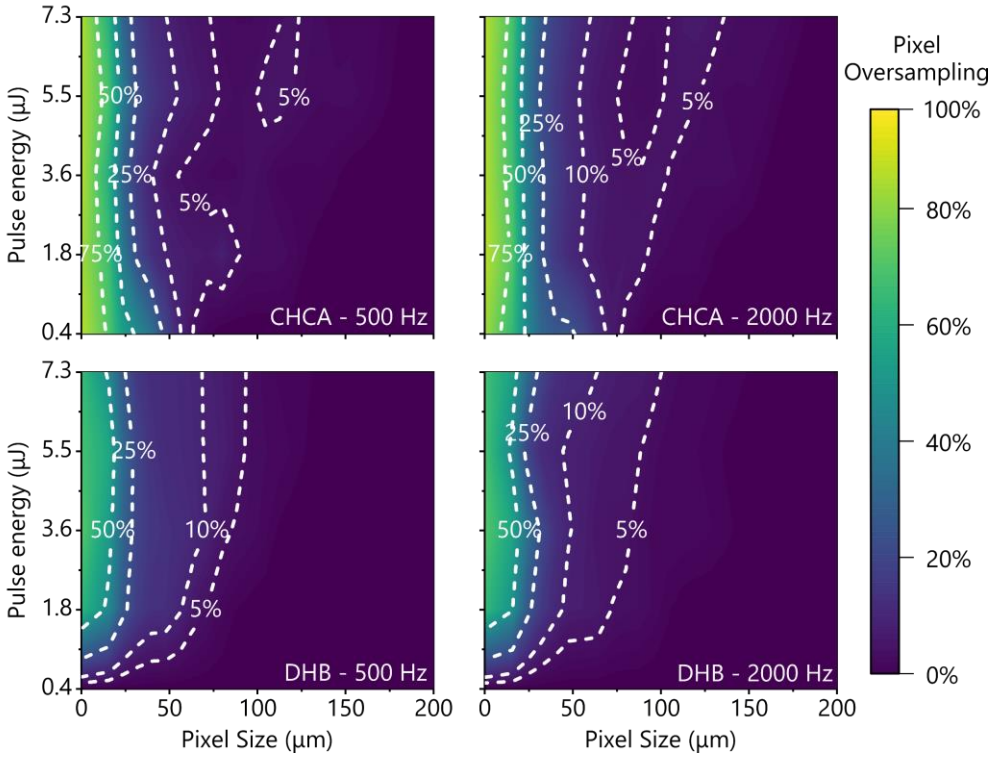


Figure 4.8. *Heatmap showing the simulated degree of pixel oversampling at different pixel sizes, for CHCA and 2,5-DHB at different pulse energies and laser repetition rates. Contour lines marking different degrees of pixel oversampling are included to aid interpretation of the data.*

The simulated data shows that significant degrees of pixel oversampling can be found for both matrix compounds as the pixel size decreases. For the two matrices, CHCA resulted in the highest pixel oversampling, reaching ~80% at 10 µm pixel size, while pixel oversampling for 2,5-DHB was ~65% for the same pixel size. While this represents a drastic degree of oversampling for the size of laser spot used here, even at more a suitable pixel size of 50 µm pixel oversampling still exceeds 10% under most conditions. This difference between matrices agrees with the S_{Eff} findings (Figure 4.6) that showed 2,5-DHB tended to produce

sharper crater edges, resulting in more efficient sampling of the matrix layer with smaller partially ablated regions.

Beyond the lowest pulse energy, where no crater was formed in 2,5-DHB, pulse energy had minimal effect at small pixel sizes for both matrix compounds, but as pixel size increased a greater degree of pixel oversampling became evident at the higher pulse energies (Figure 4.8), likely as an effect of increase in areas of partial matrix ablation. Minor local decreases in pixel oversampling were also evident for CHCA at the highest pulse energy, mirroring the increased asymmetry of crater shape seen with this matrix at higher pulse energies (Figure 4.4a). Increasing repetition rate led to a minor reduction in pixel oversampling at larger pixel sizes for 2,5-DHB, whereas CHCA showed a slight increase, likely due to the latter matrix begin more susceptible to material removal in the low energy fringe regions of the laser spot. In practical MSI terms, the simulation results here showed that even at pixel sizes showing a modest degree of pixel oversampling (50 μm), the region of the sample that nominally corresponds to a single MSI pixel will have potentially been sampled in neighbouring 3-8 pixels either side along the X axis and 2-6 pixels in Y, depending on the laser conditions and matrix used.

The simulation data shows that significant limitations can exist to oversampling in imaging experiments when using Gaussian beams. Adopting laser beam profiles incorporating a flat top energy distribution and/or square shape, or a laser spot size better matched to the desired pixel size would likely help to mitigate the extent of pixel oversampling. The results also highlight how matrix

selection and laser conditions can be used to tailor desorption conditions, helping to minimise the level of pixel oversampling.

4.4.4 - Ion yields in MSI

The absolute values of ion yields is a widely debated topic, with proposed values ranging from 10^{-1} to 10^{-8} for analyte ions and 10^{-3} to 10^{-9} for matrix ions. To date there has been no investigation into how ion yields are affected by recent UV-MALDI MSI developments, namely the use of high laser repetition rates and continuous raster mode acquisition. By combining the measurements of material ejection with the corresponding MS data, the olanzapine ion yield (Y_{Olz}) (Figure 4.9) and total ion yield (Y_{TIC}) (Figure 4.10) can be estimated for the conditions studied. It should be noted that due simplifications required when estimating Y_{TIC}, these values should be considered a first order approximation.

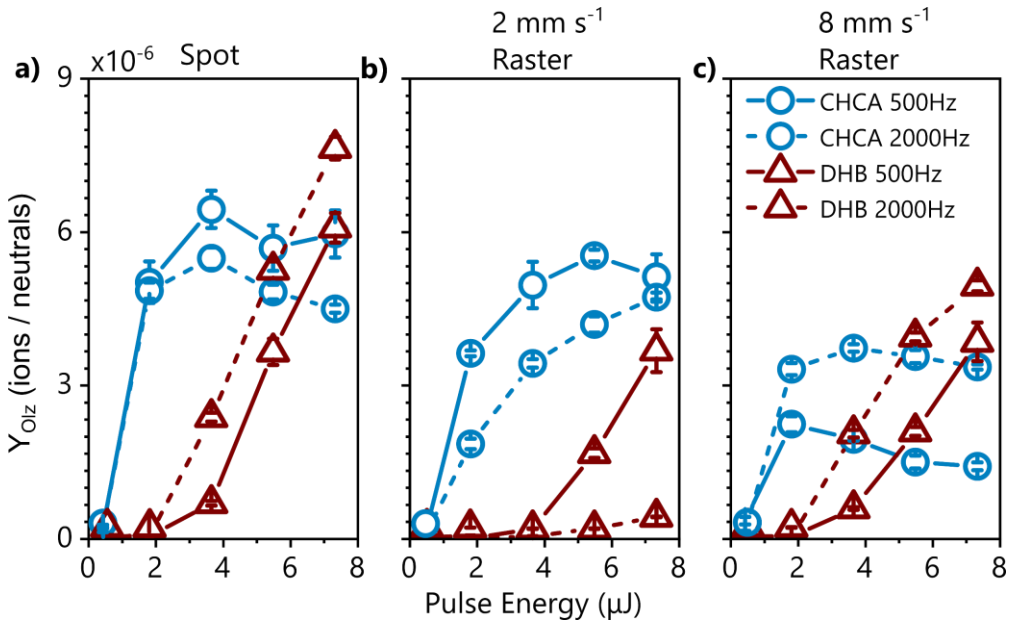


Figure 4.9. *Ion yield of olanzapine (Y_{OLZ}) with increasing pulse energy under different imaging conditions.* ***a)*** *spot mode acquisition,* ***b)*** *2 mm s^{-1} raster* ***c)*** *8 mm*

s^{-1} raster. All raster data is normalised to pixel size. Error bars show the expanded uncertainty (k=2).

Ion yields for olanzapine (Y_{Olz}) ranged from 10^{-9} to 10^{-6} (Figure 4.9), which is towards the lower end of reported analyte values[170]. The total ion yield (Y_{TIC}) ranged from 10^{-10} to 10^{-7} (Figure 4.10). While this may seem counter-intuitive, matrix ion yield is known to be orders of magnitude smaller than that of analytes[170].

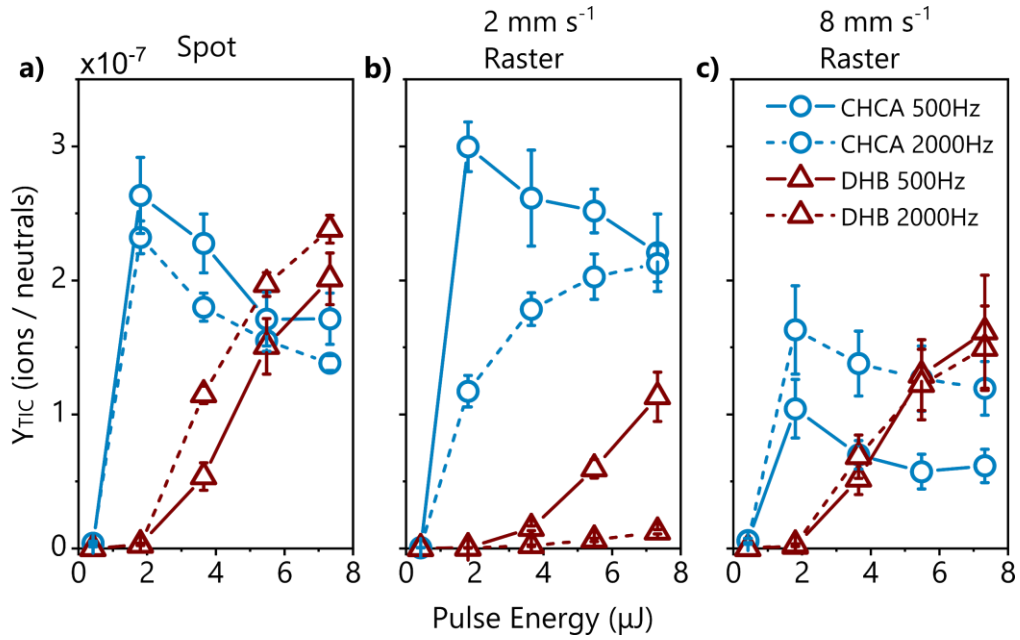


Figure 4.10. *Total ion yield (Y_{TIC}) with increasing pulse energy under different imaging conditions.* ***a)*** *spot mode acquisition,* ***b)*** *2 mm s^{-1} raster* ***c)*** *8 mm s^{-1} raster. All raster data is normalised to pixel size. Error bars show the expanded uncertainty (k=2).*

As the matrix was main contributor to the TIC here, besides the analyte, the total ion yield can be expected to be a convolution of the two components. In line with previous reports [59,99], ion yields generally increased with pulse energy

(Figure 4.9 & Figure 4.10), although given the layered nature of the samples, yields at lower pulse energies will also likely exhibit sampling depth effect. The relative stability of Y_{OLz} across higher pulse energies with CHCA is worthy of note for imaging experimentation, suggesting that there is a broad window of pulse energies before fragmentation begins to adversely affect ion yield. It is expected that 2,5-DHB will also show a similar plateau region, but the range of pulse energies used here was not sufficient to access this regime. A small decrease in Y_{OLZ} was evident with CHCA at higher pulse energies for 2000 Hz in spot mode and 500 Hz, 8 mm s^{-1} in raster mode (Figure 4.9a & 9c); this matrix also showed significant drops in total ion yields at pulse energies above 1.8 µJ under nearly all conditions (Figure 4.10). Higher laser repetition rate was found to enhance Y_{OLZ} obtained with 2,5-DHB in spot mode (Figure 4.9a), as more efficient sampling of the matrix layers can be ruled out due to similar observed S_{EFF} values (Figure 4.6a) this is likely due to enhanced material ejection, as the material ejection was also higher (Figure 4.4c).

In raster mode the combinations of repetition rate and raster speed produced resulted in somewhat counter intuitive behaviour for both matrices (Figure 4.9b & c, Figure 4.10b & c), for the faster raster speed a higher repetition rate generally enhanced ion yield, but at the slower speed a reduction was observed. The trend of ion yields with pulse energy seemed to shift towards higher pulse energies when the higher repetition rate was employed, and towards lower pulse energies with faster raster speed. Similar trends have been reported for CHCA in thin film and tissue samples, where optimal pulse energies for highest ion intensities shifted with repetition rate and raster speed[52].

Similar results were reported by Spraggins et al. who observed reduced ion intensities in raster mode with increasing repetition rate, with faster stage speeds required to maintain good ion signal[13]. The same authors also proposed a rule of <50 laser shots per unit area in raster mode to prevent ion signal degradation, which they linked to the need to ensure sufficient volumes of matrix are sampled per pixel. Here the only raster conditions that exceeded this limit (2000Hz, 2mm/s) showed reductions in ion yield (Figure 4.10b), generally supporting the proposed rule. It should be noted however that this limit is somewhat arbitrary as the effect is likely to exist as a continuum and be matrix dependant; this can be seen at high pulse energies where ion yields between the repetition rates have converged with CHCA but are still significantly different for 2,5-DHB (Figure 4.10b). As the ion yield data here was normalised to volume of removed material, the effect is unlikely due to the amount of available matrix as previously proposed[13].

The associated ejected material data suggests that these trends were a product of ion formation or ejection plume mechanisms, as they were evident in the both the olanzapine and TIC data (Figure 4.9 & Figure 4.10), but not in the amount of desorbed material (Figure 4.11). Although in the case of the latter measurement there may be changes in ablation occurring at the leading edge of the laser beam which could not be captured in these experiments.

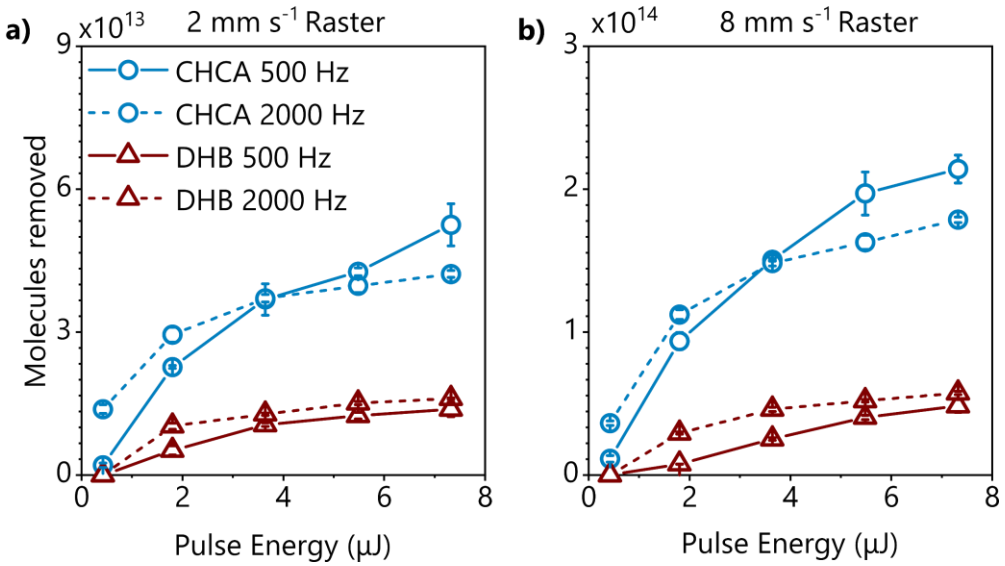


Figure 4.11. *Change in number of removed molecules per pixel with 2,5-DHB and CHCA as a function of laser pulse energy and laser repetition rate at* ***a)*** *2 mm s^{-1} and* ***b)*** *8 mm s^{-1} raster speeds. Error bars show the expanded uncertainty (k=2).*

As the raster speed and repetition rate conditions studied here both differed by a factor of four, the 500 Hz, 2 mm s^{-1} and 2000 Hz, 8 mm s^{-1} raster data both resulted in an equivalent irradiation condition of four pulses delivered for every µm of raster travel. This enables the effect of repetition rate in raster mode to be isolated from the other conditions (Figure 4.12 & Figure 4.13).

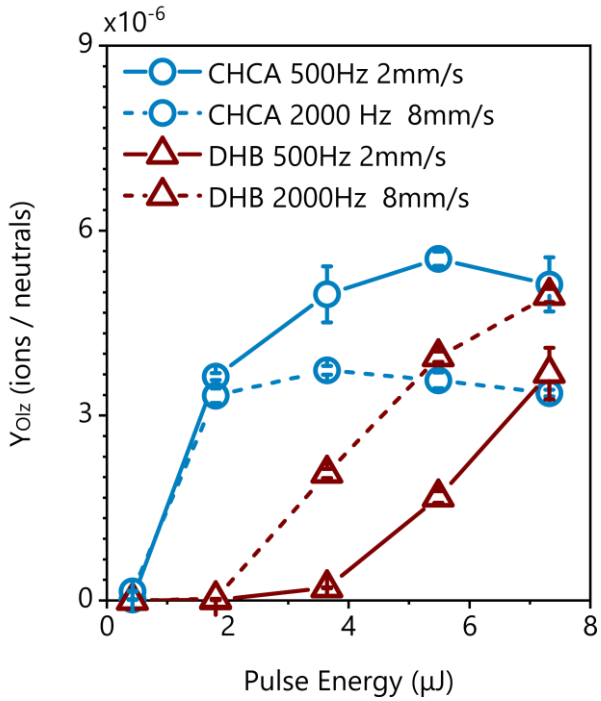


Figure 4.12. *Change in olanzapine ion yield (Y_{OLZ}) with pulse energy under equivalent irradiation conditions. Data shows raster mode acquisitions where the raster speed and laser repetition rate conditions resulted in four pulses delivered per µm of travel.*

Under these equivalent pulse number conditions, large differences in Y_{OLZ} and Y_{TIC} between repetition rates were evident (Figure 4.12 & Figure 4.13), producing similar results to that obtained in spot mode (Figure 4.9a & Figure 14.0a). The only parameter that differs between the two conditions was the time between laser pulses, which was 2 ms at 500 Hz and 500 µs at 2000 Hz.

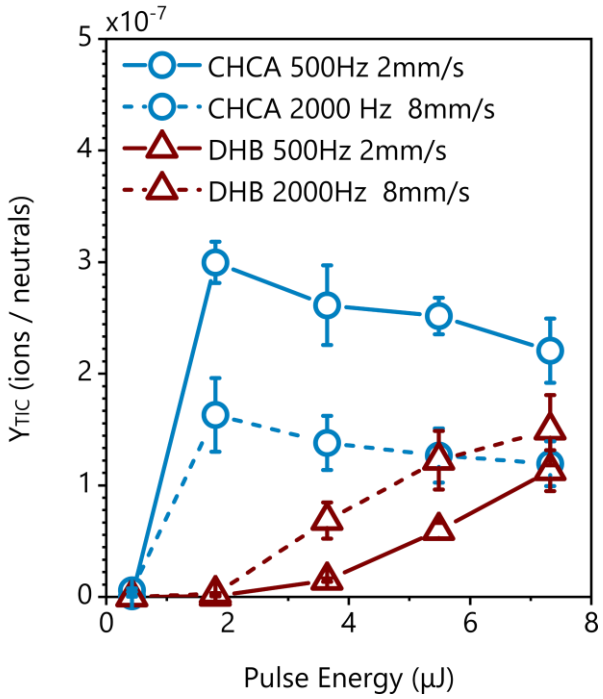


***Figure 4.13**. Change in total ion yield (Y_{TIC}) with pulse energy under equivalent irradiation conditions. Data show raster mode acquisition where the raster speed and laser repetition rate conditions resulted in four pulses delivered per µm of travel. All data is normalised to pixel size.*

This dependence of ion yield on time between delivered pulses was previously observed for detected ion intensities with CHCA by Steven et al[52], who found that ion signals for lipid species generally decreased with increasing repetition rate. The results here extend these findings to measurements of ion yield, and with an additional matrix and a different analyte. Interestingly, while the CHCA results agree with those previous findings, the current results show that 2,5-DHB behaves in completely the opposite manner (Figure 4.12 & Figure 4.13). Two potential causes for this effect can be postulated, which could occur individually, or more likely in parallel, during raster mode acquisitions.

Firstly, given the Gaussian energy distribution of the laser, irradiated matrix volumes at the periphery of the laser spot will be heated but not sufficiently to result in ejection of material. It has been previously shown that sample temperature has a direct impact on material ejection in UV-MALDI and so release of ions for detection[149]. At the time of arrival of a subsequent pulse, the extent of the heated volume would be dependent on matrix properties such as optical absorption, heat capacity and thermal diffusion. Under thermally confined conditions typical of UV nanosecond laser pulse irradiation, the change in temperature (ΔT) with depth (z) within the matrix, upon absorbing a laser pulse, can be described using equation 4.4.

$$\Delta T(z) = \frac{(\alpha\tau)H}{\rho C_p} e^{-(\alpha\tau)z} \qquad (4.4)$$

Where α is the absorption coefficient, τ is the fraction of energy available for heating after accounting for energy loss via fluorescence, H is the laser fluence, ρ is density and C_p is heat capacity. Values for α and ρ were measured in Chapter 2. C_p (CHCA = 1.00 J g^{-1} K^{-1} ; 2,5-DHB = 1.15 J g^{-1} K^{-1}) was estimated though the use of a group contribution method[247]. τ at 355nm was calculated as 0.51 for 2,5-DHB and 0.94 for CHCA using values reported by Allwood et al.[32]. Using these data the distribution of heat change within CHCA and 2,5-DHB matrix layers, resulting from the absorption of a single pulse (3.6 μJ, 355 nm, 200 μm diameter) can be simulated (Figure 4.14).

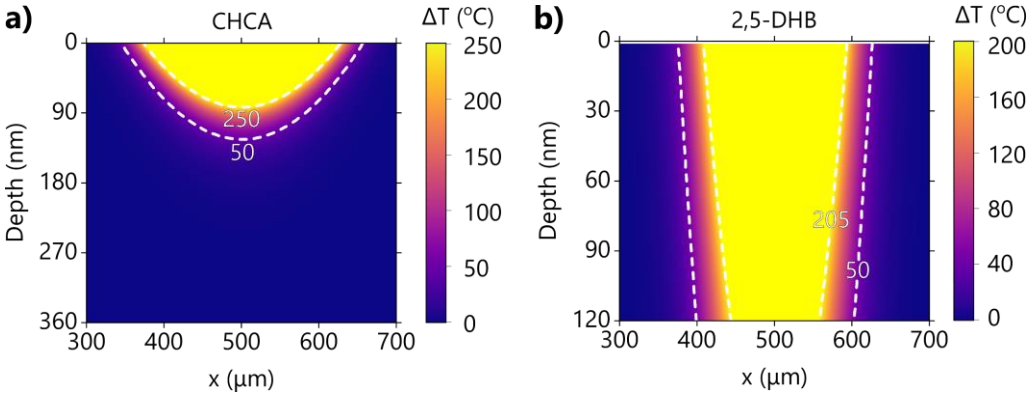


***Figure 4.14**. Simulated temperature rise from absorption of a single laser pulse (200 μm diameter, 3.6 μJ, 355 nm) in **a)** CHCA and **b)** 2,5-DHB matrix layers. Colour bars are scaled to the respective melting points of each matrix (CHCA: 250°C, 2,5-DHB: 205°C). Contour lines show the position of 50°C and the respective melting point of each matrix.*

Assuming that any heating beyond the melting point of the matrix will result in material ejection, it can be seen that 2,5-DHB has a significantly larger heated volume post laser pulse absorption (Figure 4.14b). This is due primarily to the five-fold difference in optical absorption at 355 nm between the two matrices [20,246], as well as the significantly higher fluorescent quantum efficiency of 2,5-DHB[32]. Thermal diffusivity, which is a measure of the rate of heat transfer though a material, is not known for the matrices used here, but is typically in the range on 10^{-7} m^2s^{-1} for molecular solids[248]. Over the inter-pulse timescales in Figure 4.12 & 13 (500 μs to 2 ms), heat induced by the laser will have travelled approximately 4 - 8 μm laterally from the edge of the irradiated region. This is of same order as the distance between pulses (4 μm), suggesting that any residual heat imparted by a preceding pulse (Figure 4.14) will be available to contribute to material ejection from the next pulse.

Secondly, CHCA is known to exhibit what is termed the "shot effect", whereby the ion signal from a fixed sample position decreases with successive laser shots, theorised to be resulting from a mixture of photochemical[249] and thermochemical induced changes in the matrix[52]. It has been reported that while 2,5-DHB is more stable, CHCA readily undergoes a variety of reactions upon melting, resulting in a reduction of absorption at 355 nm and an increase in fluorescence emission intensity[53], both of which are known to reduce detected ion intensities in UV-MALDI MS[17,22,23,154]. The decrease in Y_{OLZ} with CHCA when operating at the higher repetition rate may then be a result of increased photo- and thermo-degradation of the matrix within the irradiated area, potentially further evidenced by the previous observed zones in the AFM phase data for this matrix (Figure 4.3b). This would further explain why the trend in ion yields (Figure12 & 13) for this matrix did not correlate with amount of material ejected (Figure 4.11).

The results show that raster mode is able to achieve a similar degree of limits of detection to spot mode, as long as an appropriate pulse energy and repetition rate are used. Although care must be taken optimising these parameters as they are not consistent across different raster speeds and behaviour is highly dependent on the matrix employed.

4.5 - Conclusions

Using well defined model systems and volumetric measurements of material ejection the measurement of absolute ion yield under a range of different UV-MALDI MSI sampling conditions was achieved. This is the first such data on

absolute ion yields in UV-MALDI MSI and should serve as a useful aid for optimisation of acquisition parameters in UV-MALDI MS imaging experiments.

Analyte ion yields for the systems studied span approximately 10^{-9} to 10^{-6} ions per desorbed molecule, supporting more recent lower estimates of UV-MALDI MS ion yields. The observed similarities in ion yield between raster and spot mode provide assurance to UV-MALDI MSI users that continuous raster acquisition mode can be utilised with little impact to limits of detection, as long as appropriate steps are taken to ensure suitable laser parameters are applied. This caveat highlights the benefits proper knowledge of laser conditions can provide to optimisation of UV-MALDI MS imaging experiments. Better characterisation of commercial MSI instruments would enable more accurate measurements of ion yield to be conducted in the future, and a thorough inter-comparison of commonly used instrumentation in UV-MALDI MSI, and MSI in general, would be of great use to the wider community. Additionally, to gain a clearer picture of complex behaviours evidenced in the results, it would be useful to extend these measurements, incorporating a wider range of pulse energies, repetition rates and raster speeds, as well additional matrix compounds and analytes. Inclusion of other relevant UV-MALDI MSI experimental parameters such as laser spot size and beam profile would also be highly informative.

Simulations based on the acquired volumetric measurements were used to explore the effects of Gaussian laser spot sampling on material ejection in oversampling mode UV-MALDI MSI; the high levels of pixel oversampling, up to 85% under some conditions, points to significant limitations to the application

of this common imaging approach. The significant observed differences in material ejection between the studied conditions suggests that beyond widely accepted influences on resolution, (laser spot size, step size, matrix crystal size and degree of analyte delocalisation), other factors such as properties of the matrix utilised, laser pulse energy, repetition rate and beam profile can have significant effects. The results highlight the drawbacks of using lasers with Gaussian beam profiles and suggest that the adoption of more suitable beam profiles, such as flat top square, should be seriously considered.

Chapter 5 - Characterising the influence of tissue microenvironment on desorption and ionisation in UV-MALDI MSI

5.1 – Introduction

Understanding the complex interactions occurring between the laser, matrix and sample in UV-MALDI MSI experiments is essential to obtaining accurate and robust imaging data. A substantial barrier to more quantitative assessments of UV-MALDI MSI data comes from the variable suppression or enhancement of ion formation often seen in biological tissues[67,68,109,143,250]. This variation in detected ion intensities is also routinely observed between different tissue regions for highly heterogeneous tissues such as brain. Normalisation strategies have been developed to address the problem through the application of internal standards to inform "tissue extinction coefficients" (TEC) for normalising ion data[109,143,144], but these approached are limited to targeted analyses, and as such are not used in the majority of UV-MALDI MSI.

The origins ion suppression/enhancement in MALDI MSI are believed to be a convolution of multiple factors, such as desorption[68], charge competition, the influence of the underlying tissue[251,252] and analyte extraction[131], but the relative significances are poorly understood[67,144].

As demonstrated in the previous chapter, accurate topographical measurements provide a powerful tool to study aspects of the UV-MALDI process. Here Coherence Correlation Interferometry (CCI), a non-contact optical profilometry technique, was used to characterise the surface features of a tissue sample during the various stages of a typical MALDI MS imaging experiment of

mouse brain. These measurements provide insights into the role played by aspects of tissue micro-environment, such as thickness and tissue type, on matrix deposition, desorption and ion enhancement/suppression. By combing this technique with precisely deposited amounts of internal standard (haloperidol) and matrix, on tissue measurements of absolute ion yields are determined for the first time in UV-MALDI MSI.

5.2 - Materials

CHCA, Haloperidol and red phosphorus were purchased from Sigma Aldrich (UK). C57BL/6 mouse brain was kindly donated by Yulia Panina and Mariia Yuneva from the Francis Crick Institute (UK).

5.3 - Methods

5.3.1 - Experimental overview

To obtain the necessary topographic data to determine volumes of removed material and ion yield, as well as understand the effect of tissue thickness on ionisation, an imaging plan was created to capture the sample topography at key points in the UV-MALDI MSI sample preparation and analysis (Figure 5.1)

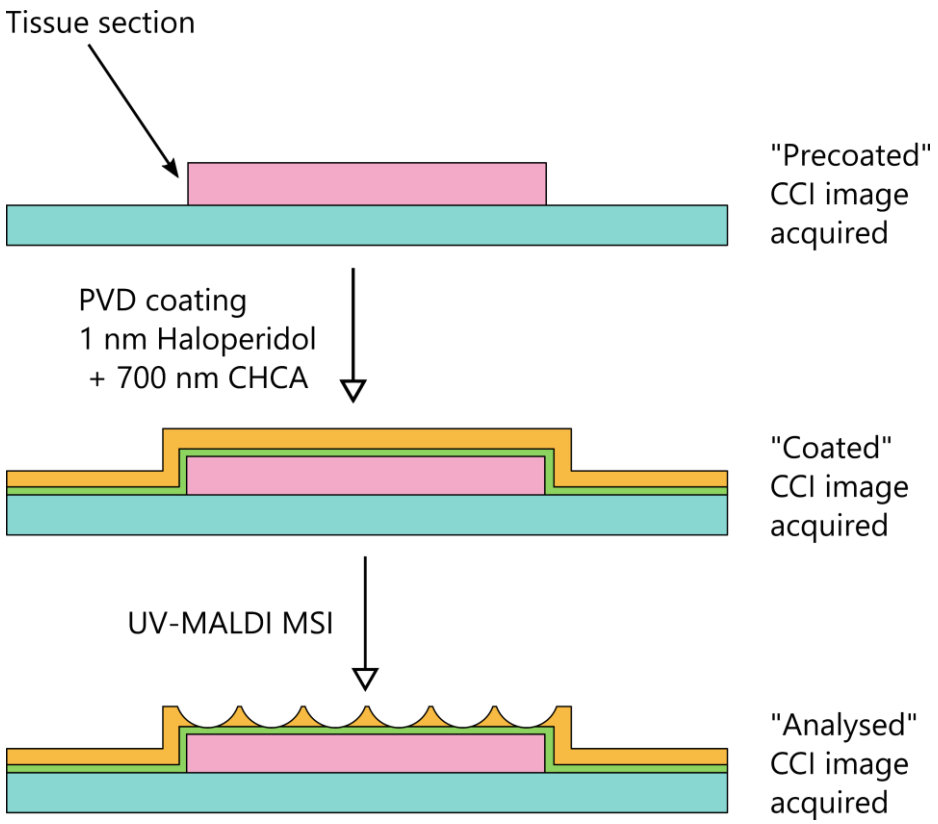


Figure 5.1. *Sequence of sample preparation and analysis. CCI topography images are collected at each stage, allowing the tissue topography, as well as material changes from matrix deposition and UV-MALDI MSI analysis to be fully quantified.*

In total three CCI topography datasets were collected from the sample, after sectioning and dehydration of the tissue, after deposition of the internal standard and matrix, and finally after the UV-MALDI MSI experiment.

By registering the three datasets, simple arithmetic operations could be performed to obtain maps of the sample for matrix thickness (Coated - Precoated) and volumes removed at each pixel (Coated - Analysed). Additionally, the post UV-MALDI MSI dataset enabled comparison to MSI data, as the laser ablation craters in the matrix could be directly matched to pixel locations. This enabled tissue thickness and matrix thickness to be correlated to

the MSI results, as well as calculation of absolute ion yields from volumes removed at each pixel.

5.3.2 - Tissue preparation

The mouse brain was section transversely at 12 um thickness, at the approximate mid-point of the tissue, in a CryoStar NX70 Cryostat (Thermo Scientific, Germany). Sections were thaw mounted onto Superfrost microscope slides (Fisher Scientific, Germany) and stored in vacuum sealed bags at -80 °C until needed. Tissue sections were brought up to room temperature by placing them in a vacuum desiccator for 30 minutes prior use.

5.3.3 - Matrix and internal standard deposition

Application of the matrix and internal standard were carried out using a NexDep PVD coater (Angstrom Engineering, Canada). Samples were loaded into the coater sample holder which was kept at a constant temperature of 10 °C and source to sample distance of 30 cm; the sample holder was also rotated at 30 rpm to improve the uniformity of material deposition. The deposition chamber pressure was held at $5x10^{-5}$ mbar for the duration of the coating process. Deposition was carried out in a sequentially manner using the coaters two evaporation sources. Haloperidol was first deposited at a rate of 0.1 Å s^{-1} to a total layer thickness 1 nm followed by CHCA at a rate of 1 Å s^{-1} to a total layer thickness of 700 nm. Deposition rates were monitored via Quartz crystal microbalance (QCM) sensors with the coater chamber. The QCM sensors were calibrated for each material by depositing films of at a nominal thickness of 100 nm, and then measuring the real thickness using CCI profilometry. The

measurements were used to calculate a correcting "tooling factor" (F_m) using equation 5.1.

$$F_m = F_i \frac{T_m}{T_i} \qquad (5.1)$$

Where is F_i is the initial tooling factor, T_m is the real film thickness and T_i is the nominal film thickness. The validity of the new tooling factors was confirmed by depositing new 100 nm films of each material and confirming the correct thicknesses were being applied using CCI profilometry.

Direct measurements of haloperidol density have not been reported but can be estimated from crystal structure data[253], providing a value of 1.30 g cm^{-3}. The density of CHCA was 1.44 g cm^{-3}, as measured in Chapter 3. This resulting in surface concentrations of CHCA and haloperidol were 534 nmol cm^{-2} and 346 pmol cm^{-2} respectively, resulting in an analyte to matrix molar ratio of 1544.

5.3.4 - Topographic imaging by Coherence Correlation Interferometry (CCI)

Topographic imaging of the sample was carried out using a Coherence Correlation Interferometry microscope (CCI HD, Taylor Hobson, UK). To acquire topographic data across the whole area imaged by UV-MALDI MSI while still maintain sufficient resolution in X, Y and Z dimensions to resolve ablation craters and local tissue features, it was necessary to CCI microscope in a tiled acquisition mode. To cover the whole tissue this required ~460 individual images to be acquired at each timepoint in the experiment, which with the default settings amounted to 8 hours of measurement time. As the sample had to be held in ambient conditions during CCI measurements it was therefore important to reduce the total imaging time to reduce any potential degradation of the tissue.

To this end a short optimisation experiment was carried out to, the results of which are summarised in Table 5.1 and Figure 5.2

Table 5.1. *Characteristics of the different CCI images options. Measurements were conducted on the same region of tissue keeping all other CCI parameters fixed (Table 5.2)*

Mode	Optimisation setting	Image size (Pixels)	Measurement time (s)	Relative measurement time	Void pixels
Default	N/A	2048 x 2048	73	100%	5%
XY	Resolution Optimised	1024 x 1024	56	77%	2%
	No Optimisation	1024 x 1024	29	40%	4%
	Speed Optimised	1024 x 1024	29	40%	4%
XYZ	Resolution Optimised	512 x 512	56	77%	1%
	No Optimisation	512 x 512	29	40%	3%
	Speed Optimised	512 x 512	15	21%	5%
Z	Resolution Optimised	256 x 256	29	40%	3%
	No Optimisation	256 x 256	29	40%	3%
	Speed Optimised	256 x 256	15	21%	5%

From the testing of the different imaging modes and optimisation settings (Table 5.1) it was found that measurement time could be significantly reduced compared to that obtained with the default settings, with the speed optimised XY and XYZ modes allowing for the fastest measurement times (21% relative to default). The percentage of void pixels in the images, points on the sample surface the microscope failed to measure, were relatively similar between the

different settings. For practical purposes the degree of missing points for all datasets was insignificant and could be easily corrected for via interpolation of the data. There was, however, a significant change in pixel number, and due to the imaged area remaining fixed, lateral resolution, occurred between the different modes. It was therefore necessary to understand the effect this could have on measurements of crater volume before optimised imaging parameters could be selected (Figure 5.2).

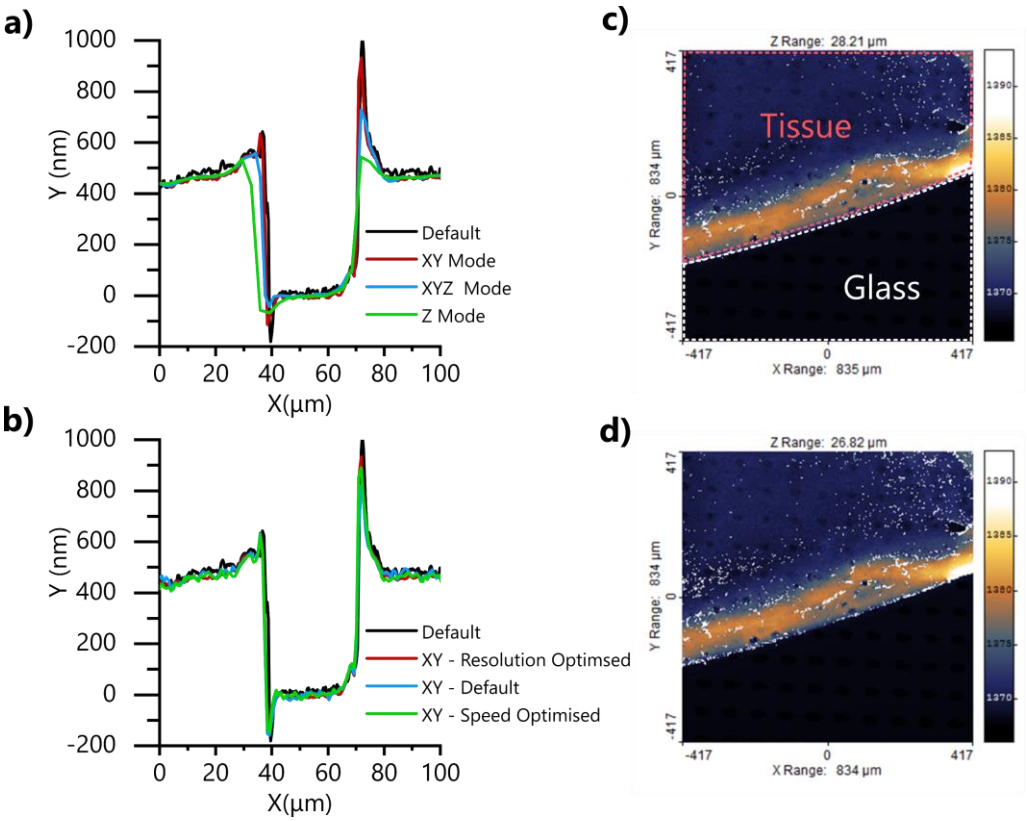


Figure 5.2. *Optimisation of CCI acquisition parameters. Cross sectional profile of an ablation crater in a CHCA thin film,* ***a)*** *acquired with four different microscope modes,* ***b)*** *in "XY" mode with the three different optimisation modes,* ***c)*** *example topography data in the default microscope mode and* ***d)*** *acquired with the speed optimised "XY" mode that was selected for the remainder of the study.*

Comparison of the different imaging modes reveal that the measured Z height is by and large the same between each mode, evidenced by the similar values for regions such as the base of the crater or the matrix film. Lateral resolution on the other hand significantly changes between modes, with the Z mode in particular showing a 20% increase in the crater width. This is to be expected as the XY, XYZ and Z modes use progressively larger degrees of pixel binning (4, 16 & 64), reducing the resolution of the final image. From this result it was determined that the Z imaging mode was not suitable for measuring ablation volumes due to the reduced lateral resolution causing significant overestimation of crater size. Height data remained consistent between the different optimisation settings in XY mode, but there was slight deviation for the XYZ mode. Inspection of the image data reveals that the primary cause of this was the increase in noise, resulting in spikes in the data.

Based on these results it was determined that XY mode with No Optimisation was the most suitable for the imaging of tissues. This is due to allowing a significantly shorter measurement times (40%) while still retaining sufficient spatial resolution to measure the ablation craters accurately. The finalised CCI imaging parameters are listed in Table 5.2.

***Table 5.2**. Optimised CCI imaging parameters used in this study.*

Imaging Mode	**Objective**	**Z stack range**	**Measurement surface settings**	**Lamp brightness**
XY, Speed Optimised	X 20	31 µm	Rough surface (peaks only), Filter 1, General, Single Surface	70

5.3.5 - UV-MALDI MSI optimisation

UV-MALDI MSI was conducted using a Synapt G2-Si HDMS (Waters, UK) fitted with a prototype "universal MALDI" (uMALDI) source. Compared to the commercial Synapt MALDI source, the uMALDI source has the ability to run in both continuous raster and spot mode acquisitions, has more accurate stage (minimum step = 2.5 µm), and the ability to vary the laser focusing lens position via adjustment of a linear translation stage. In addition to a variable neutral density filter to adjust laser pulse energy, the source also includes a fixed attenuator that can be inserted into the beam path, allowing access to a wide range of pulse energies. Further details on the uMALDI source are described elsewhere[97].

Optimisation of uMALDI source laser energy for tissue imaging was carried out on pork liver sections coated in 700 nm of CHCA (Figure 5.3). A pixel size of 120 µm was used to guarantee the instrument was operating in under-sampling spot mode, allowing comparability to the planned tissue imaging experiment. 5 mm x 5 mm regions of tissue were imaged at 8 different laser attenuation levels, with and without the fixed attenuator in place. Laser pulse energy data were collected post experiment using a photodiode energy sensor (PD10-C, Ophir, Germany) placed in the source region and firing the instrument laser for 1 minute at the same laser attenuation levels. The results are shown in Figure 5.3.

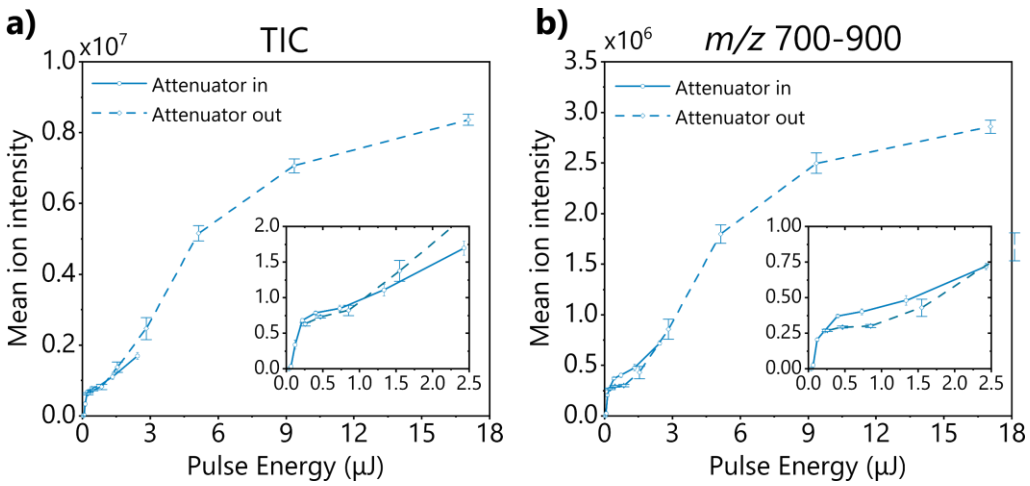


***Figure 5.3**. Optimisation of uMALDI laser energy. **a)** on tissue summed lipid region (m/z 700-900) intensities and **b)** on-tissue TIC intensity as a function of laser pulse energy. Data were acquired in positive polarity and spot mode acquisition, from a mouse brain section coated with 700 nm CHCA. Laser repetition rate was 2500 Hz. Data points connected by solid lines were acquired using the fixed attenuator and data points connected by dash lines without. Error bars show the combined uncertainty (k=2).*

The change in ion intensity with pulse energy show a double sigmoidal like response. The lower sigmoidal curve (Figure 5.3. inset figures) appears to be the classic ion intensity pulse energy curve while the upper curve was most likely dominated by the geometric increase in effective area of ablation for the Gaussian laser beam as the pulse energy increases. At the highest pulse energies this eventually flattens out as the energy density exceeds the matrix ablation threshold over the full area of the beam. From the plots is can be seen that the plateau region of the ionisation curve begins around 0.5 - 0.7 µJ, with this in mind a pulse energy of 0.7 µJ was chosen as the optimal for further experiments.

Optimisation of the laser focus was also important to understand the geometry of the resulting craters in the matrix (Figure 5.4). This was necessary to allow for the selection of an appropriate pixel size for the MSI experiment, to ensure the craters associated with MSI pixels could be individually resolved in the subsequent CCI profilometry.

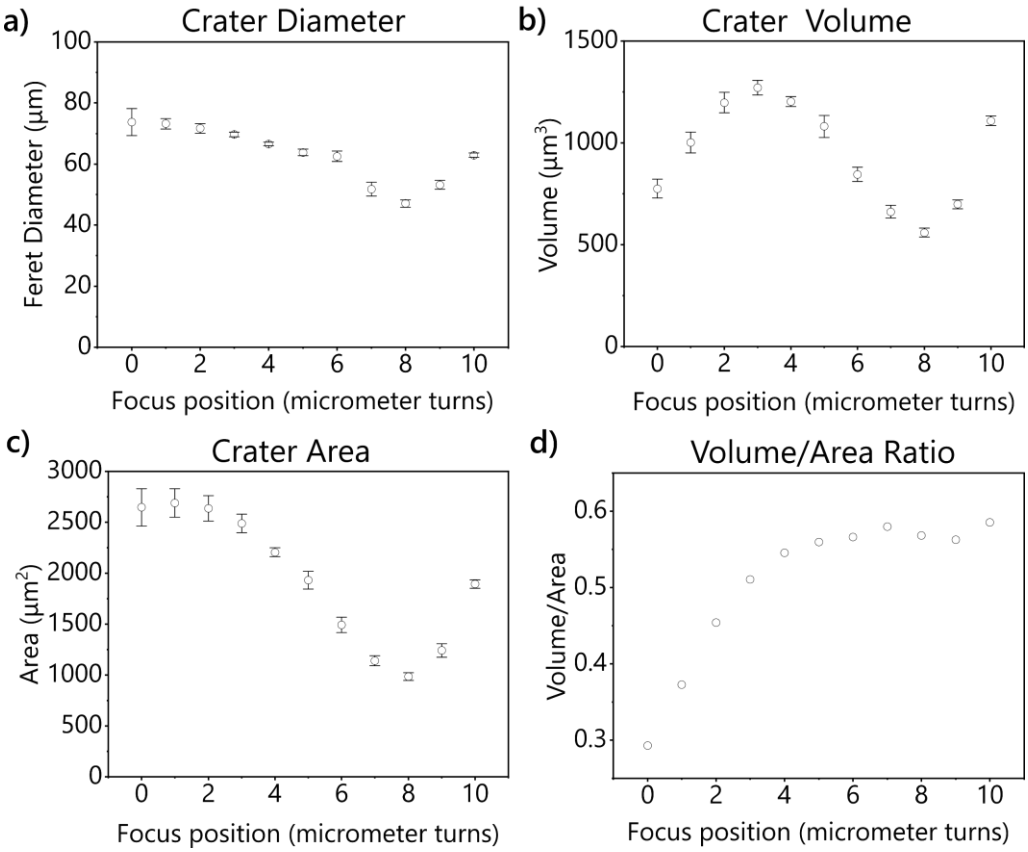


***Figure 5.4**. Optimisation of uMALDI laser focus using CCI optical profilometry of ablation craters in 700 nm CHCA thin film. **a)** crater diameter **b)** crater volume **c)** crater area **d)** ratio of crater volume to area. A laser pulse energy of 0.7 µJ and repetition rate of 2500 Hz was used. Focus position is taken as the number of full micrometer turns from the end of the linear translation stage where the lens is closest to the sample region of the source. Datapoints are the averaged measurement of 25 craters; error bars show the combined uncertainty (k=2).*

From the CCI measurements of crater characteristics at the different focal positions it was found that the smallest crater diameter (47 µm) and area (984 μm^2) was obtained at eight micrometer turns (Figure 5.4a & c), indicating the tightest focusing of the laser was achieved at this position. Crater volume (Figure 5.4b) also showed a minimum (559 μm^3) at this focus position. A decrease at focal positions 0-3 was also observed, despite crater diameter and area remaining constant. This was due to the changing energy profile of the laser spot as it became more defocused, resulting in craters with shallow edges, thus reducing overall crater volume.

To provide an estimate of sampling efficiency and identify the optimal focal position, the ratio of crater volume to the area was used (Figure 5.4d). A maximum ratio of 0.59 was obtained at focal position 10, but there was only marginal difference in values for focal points 5-10. For the tissue imaging experiments obtaining the best sampling of the film in the smallest crater size was paramount. With this in mind, focal position 8 was determined to be the optimum, as it resulted in the smallest craters while also maintaining a good volume-area ratio of 0.56. To ensure the change in laser focus had not caused any significant shift in optimal pulse energy, MS data were acquired from tissue at 0.7 µJ; TIC and base peak intensities were within 10% of those observed in the pulse energy optimisation experiments.

5.3.6 - UV-MALDI MSI

UV-MALDI MSI data were collected in positive polarity from *m/z* 50-1200, at 20 pixels/s. The instrument was operated in under-sampling spot mode with a pixel

size of 80 µm. Laser energy was set to 0.7 µJ with a repetition rate of 2500 Hz, resulting in ~88 laser pulses per pixel once the instruments inter-scan delay was factored in. The instruments laser focusing lens position was set at eight micrometer turns. Mass calibration of the instrument was performed before the imaging experiment across the same mass range using red phosphorus, with a residual RMS error of <1 ppm sets as the limit for an acceptable calibration.

5.3.6 - Data processing

5.3.6.1 - UV-MALDI MSI

UV-MALDI MSI data were converted from the Waters .raw file to .imzML via imzMLConverter[209]. MSI data were processed in SpectralAnalysis[210] and MATLAB (2018b, Mathworks, USA). Spectral data underwent an interpolation re-binning process (bin size = *m/z* 0.002) followed by a peak picking process based on intensity thresholding (>5 counts) of the mean spectrum from the tissue. Using the picked peak list, a reduced MSI dataset was generated, with peak intensities taken as the integrated peak area at full width half maximum (FWHM).

MSI data for haloperidol ion yield calculations were taken from the $[M+H]^+$ ion including all detected isotopic peaks; no $[M+Na]^+$ or $[M+K]^+$ ions were detected. Principal component analysis (PCA) was run on the MSI data as implemented in SpectralAnalysis. Two-Phase Graph Cuts segmentation was run in an in-house modified version of SpectralAnalysis, using the implementation described in Dexter et. al.[254].

5.3.6.2 - CCI profilometry

The collected CCI profilometry images were patched together in MATLAB using in-house scripts developed at NPL. The resulting combined topographic map had to be corrected for tilt and bowing distortions arising from the microscope stage. Due to the large size of the combined topographic datasets (~1 gigapixel) form correction was performed by fitting a 4th order polynomial surface to the non-tissue regions of x20 down binned data in MountainsMap (DigitalSurf, France). The fitted surface was then resized and subtracted from the original data in MATLAB. Additional visualisations of the topographic data were carried out in SPIP (v6.75, Image Metrology, Denmark)

5.3.6.3 - Image registration

Registration of the CCI microscopy data was carried out using an intensity based approach as implemented in the elastix registration toolbox[255]. An initial rigid transformation was applied to properly align the images and improve the final registration result, non-rigid registration was then carried out on the data using an affine transformation. Registration of CCI microscopy images to the MSI data were carried out in MATLAB using manual selection of control points (n = 50) and applying a local weighted mean fitting (LWMF) algorithm to account for local distortion arising from stitching artefacts in the CCI data.

5.3.7 - Calculation of number of ions generated and ion transmission

To convert detected ion intensity to absolute number ions generated at the sample the same process as used in Chapter 3 was applied, using equation 5.2.

$$number\ of\ ions\ generated = ion\ transmission * \frac{ion\ intensity}{single\ ion\ intensity} \quad (5.2)$$

Where single ion intensity was 49, as determined from electrospray experiments using Leucine Enkephalin, as outlined in Chapter 3. Ion transmission was calculated using the following equation 5.3

$$Ion\ transmission = T_{transfer} \times duty\ cycle \times T_{TOF} \qquad (5.3)$$

Unlike the ion yield study in Chapter 3, the instrument in these experiments was operating in "Sensitivity" and opposed to "Resolution" mode. This mode uses the same "V" ToF configuration (T_{TOF} = 0.43) but has a significantly higher transmission through the transfer optics ($T_{transfer}$ = 0.9). The duty cycle was calculated using the following equation 5.4

$$Duty\ Cycle = 0.225\sqrt{\frac{m/z_i}{m/z_{max}}} \qquad (5.4)$$

Where the m/z_{max} = 1200. m/z_i was set to *m/z* 376.14 for Haloperidol, as only the $[M+H]^+$ adduct was detected. For TIC data m/z_i was set to the midpoint of the studied mass range (*m/z* 625), this was done to minimise the error in Duty Cycle calculation across the mass range.

The final transmission efficiencies of the instrument for Haloperidol $[M+H]^+$ and TIC were calculated to be 4.88% and 6.28% respectively.

5.4 - Results

5.4.1 - Tissue topography

Dehydration of tissue prior to analysis is a typical step in sample preparation for MSI. Composition differences between tissue regions is suspected to result in varying tissue thickness upon drying, which is known have an effect on the resulting ionisation efficiency[251,252]. Additionally, recent trends in UV-MALDI MSI towards high spatial resolution imaging necessitates near diffraction limited

laser spot sizes, where the focal depth approaches that of the tissue thickness[256]. As the initial topography of the tissue section was required as starting point for further measurements, this provided an opportunity to characterise tissue thickness changes between different tissue regions. The topographic height map of the brain section after dehydration, but prior to matrix coating, is shown in Figure 5.5.

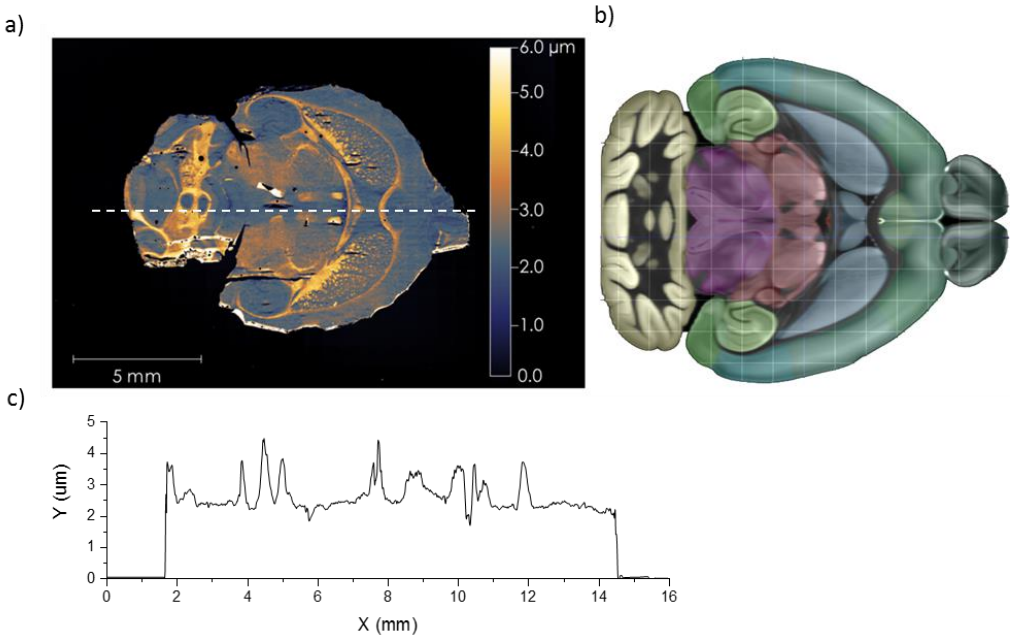


Figure 5.5. a) *Height map of dehydrated mouse brain tissue section obtained by CCI microscopy.* ***b)*** *Corresponding brain region from Allen Mouse Brain Atlas.* ***c)*** *cross section height profile corresponding to the white dashed line in* ***a).***

CCI microscopy of the brain tissue section revealed significant reduction in tissue thickness occurs upon dehydration, with the tissue section ranging from 2.0– 4.5 µm in thickness (Figure 5.5a). As the original frozen tissue was sectioned at a nominal thickness of 12 µm, the dehydration step induced a reduction in tissue thickness to between 17- 38% of the original frozen thickness. The

topographic data also revealed significant variation in the thickness of the tissue, with the white matter (WM) regions of the brain showing a thickness on average twice that of the grey matter (GM) regions (Figure 5.5a & c). The water content of mouse brain regions has been previously measured by gravimetric and Magnetic resonance imaging (MRI) methods[257,258],with the approximate water content of GM and WM regions reported as 80-85% and 75-80% respectively. Assuming complete remove of water during the dehydration of the 12 µm thick tissue section, this would result in tissue thicknesses of GM and WM regions of 1.8-2.4 µm and 2.4-3.0 µm respectively. For the GM regions, water loss was sufficient to explain the observed tissue thickness (2-2.5 µm), but tissue thicknesses of WM regions (2.5-4.5 µm) could not be fully explained by water loss alone, therefore compositional or structural differences must be having an effect. There are significant compositional differences between GM and WM, GM consists of primarily of various cellular bodies, dendrites and axon terminals, while WM is primarily composed of densely packed myelinated axons. This difference in biological composition may explain the observed difference in tissue thickness, with the relative density and/or structural properties of the myelinated axons on the WM likely inhibiting collapse of the tissue upon dehydration.

This variation in height could have some important implication for UV-MALDI MSI at very small laser spot sizes. In Gaussian optics, the Rayleigh length (z_R), defined as the distance from the focal point (ω_0) at which the beam area doubles in size, is governed by the equation 5.5.

$$z_R = \frac{\pi \omega_0^2}{\lambda} \qquad (5.5)$$

Where ω_0 is the radius of the beam at the focal point, and λ is the wavelength of the laser, which in UV-MALDI MSI is typically 337 nm or 355 nm. For high resolution UV-MALDI MSI, where the focal spot can be of the order of 1-5 μm in diameter, the Rayleigh length is approximately 2-55 μm, the lower bound of which is within the range of height variation observed here. Due to the ion signal obtained in UV-MALDI MSI at a fixed wavelength being proportional to the laser fluence, a doubling of the laser spot area will halve the laser fluence at the sample surface, altering the resulting ion signal; evidence of this effect has recently been reported by Kompauer et al.[259]

Using topographic data to preform automatic focal correction of the laser could be used to mitigate this, and has been demonstrated for samples with large topographic variation, as well as mouse brain sections[259]. Alternatively, as the variation in thickness between tissue regions would be relative to the original section thickness, one could simply make use of thinner sections to reduce the difference to a more acceptable level, although this may complicate sample preparation due to the increasing fragility of thinner sections.

5.4.2 - Matrix application homogeneity

Difference in matrix crystallisation between different tissue region have been previous reported in mouse brain, and hypothesised as a potential source of the variation in the ionisation efficiency between different tissue micro-environments[68]. The collected CCI microscopy datasets for the sample pre and post matrix coating provides an opportunity to explore some of these features,

allowing the thickness of the deposited matrix film to be quantified across the whole tissue section. This can be achieved by registration of the two datasets, followed by a simple subtraction of the pre-coating topography from the post-coated topography; the resulting height difference is due to the deposition of the matrix, and so corresponds to the thickness of the matrix layer (Figure 5.6).

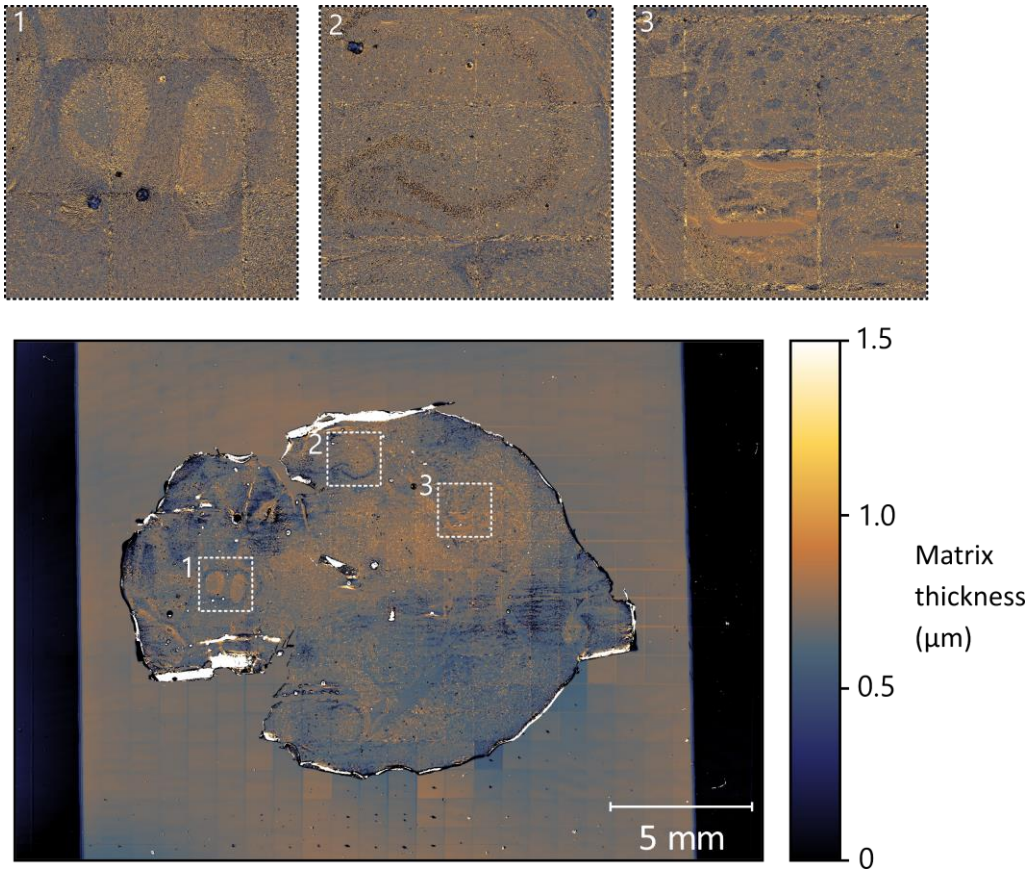


Figure 5.6. *Map of the thickness of deposited matrix over the sample. Inset images show tissue region specific changes in matrix thickness and morphology.*

Average matrix thickness across the substrate was 696 ± 27 nm, confirming the accuracy and uniformity of the matrix deposition. On-tissue matrix thickness was 663 ± 137 nm, which was slightly lower to that observed on the substrate, but with a greater degree of variation. Inspection of the matrix thickness map

(Figure 5.6) reveals small levels of inhomogeneity that correlate to structural features of the underlying tissue. Notable changes in matrix thickness of approximately 50-100 nm, seeming a result of different crystallisation behaviours, can be seen for tissue features such as the granular cell layers of cornu ammonis, as well as white matter regions such as the arbour vitae and fibre bundles in the caudoputamen. This differing matrix crystallisation behaviours between GM and WM has been noted previously for sublimation deposited 2,5-DHB[68] and sputtered Ag metal films[260], and is likely due to differences in tissue surface composition resulting variation in the number and nature of nucleation sites for crystal growth.

Some larger regions also appeared to have thinner matrix layer, but this was quite probably the result of errors in form correction and tiling issues of the height data, as variation in the matrix film and glass background were also evident.

5.4.3 - UV-MALDI MSI results

The coated tissue sample was imaged at 80 µm pixel sizes in spot mode, so as to ensure the UV-MALDI MSI was operating in under-sampling mode, allowing the removal of material at each pixel to be measured in subsequent CCI imaging. A sample of the collected ion images are shown in Figure 5.7.

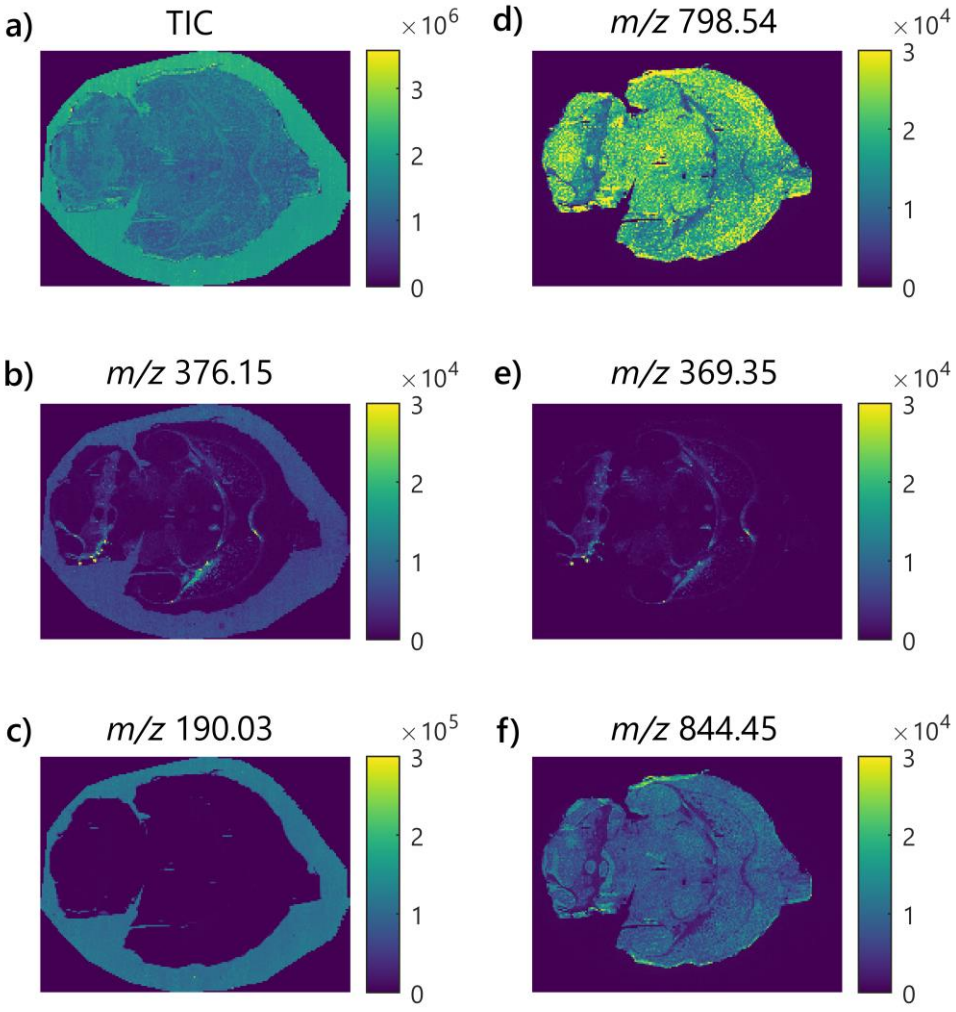


Figure 5.7. *UV-MALDI MSI images of the mouse brain sample.* ***a)*** *Total ion current (TIC)* ***b)*** *Haloperidol* $[M+H]^+$ ***c)*** *CHCA* $[M+H]^+$ ***d)*** *PC (34:1)* $[M+K]^+$ ***e)*** *Cholesterol* $[M-OH]^+$ ***f)*** *PC (38:6)* $[M+K]^+$.

The TIC image confirms the highly uniform deposition of the matrix, with minimal variation in intensity across the substrate region (Figure 5.7a). On the tissue there was some small variation in the TIC with a slight enhancement in ion signals from WM regions, compared to the rest of the tissue. Additionally, compared to the substrate there was a notable decrease in TIC on the tissue. These features are in agreement with the observed variation in ionisation

threshold between substrate and tissue, and between tissue regions, reported by Steven et al.[67] and variation in laser spot size effect reported by Weigelmann et al.[68]. The enhancement of TIC in WM was somewhat counter-intuitive as the matrix layer thickness was apparently smaller in some of these regions (Figure 5.6). Additionally, the global lowering of TIC could not be explained by the matrix thickness alone, suggesting suppression of ion formation, or relative increase in proportion of ions that were not detected by the mass spectrometry, was occurring.

With the exception fragment products, haloperidol was only detected as $[M+H]^+$, agreeing the UV-MALDI MS results for this analyte from Chapters 1 and 2. Given the compounds uniform coverage across the sample, the haloperidol $[M+H]^+$ image clearly evidences a suppression effect, in particular it can be seen that haloperidol $[M+H]^+$ severely supressed in most of the tissue regions of the brain (Figure 5.7b). A notable exception to these was in the WM regions, where haloperidol $[M+H]^+$ appears a similar intensity, or in some cases enhanced, relative to the substrate. Tissue region specific suppression has been previously noted in the literature[109,143,144]. In particular the differing suppression seen in WM and GM regions of brain was reported in both UV-MALDI and DESI by Taylor et al. who uniformly coated mouse brain sections in olanzapine[144], confirming that the effect was not a feature specific to haloperidol.

A particularly interesting feature of the observed haloperidol $[M+H]^+$ distribution was the striking similarity to the tissue thickness data (Figure 5.5), with the thinner regions of the tissue corresponding to high suppression of

haloperidol. To determine if there was a relationship the thickness of the tissue at each pixel location was determined and compared to the TIC and haloperidol $[M+H]^+$ ion images (Figure 5.8).

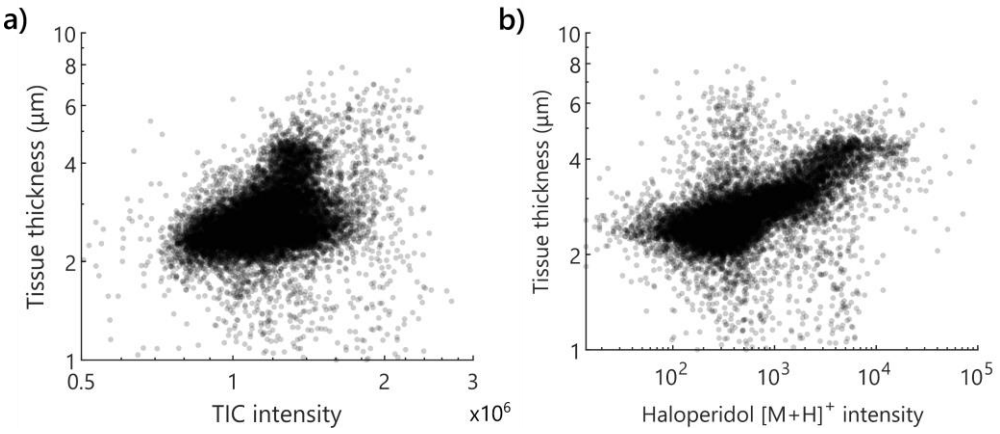


Figure 5.8. *Detected ion intensity for* ***a)*** *TIC and* ***b)*** *Haloperidol* $[M+H]^+$ *as a function of tissue thickness at each on-tissue pixel location in the acquires MSI data.*

The correlation of TIC to tissue thickness suggests that a there was only a very weak positive relationship between tissue thickness and TIC, as the scatter of the data was very large (Figure 5.8a). Comparison of Haloperidol $[M+H]^+$ intensity to tissue thickness revealed a stronger positive relationship (Figure 5.8b), but as before the scatter of the data was large. Attempts to fit the either the TIC or Haloperidol $[M+H]^+$ intensity to the tissue thickness were not successful. To explore if the tissue thickness measurements could be used to improve MSI data, ion images for the TIC and Haloperidol $[M+H]^+$ were normalised to tissue thickness (Figure 5.9).

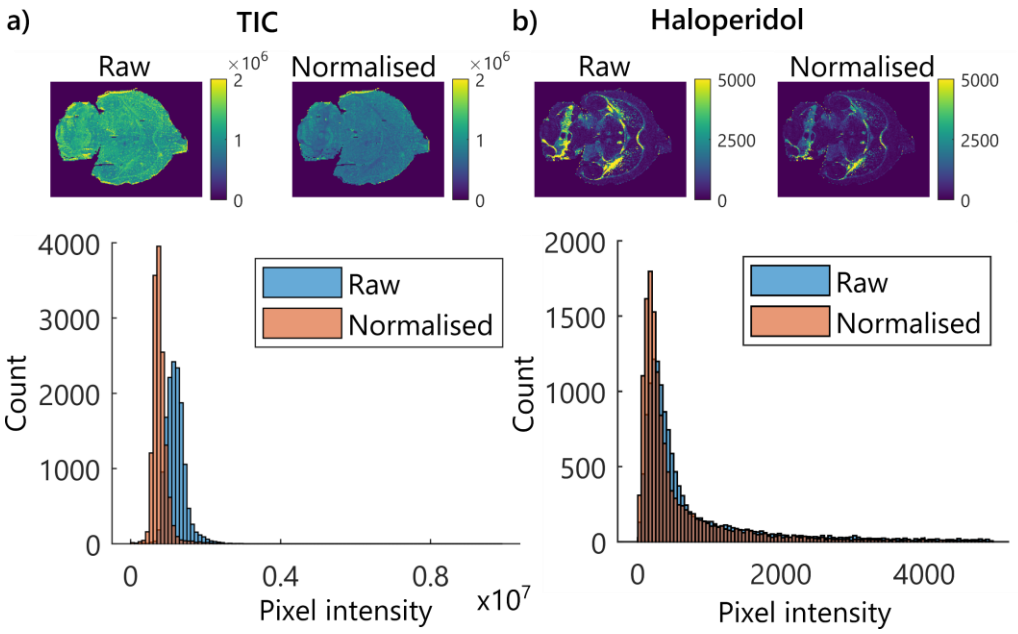


Figure 5.9. *Effect of tissue thickness on ion signal in MALDI MSI.* ***a)*** *Distribution of TIC pixel intensities before and after normalisation to tissue thickness at each pixel location* ***b)*** *Distribution of Haloperidol [M+H]⁺ pixel intensities before and after normalisation to tissue thickness at each pixel location . All data comes from the on-tissue pixels.*

Comparison of the TIC and Haloperidol [M+H]⁺ images before and after normalisation to tissue thickness appears to show a minor decrease in heterogeneity across the tissue (Figure 5.9). This was confirmed by comparing histograms of the corresponding pixel intensities (Figure 5.9), revealing a tighter spread of pixel intensities after normalisation was applied. The normalisation results suggest weak positive relationship between tissue thickness and ion intensity, either due to thicker tissue regions exhibiting weaker ion suppression, containing more material, or higher abundances of chemical species that were detectable in the mass range used here (*m/z* 50-1200).

Previous studies have observed that ion intensity increases with decreasing tissue thickness[251,252,261,262] although the results here appear to contradict this finding, showing a small increase with tissue thickness. A probable explanation for this discrepancy is that previous reports of the tissue thickness effect were found using high vacuum MALDI-ToF instruments, where it has been linked to increased surface charging in thicker tissue samples interfering with the high voltage extraction potential applied between the sample and the extraction ion optics. The intermediate pressure Qq-ToF instrument used here (Synapt G2-Si HDMS) used here does not require a large biasing potential across the sample, and so is not susceptible to the surface charging effects observed in ToF instruments. Linked to these different modes of operation, the high extraction voltage of ToF instruments necessitate the sample to be placed on conductive substrates, typically metal plates or ITO slides, whereas this is not a requirement of the Synapt G2-Si HDMS, where standard non-conducting microscope slides are routinely used. It is known from UV-MALDI MS studies that ionisation can be enhanced near the surface of conductive materials[141], the observed discrepancy may also therefore be related to the absence here of any conductive surface to enhance ionisation in the thinner parts of the tissue.

5.4.4 - Effects of tissue region on ion intensity

To understand how different region within the heterogeneous brain tissue can affect ionisation it is useful to identify the image pixels associated with them. Here a previously reported 2-phase graph cuts segmentation algorithm [254] was used to segment the MSI data into 10 clusters of chemically similar pixels. This number of clusters was chosen as it allowed for division of the MSI brain data

into readily identifiable biological structures without overly segmenting the data and complicating further analysis. The segmentation results, as well as the distribution of pixel intensity values for the TIC and Haloperidol $[M+H]^+$ images within the segmented tissue regions are shown in Figures 10 & 11.

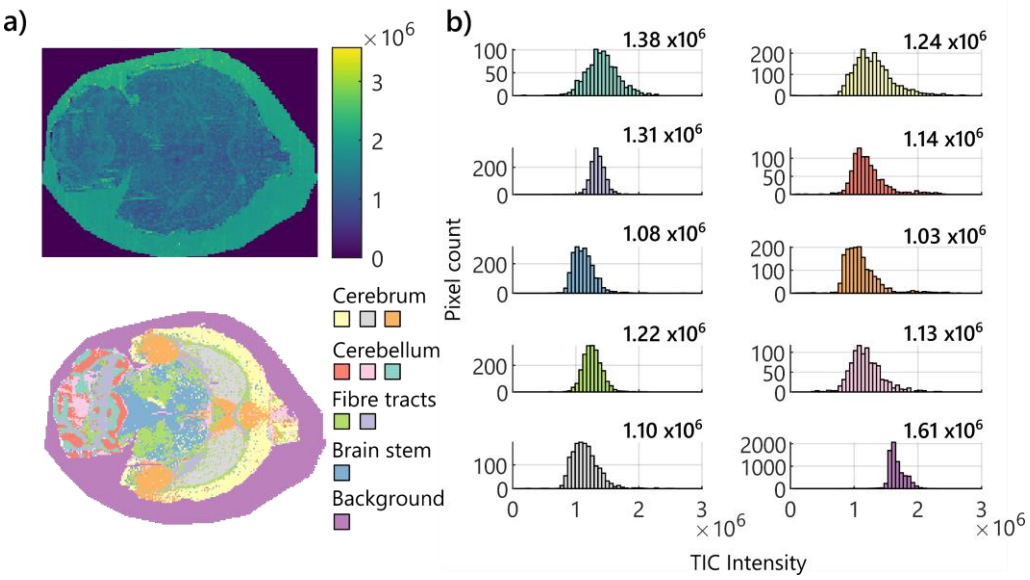


Figure 5.10. a) *TIC ion image and 2-Phase Graph cuts clustering segmentation of the MALDI MSI data. Colour coded clusters are grouped by the anatomical brain regions they represent, as identified from comparison to Allen Mouse Brain Atlas.* ***b)*** *Corresponding distributions of pixel TIC intensities within the different clusters. Median intensity values for each region are also reported.*

Segmentation results for the MSI data enable clear delineation of the white matter (light purple and green) and grey matter (grey, yellow, orange, red, pink, light blue and dark blue) regions of the brain, as well as segmenting the tissue from the substrate (purple) (Figure 5.10a). Various biological structures were also evident, such as the molecular (light blue) and granular layers (red) of the cerebellum, the brain stem (dark blue), the isocortex (yellow), caudoputamen

(grey) and various fibre tract regions (green and light purple); the hippocampus, lateral septal complex and infralimbic area of the isocortex were clustered together (orange).

The distribution of TIC pixel intensities within each cluster were broadly similar for the different tissue regions, with median values ranging from 1.03 - 1.38 x 10^6, and about 14 - 36% lower that than of the substrate pixels (Figure 5.10b). The WM fibre tract regions, as well as the isocortex and molecular layer of the cerebellum all evidenced a somewhat elevated TIC intensities compared to the rest of the tissue.

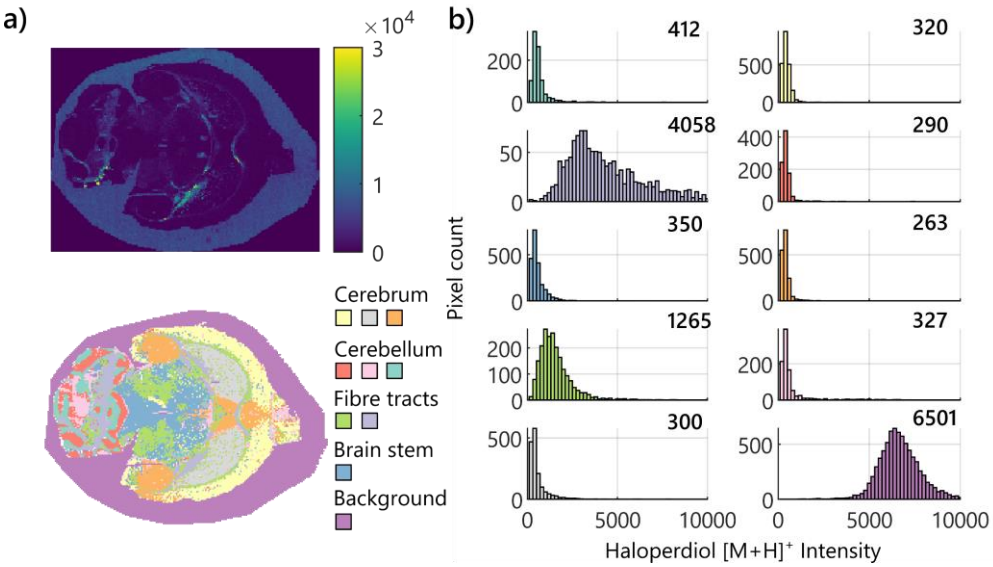


Figure 5.11. a) *Graph-cuts clustering segmentation of the MALDI MSI data. Colour coded clusters are group by the anatomical brain regions they represent, as identified from Allen Mouse Brain Atlas data.* ***b)*** *Corresponding distributions of pixel intensities for Haloperidol* $[M+H]^+$ *within the different clusters. Median intensity values for each region are also reported.*

Compared to the TIC results, variation in cluster pixel intesitities were much more stark for Haloperidol $[M+H]^+$ (Figure 5.11b). Median values in the tissue regions ranged from 263 – 4058, compare to 6501 on the background substrate. This represent a signficant level of ion supression, with Haloperidol [M+H]+ intensites only 4-6% of that seen in the substrate background, with the notable exception of the WM fibre tract regions, where median values were 18-64%.

The concept of tissue extinction coefficient (TEC) for was proposed by Hamm et al. to quatifiy the extent of ion supression occuring for a given analyte in tissue in UV-MALDI MSI[143]. Where the TEC was taken as the ratio of the average analyte ion intensities between tissue and reference regions of the background substrate. Two TEC values for the drug propranolol in brain tissue (0.07 and 0.3) were reported in that work, with the lower value being identical to average TEC value obtained for the grey matter regions here (0.07), while the larger value was about double the whole brain TEC found here (0.18) . A whole brain TEC value of 0.06 was reported by Taylor et al for olanzapine[144], although they noted signifanctly higher TEC for white matter regions (0.21), which was lower than than observed here (0.56).

In its current form TEC makes use of average ion intensties to determined ratio between tissue background, making it highly succeptable to the influence of outlier pixels. Given the notable skewness of the data distribution towards higher pixel intensities (Figure 5.10b & 11b), the median is a more appropriate statisical measure to describe the central tendancy the data. For the brain tissue as a whole the median TEC was 0.063, with WM regions showing a much higher

median TEC (0.293) than GM regions (0.049). The large discrepancies between TEC values obtained here using median compared average pixel intensities, sometimes differing by up to 50%, highlights the highly variable nature of ionisation in UV-MALDI-MSI of tissues, and suggests that the method for calculating TECs should be modifed in future to better account for outliers and skewness in MSI data.

5.4.5 - Principal Component Analysis (PCA) of UV-MALDI MSI data

To understand some of the differences in molecular composition between the different region of the tissue PCA was performed on the data (Figure 5.12). To minimise interference from haloperidol species, the mass range of the data was restricted to *m/z* 400-1200, removing the haloperidol molecular ions and fragments.

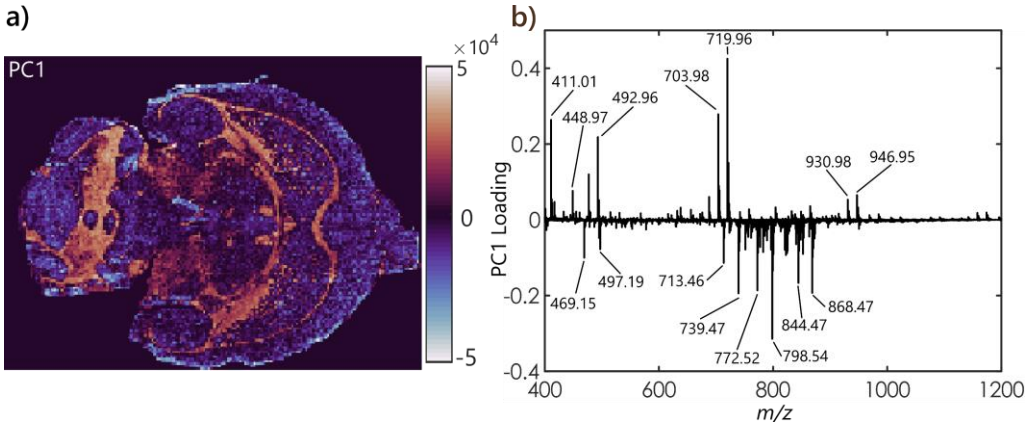


Figure 5.12. *PCA of the acquired brain UV-MALDI MSI data.* ***a)*** *PC1 image of the collected brain data.* ***b)*** *Corresponding PC1 spectral loadings.*

The first PC image clearly separated out the WM and GM of the tissue (Figure 5.12a). The corresponding loadings plot showed the presence of numerous peaks that were driving the variation that distinguished these regions. Peaks at

m/z 411.01, 448.97, 492.96, 703.98 and 719.96 were highly loaded towards WM regions where haloperidol ion intensities were preserved (Figure 5.12b).

Table 5.3. *Tentative assignments of highly loaded (± 0.05) peaks from PC1. Assignments were made via matching to the Human Metabolome Database (HMDB) and theoretical CHCA cluster adduct values obtained from Ingrell et al.*[263].

	Theo. *m/z*	**Meas. *m/z***	**Assignment**	**Adduct**	**δ (ppm)**
Positive loading	411.010	411.012	Inosine diphosphate	$[M-OH]^+$	5
	448.973	448.972	Uridine 5'-diphosphate	$[M+2Na-H]^+$	3
	476.987	476.988	CHCA cluster	$[2M-2H+2K+Na]^+$	2
	492.961	492.960	CHCA cluster	$[2M-2H+3K]^+$	2
	688.011	688.014	CHCA cluster	$[3M-3H+2K+2Na]^+$	4
	703.985	703.982	CHCA cluster	$[3M-3H+3K+Na]^+$	5
	719.959	719.956	CHCA cluster	$[3M-3H+4K]^+$	5
	930.984	930.980	CHCA cluster	$[4M-4H+4K+Na]^+$	4
	946.958	946.956	CHCA cluster	$[4M-4H+5K]^+$	2
Negative loading	469.152	469.152	cPA(16:0)	$[M+2K-H]^+$	0
	497.186	497.186	Citric Acid 1,2-Diethyl Ester	$[2M+H]^+$	1
	713.452	713.456	PA(34:1)	$[M+K]^+$	6
	739.467	739.466	PA(36:2)	$[M+K]^+$	2
	751.416	751.412	PGP(26:0)	$[M+CH3OH+H]^+$	5
	772.523	772.520	PE(18:2)	$[M+2Na-H]^+$	4
	777.423	777.420	PA(36:2)	$[M+2K-H]^+$	4
	782.567	782.566	PC(34:1)	$[M+Na]^+$	1
	789.350	789.360	Dihydrozeatin glucoside	$[2M+Na]^+$	12
	796.466	796.468	PC(31:0)	$[M+2K-H]^+$	3
	798.541	798.540	PC(34:1)	$[M+K]^+$	1
	820.523	820.518	PE(22:6)	$[M+2Na-H]^+$	6
	822.481	822.482	PE(36:1)	$[M+2K-H]^+$	1
	824.463	824.462	PE(40:9)	$[M+K]^+$	1
	840.434	840.438	PE-NMe(37:6)	$[M+2K-H]^+$	4
	844.466	844.470	PC(35:4)	$[M+2K-H]^+$	5
	848.559	848.560	PE-NMe2(44:11)	$[M+H-H2O]^+$	1
	852.471	852.470	PE(40:6)	$[M+2K-H]^+$	1
	868.466	868.468	PE-NMe2(38:6)	$[M+2K-H]^+$	3

Tentative assignment of these peaks (Table 5.3) suggests the majority are alkali metal adducts of CHCA clusters[263], with high degrees of potassium adduction. Notably these matrix peaks were not observed off tissue, where matrix clusters were species predominately sodiated. The most highly loaded peaks for GM regions, where high haloperidol suppression occurred, were primarily phospholipids of various classes, typically PA, PE, and PC lipids.

The PCA results indicate that the variation in the haloperidol ionisation was linked to the amount of endogenous compounds present in the matrix layer, suggesting an extraction effect, as well as the influence of analyte-analyte ion suppression. Lower levels of endogenous compound extraction into the matrix layer in WM regions, likely linked to structural or chemical properties of the tissue, may explain the lower ion suppression seen in those regions, although the significant difference in observed matrix peaks seen on the glass substrate and the WM tissue regions suggested some level analyte migration must be occurring.

The tissue region specific distribution of CHCA clusters with high levels of cation adduction, a feature associated here with preservation of haloperidol ion intensity, may be correlated to the effects observed by Weigelmann et al.[68], who noted that the presence of high salt levels in the sample as a potential cause for variation in matrix ionisation and differing crystallisation between white and grey matter.

5.4.6 - Material removal in UV-MALDI MSI

It has been suggested[68] that shifts in ablation mechanisms may be the reason behind observed increases in ionisation threshold on tissue[67], and the variation of ionisation between different tissue regions in UV-MALDI MSI[68]. The ability to measure the volume of removed material per pixel in a UV-MALDI MSI experiment of heterogenous tissue would therefore offer a powerful tool to investigate if such an effect was indeed occurring. Due to the co-registered topographic data collected from the sample, before and after UV-MALDI MSI analysis, this can be achieved in a facile manner by comparing the difference between the two surfaces, allowing the volume of removed material at each pixel location can be determined. The results are of this are shown in Figure 5.13. It should be noted that the regions of high intensity seen around the edge of the tissue in the volume map are the result of measurement errors in the CCI data associated with the steep topography at the tissue edge and do not represent real values for material removal.

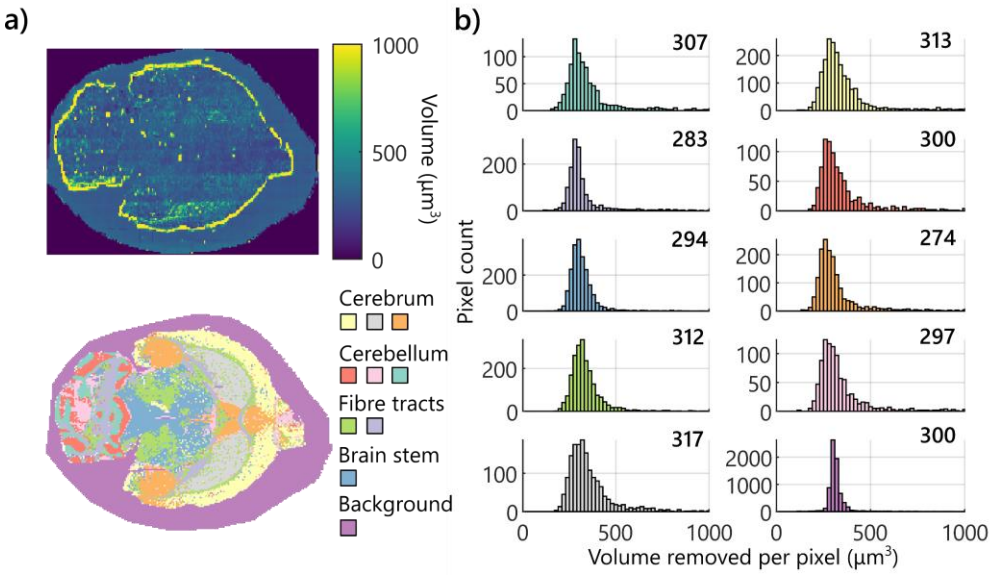


Figure 5.13. a) *Volume of removed material per pixel image and tissue regions segmented from the MSI data* ***b)*** *corresponding distributions Volume removed per pixel within the different tissue regions. Median Volume removed values for each region are also reported.*

Across the tissue as a whole, volumes of removed material per pixel were almost identical, at around 300 μm^3, to those observed on the glass substrate background (Figure 5.13a), with the median tissue value 99.6% that from the substrate.

Variation in median volumes for the different tissue regions was relatively small, ranging from 91-106% of the substrate background. A notable broadening of the distribution of removed volume per pixel was observed on tissue, signifying greater variation in crater volumes (Figure 5.13b). This may be due to differing mechanical effects of the underlying tissue, in particular the pixel volume values above those observed on the substrate suggesting that ablation of the tissue may be occurring. The suggestion of tissue induced changes to ablation

mechanisms was proposed by Wiegelmann et al., who attributed changes in the spot size effect between GM and WM to shifts in material ejection behaviours arising from the different observed matrix morphologies found between the tissue types[68]. Ultimately the volume data here showed little evidence for changes in material ejection, as could be determined by measured by total volume of material ejection.

5.4.7 - Ion yield in UV-MALDI MSI of tissue

As the volume of removed material contributing to each pixel has been determined, it is possible to calculate the ion yield at each pixel, using the same process as outlined in Chapter 3. This data were collected using a different instrument from the one used in Chapter 3, but as they were the same model (Synapt G2-Si HDMS) they should be comparable, after compensation for the somewhat different instrument settings used. The transmission efficiency of the instrument for Haloperidol $[M+H]^+$ (*m/z* 376.14) and TIC were calculated to be 4.88% and 6.28% respectively.

To this authors knowledge this is the first example of quantitative measurements of ion yield from tissue in UV-MALDI MS, and the first ion yield UV-MALDI MS imaging data. The resulting ion yield images and distribution of pixel intensity values for the TIC and Haloperidol $[M+H]^+$ images within the previously segmented tissue regions are shown in Figures 14 & 15.

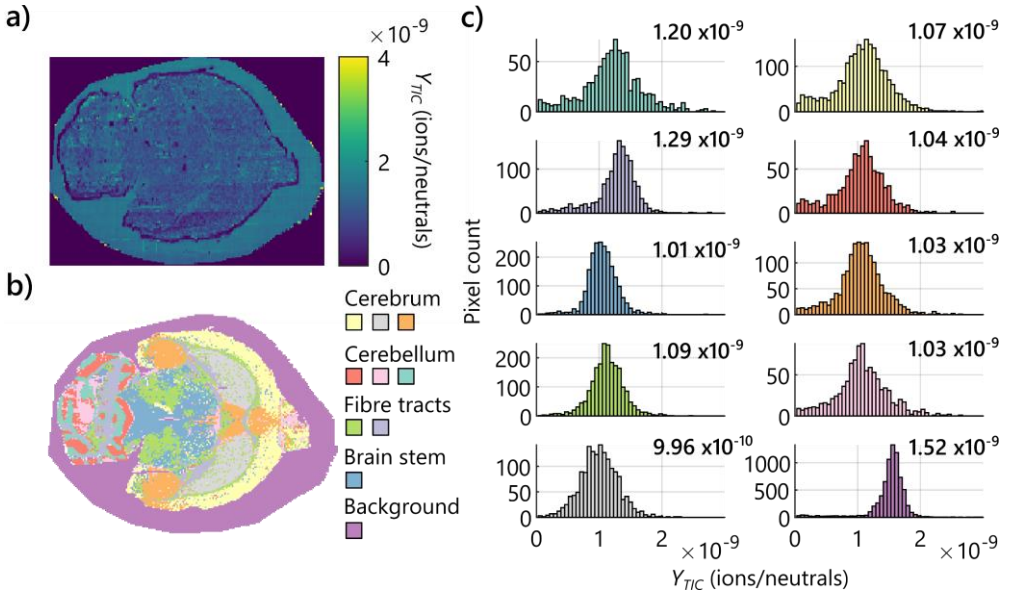


Figure 5.14. a) *Total ion yield (Y_{TIC}) image of the tissue* ***b)*** *tissue regions segmented from the MSI data* ***v)*** *corresponding distribution of Y_{TIC} pixel values within the different tissue regions. Median Y_{TIC} values for each region are also reported.*

Total ion yields (Y_{TIC}) were of the order of 10^{-9} with the median Y_{TIC} on tissue was around 61-82% of that found on the glass substrate (Figure 5.14b). Y_{TIC} distributions varied somewhat between tissue regions, with median Y_{TIC} for GM and WM regions 1.17×10^{-9} and 1.03×10^{-9} respectively. Reflecting the patterns previously observed in the TIC data (Figure 5.10), the WM fibre tract, isocortex and molecular layer of the cerebellum showed greater ion yields compared to the rest of the tissue. The Y_{TIC} results suggests the efficiency of ion generation can be affected by the underlying tissue type, although this could also be a result of the fixed amount of charge generated by the matrix being distributed to onto species not detected in the mass range used here (e.g. proteins), rather than a reduction in ionisation efficiency.

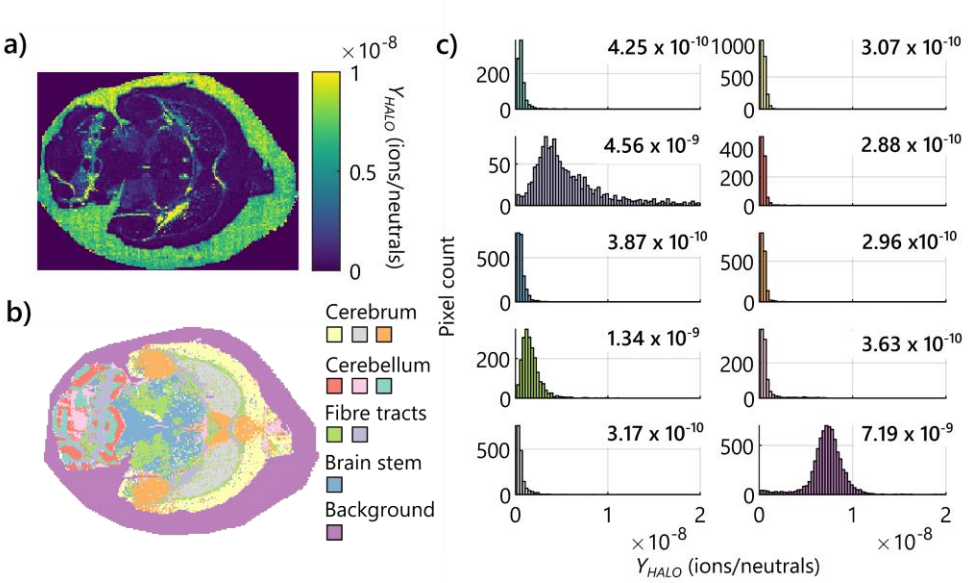


Figure 5.15. a) *Haloperidol $[M+H]^+$ ion yield (Y_{HALO}) image of the tissue* ***b)*** *tissue regions segmented from the MSI data* ***c)*** *corresponding distribution of Y_{HALO} pixel values within the different tissue regions. Median Y_{HALO} values for each region are also reported.*

The observed ion yields for Haloperidol $[M+H]^+$(Y_{HALO}) were of the order of 10^{-10} - 10^{-9} (Figure 5.15a), lower than those that observed for Olanzapine in Chapter 3 (10^{-9} - 10^{-6}), and in the bottom range of reported values for analytes in UV-MALDI MS[170]. These low values are not surprising given the high degree of ion suppression seen here, and the fact previous ion yield measurements have all being conducted with simple analyte-matrix systems, and never on tissue.

Trends seen in the Y_{HALO} data between the different tissue regions (Figure 5.15) reflect those seen in the original ion intensity data. On tissue median Y_{HALO} values were 4-62% that of the background substrate, with WM regions showing significantly less suppression (19-64%) than the GM, showing similar degrees of suppression to the original ion intensity data.

As a whole, the ion yield data show that the picture is the same as can be seen from ion intensity data. This is due to the relatively minor change in volume of material ejection noted previously (Figure 5.13) and suggests that to a relatively high degree of accuracy the characterisation of ion suppression can be realised using the original ion intensity data.

5.5 - Conclusions

Using optical profilometry and precisely controlled deposition of matrix and haloperidol internal standard, quantitative measurement of the effects of tissue microenvironment on desorption and ionisation in UV-MALDI MSI of mouse brain are reported. These data represent the first measurements of material ejection and absolute ion yield from tissue in UV-MALDI MSI.

Initial profilometry of the brain sample revealed significant variations in tissue thickness can occur during the tissue dehydration step, highlighting a potential a concern for UV-MALDI MSI using highly focused laser beams (<5 μm).

In line with previous reports[143,144], significant suppression of the haloperidol internal standard, by up to two orders of magnitude, was observed. Additionally, the degree of suppression varied significantly between the tissue types, with GM regions found to provide the highest degree of ion suppression and WM the least. Analysis of the MSI data suggests that the suppression of the haloperidol was linked to the extraction of endogenous molecules from the tissue and the level of salts, which in turn was likely governed by structural and chemical properties of the underlying tissue. A weak influence of local tissue thickness on total ion signal was also observed, suggesting this may be a useful normalisation

step to apply when such measurements are available. Additionally, analysis of regional ion suppression in the context of previously reported TECs suggests that the method for calculating this correction factor in quantitative UV-MALDI MSI studies may have to be amended, to better account for the statistical distributions of ion intensities within different tissue regions.

Material ejection was found to be reasonably stable across different tissue regions, and between tissue and the substrate, with ablated volumes ranging from 274 - 317 μm^3. This relatively small variation suggests that changes in material ejection mechanisms, previously proposed as the cause for various tissue related UV-MALDI MSI phenomena[67,68], were likely not occurring.

Ion yields for Haloperidol ranged from 10^{-11}-10^{-10} on tissue and were 10^{-9} on the substrate, whereas yield for all detected ions was of the order of 10^{-10}. As a result of the minimal variation in material ejection, ion yields generally reflected the trends observed in the ion intensity data. The very low yields observed here explain the significant enhancements seen for various UV-MALDI MSI post-ionisation strategies reported in recent years[15,16,264], and suggests that there is still plenty of room for further improvement.

The work here was restricted to a single matrix and tissue type, and one set of laser and sampling conditions. Considering the findings outlined here and in Chapter 3, it would be informative to extend the measurements here to multiple matrices and different laser, sampling conditions and mass ranges, as well as different tissue types. Incorporating further tissue characterisation, such as cell density[265], staining for selected tissue components or elemental distributions

would also aid in developing a more complete understanding of the factors influencing tissue section morphology, matrix crystallisation and ion suppression.

Finally, the analytical methods applied here to measure material ejection and ion yield can be easily applied to other MSI modalities. This would provide the opportunity to compare the efficiency of different modes of ionisation, and potentially offer insight into routes towards improving important MSI characteristics such as sensitivity, limits of detection and spatial resolution.

Chapter 6 – Future Work

In Chapter 2 the influence of two common UV-MALDI MS sample preparation parameters, analyte-matrix molar ratio and use of TFA, were investigated for a series of matrices and analytes. The findings revealed highly complex, and matrix and/or analyte specific, relationships between of analyte-matrix molar ratios on analyte ion intensities and identified the unsuitably of TFA for use in untargeted UV-MALDI MS analyses, particularly for imaging experiments. As noted in the Chapter 2 conclusions, the dried droplet method of sample preparation utilised resulted in large variability in variation in quality of samples, primarily due to crystallisation effects. The wide range of matrices, many evidencing markedly different crystallisation behaviours, means that substantial impact on the results cannot be ruled out. Additionally, the use of a single laser fluence and MS polarity quite likely biased the results to a degree, given that the matrices and analytes studied would have different optimal laser fluences and MS polarities.

One particularly promising route would be the use of printed compound microarrays in a high throughput screening experiments, enabling highly multiplexed analysis. Such an approach would benefit from greater reproducibility in sample preparation and substantial reduction in experimental time. A significant advantage of this approach would be the ability to exponentially increase the breath of conditions studied. With advanced modern printing systems capable of achieving up to 10,000 sample locations per cm^2, one could envisage a study investigating 100s or 1000s of analytes, at multiple analyte-to-matrix ratios and laser energies, on a single microscope slide.

Incorporation of additional information relating to analyte and matrix physicochemical properties could provide a powerful tool to explore the fundamentals of UV-MALDI MS ionisation processes. The handling of such complex studies, particularly controlling the proliferation experiments associated with testing large numbers of variables, would also benefit from the application of Design of Experiment (DoE) methodologies[266], obtaining results with equivalent statistical power in fewer experiments.

In Chapter 3 the optical absorptions of a range of matrices were measured in solution and solid phase, and the influence of this physicochemical property has on desorption/ionisation characteristics was investigated for three compounds, representative of common UV-MALDI MSI analyte classes. New quantitative solid phase optical absorption measurements were provided for five matrices, most for the first time, supporting the extension of current theoretical models of UV-MALDI ionisation mechanisms a broader range of matrix compounds. CHCA absorption values obtained at standard UV-MALDI wavelengths were similar to previously reported semi-quantitative measurements, but substantially different from those reported by Allwood et al.[20] which have been extensively used in the development of theoretical models of UV-MALDI ionisation mechanisms, suggesting that adjustments such models may be required.

The characterisation of matrix optical absorption in Chapter 3 was achieved using measurements of optical transmission. It is well understood that optical processes other than absorption were occurring in the matrix samples therefore

the transmission measurements results reported were the total of all these processes, rather than a true absorption measurement. To accurately quantify the energy available for desorption and ionisation in a matrix one must fully account for all the pathways by which the incident laser energy is consumed. To this end the optical characterisation of the matrices could be extended to account for these additional pathways, the most obvious of which would be reflection and scattering, as well as radiative decay processes such as fluorescence. The correlation of estimated energy densities at threshold fluence with matrix melting point suggests measurement of thermophysical properties would be also be useful subject for experimental study. In particular the addition of heat capacity measurements to the aforementioned optical properties would eliminate variable estimation from current models of UV-MALDI desorption and ablation.

The indirect evidence for an effective lower limit to optical absorption for a compound to function as a matrix, backing up previous experimental observations, also merits further study. This could be realised through the selection of matrix analogues with absorption below the limit, or though chemical modification of current matrices to tune absorption profiles[45]; alternatively tuneable wavelength lasers, such as dye lasers or systems incorporating an optical parametric oscillator (OPO), could be used to directly probe these wavelength regions.

Wavelength tuneable lasers have been applied to great effect in studies pertaining to UV-MALDI MS ionisation[24], but as of yet there has been no

investigation of how these findings translate to UV-MALDI MSI. An obvious next step would therefore be to employ a wavelength tuneable laser system in UV-MALDI MSI experiments. This could potentially offer significant enhancements in sensitivity and limits of detection for current matrices, as well as loosening the restrictions on matrix compound selection and potentially enable the use of novel matrix candidates previous unsuitable for use at standard UV-MALDI wavelengths.

Chapters 4 focused on the quantitative measurements of material ejection and ion yield in thin film system model systems of two matrices and one analyte, under different laser and sampling conditions relevant to UV-MALDI MSI. The chapter reports the first results characterising the effects of laser repetition rate and raster speed, as well as the first comparison of spot mode and continuous raster sampling, on material ejection and ion yield in UV-MALDI MSI. The measured analyte ion yields, 10^{-9} to 10^{-6} ions per desorbed molecule, supporting lower estimates of UV-MALDI MS ion yield which have in recent years sparked lively debate regarding UV-MALDI ionisation mechanisms. The comparable ion yields between raster and spot mode showed that the large reductions in analysis time enabled by continuous raster mode does not impact UV-MALDI MSI sensitivity and limits of detection. Although the complex relationship between repetition rate and raster speed emphasises the importance of laser condition optimisation in UV-MALDI MS imaging experiments.

As stated in the conclusions of Chapter 4, improved characterisation of ion transmission in commercial MS instruments and MSI ion sources would allow more accurate measurements of ion yield to be conducted in the future. A thorough inter-comparison of commonly used instrumentation in UV-MALDI MSI, and comparison to other MSI modalities, would be highly valuable to the MSI community, and provide valuable information towards further refinements of MSI techniques.

The work in Chapter 4 was restricted small range of repetition rates, raster speeds and pulse energies, primarily due to limitations of the FOV and acquisition speed of the CLSM, and therefore was limited in the conclusions that could be drawn. An obvious extension of the work would be the inclusion of a wider range of these variables, as well as the addition of laser spot size and beam profile, to fully account for the effects of common laser and sampling conditions. Such a dataset could be used to build up a detailed picture of the parameter space that typical UV-MALDI MSI experiments operate in, providing reference data to inform experiments and instrument development. Due to the much large number of variables, such a study would likely require a different method for measuring material ejection than was employed in Chapter 4. The CCI profilometry technique used in Chapter 5, which can acquire similar measurements to the CLSM but with a much higher throughput, would be a obvious choice. Alternatively the use of photoacoustic measurements has been demonstrated[24], which in theory would allow on-line monitoring of material ejection during a MS imaging experiment, although this technique is currently limited to ambient pressure conditions.

The simulations of pixel oversampling while operating in oversampling imaging mode, while informative, ultimately require confirmation through experimental study. It would be very informative to quantify the influence of pixel oversampling on spatial resolution, a feature of UV-MALDI MSI that remains poorly described. Such a study would benefit from the development of resolution standard akin to those developed for other imaging methods, but consisting of relevant organic molecules, a simple example of with was recently demonstrated for use in SIMS[267].

In Chapter 5, the use of optical profilometer to measure material ejection and ion yield were extended into the imaging of biological tissue. The profilometry measurements, combined with carefully controlled sample preparation routines and the MS data were used to obtain quantitative measurement of the effects of tissue microenvironment on desorption and ionisation in UV-MALDI MSI of mouse brain, representing the first measurements of material ejection and absolute ion yield from tissue in UV-MALDI MSI, or to this authors knowledge, in any MSI technique. The influence of local tissue environment on matrix crystallisation and ion suppression/enhancement were also explored.

The results presented in Chapter 5 relate to a single matrix, one tissue type, and one set of laser and sampling conditions. While this provided useful information regarding the effect of tissue microenvironment in UV-MALDI MSI, further extension of the work would be needed to draw more robust conclusions. In the first instance further experiments should be carried out to include another common matrix, such as 2,5-DHB, and MS polarity, as well as additional tissue

types to confirm that the results can be replicated in other systems. Further characterisation of the tissue samples, either using serial sections or post UV-MALDI MSI analysis, could provide further insights on the origins of region-specific ion suppression. Histological stains or fluorescence microscopy could be utilised to visualise different tissue components, such as proteins, cell nuclei and lipids, to see if there is any correlation to the observed ion suppression effects; this approach would be particularly useful when studying tissues, such as tumours, that are not as well characterised as mouse brain. This could shed some light on the overserved tissue thickness effect, in particular it would be useful to discern what tissue characteristics correlate to global changes in UV-MALDI ion intensities, as recently demonstrated for DESI MSI where cytoplasmic area was found to corelate to lipid signals[265]. Such information would enable new methods for data normalisation informed by the physical characteristics of the sample, which may prove more robust, or at least enhance, current normalisation methods which are typically based on the UV-MALDI MSI data alone.

The suspected role of endogenous salts in ion suppression could also be explored though further chemical imaging techniques such as SIMS, Laser Ablation Inductively Coupled Plasma Mass Spectrometry (LA-ICP MS) or Micro X-ray Fluorescence (μ-XRF), which would allow of the distribution and concentration of atomic species such K or Na, to be compared to the UV-MALDI MSI.

The method of matrix deposition used here was sublimation deposition with no subsequent recrystallisation step, which was selected primarily over concerns that solvent based techniques would deform the tissue and hamper subsequent profilometry measurements. That said it would be a highly pertinent to attempt the same experiment in Chapter 5 on samples prepared using sprayer deposition devices, as well as sublimation coated samples that have undergone a recrystallisation step. This would allow for comparison between the most widely used matrix deposition methods, helping to inform appropriate selection of methods to use for a given application, and provide useful data to aid future development of deposition protocols. This could be further extended to commonly used tissue pre-treatments, for example tissue washing, which can be reasonably expected to significantly alter the results found in Chapter 5.

As stated in the conclusion of Chapter 5, the CCI profilometry method applied here to measure material ejection and ion yield could be adapted for use in other common MSI modalities, for example DESI and SIMS, as well as ionisation sources that have recently been adapted to MSI, such as Rapid Evaporative Ionisation Mass Spectrometry (REIMS) and Liquid Extraction Surface Analysis (LESA) based techniques. This would provide the opportunity to compare the efficiency of different modes of ionisation, providing a more quantitative assessment of the respective advantages and disadvantages, and help identify suitable combinations for multi-modal MSI studies. Such comparisons would also help identify promising routes for enhancing the capabilities of individual MSI modalities, or even opportunities for the development of novel ionisation techniques.

References

(1) Hillenkamp, F.; Karas, M.; Holtkamp, D.; Klüsener, P. Energy Deposition in Ultraviolet Laser Desorption Mass Spectrometry of Biomolecules. *Int. J. Mass Spectrom. Ion Process.* **1986**, *69* (3), 265–276. https://doi.org/10.1016/0168-1176(86)87018-5.

(2) Karas, M.; Bachmann, D.; Hillenkamp, F. Influence of the Wavelength in High-Irradiance Ultraviolet Laser Desorption Mass Spectrometry of Organic Molecules. *Anal. Chem.* **1985**, *57* (14), 2935–2939. https://doi.org/10.1021/ac00291a042.

(3) Karas, M.; Bachmann, D.; Bahr, U.; Hillenkamp, F. Matrix-Assisted Ultraviolet Laser Desorption of Non-Volatile Compounds. *Int. J. Mass Spectrom. Ion Process.* **1987**, *78* (C), 53–68. https://doi.org/10.1016/0168-1176(87)87041-6.

(4) Tanaka, K.; Waki, H.; Ido, Y.; Akita, S.; Yoshida, Y.; Yoshida, T.; Matsuo, T. Protein and Polymer Analyses up to *m/z* 100 000 by Laser Ionization Time-of-Flight Mass Spectrometry. *Rapid Commun. Mass Spectrom.* **1988**, *2* (8), 151–153. https://doi.org/10.1002/rcm.1290020802.

(5) Beavis, R. C.; Chaudhary, T.; Chait, B. T. α-Cyano-4-Hydroxycinnamic Acid as a Matrix for Matrixassisted Laser Desorption Mass Spectromtry. *Org. Mass Spectrom.* **1992**, *27* (2), 156–158. https://doi.org/10.1002/oms.1210270217.

(6) Strupat, K.; Karas, M.; Hillenkamp, F. 2,5-Dihydroxybenzoic Acid: A New Matrix for Laser Desorption—Ionization Mass Spectrometry. *Int. J. Mass Spectrom. Ion Process.* **1991**, *111* (C), 89–102. https://doi.org/10.1016/0168-1176(91)85050-V.

(7) Overberg, A.; Karas, M.; Bahr, U.; Kaufmann, R.; Hillenkamp, F. Matrix-Assisted Infrared-Laser (2.94 Mm) Desorption/Ionization Mass Spectrometry of Large Biomolecules. *Rapid Commun. Mass Spectrom.* **1990**, *4* (8), 293–296. https://doi.org/10.1002/rcm.1290040808.

(8) Spengler, B.; Hubert, M.; Kaufmann, R. MALDI Ion Imaging and Biological Ion Imaging with a New Scanning UV-Laser Microprobe. In *Proceedings of the 42nd Annual Conference on Mass Spectrometry and Allied Topics*; 1994; p 1041.

(9) Caprioli, R. M.; Farmer, T. B.; Gile, J. Molecular Imaging of Biological Samples: Localization of Peptides and Proteins Using MALDI-TOF MS. *Anal. Chem.* **1997**, *69* (23), 4751–4760. https://doi.org/Doi 10.1021/Ac970888i.

(10) Stoeckli, M.; Chaurand, P.; Hallahan, D. E.; Caprioli, R. M. Imaging Mass

Spectrometry: A New Technology for the Analysis of Protein Expression in Mammalian Tissues. *Nat. Med.* **2001**, *7* (4), 493–496. https://doi.org/10.1038/86573.

(11) Li, Y.; Shrestha, B.; Vertes, A. Atmospheric Pressure Molecular Imaging by Infrared MALDI Mass Spectrometry. *Anal. Chem.* **2007**, *79* (2), 523–532. https://doi.org/10.1021/ac061577n.

(12) Spengler, B.; Hubert, M. Scanning Microprobe Matrix-Assisted Laser Desorption Ionization (SMALDI) Mass Spectrometry: Instrumentation for Sub-Micrometer Resolved LDI and MALDI Surface Analysis. *J. Am. Soc. Mass Spectrom.* **2002**, *13* (6), 735–748. https://doi.org/10.1016/S1044-0305(02)00376-8.

(13) Spraggins, J. M.; Caprioli, R. M. High-Speed MALDI-TOF Imaging Mass Spectrometry: Rapid Ion Image Acquisition and Considerations for next Generation Instrumentation. *J. Am. Soc. Mass Spectrom.* **2011**, *22* (6), 1022–1031. https://doi.org/10.1007/s13361-011-0121-0.

(14) Trim, P. J.; Djidja, M. C.; Atkinson, S. J.; Oakes, K.; Cole, L. M.; Anderson, D. M. G.; Hart, P. J.; Francese, S.; Clench, M. R. Introduction of a 20 KHz Nd:YVO4 Laser into a Hybrid Quadrupole Time-of-Flight Mass Spectrometer for MALDI-MS Imaging. *Anal. Bioanal. Chem.* **2010**, *397* (8), 3409–3419. https://doi.org/10.1007/s00216-010-3874-6.

(15) Soltwisch, J.; Kettling, H.; Vens-Cappell, S.; Wiegelmann, M.; Müthing, J.; Dreisewerd, K. Mass Spectrometry Imaging with Laser-Induced Postionization. *Science (80-.).* **2015**, *348* (6231), 211–215. https://doi.org/10.1126/science.aaa1051.

(16) Steven, R. T.; Shaw, M.; Dexter, A.; Murta, T.; Green, F. M.; Robinson, K. N.; Gilmore, I. S.; Takats, Z.; Bunch, J. Construction and Testing of an Atmospheric-Pressure Transmission-Mode Matrix Assisted Laser Desorption Ionisation Mass Spectrometry Imaging Ion Source with Plasma Ionisation Enhancement. *Anal. Chim. Acta* **2018**, *1051* (xxxx), 110–119. https://doi.org/10.1016/j.aca.2018.11.003.

(17) Niehaus, M.; Schnapp, A.; Koch, A.; Soltwisch, J.; Dreisewerd, K. New Insights into the Wavelength Dependence of MALDI Mass Spectrometry. *Anal. Chem.* **2017**, *89* (14), 7734–7741. https://doi.org/10.1021/acs.analchem.7b01744.

(18) Boekelmann, V.; Spengler, B.; Kaufmann, R. Dynamical Parameters of Ion Ejection and Ion Formation in Matrix-Assisted Laser Desorption/Ionization. *Eur. Mass Spectrom.* **1995**, *1* (1), 81–93. https://doi.org/10.1255/ejms.163.

(19) Heise, T. W.; Yeung, E. S. Dynamics of Matrix-Assisted Laser Desorption as Revealed by the Associated Acoustic Signal. *Anal. Chim. Acta* **1995**,

299 (3), 377–385. https://doi.org/10.1016/0003-2670(94)00309-A.

(20) Allwood, D. A.; Dreyfus, R. W.; Perera, I. K.; Dyer, P. E. UV Optical Absorption of Matrices Used for Matrix-Assisted Laser Desorption/Ionization. *Rapid Commun. Mass Spectrom.* **1996**, *10* (13), 1575–1578. https://doi.org/10.1002/(SICI)1097-0231(199610)10:13<1575::AID-RCM658>3.0.CO;2-C.

(21) Horneffer, V.; Dreisewerd, K.; Lüdemann, H. C.; Hillenkamp, F.; Läge, M.; Strupat, K. Is the Incorporation of Analytes into Matrix Crystals a Prerequisite for Matrix-Assisted Laser Desorption/Ionization Mass Spectrometry? A Study of Five Positional Isomers of Dihydroxybenzoic Acid. *Int. J. Mass Spectrom.* **1999**, *185*, 859–870. https://doi.org/10.1016/S1387-3806(98)14218-5.

(22) Soltwisch, J.; Jaskolla, T. W.; Hillenkamp, F.; Karas, M.; Dreisewerd, K. Ion Yields in UV-MALDI Mass Spectrometry As a Function of Excitation Laser Wavelength and Optical and Physico-Chemical Properties of Classical and Halogen-Substituted MALDI Matrixes. *Anal. Chem.* **2012**, *84* (15), 6567–6576. https://doi.org/10.1021/ac3008434.

(23) Wiegelmann, M.; Soltwisch, J.; Jaskolla, T. W.; Dreisewerd, K. Matching the Laser Wavelength to the Absorption Properties of Matrices Increases the Ion Yield in UV-MALDI Mass Spectrometry. *Anal. Bioanal. Chem.* **2013**, *405* (22), 6925–6932. https://doi.org/10.1007/s00216-012-6478-5.

(24) Soltwisch, J.; Jaskolla, T. W.; Dreisewerd, K. Color Matters - Material Ejection and Ion Yields in UV-MALDI Mass Spectrometry as a Function of Laser Wavelength and Laser Fluence. *J. Am. Soc. Mass Spectrom.* **2013**, *24* (10), 1477–1488. https://doi.org/10.1007/s13361-013-0699-5.

(25) Tang, K.; Taranenko, N. I.; Allman, S. L.; Chen, C. H.; Chág, L. Y.; Jacobson, K. B. Picolinic Acid as a Matrix for Laser Mass Spectrometry of Nucleic Acids and Proteins. *Rapid Commun. Mass Spectrom.* **1994**, *8* (9), 673–677. https://doi.org/10.1002/rcm.1290080902.

(26) Taranenko, N. I.; Tang, K.; Allman, S. L.; Ch'ang, L. Y.; Chen, C. H. 3-Aminopicolinic Aid as a Matrix for Laser Desorption Mass Spectrometry of Biopolymers. *Rapid Commun. Mass Spectrom.* **1994**, *8* (12), 1001–1006. https://doi.org/10.1002/rcm.1290081219.

(27) Schiller, J.; Süß, R.; Fuchs, B.; Müller, M.; Petković, M.; Zschörnig, O.; Waschipky, H. The Suitability of Different DHB Isomers as Matrices for the MALDI-TOF MS Analysis of Phospholipids: Which Isomer for What Purpose? *Eur. Biophys. J.* **2007**, *36* (4–5), 517–527. https://doi.org/10.1007/s00249-006-0090-6.

(28) Mccarley, T. D.; Mccarley, R. L.; Limbach, P. A. Electron-Transfer Ionization in Matrix-Assisted Laser Desorption / Ionization Mass

Spectrometry. *Anal. Chem.* **1998**, *70* (20), 4376–4379. https://doi.org/10.1021/ac980527i.

(29) Luo, G.; Marginean, I.; Vertes, A. Internal Energy of Ions Generated by Matrix-Assisted Laser Desorption/Ionization. *Anal. Chem.* **2002**, *74* (24), 6185–6190. https://doi.org/10.1021/ac020339z.

(30) Allwood, D. A.; Dreyfus, R. W.; Perera, I. K.; Dyer, P. E. Optical Absorption of Matrix Compounds for Laser-Induced Desorption and Ionization (MALDI). *Appl. Surf. Sci.* **1997**, *109–110*, 154–157. https://doi.org/10.1016/S0169-4332(96)00652-6.

(31) Chen, X.; Carroll, J. A.; Beavis, R. C. Near-Ultraviolet-Induced Matrix-Assisted Laser Desorption/Ionization as a Function of Wavelength. *J. Am. Soc. Mass Spectrom.* **1998**, *9* (9), 885–891. https://doi.org/10.1016/S1044-0305(98)00059-2.

(32) Allwood, D. A.; Dyer, P. E. Quantitative Fluorescence Measurements Performed on Typical Matrix Molecules in Matrix-Assisted Laser Desorption/Ionisation. *Chem. Phys.* **2000**, *261* (3), 457–467. https://doi.org/10.1016/S0301-0104(00)00279-2.

(33) Ehring, H.; Sundqvist, B. U. R. Studies of the MALDI Process by Luminescence Spectroscopy. *J. Mass Spectrom.* **1995**, *30* (9), 1303–1310. https://doi.org/10.1002/jms.1190300915.

(34) Lüdemann, H. C.; Redmond, R. W.; Hillenkamp, F. Singlet-Singlet Annihilation in Ultraviolet Matrix-Assisted Laser Desorption/Ionization Studied by Fluorescence Spectroscopy. *Rapid Commun. Mass Spectrom.* **2002**, *16* (13), 1287–1294. https://doi.org/10.1002/rcm.712.

(35) Lin, H. Y.; Song, B.; Lu, I. C.; Hsu, K. T.; Liao, C. Y.; Lee, Y. Y.; Tseng, C. M.; Lee, Y. T.; Ni, C.-K. Is Energy Pooling Necessary in Ultraviolet Matrix-Assisted Laser Desorption/Ionization? *Rapid Commun. Mass Spectrom.* **2014**, *28* (1), 77–82. https://doi.org/10.1002/rcm.6765.

(36) Lin, H. Y.; Hsu, H. C.; Lu, I. C.; Hsu, K. T.; Liao, C. Y.; Lee, Y. Y.; Tseng, C. M.; Lee, Y. T.; Ni, C.-K. Fluorescence Spectroscopy of UV-MALDI Matrices and Implications of Ionization Mechanisms. *J. Chem. Phys.* **2014**, *141* (16). https://doi.org/10.1063/1.4898372.

(37) Steenvoorden, R.; Breuker, K.; Zenobi, R. The Gas-Phase Basicities of Matrix-Assisted Laser Desorption/Ionization Matrices. *Eur. J. Mass Spectrom.* **1997**, *3* (1), 339. https://doi.org/10.1255/ejms.165.

(38) Mirza, S. P.; Raju, N. P.; Vairamani, M. Estimation of the Proton Affinity Values of Fifteen Matrix-Assisted Laser Desorption/Ionization Matrices under Electrospray Ionization Conditions Using the Kinetic Method. *J. Am. Soc. Mass Spectrom.* **2004**, *15* (3), 431–435.

https://doi.org/10.1016/j.jasms.2003.12.001.

(39) Mormann, M.; Bashir, S.; Derrick, P. J.; Kuck, D. Gas-Phase Basicities of the Isomeric Dihydroxybenzoic Acids and Gas-Phase Acidities of Their Radical Cations. *J. Am. Soc. Mass Spectrom.* **2000**, *11* (6), 544–552. https://doi.org/10.1016/S1044-0305(00)00112-4.

(40) Burton, R. D.; Watson, C. H.; Eyler, J. R.; Lang, G. L.; Powell, D. H.; Avery, M. Y. Proton Affinities of Eight Matrices Used for Matrix-Assisted Laser Desorption/Ionization. *Rapid Commun. Mass Spectrom.* **1997**, *11* (5), 443–446. https://doi.org/10.1002/(SICI)1097-0231(199703)11:5<443::AID-RCM897>3.0.CO;2-3.

(41) Breuker, K.; Knochenmuss, R.; Zenobi, R. Gas-Phase Basicities of Deprotonated Matrix-Assisted Laser Desorption/Ionization Matrix Molecules. *Int. J. Mass Spectrom.* **1999**, *184* (1), 25–38. https://doi.org/10.1016/S1387-3806(98)14200-8.

(42) Bourcier, S.; Hoppilliard, Y. B3LYP DFT Molecular Orbital Approach, an Efficient Method to Evaluate the Thermochemical Properties of MALDI Matrices. *Int. J. Mass Spectrom.* **2002**, *217* (1–3), 231–244. https://doi.org/10.1016/S1387-3806(02)00578-X.

(43) Yassin, F. H.; Marynick *, D. S. Computational Estimates of the Gas-Phase Basicities, Proton Affinities and Ionization Potentials of the Six Isomers of Dihydroxybenzoic Acid. *Mol. Phys.* **2005**, *103* (2–3), 183–189. https://doi.org/10.1080/00268970512331316210.

(44) Mirabelli, M. F.; Zenobi, R. Observing Proton Transfer Reactions Inside the MALDI Plume: Experimental and Theoretical Insight into MALDI Gas-Phase Reactions. *J. Am. Soc. Mass Spectrom.* **2017**. https://doi.org/10.1007/s13361-017-1677-0.

(45) Jaskolla, T. W.; Lehmann, W.-D.; Karas, M. 4-Chloro-Alpha-Cyanocinnamic Acid Is an Advanced, Rationally Designed MALDI Matrix. *Proc. Natl. Acad. Sci. U. S. A.* **2008**, *105* (34), 12200–12205. https://doi.org/10.1073/pnas.0803056105.

(46) Teuber, K.; Schiller, J.; Fuchs, B.; Karas, M.; Jaskolla, T. W. Significant Sensitivity Improvements by Matrix Optimization: A MALDI-TOF Mass Spectrometric Study of Lipids from Hen Egg Yolk. *Chem. Phys. Lipids* **2010**, *163* (6), 552–560. https://doi.org/10.1016/J.CHEMPHYSLIP.2010.04.005.

(47) Price, D. M.; Bashir, S.; Derrick, P. R. Sublimation Properties of x,y-Dihydroxybenzoic Acid Isomers as Model Matrix Assisted Laser Desorption Ionisation (MALDI) Matrices. *Thermochim. Acta* **1999**, *327* (1–2), 167–171. https://doi.org/10.1016/S0040-6031(98)00606-6.

(48) Monte, M. J. S.; Gonçalves, M. V.; Ribeiro da Silva, M. D. M. C.; Gonçalves, M. V.; Ribeiro da Silva, M. D. M. C. Vapor Pressures and Enthalpies of Combustion of the Dihydroxybenzoic Acid Isomers. *J. Chem. Eng. Data* **2010**, *55* (6), 2246–2251. https://doi.org/10.1021/je900777q.

(49) Steven, R. T.; Race, A. M.; Bunch, J. Para-Nitroaniline Is a Promising Matrix for MALDI-MS Imaging on Intermediate Pressure MS Systems. *J. Am. Soc. Mass Spectrom.* **2013**, *24* (5), 801–804. https://doi.org/10.1007/s13361-013-0586-0.

(50) Westman, A.; Huth-Fehre, T.; Demirev, P.; Sundqvist, B. U. R. Sample Morphology Effects in Matrix-assisted Laser Desorption/Ionization Mass Spectrometry of Proteins. *J. Mass Spectrom.* **1995**, *30* (1), 206–211. https://doi.org/10.1002/jms.1190300131.

(51) Fournier, I.; Beavis, R. C.; Blais, J. C.; Tabet, J. C.; Bolbach, G. Hysteresis Effects Observed in MALDI Using Oriented, Protein-Doped Matrix Crystals. *Int. J. Mass Spectrom. Ion Process.* **1997**, *169–170*, 19–29. https://doi.org/10.1016/S0168-1176(97)00212-7.

(52) Steven, R. T.; Dexter, A.; Bunch, J. Investigating MALDI MSI Parameters (Part 1) – A Systematic Survey of the Effects of Repetition Rates up to 20kHz in Continuous Raster Mode. *Methods* **2016**, *104*, 101–110. https://doi.org/10.1016/j.ymeth.2016.04.010.

(53) Tarzi, O. I.; Nonami, H.; Erra-Balsells, R. The Effect of Temperature on the Stability of Compounds Used as UV-MALDI-MS Matrix: 2,5-Dihydroxybenzoic Acid, 2,4,6-Trihydroxyacetophenone, α-Cyano-4-Hydroxycinnamic Acid, 3,5-Dimethoxy-4-Hydroxycinnamic Acid, nor-Harmane and Harmane. *J. Mass Spectrom.* **2009**, *44* (2), 260–277. https://doi.org/10.1002/jms.1506.

(54) Tarzi, O. I.; Stéfano, L. Di; Argüello, J. E.; Oksdath-Mansilla, G.; Erra-Balsells, R. Photochemical and Thermal Stability of Some Dihydroxyacetophenones Used as UV-MALDI-MS Matrices. *Photochem. Photobiol.* **2013**, *89* (6), 1368–1374. https://doi.org/10.1111/php.12130.

(55) Demirev, P.; Westman, A.; Reimann, C. T.; Håkansson, P.; Barofsky, D.; Sundqvist, B. U. R.; Cheng, Y. D.; Seibt, W.; Siegbahn, K. Matrix-assisted Laser Desorption with Ultra-short Laser Pulses. *Rapid Commun. Mass Spectrom.* **1992**, *6* (3), 187–191. https://doi.org/10.1002/rcm.1290060307.

(56) Dreisewerd, K.; Schürenberg, M.; Karas, M.; Hillenkamp, F. Matrix-Assisted Laser Desorption/Ionization with Nitrogen Lasers of Different Pulse Widths. *Int. J. Mass Spectrom. Ion Process.* **2003**, *154* (3), 171–178. https://doi.org/10.1016/0168-1176(96)04377-7.

(57) Knochenmuss, R. MALDI Mechanisms: Wavelength and Matrix

Dependence of the Coupled Photophysical and Chemical Dynamics Model. *Analyst* **2014**, *139* (1), 147–156. https://doi.org/10.1039/c3an01446k.

(58) Soltwisch, J.; Jaskolla, T. W.; Dreisewerd, K. Erratum to: Color Matters—Material Ejection and Ion Yields in UV-MALDI Mass Spectrometry as a Function of Laser Wavelength and Laser Fluence. *J. Am. Soc. Mass Spectrom.* **2015**, *26* (9), 1641–1641. https://doi.org/10.1007/s13361-015-1215-x.

(59) Westmacott, G.; Ens, W.; Hillenkamp, F.; Dreisewerd, K.; Schürenberg, M. The Influence of Laser Fluence on Ion Yield in Matrix-Assisted Laser Desorption Ionization Mass Spectrometry. *Int. J. Mass Spectrom.* **2002**, *221* (1), 67–81. https://doi.org/10.1016/S1387-3806(02)00898-9.

(60) Qiao, H.; Spicer, V.; Ens, W. The Effect of Laser Profile, Fluence, and Spot Size on Sensitivity in Orthogonal-Injection Matrix-Assisted Laser Desorption/Ionization Time-of-Flight Mass Spectrometry. *Rapid Commun. Mass Spectrom.* **2008**, *22* (18), 2779–2790. https://doi.org/10.1002/rcm.3675.

(61) Niehaus, M.; Soltwisch, J. New Insights into Mechanisms of Material Ejection in MALDI Mass Spectrometry for a Wide Range of Spot Sizes. *Sci. Rep.* **2018**, *8* (1), 7755. https://doi.org/10.1038/s41598-018-25946-z.

(62) Dreisewerd, K. The Desorption Process in MALDI. *Chem. Rev.* **2003**, *103* (2), 395–426. https://doi.org/10.1021/cr010375i.

(63) Dreisewerd, K.; Schürenberg, M.; Karas, M.; Hillenkamp, F. Influence of the Laser Intensity and Spot Size on the Desorption of Molecules and Ions in Matrix-Assisted Laser Desorption/Ionization with a Uniform Beam Profile. *Int. J. Mass Spectrom. Ion Process.* **1995**, *141* (2), 127–148. https://doi.org/10.1016/0168-1176(94)04108-J.

(64) Ens, W.; Mao, Y.; Mayer, F.; Standing, K. G. Properties of Matrix-assisted Laser Desorption. Measurements with a Time-to-digital Converter. *Rapid Commun. Mass Spectrom.* **1991**, *5* (3), 117–123. https://doi.org/10.1002/rcm.1290050306.

(65) Vestal, M. L. Modern MALDI Time-of-Flight Mass Spectrometry. *J. Mass Spectrom.* **2009**, *44* (3), 303–317. https://doi.org/10.1002/jms.1537.

(66) Chernushevich, I. V.; Loboda, A. V.; Thomson, B. a. An Introduction to Quadrupole-Time-of-Flight Mass Spectrometry. *J. Mass Spectrom.* **2001**, *36* (8), 849–865. https://doi.org/10.1002/jms.207.

(67) Steven, R. T.; Race, A. M.; Bunch, J. Probing the Relationship Between Detected Ion Intensity, Laser Fluence, and Beam Profile in Thin Film and Tissue in MALDI MSI. *J. Am. Soc. Mass Spectrom.* **2016**, *27* (8), 1419–

1428. https://doi.org/10.1007/s13361-016-1414-0.

(68) Wiegelmann, M.; Dreisewerd, K.; Soltwisch, J. Influence of the Laser Spot Size, Focal Beam Profile, and Tissue Type on the Lipid Signals Obtained by MALDI-MS Imaging in Oversampling Mode. *J. Am. Soc. Mass Spectrom.* **2016**, *27* (12), 1952–1964. https://doi.org/10.1007/s13361-016-1477-y.

(69) McLean, J. A.; Russell, W. K.; Russell, D. H. A High Repetition Rate (1 KHz) Microcrystal Laser for High Throughput Atmospheric Pressure MALDI-Quadrupole-Time-of-Flight Mass Spectrometry. *Anal. Chem.* **2003**, *75* (3), 648–654. https://doi.org/10.1021/ac026029y.

(70) Moskovets, E.; Preisler, J.; Chen, H. S.; Rejtar, T.; Andreev, V.; Karger, B. L. High-Throughput Axial MALDI-TOF MS Using a 2-KHz Repetition Rate Laser. *Anal. Chem.* **2006**, *78* (3), 912–919. https://doi.org/10.1021/ac051393t.

(71) Trim, P. J.; Henson, C. M.; Avery, J. L.; McEwen, A.; Snel, M. F.; Claude, E.; Marshall, P. S.; West, A.; Princivalle, A. P.; Clench, M. R. Matrix-Assisted Laser Desorption/Ionization-Ion Mobility Separation-Mass Spectrometry Imaging of Vinblastine in Whole Body Tissue Sections. *Anal. Chem.* **2008**, *80* (22), 8628–8634. https://doi.org/10.1021/ac8015467.

(72) Bokhart, M. T.; Rosen, E.; Thompson, C.; Sykes, C.; Kashuba, A. D. M.; Muddiman, D. C. Quantitative Mass Spectrometry Imaging of Emtricitabine in Cervical Tissue Model Using Infrared Matrix-Assisted Laser Desorption Electrospray Ionization. *Anal. Bioanal. Chem.* **2015**, *407* (8), 2073–2084. https://doi.org/10.1007/s00216-014-8220-y.

(73) Hu, X. K.; Lacey, D.; Li, J.; Yang, C.; Loboda, A. V.; Lipson, R. H. Visible Wavelength MALDI Using Coumarin Laser Dyes. *Int. J. Mass Spectrom.* **2008**, *278* (1), 69–74. https://doi.org/10.1016/j.ijms.2008.08.009.

(74) Xiong, C.; Zhou, X.; He, Q.; Huang, X.; Wang, J.; Peng, W.-P.; Chang, H.-C.; Nie, Z. Development of Visible-Wavelength MALDI Cell Mass Spectrometry for High-Efficiency Single-Cell Analysis. *Anal. Chem.* **2016**, *88* (23), 11913–11918. https://doi.org/10.1021/acs.analchem.6b03789.

(75) Yang, C.; Hu, X.; Loboda, A. V; Lipson, R. H. A Useful Binary Matrix for Visible-MALDI of Low Molecular Weight Analytes. **2009**. https://doi.org/10.1016/j.jasms.2009.10.016.

(76) Sun, Z.; Findsen, E. W.; Isailovic, D. Atmospheric Pressure Visible-Wavelength MALDI-MS. *Int. J. Mass Spectrom.* **2012**, *315*, 66–73. https://doi.org/10.1016/J.IJMS.2012.03.002.

(77) Allwood, D. A.; Dyer, P. E.; Dreyfus, R. W.; Perera, I. K. Plasma Modelling of Matrix Assisted UV Laser Desorption/Ionisation (MALDI). *Appl. Surf.*

Sci. **1997**, *109/110* (1), 616–620. https://doi.org/10.1016/S0169-4332(96)00643-5.

(78) Karbach, V.; Knochenmuss, R. Do Single Matrix Molecules Generate Primary Ions in Ultraviolet Matrix-Assisted Laser Desorption/Ionization. *Rapid Commun. Mass Spectrom.* **1998**, *12* (14), 968–974. https://doi.org/10.1002/(SICI)1097-0231(19980731)12:14<968::AID-RCM255>3.0.CO;2-4.

(79) Knochenmuss, R. The Coupled Chemical and Physical Dynamics Model of MALDI. *Annu. Rev. Anal. Chem.* **2016**, *9* (1), 365–385. https://doi.org/10.1146/annurev-anchem-071015-041750.

(80) Koch, A.; Schnapp, A.; Soltwisch, J.; Dreisewerd, K. Generation of Multiply Charged Peptides and Proteins from Glycerol-Based Matrices Using Lasers with Ultraviolet, Visible and near-Infrared Wavelengths and an Atmospheric Pressure Ion Source. *Int. J. Mass Spectrom.* **2017**, *416*, 61–70. https://doi.org/10.1016/j.ijms.2016.11.007.

(81) Phipps, C. *Laser Ablation and Its Applications*; Phipps, C., Ed.; Springer Series in Optical Sciences; Springer US: Boston, MA, 2007; Vol. 129. https://doi.org/10.1007/978-0-387-30453-3.

(82) Zhigilei, L. V.; Garrison, B. J. Microscopic Mechanisms of Laser Ablation of Organic Solids in the Thermal and Stress Confinement Irradiation Regimes. *J. Appl. Phys.* **2000**, *88* (3), 1281–1298. https://doi.org/10.1063/1.373816.

(83) Wichmann, J. M.; Lypulescy, C.; Wöste, L.; Lindinger, A. Matrix-Assisted Laser Desorption/Ionizatiort by Using Femtosecond Laser Pulses in the near-Infrared Wavelength Regime. *Rapid Commun. Mass Spectrom.* **2009**, *23* (8), 1105–1108. https://doi.org/10.1002/rcm.3974.

(84) Wichmann, J. M.; Schwaneberg, F.; Lupulescu, C.; Lindinger, A. Chirp Dependent Matrix-Assisted Laser Desorption/Ionization Measurements of Alkali Metal Adapted Angiotensine II by Using Ultrashort Laser Pulses in the near IR Regime. *Int. J. Mass Spectrom.* **2010**, *296* (1–3), 30–35. https://doi.org/10.1016/J.IJMS.2010.07.018.

(85) Liang, S.-P.; Lu, I.-C.; Tsai, S.-T.; Chen, J.-L.; Lee, Y. T.; Ni, C.-K. Laser Pulse Width Dependence and Ionization Mechanism of Matrix-Assisted Laser Desorption/Ionization. *J. Am. Soc. Mass Spectrom.* **2017**, *28* (10), 2235–2245. https://doi.org/10.1007/s13361-017-1734-8.

(86) Zhigilei, L. V.; Garrison, B. J. Mechanisms of Laser Ablation from Molecular Dynamics Simulations: Dependence on the Initial Temperature and Pulse Duration. *Appl. Phys. A Mater. Sci. Process.* **1999**, *69* (S1), S75–S80. https://doi.org/10.1007/s003399900347.

(87) Zhigilei, L. V.; Yingling, Y. G.; Itina, T. E.; Schoolcraft, T. A.; Garrison, B. J. Molecular Dynamics Simulations of Matrix-Assisted Laser Desorption—Connections to Experiment. *Int. J. Mass Spectrom.* **2003**, *226* (1), 85–106. https://doi.org/10.1016/S1387-3806(02)00962-4.

(88) Yingling, Y. G.; Conforti, F. F.; Garrison, B. J. Theoretical Investigation of Laser Pulse Width Dependence in a Thermal Confinement Regime. In *Applied Physics A: Materials Science and Processing*; Springer Berlin Heidelberg, 2004; Vol. 79, pp 757–759. https://doi.org/10.1007/s00339-004-2575-4.

(89) Knochenmuss, R.; Zhigilei, L. V. Molecular Dynamics Simulations of MALDI: Laser Fluence and Pulse Width Dependence of Plume Characteristics and Consequences Formatrix and Analyte Ionization. *J. Mass Spectrom.* **2010**, *45* (4), 333–346. https://doi.org/10.1002/jms.1732.

(90) Holle, A.; Haase, A.; Kayser, M.; Höhndorf, J. Optimizing UV Laser Focus Profiles for Improved MALDI Performance. *J. Mass Spectrom.* **2006**, *41* (6), 705–716. https://doi.org/10.1002/jms.1041.

(91) Zavalin, A. I.; Yang, J.; Haase, A.; Holle, A.; Caprioli, R. M. Implementation of a Gaussian Beam Laser and Aspheric Optics for High Spatial Resolution MALDI Imaging MS. *J. Am. Soc. Mass Spectrom.* **2014**, *25* (6), 1079–1082. https://doi.org/10.1007/s13361-014-0872-5.

(92) Zavalin, A. I.; Yang, J.; Caprioli, R. M. Laser Beam Filtration for High Spatial Resolution MALDI Imaging Mass Spectrometry. *J. Am. Soc. Mass Spectrom.* **2013**, *24* (7), 1153–1156. https://doi.org/10.1007/s13361-013-0638-5.

(93) Sherrod, S. D.; Castellana, E. T.; McLean, J. A.; Russell, D. H. Spatially Dynamic Laser Patterning Using Advanced Optics for Imaging Matrix Assisted Laser Desorption/Ionization (MALDI) Mass Spectrometry. *Int. J. Mass Spectrom.* **2007**, *262* (3), 256–262. https://doi.org/10.1016/j.ijms.2006.12.003.

(94) Jurchen, J. C.; Rubakhin, S. S.; Sweedler, J. V. MALDI-MS Imaging of Features Smaller than the Size of the Laser Beam. *J. Am. Soc. Mass Spectrom.* **2005**, *16*, 1654–1659. https://doi.org/10.1016/j.jasms.2005.06.006.

(95) Hansen, R. L.; Lee, Y. J. Overlapping MALDI-Mass Spectrometry Imaging for In-Parallel MS and MS/MS Data Acquisition without Sacrificing Spatial Resolution. *J. Am. Soc. Mass Spectrom.* **2017**, 1–9. https://doi.org/10.1007/s13361-017-1699-7.

(96) Ogrinc Potočnik, N.; Porta, T.; Becker, M.; Heeren, R. M. A.; Ellis, S. R. Use of Advantageous, Volatile Matrices Enabled by next-Generation High-Speed Matrix-Assisted Laser Desorption/Ionization Time-of-Flight

Imaging Employing a Scanning Laser Beam. *Rapid Commun. Mass Spectrom.* **2015**, *29* (23), 2195–2203. https://doi.org/10.1002/rcm.7379.

(97) Barré, F.; Rocha, B.; Towers, M.; Murray, P.; Claude, E.; Pastor, B. C.; Heeren, R. M. A.; Siegel, T. P. Fast Raster Matrix-Assisted Laser Desorption/Ionization Mass Spectrometry Imaging of Lipids at High Lateral Resolution. *Int. J. Mass Spectrom.* **2018**. https://doi.org/10.1016/j.ijms.2018.09.015.

(98) Zavalin, A. I.; Yang, J.; Hayden, K.; Vestal, M.; Caprioli, R. M. Tissue Protein Imaging at 1 Mm Laser Spot Diameter for High Spatial Resolution and High Imaging Speed Using Transmission Geometry MALDI TOF MS. *Anal. Bioanal. Chem.* **2015**, *407* (8), 2337–2342. https://doi.org/10.1007/s00216-015-8532-6.

(99) Westman, A.; Huth-Fehre, T.; Demirev, P.; Bielawski, J.; Medina, N.; Sundqvist, B. U. R.; Karas, M. Matrix-Assisted Laser Desorption/Ionization: Dependence of the Ion Yield on the Laser Beam Incidence Angle. *Rapid Commun. Mass Spectrom.* **1994**, *8* (5), 388–393. https://doi.org/10.1002/rcm.1290080510.

(100) Schürenberg, M.; Schulz, T.; Dreisewerd, K.; Hillenkamp, F. Matrix-Assisted Laser Desorption/Ionization in Transmission Geometry: Instrumental Implementation and Mechanistic Implications. *Rapid Commun. Mass Spectrom.* **1996**, *10* (15), 1873–1880. https://doi.org/10.1002/(SICI)1097-0231(199612)10:15<1873::AID-RCM719>3.0.CO;2-3.

(101) Zavalin, A. I.; Todd, E. M.; Rawhouser, P. D.; Yang, J.; Norris, J. L.; Caprioli, R. M. Direct Imaging of Single Cells and Tissue at Sub-Cellular Spatial Resolution Using Transmission Geometry MALDI MS. *J. Mass Spectrom.* **2012**, *47* (11), 1473–1481. https://doi.org/10.1002/jms.3108.

(102) Thiery-Lavenant, G.; Zavalin, A. I.; Caprioli, R. M. Targeted Multiplex Imaging Mass Spectrometry in Transmission Geometry for Subcellular Spatial Resolution. *J. Am. Soc. Mass Spectrom.* **2013**, *24* (4), 609–614. https://doi.org/10.1007/s13361-012-0563-z.

(103) Kim, J. Y.; Lee, S. Y.; Kim, H.; Park, J.-W.; Lim, D.-K.; Moon, D. W. Biomolecular Imaging of Regeneration of Zebrafish Caudal Fins Using High Spatial Resolution Ambient Mass Spectrometry. *Anal. Chem.* **2018**, acs.analchem.8b03066. https://doi.org/10.1021/acs.analchem.8b03066.

(104) Hillenkamp, F.; Karas, M. The MALDI Process and Method. In *MALDI MS*; Wiley-VCH Verlag GmbH & Co. KGaA: Weinheim, Germany, 2014; pp 1–28. https://doi.org/10.1002/9783527610464.ch1.

(105) Knochenmuss, R.; Karbach, V.; Wiesli, U.; Breuker, K.; Zenobi, R. The Matrix Suppression Effect in Matrix-Assisted Laser

Desorption/Ionization: Application to Negative Ions and Further Characteristics. *Rapid Commun. Mass Spectrom.* **1998**, *12* (9), 529–534. https://doi.org/10.1002/(SICI)1097-0231(19980515)12:9<529::AID-RCM188>3.0.CO;2-E.

(106) Knochenmuss, R.; Stortelder, A.; Breuker, K.; Zenobi, R. Secondary Ion-Molecule Reactions in Matrix-Assisted Laser Desorption/Ionization. *J. Mass Spectrom.* **2000**, *35* (11), 1237–1245. https://doi.org/10.1002/1096-9888(200011)35:11<1237::AID-JMS74>3.0.CO;2-O.

(107) Knochenmuss, R. A Quantitative Model of Ultraviolet Matrix-Assisted Laser Desorption/Ionization Including Analyte Ion Generation. *Anal. Chem.* **2003**, *75* (10), 2199–2207. https://doi.org/10.1021/ac034032r.

(108) Knochenmuss, R. A Bipolar Rate Equation Model of MALDI Primary and Secondary Ionization Processes, with Application to Positive/Negative Analyte Ion Ratios and Suppression Effects. *Int. J. Mass Spectrom.* **2009**, *285* (3), 105–113. https://doi.org/10.1016/j.ijms.2009.05.002.

(109) Swales, J. G.; Dexter, A.; Hamm, G.; Nilsson, A.; Strittmatter, N.; Michopoulos, F.; Hardy, C.; Morentin-Gutierrez, P.; Mellor, M.; Andrén, P. E.; et al. Quantitation of Endogenous Metabolites in Mouse Tumors Using Mass-Spectrometry Imaging. *Anal. Chem.* **2018**, *90* (10), 6051–6058. https://doi.org/10.1021/acs.analchem.7b05239.

(110) Dai, Y.; Whittal, R. M.; Li, L. Two-Layer Sample Preparation: A Method for MALDI-MS Analysis of Complex Peptide and Protein Mixtures. *Anal. Chem.* **1999**, *71* (5), 1087–1091. https://doi.org/10.1021/ac980684h.

(111) Chapman, J. R. *Mass Spectrometry of Proteins and Peptides*; Humana Press: New Jersey, 2000; Vol. 146. https://doi.org/10.1385/1592590454.

(112) Allwood, D. A.; Perera, I. K.; Perkins, J.; Dyer, P. E.; Oldershaw, G. A. Preparation of 'near' Homogeneous Samples for the Analysis of Matrix-Assisted Laser Desorption/Ionisation Processes. *Appl. Surf. Sci.* **1996**, *103* (3), 231–244. https://doi.org/10.1016/0169-4332(96)00530-2.

(113) Kudina, O.; Eral, B.; Mugele, F. E-MALDI: An Electrowetting-Enhanced Drop Drying Method for MALDI Mass Spectrometry. *Anal. Chem.* **2016**, 1–16. https://doi.org/10.1021/acs.analchem.5b04283.

(114) Lai, Y.-H.; Cai, Y.-H.; Lee, H.; Ou, Y.-M.; Hsiao, C.-H.; Tsao, C.-W.; Chang, H.-T.; Wang, Y.-S. Reducing Spatial Heterogeneity of MALDI Samples with Marangoni Flows During Sample Preparation. *J. Am. Soc. Mass Spectrom.* **2016**, *27* (8), 1314–1321. https://doi.org/10.1007/s13361-016-1406-0.

(115) Trimpin, S.; Keune, S.; Räder, H. J.; Müllen, K. Solvent-Free MALDI-MS: Developmental Improvements in the Reliability and the Potential of

MALDI in the Analysis of Synthetic Polymers and Giant Organic Molecules. *J. Am. Soc. Mass Spectrom.* **2006**, *17* (5), 661–671. https://doi.org/10.1016/j.jasms.2006.01.007.

(116) Trimpin, S.; Räder, H. J.; Müllen, K. Investigations of Theoretical Principles for MALDI-MS Derived from Solvent-Free Sample Preparation. Part I. Preorganization. *Int. J. Mass Spectrom.* **2006**, *253* (1–2), 13–21. https://doi.org/10.1016/j.ijms.2005.10.008.

(117) Hanton, S. D.; Parees, D. M. Extending the Solvent-Free MALDI Sample Preparation Method. *J. Am. Soc. Mass Spectrom.* **2005**, *16* (1), 90–93. https://doi.org/10.1016/j.jasms.2004.09.019.

(118) Hanton, S. D.; McEvoy, T. M.; Stets, J. R. Imaging the Morphology of Solvent-Free Prepared MALDI Samples. *J. Am. Soc. Mass Spectrom.* **2008**, *19* (6), 874–881. https://doi.org/10.1016/j.jasms.2008.02.009.

(119) Anderton, C. R.; Chu, R. K.; Tolić, N.; Creissen, A.; Paša-Tolić, L. Utilizing a Robotic Sprayer for High Lateral and Mass Resolution MALDI FT-ICR MSI of Microbial Cultures. *J. Am. Soc. Mass Spectrom.* **2016**, *27* (3), 556–559. https://doi.org/10.1007/s13361-015-1324-6.

(120) Chen, Y.; Allegood, J.; Liu, Y.; Wang, E.; Cachón-González, B.; Cox, T. M.; Merrill, A. H.; Sullards, M. C. Imaging MALDI Mass Spectrometry Using an Oscillating Capillary Nebulizer Matrix Coating System and Its Application to Analysis of Lipids in Brain from a Mouse Model of Tay-Sachs/Sandhoff Disease. *Anal. Chem.* **2008**, *80* (8), 2780–2788. https://doi.org/10.1021/ac702350g.

(121) Hanton, S. D.; Hyder, I. Z.; Stets, J. R.; Owens, K. G.; Blair, W. R.; Guttman, C. M.; Giuseppetti, A. A. Investigations of Electrospray Sample Deposition for Polymer MALDI Mass Spectrometry. *J. Am. Soc. Mass Spectrom.* **2004**, *15* (2), 168–179. https://doi.org/10.1016/j.jasms.2003.09.012.

(122) Li, S.; Zhang, Y.; Liu, J.; Han, J.; Guan, M.; Yang, H.; Lin, Y.; Xiong, S.; Zhao, Z. Electrospray Deposition Device Used to Precisely Control the Matrix Crystal to Improve the Performance of MALDI MSI. *Sci. Rep.* **2016**, *6* (June), 1–10. https://doi.org/10.1038/srep37903.

(123) Aerni, H.-R.; Cornett, D. S.; Caprioli, R. M. Automated Acoustic Matrix Deposition for MALDI Sample Preparation. *Anal. Chem.* **2006**, *78* (3), 827–834. https://doi.org/10.1021/ac051534r.

(124) Urbanek, A.; Hölzer, S.; Knop, K.; Schubert, U. S.; von Eggeling, F. Multigrid MALDI Mass Spectrometry Imaging (MMALDI MSI). *Anal. Bioanal. Chem.* **2016**, *408* (14), 3769–3781. https://doi.org/10.1007/s00216-016-9465-4.

(125) Delaney, J. T.; Urbanek, A.; Wehder, L.; Perelaer, J.; Crecelius, A. C.; Von Eggeling, F.; Schubert, U. S. Combinatorial Optimization of Multiple MALDI Matrices on a Single Tissue Sample Using Inkjet Printing. *ACS Comb. Sci.* **2011**, *13* (3), 218–222. https://doi.org/10.1021/co100024d.

(126) Hankin, J. a.; Barkley, R. M.; Murphy, R. C. Sublimation as a Method of Matrix Application for Mass Spectrometric Imaging. *J. Am. Soc. Mass Spectrom.* **2007**, *18*, 1646–1652. https://doi.org/10.1016/j.jasms.2007.06.010.

(127) Murphy, R. C.; Hankin, J. a; Barkley, R. M. Imaging of Lipid Species by MALDI Mass Spectrometry. *J. Lipid Res.* **2008**, *50* (Supplement), S317–S322. https://doi.org/10.1194/jlr.R800051-JLR200.

(128) Murphy, R. C.; Hankin, J. A.; Barkley, R. M.; Zemski Berry, K. A. MALDI Imaging of Lipids after Matrix Sublimation/Deposition. *Biochim. Biophys. Acta - Mol. Cell Biol. Lipids* **2011**, *1811* (11), 970–975. https://doi.org/10.1016/j.bbalip.2011.04.012.

(129) Puolitaival, S. M.; Burnum, K. E.; Cornett, D. S.; Caprioli, R. M. Solvent-Free Matrix Dry-Coating for MALDI Imaging of Phospholipids. *J. Am. Soc. Mass Spectrom.* **2008**, *19* (6), 882–886. https://doi.org/10.1016/j.jasms.2008.02.013.

(130) Goodwin, R. J. A.; MacKay, C. L.; Nilsson, A.; Harrison, D. J.; Farde, L.; Andren, P. E.; Iverson, S. L. Qualitative and Quantitative MALDI Imaging of the Positron Emission Tomography Ligands Raclopride (a D2 Dopamine Antagonist) and SCH 23390 (a D1 Dopamine Antagonist) in Rat Brain Tissue Sections Using a Solvent-Free Dry Matrix Application Method. *Anal. Chem.* **2011**, *83* (24), 9694–9701. https://doi.org/10.1021/ac202630t.

(131) Van Nuffel, S.; Elie, N.; Yang, E.; Nouet, J.; Touboul, D.; Chaurand, P.; Brunelle, A. Insights into the MALDI Process after Matrix Deposition by Sublimation Using 3D ToF-SIMS Imaging. *Anal. Chem.* **2018**, acs.analchem.7b03993. https://doi.org/10.1021/acs.analchem.7b03993.

(132) Yang, J.; Caprioli, R. M. Matrix Sublimation/Recrystallization for Imaging Proteins by Mass Spectrometry at High Spatial Resolution. *Anal. Chem.* **2011**, *83* (14), 5728–5734. https://doi.org/10.1021/ac200998a.

(133) Bouschen, W.; Schulz, O.; Eikely, D.; Spengler, B.; Eikel, D.; Spengler, B. Matrix Vapor Deposition/Recrystallization and Dedicated Spray Preparation for High-Resolution Scanning Microprobe Matrix-Assisted Laser Desorption/Ionization Imaging Mass Spectrometry (SMALDI-MS) of Tissue and Single Cells. *Rapid Commun. Mass Spectrom.* **2010**, *24* (3), 355–364. https://doi.org/10.1002/rcm.4401.

(134) Dueñas, M. E.; Carlucci, L.; Lee, Y. J. Matrix Recrystallization for MALDI-

MS Imaging of Maize Lipids at High-Spatial Resolution. *J. Am. Soc. Mass Spectrom.* **2016**, 5–8. https://doi.org/10.1007/s13361-016-1422-0.

(135) Cohen, S. L.; Chait, B. T. Influence of Matrix Solution Conditions on the MALDI-MS Analysis of Peptides and Proteins. *Anal. Chem.* **1996**, *68* (1), 31–37. https://doi.org/10.1021/ac9507956.

(136) Leite, J. F.; Hajivandi, M. R.; Diller, T.; Pope, R. M. Removal of Sodium and Potassium Adducts Using a Matrix Additive during Matrix-Associated Laser Desorption/Ionization Time-of-Flight Mass Spectrometric Analysis of Peptides. *Commun. MASS Spectrom. Rapid Commun. Mass Spectrom* **2004**, *18*, 2953–2959. https://doi.org/10.1002/rcm.1711.

(137) Kim, J. S.; Kim, J. Y.; Kim, H. J. Suppression of Matrix Clusters and Enhancement of Peptide Signals in MALDI-TOF Mass Spectrometry Using Nitrilotriacetic Acid. *Anal. Chem.* **2005**, *77* (22), 7483–7488. https://doi.org/10.1021/ac051152l.

(138) Cerruti, C. D.; Touboul, D.; Guérineau, V.; Petit, V. W.; Laprévote, O.; Brunelle, A. MALDI Imaging Mass Spectrometry of Lipids by Adding Lithium Salts to the Matrix Solution. https://doi.org/10.1007/s00216-011-4814-9.

(139) Griffiths, R. L.; Bunch, J. A Survey of Useful Salt Additives in Matrix-Assisted Laser Desorption/Ionization Mass Spectrometry and Tandem Mass Spectrometry of Lipids: Introducing Nitrates for Improved Analysis. *Rapid Commun. Mass Spectrom.* **2012**, *26* (13), 1557–1566. https://doi.org/10.1002/rcm.6258.

(140) Frankevich, V. E.; Zhang, J.; Friess, S. D.; Dashtiev, M.; Zenobi, R. Role of Electrons in Laser Desorption/Ionization Mass Spectrometry. *Anal. Chem.* **2003**, *75* (22), 6063–6067. https://doi.org/10.1021/ac034436j.

(141) McCombie, G.; Knochenmuss, R. Enhanced MALDI Ionization Efficiency at the Metal-Matrix Interface: Practical and Mechanistic Consequences of Sample Thickness and Preparation Method. *J. Am. Soc. Mass Spectrom.* **2006**, *17* (5), 737–745. https://doi.org/10.1016/j.jasms.2006.02.005.

(142) Knochenmuss, R.; McCombie, G.; Faderl, M. Ion Yields of Thin MALDI Samples: Dependence on Matrix and Metal Substrate and Implications for Models. *J. Phys. Chem. A* **2006**, *110* (47), 12728–12733. https://doi.org/10.1021/jp064760t.

(143) Hamm, G.; Bonnel, D.; Legouffe, R.; Pamelard, F.; Delbos, J.-M.; Bouzom, F.; Stauber, J. Quantitative Mass Spectrometry Imaging of Propranolol and Olanzapine Using Tissue Extinction Calculation as Normalization Factor ☆. *J. Proteomics* **2012**, *75*, 4952–4961. https://doi.org/10.1016/j.jprot.2012.07.035.

(144) Taylor, A. J.; Dexter, A.; Bunch, J. Exploring Ion Suppression in Mass Spectrometry Imaging of a Heterogeneous Tissue. *Anal. Chem.* **2018**, *90* (9), 5637–5645. https://doi.org/10.1021/acs.analchem.7b05005.

(145) Zhigilei, L. V. Dynamics of the Plume Formation and Parameters of the Ejected Clusters in Short-Pulse Laser Ablation. *Appl. Phys. A Mater. Sci. Process.* **2003**, *76* (3), 339–350. https://doi.org/10.1007/s00339-002-1818-5.

(146) Handschuh, M.; Nettesheim, S.; Zenobi, R. Laser-Induced Molecular Desorption and Particle Ejection from Organic Films. *Appl. Surf. Sci.* **1999**, *137* (1–4), 125–135. https://doi.org/10.1016/S0169-4332(98)00379-1.

(147) Jackson, S. N.; Mishra, S.; Murray, K. K. Characterization of Coarse Particles Formed by Laser Ablation of MALDI Matrixes. *J. Phys. Chem. B* **2003**, *107* (47), 13106–13110. https://doi.org/10.1021/jp030600v.

(148) Musapelo, T.; Murray, K. K. Particle Production in Reflection and Transmission Mode Laser Ablation: Implications for Laserspray Ionization. *J. Am. Soc. Mass Spectrom.* **2013**, *24* (7), 1108–1115. https://doi.org/10.1007/s13361-013-0631-z.

(149) Schürenberg, M.; Dreisewerd, K.; Kamanabrou, S.; Hillenkamp, F. Influence of the Sample Temperature on the Desorption of Matrix Molecules and Ions in Matrix-Assisted Laser Desorption Ionization. *Int. J. Mass Spectrom. Ion Process.* **1998**, *172* (1–2), 89–94. https://doi.org/10.1016/S0168-1176(97)00253-X.

(150) Rohlfing, A.; Leisner, A.; Hillenkamp, F.; Dreisewerd, K. Investigation of the Desorption Process in UV Matrix-Assisted Laser Desorption/Ionization with a Liquid 3-Nitrobenzyl Alcohol Matrix by Photoacoustic Analysis, Fast-Flash Imaging, and UV-Laser Postionization †. *J. Phys. Chem. C* **2010**, *114* (12), 5367–5381. https://doi.org/10.1021/jp905251r.

(151) Zenobi, R.; Knochenmuss, R. Ion Formation in MALDI Mass Spectrometry. *Mass Spectrom. Rev.* **1998**, *17*, 337–366. https://doi.org/10.1002/(SICI)1098-2787(1998)17:5<337::AID-MAS2>3.3.CO;2-J.

(152) Knochenmuss, R. A Quantitative Model of Ultraviolet Matrix-Assisted Laser Desorption/Ionization. *J. Mass Spectrom.* **2002**, *37* (8), 867–877. https://doi.org/10.1002/jms.349.

(153) Knochenmuss, R. MALDI Ionization Mechanisms: The Coupled Photophysical and Chemical Dynamics Model Correctly Predicts 'Temperature'-Selected Spectra. *J. Mass Spectrom.* **2013**, *48* (9), 998–1004. https://doi.org/10.1002/jms.3248.

(154) Setz, P. D.; Knochenmuss, R. Exciton Mobility and Trapping in a MALDI Matrix. *J. Phys. Chem. A* **2005**, *109* (18), 4030–4037. https://doi.org/10.1021/jp050622c.

(155) Knochenmuss, R. Positive/Negative Ion Ratios and in-Plume Reaction Equilibria in MALDI. *Int. J. Mass Spectrom.* **2008**, *273* (1–2), 84–86. https://doi.org/10.1016/j.ijms.2008.03.004.

(156) Knochenmuss, R.; Zhigilei, L. V. What Determines MALDI Ion Yields? A Molecular Dynamics Study of Ion Loss Mechanisms. *Anal. Bioanal. Chem.* **2012**, *402* (8), 2511–2519. https://doi.org/10.1007/s00216-011-5194-x.

(157) Bökelmann, V.; Spengler, B.; Kaufmann, R. Dynamical Parameters of Ion Ejection and Ion Formation in Matrix- Assisted Laser Desorption/Ionization. *Eur. J. Mass Spectrom.* **1995**, *1* (1), 81. https://doi.org/10.1255/ejms.163.

(158) Guenther, S.; Koestler, M.; Schulz, O.; Spengler, B. Laser Spot Size and Laser Power Dependence of Ion Formation in High Resolution MALDI Imaging. *Int. J. Mass Spectrom.* **2010**, *294* (1), 7–15. https://doi.org/10.1016/j.ijms.2010.03.014.

(159) Wallace, W. E.; Arnould, M. A.; Knochenmuss, R. 2,5-Dihydroxybenzoic Acid: Laser Desorption/Ionisation as a Function of Elevated Temperature. *Int. J. Mass Spectrom.* **2005**, *242* (1), 13–22. https://doi.org/10.1016/j.ijms.2004.11.011.

(160) Jaskolla, T. W.; Karas, M. Compelling Evidence for Lucky Survivor and Gas Phase Protonation: The Unified MALDI Analyte Protonation Mechanism. *J. Am. Soc. Mass Spectrom.* **2011**, *22* (6), 976–988. https://doi.org/10.1007/s13361-011-0093-0.

(161) Karas, M.; Glückmann, M.; Schäfer, J. Ionization in Matrix-Assisted Laser Desorption/Ionization: Singly Charged Molecular Ions Are the Lucky Survivors. *J. Mass Spectrom.* **2000**, *35* (1), 1–12. https://doi.org/10.1002/(SICI)1096-9888(200001)35:1<1::AID-JMS904>3.0.CO;2-0.

(162) Karas, M.; Krüger, R. Ion Formation in MALDI: The Cluster Ionization Mechanism. *Chem. Rev.* **2003**, *103* (2), 427–440. https://doi.org/10.1021/cr010376a.

(163) Krüger, R.; Pfenninger, A.; Fournier, I.; Glückmann, M.; Karas, M. Analyte Incorporation and Ionization in Matrix-Assisted Laser Desorption/Ionization Visualized by PH Indicator Molecular Probes. *Anal. Chem.* **2001**, *73* (24), 5812–5821. https://doi.org/10.1021/ac010827r.

(164) Krüger, R.; Karas, M. Formation and Fate of Ion Pairs during MALDI Analysis: Anion Adduct Generation as an Indicative Tool to Determine Ionization Processes. *J. Am. Soc. Mass Spectrom.* **2002**, *13* (10), 1218–1226. https://doi.org/10.1016/S1044-0305(02)00450-6.

(165) Trimpin, S.; Inutan, E. D. Matrix Assisted Ionization in Vacuum, a Sensitive and Widely Applicable Ionization Method for Mass Spectrometry. *J. Am. Soc. Mass Spectrom.* **2013**, *24* (5), 722–732. https://doi.org/10.1007/s13361-012-0571-z.

(166) Trimpin, S. "Magic" Ionization Mass Spectrometry. *J. Am. Soc. Mass Spectrom.* **2016**, *27* (1), 4–21. https://doi.org/10.1007/s13361-015-1253-4.

(167) Ahn, S. H.; Park, K. M.; Bae, Y. J.; Kim, M. S. Quantitative Reproducibility of Mass Spectra in Matrix-Assisted Laser Desorption Ionization and Unraveling of the Mechanism for Gas-Phase Peptide Ion Formation. *J. Mass Spectrom.* **2013**, *48* (3), 299–305. https://doi.org/10.1002/jms.3155.

(168) Chu, K. Y.; Lee, S.; Tsai, M. T.; Lu, I. C.; Dyakov, Y. A.; Lai, Y. H.; Lee, Y. T.; Ni, C.-K. Thermal Proton Transfer Reactions in Ultraviolet Matrix-Assisted Laser Desorption/Ionization. *J. Am. Soc. Mass Spectrom.* **2014**, *25* (3), 310–318. https://doi.org/10.1007/s13361-013-0792-9.

(169) Lu, I.-C.; Chu, K. Y.; Lin, C.-Y.; Wu, S.-Y.; Dyakov, Y. a.; Chen, J.-L.; Gray-Weale, A.; Lee, Y.-T.; Ni, C.-K. Ion-to-Neutral Ratios and Thermal Proton Transfer in Matrix-Assisted Laser Desorption/Ionization. *J. Am. Soc. Mass Spectrom.* **2015**, *26* (7), 1242–1251. https://doi.org/10.1007/s13361-015-1112-3.

(170) Tsai, M. T.; Lee, S.; Lu, I. C.; Chu, K. Y.; Liang, C. W.; Lee, C. H.; Lee, Y. T.; Ni, C.-K. Ion-to-Neutral Ratio of 2,5-Dihydroxybenzoic Acid in Matrix-Assisted Laser Desorption/Ionization. *Rapid Commun. Mass Spectrom.* **2013**, *27* (9), 955–963. https://doi.org/10.1002/rcm.6534.

(171) Yukihira, D.; Miura, D.; Saito, K.; Takahashi, K.; Wariishi, H. MALDI−MS-Based High-Throughput Metabolite Analysis for Intracellular Metabolic Dynamics. *Anal. Chem.* **2010**, *82* (10), 4278–4282. https://doi.org/10.1021/ac100024w.

(172) Pan, S.; Zhang, H.; Rush, J.; Eng, J.; Zhang, N.; Patterson, D.; Comb, M. J.; Aebersold, R. High Throughput Proteome Screening for Biomarker Detection. *Mol. Cell. Proteomics* **2005**, *4* (2), 182–190. https://doi.org/10.1074/mcp.M400161-MCP200.

(173) Stanssens, P. High-Throughput MALDI-TOF Discovery of Genomic Sequence Polymorphisms. *Genome Res.* **2003**, *14* (1), 126–133. https://doi.org/10.1101/gr.1692304.

(174) Wieser, A.; Schneider, L.; Jung, J.; Schubert, S. MALDI-TOF MS in Microbiological Diagnostics—Identification of Microorganisms and beyond (Mini Review). *Appl. Microbiol. Biotechnol.* **2012**, *93* (3), 965–974. https://doi.org/10.1007/s00253-011-3783-4.

(175) Opota, O.; Prod'hom, G.; Greub, G. Applications of MALDI-TOF Mass Spectrometry in Clinical Diagnostic Microbiology. In *MALDI-TOF and Tandem MS for Clinical Microbiology*; Oxford University Press, 2016; Vol. 36, pp 55–92. https://doi.org/10.1002/9781118960226.ch3.

(176) Nilsson, A.; Goodwin, R. J. A.; Shariatgorji, M.; Vallianatou, T.; Webborn, P. J. H.; Andrén, P. E. Mass Spectrometry Imaging in Drug Development. *Anal. Chem.* **2015**, *87* (3), 1437–1455. https://doi.org/10.1021/ac504734s.

(177) Khatib-shahidi, S.; Andersson, M.; Herman, J. L.; Gillespie, T. a; Caprioli, R. M. Direct Molecular Analysis of Whole-Body Animal Tissue Sections by Imaging MALDI Mass Spectrometry Direct Molecular Analysis of Whole-Body Animal Tissue Sections by Imaging MALDI Mass Spectrometry. *Anal. Chem.* **2006**, *78* (18), 6448–6456. https://doi.org/10.1021/ac060788p.

(178) Rauser, S.; Marquardt, C.; Balluff, B.; Deininger, S.-O.; Albers, C.; Belau, E.; Hartmer, R.; Suckau, D.; Specht, K.; Ebert, M. P.; et al. Classification of HER2 Receptor Status in Breast Cancer Tissues by MALDI Imaging Mass Spectrometry. *J. Proteome Res.* **2010**, *9* (4), 1854–1863. https://doi.org/10.1021/pr901008d.

(179) Mirnezami, R.; Spagou, K.; Vorkas, P. A.; Lewis, M. R.; Kinross, J.; Want, E.; Shion, H.; Goldin, R. D.; Darzi, A.; Takats, Z.; et al. Chemical Mapping of the Colorectal Cancer Microenvironment via MALDI Imaging Mass Spectrometry (MALDI-MSI) Reveals Novel Cancer-Associated Field Effects. *Mol. Oncol.* **2014**, *8* (1), 39–49. https://doi.org/10.1016/j.molonc.2013.08.010.

(180) Buck, A.; Ly, A.; Balluff, B.; Sun, N.; Gorzolka, K.; Feuchtinger, A.; Janssen, K.-P.; Kuppen, P. J.; van de Velde, C. J.; Weirich, G.; et al. High-Resolution MALDI-FT-ICR MS Imaging for the Analysis of Metabolites from Formalin-Fixed, Paraffin-Embedded Clinical Tissue Samples. *J. Pathol.* **2015**, *237* (1), 123–132. https://doi.org/10.1002/path.4560.

(181) Carlred, L.; Michno, W.; Kaya, I.; Sjövall, P.; Syvänen, S.; Hanrieder, J. Probing Amyloid-β Pathology in Transgenic Alzheimer's Disease (TgArcSwe) Mice Using MALDI Imaging Mass Spectrometry. *J. Neurochem.* **2016**. https://doi.org/10.1111/jnc.13645.

(182) Ruh, H.; Salonikios, T.; Fuchser, J.; Schwartz, M.; Sticht, C.; Hochheim, C.; Wirnitzer, B.; Gretz, N.; Hopf, C. MALDI Imaging MS Reveals Candidate Lipid Markers of Polycystic Kidney Disease. *J. Lipid Res.* **2013**, *54* (10),

2785–2794. https://doi.org/10.1194/jlr.M040014.

(183) Wolstenholme, R.; Bradshaw, R.; Clench, M. R.; Francese, S. Study of Latent Fingermarks by Matrix-Assisted Laser Desorption/Ionisation Mass Spectrometry Imaging of Endogenous Lipids. *Rapid Commun. Mass Spectrom.* **2009**, *23* (19), 3031–3039. https://doi.org/10.1002/rcm.4218.

(184) Groeneveld, G.; de Puit, M.; Bleay, S.; Bradshaw, R.; Francese, S. Detection and Mapping of Illicit Drugs and Their Metabolites in Fingermarks by MALDI MS and Compatibility with Forensic Techniques. *Sci. Rep.* **2015**, *5* (1), 11716. https://doi.org/10.1038/srep11716.

(185) Scotcher, K.; Bradshaw, R. The Analysis of Latent Fingermarks on Polymer Banknotes Using MALDI-MS. *Sci. Rep.* **2018**, *8* (1), 8765. https://doi.org/10.1038/s41598-018-27004-0.

(186) Ferguson, L. S.; Wulfert, F.; Wolstenholme, R.; Fonville, J. M.; Clench, M. R.; Carolan, V. A.; Francese, S. Direct Detection of Peptides and Small Proteins in Fingermarks and Determination of Sex by MALDI Mass Spectrometry Profiling. *Analyst* **2012**, *137* (20), 4686. https://doi.org/10.1039/c2an36074h.

(187) Francese, S.; Bradshaw, R.; Denison, N. An Update on MALDI Mass Spectrometry Based Technology for the Analysis of Fingermarks-Stepping into Operational Deployment. *Analyst*. The Royal Society of Chemistry July 10, 2017, pp 2518–2546. https://doi.org/10.1039/c7an00569e.

(188) Monroe, E. B.; Annangudi, S. P.; Hatcher, N. G.; Gutstein, H. B.; Rubakhin, S. S.; Sweedler, J. V. SIMS and MALDI MS Imaging of the Spinal Cord. *Proteomics* **2008**, *8* (18), 3746–3754. https://doi.org/10.1002/pmic.200800127.

(189) Lanni, E. J.; Masyuko, R. N.; Driscoll, C. M.; Aerts, J. T.; Shrout, J. D.; Bohn, P. W.; Sweedler, J. V. MALDI-Guided SIMS: Multiscale Imaging of Metabolites in Bacterial Biofilms. *Anal. Chem.* **2014**, *86* (18), 9139–9145. https://doi.org/10.1021/ac5020222.

(190) Eberlin, L. S.; Liu, X.; Ferreira, C. R.; Santagata, S.; Agar, N. Y. R.; Cooks, R. G. Desorption Electrospray Ionization Then MALDI Mass Spectrometry Imaging of Lipid and Protein Distributions in Single Tissue Sections. *Anal. Chem.* **2011**, *83* (22), 8366–8371. https://doi.org/10.1021/ac202016x.

(191) Siegel, T. P.; Hamm, G.; Bunch, J.; Cappell, J.; Fletcher, J. S.; Schwamborn, K. Mass Spectrometry Imaging and Integration with Other Imaging Modalities for Greater Molecular Understanding of Biological Tissues. *Mol Imaging Biol* **2018**. https://doi.org/10.1007/s11307-018-1267-y.

(192) Randall, E. C.; Race, A. M.; Cooper, H. J.; Bunch, J. MALDI Imaging of Liquid Extraction Surface Analysis Sampled Tissue. *Anal. Chem.* **2016**, *88* (17), 8433–8440. https://doi.org/10.1021/acs.analchem.5b04281.

(193) Kim, A. J.; Basu, S.; Glass, C.; Ross, E. L.; Agar, N.; He, Q.; Calligaris, D. Unique Intradural Inflammatory Mass Containing Precipitated Morphine: Confirmatory Analysis by LESA-MS and MALDI-MS. *Pain Pract.* **2018**, *18* (7), 889–894. https://doi.org/10.1111/papr.12688.

(194) Attia, A. S.; Schroeder, K. A.; Seeley, E. H.; Wilson, K. J.; Hammer, N. D.; Colvin, D. C.; Manier, M. L.; Nicklay, J. J.; Rose, K. L.; Gore, J. C.; et al. Monitoring the Inflammatory Response to Infection through the Integration of MALDI IMS and MRI. *Cell Host Microbe* **2012**, *11* (6), 664–673. https://doi.org/10.1016/j.chom.2012.04.018.

(195) Henderson, F.; Hart, P. J.; Pradillo, J. M.; Kassiou, M.; Christie, L.; Williams, K. J.; Boutin, H.; McMahon, A. Multi-Modal Imaging of Long-Term Recovery Post-Stroke by Positron Emission Tomography and Matrix-Assisted Laser Desorption/Ionisation Mass Spectrometry. *Rapid Commun. Mass Spectrom.* **2018**, *32* (9), 721–729. https://doi.org/10.1002/rcm.8090.

(196) Karas, M.; Bahr, U. Laser Desorption Ionization Mass Spectrometry of Large Biomolecules. *TrAC Trends Anal. Chem.* **1990**, *9* (10), 321–325. https://doi.org/10.1016/0165-9936(90)85065-F.

(197) Furey, A.; Moriarty, M.; Bane, V.; Kinsella, B.; Lehane, M. Ion Suppression; A Critical Review on Causes, Evaluation, Prevention and Applications. *Talanta* **2013**, *115*, 104–122. https://doi.org/10.1016/j.talanta.2013.03.048.

(198) Jespersen, S.; Niessen, W. M.; Tjaden, U. R.; van der Greef, J. Basic Matrices in the Analysis of Non-Covalent Complexes by Matrix-Assisted Laser Desorption/Ionization Mass Spectrometry. *J. Mass Spectrom.* **1998**, *33* (11), 1088–1093. https://doi.org/10.1002/(SICI)1096-9888(199811)33:11<1088::AID-JMS725>3.0.CO;2-8.

(199) Fukuyama, Y.; Iwamoto, S.; Tanaka, K. Rapid Sequencing and Disulfide Mapping of Peptides Containing Disulfide Bonds by Using 1,5-Diaminonaphthalene as a Reductive Matrix. *J. Mass Spectrom.* **2006**, *41* (2), 191–201. https://doi.org/10.1002/jms.977.

(200) Xu, N.; Huang, Z.-H.; Watson, J. T.; Gagecor, D. A. Mercaptobenzothiazoles: A New Class of Matrices for Laser Desorption Ionization Mass Spectrometry. *J. Am. Soc. Mass Spectrom.* **1997**, *8* (2), 116–124. https://doi.org/10.1016/S1044-0305(96)00233-4.

(201) Le, C. H.; Han, J.; Borchers, C. H. Dithranol as a MALDI Matrix for Tissue Imaging of Lipids by Fourier Transform Ion Cyclotron Resonance Mass

Spectrometry. *Anal. Chem.* **2012**, *84* (19), 8391–8398. https://doi.org/10.1021/ac301901s.

(202) Pieles, U.; Zürcher, W.; Schär, M.; Moser, H. Matrix-Assisted Laser Desorption Ionization Time-of-Flight Mass Spectrometry: A Powerful Tool for the Mass and Sequence Analysis of Natural and Modified Oligonucleotides. *Nucleic Acids Res.* **1993**, *21* (14), 3191–3196. https://doi.org/10.1093/nar/21.14.3191.

(203) Wenzel, T.; Sparbier, K.; Mieruch, T.; Kostrzewa, M. 2,5-Dihydroxyacetophenone: A Matrix for Highly Sensitive Matrix-Assisted Laser Desorption/Ionization Time-of-Flight Mass Spectrometric Analysis of Proteins Using Manual and Automated Preparation Techniques. *Rapid Commun. Mass Spectrom.* **2006**, *20* (5), 785–789. https://doi.org/10.1002/rcm.2378.

(204) Jessome, L.; Hsu, N.-Y.; Wang, Y.-S.; Chen, C.-H. Matrix-Assisted Laser Desorption/Ionization Mechanism Study with Dihydroxybenzoic Acid Isomers as Matrices. *Rapid Commun. Mass Spectrom.* **2008**, *22* (2), 130–134. https://doi.org/10.1002/rcm.3343.

(205) Meier, M. a R.; Adams, N.; Schubert, U. S. Statistical Approach to Understand MALDI-TOFMS Matrices: Discovery and Evaluation of New MALDI Matrices. *Anal. Chem.* **2007**, *79* (3), 863–869. https://doi.org/10.1021/ac061173v.

(206) Steven, R. T.; Dexter, A.; Bunch, J. Investigating MALDI MSI Parameters (Part 2) – On the Use of a Mechanically Shuttered Trigger System for Improved Laser Energy Stability. *Methods* **2016**, *104*, 111–117. https://doi.org/10.1016/j.ymeth.2016.04.013.

(207) Steven, R. T.; Palmer, A. D.; Bunch, J. Fluorometric Beam Profiling of UV MALDI Lasers. *J. Am. Soc. Mass Spectrom.* **2013**, *24* (7), 1146–1152. https://doi.org/10.1007/s13361-013-0650-9.

(208) Schneider, C. A.; Rasband, W. S.; Eliceiri, K. W. NIH Image to ImageJ: 25 Years of Image Analysis. *Nat. Methods* **2012**, *9* (7), 671–675. https://doi.org/10.1038/nmeth.2089.

(209) Race, A. M.; Styles, I. B.; Bunch, J. Inclusive Sharing of Mass Spectrometry Imaging Data Requires a Converter for All. *J. Proteomics* **2012**, *75* (16), 5111–5112. https://doi.org/10.1016/j.jprot.2012.05.035.

(210) Race, A. M.; Palmer, A. D.; Dexter, A.; Steven, R. T.; Styles, I. B.; Bunch, J. SpectralAnalysis: Software for the Masses. *Anal. Chem.* **2016**, *88* (19), 9451–9458. https://doi.org/10.1021/acs.analchem.6b01643.

(211) Van Der Maaten, L.; Hinton, G. *Visualizing Data Using T-SNE*; 2008; Vol. 9.

(212) Belkina, A. C.; Ciccolella, C. O.; Anno, R.; Spidlen, J.; Halpert, R.; Snyder-Cappione, J. Automated Optimal Parameters for T-Distributed Stochastic Neighbor Embedding Improve Visualization and Allow Analysis of Large Datasets. *bioRxiv* **2018**, 451690. https://doi.org/10.1101/451690.

(213) Donegan, M.; Tomlinson, A. J.; Nair, H.; Juhasz, P. Controlling Matrix Suppression for Matrix-Assisted Laser Desorption/Ionization Analysis of Small Molecules. *Rapid Commun. Mass Spectrom.* **2004**, *18* (17), 1885–1888. https://doi.org/10.1002/rcm.1568.

(214) Martic, S.; Brennan, J. D.; Brook, M. a; Ackloo, S.; Nagy, N. Towards the Development of a Covalently Tethered MALDI System — A Study of Allyl-Modified MALDI Matrixes. *Can. J. Chem.* **2007**, *85* (1), 66–76. https://doi.org/10.1139/v06-185.

(215) Roepstorff, P.; Fohlman, J. Letter to the Editors. *Biol. Mass Spectrom.* **1984**, *11* (11), 601–601. https://doi.org/10.1002/bms.1200111109.

(216) Biemann, K. Contributions of Mass Spectrometry to Peptide and Protein Structure. *Biol. Mass Spectrom.* **1988**, *16* (1–12), 99–111. https://doi.org/10.1002/bms.1200160119.

(217) Blessington, B. Mass Spectra of Haloperidol and Related Neuroleptics (Major Tranquilisers). *Org. Mass Spectrom.* **1971**, *5* (9), 1113–1117. https://doi.org/10.1002/oms.1210050912.

(218) Jaskolla, T. W.; Onischke, K.; Schiller, J. 2,5-Dihydroxybenzoic Acid Salts for Matrix-Assisted Laser Desorption/Ionization Time-of-Flight Mass Spectrometric Lipid Analysis: Simplified Spectra Interpretation and Insights into Gas-Phase Fragmentation. *Rapid Commun. Mass Spectrom.* **2014**, *28* (12), 1353–1363. https://doi.org/10.1002/rcm.6910.

(219) Löhmann, C.; Schachmann, E.; Dandekar, T.; Villmann, C.; Becker, C.-M. Developmental Profiling by Mass Spectrometry of Phosphocholine Containing Phospholipids in the Rat Nervous System Reveals Temporo-Spatial Gradients. *J. Neurochem.* **2010**, *114* (4), no-no. https://doi.org/10.1111/j.1471-4159.2010.06836.x.

(220) Jovanović, M.; Peter-Katalinić, J. Negative Ion MALDI-TOF MS, ISD and PSD of Neutral Underivatized Oligosaccharides without Anionic Dopant Strategies, Using 2,5-DHAP as a Matrix. *J. Mass Spectrom.* **2016**, *51* (2), 111–122. https://doi.org/10.1002/jms.3727.

(221) Ehring, H.; Karas, M.; Hillenkamp, F. Role of Photoionization and Photochemistry in Ionization Processes of Organic Molecules and Relevance for Matrix-Assisted Laser Desorption Lonization Mass Spectrometry. *Org. Mass Spectrom.* **1992**, *27* (4), 472–480. https://doi.org/10.1002/oms.1210270419.

(222) Hsieh, Y.; Casale, R.; Fukuda, E.; Chen, J.; Knemeyer, I.; Wingate, J.; Morrison, R.; Korfmacher, W. Matrix-Assisted Laser Desorption/Ionization Imaging Mass Spectrometry for Direct Measurement of Clozapine in Rat Brain Tissue. *Rapid Commun. Mass Spectrom.* **2006**, *20* (6), 965–972. https://doi.org/10.1002/rcm.2397.

(223) Rheims, J.; Köser, J.; Wriedt, T. Refractive-Index Measurements in the near-IR Using an Abbe Refractometer. *Meas. Sci. Technol.* **1999**, *8* (6), 601–605. https://doi.org/10.1088/0957-0233/8/6/003.

(224) Kedenburg, S.; Vieweg, M.; Gissibl, T.; Giessen, H. Linear Refractive Index and Absorption Measurements of Nonlinear Optical Liquids in the Visible and Near-Infrared Spectral Region. *Opt. Mater. Express* **2012**, *2* (11), 1588. https://doi.org/10.1364/OME.2.001588.

(225) Schwoerer, M.; Wolf, H. C. *Organic Molecular Solids*; Schwoerer, M., Wolf, H. C., Eds.; Wiley-VCH Verlag GmbH: Weinheim, Germany, 2006. https://doi.org/10.1002/9783527618651.

(226) Reichardt, C.; Welton, T. *Solvents and Solvent Effects in Organic Chemistry*; Wiley-VCH Verlag GmbH & Co. KGaA: Weinheim, Germany, 2010. https://doi.org/10.1002/9783527632220.

(227) Flakus, H. T.; Miros, A.; Jones, P. G. Influence of Molecular Electronic Properties on the IR Spectra of Dimeric Hydrogen Bond Systems: Polarized Spectra of 2-Hydroxybenzothiazole and 2-Mercaptobenzothiazole Crystals. *J. Mol. Struct.* **2002**, *604* (1), 29–44. https://doi.org/10.1016/S0022-2860(01)00620-2.

(228) Tanaka, J. The Electronic Spectra of Aromatic Molecular Crystals. I. Substitued Benzene Molecules. *Bull. Chem. Soc. Jpn.* **1963**, *36* (7), 833–847. https://doi.org/10.1246/bcsj.36.833.

(229) Karas, M.; Bahr, U.; Strupat, K.; Hillenkamp, F.; Tsarbopoulos, A.; Pramanik, B. N. Matrix Dependence of Metastable Fragmentation of Glycoproteins in MALDI TOF Mass Spectrometry. *Anal. Chem.* **1995**, *67* (3), 675–679. https://doi.org/10.1021/ac00099a029.

(230) Stübiger, G.; Belgacem, O. Analysis of Lipids Using 2,4,6-Trihydroxyacetophenone as a Matrix for MALDI Mass Spectrometry. *Anal. Chem.* **2007**, *79* (8), 3206–3213. https://doi.org/10.1021/ac062236c.

(231) Liu, B.; Charkin, O. P.; Klemenko, N.; Chen, C. W.; Wang, Y. Initial Ionization Reaction in Matrix-Assisted Laser Desorption/Ionization. *J. Phys. Chem. B* **2010**, *114* (33), 10853–10859. https://doi.org/10.1021/jp104178m.

(232) Sadeghi, M.; Vertes, A. Crystallite Size Dependence of Volatilization in

Matrix-Assisted Laser Desorption Ionization. *Appl. Surf. Sci.* **1998**, *127–129*, 226–234. https://doi.org/10.1016/S0169-4332(97)00636-3.

(233) Roux, M. V.; Temprado, M.; Jiménez, P.; Foces-Foces, C.; Notario, R.; Parameswar, A. R.; Demchenko, A. V; Chickos, J. S.; Deakyne, C. a; Liebman, J. F. Experimental and Theoretical Study of the Structures and Enthalpies of Formation of 3 H -1,3-Benzoxazole-2-Thione, 3 H -1,3-Benzothiazole-2-Thione, and Their Tautomers. *J. Phys. Chem. A* **2010**, *114* (21), 6336–6341. https://doi.org/10.1021/jp102126j.

(234) Monte, M. J. S.; Gonçalves, M. V.; Ribeiro Da Silva, M. D. M. C. Vapor Pressures and Enthalpies of Combustion of the Dihydroxybenzoic Acid Isomers. *J. Chem. Eng. Data* **2010**, *55* (6), 2246–2251. https://doi.org/10.1021/je900777q.

(235) Astigarraga, E.; Barreda-Gómez, G.; Lombardero, L.; Fresnedo, O.; Castaño, F.; Giralt, M. T.; Ochoa, B.; Rodríguez-Puertas, R.; Fernández, J. A. Profiling and Imaging of Lipids on Brain and Liver Tissue by Matrix-Assisted Laser Desorption/Ionization Mass Spectrometry Using 2-Mercaptobenzothiazole as a Matrix. *Anal. Chem.* **2008**, *80* (23), 9105–9114. https://doi.org/10.1021/ac801662n.

(236) Fournier, I.; Marinach, C.; Tabet, J. C.; Bolbach, G. Irradiation Effects in MALDI, Ablation, Ion Production, and Surface Modifications. Part II: 2,5-Dihydroxybenzoic Acid Monocrystals. *J. Am. Soc. Mass Spectrom.* **2003**, *14* (8), 893–899. https://doi.org/10.1016/S1044-0305(03)00347-7.

(237) Knochenmuss, R. Energetics and Kinetics of Thermal Ionization Models of MALDI. *J. Am. Soc. Mass Spectrom.* **2014**, *25* (9), 1521–1527. https://doi.org/10.1007/s13361-014-0931-y.

(238) Knochenmuss, R. Ion Yields in the Coupled Chemical and Physical Dynamics Model of Matrix-Assisted Laser Desorption/Ionization. *J. Am. Soc. Mass Spectrom.* **2015**, *26* (10), 1645–1648. https://doi.org/10.1007/s13361-015-1225-8.

(239) Moon, J. H.; Shin, Y. S.; Bae, Y. J.; Kim, M. S. Ion Yields for Some Salts in MALDI: Mechanism for the Gas-Phase Ion Formation from Preformed Ions. *J. Am. Soc. Mass Spectrom.* **2012**, *23* (1), 162–170. https://doi.org/10.1007/s13361-011-0278-6.

(240) Bae, Y. J.; Shin, Y. S.; Moon, J. H.; Kim, M. S. Degree of Ionization in MALDI of Peptides: Thermal Explanation for the Gas-Phase Ion Formation. *J. Am. Soc. Mass Spectrom.* **2012**, *23* (8), 1326–1335. https://doi.org/10.1007/s13361-012-0406-y.

(241) Bae, Y. J.; Park, K. M.; Kim, M. S. Reproducibility of Temperature-Selected Mass Spectra in Matrix-Assisted Laser Desorption Ionization of Peptides. *Anal. Chem.* **2012**, *84* (16), 7107–7111.

https://doi.org/10.1021/ac3014077.

(242) Bae, Y. J.; Choe, J. C.; Moon, J. H.; Kim, M. S. Why Do the Abundances of Ions Generated by MALDI Look Thermally Determined? *J. Am. Soc. Mass Spectrom.* **2013**, *24* (11), 1807–1815. https://doi.org/10.1007/s13361-013-0717-7.

(243) Nečas, D.; Klapetek, P. Gwyddion: An Open-Source Software for SPM Data Analysis. *Open Phys.* **2012**, *10* (1), 181–188. https://doi.org/10.2478/s11534-011-0096-2.

(244) Kampmeier, J.; Dreisewerd, K.; Schürenberg, M.; Strupat, K. Investigations of 2,5-DHB and Succinic Acid as Matrices for IR and UV MALDI. Part: I UV and IR Laser Ablation in the MALDI Process. *Int. J. Mass Spectrom. Ion Process.* **1997**, *169–170* (97), 31–41. https://doi.org/10.1016/S0168-1176(97)00224-3.

(245) Cleveland, J. P.; Anczykowski, B.; Schmid, A. E.; Elings, V. B. Energy Dissipation in Tapping-Mode Atomic Force Microscopy. *Appl. Phys. Lett.* **1998**, *72* (20), 2613–2615. https://doi.org/10.1063/1.121434.

(246) Robinson, K. N.; Steven, R. T.; Bunch, J. Matrix Optical Absorption in UV-MALDI MS. *J. Am. Soc. Mass Spectrom.* **2018**, *29* (3), 501–511. https://doi.org/10.1007/s13361-017-1843-4.

(247) Chickos, J. S.; Hesse, D. G.; Liebman, J. F. *A Group Additivity Approach for the Estimation of Heat Capacities of Organic Liquids and Solids at 298 K*; 1993; Vol. 4.

(248) Koubenakis, A.; Frankevich, V.; Zhang, J.; Zenobi, R. Time-Resolved Surface Temperature Measurement of MALDI Matrices under Pulsed UV Laser Irradiation. *J. Phys. Chem. A* **2004**, *108* (13), 2405–2410. https://doi.org/10.1021/jp037811k.

(249) Mesaros, M.; Tarzi, O. I.; Erra-Balsells, R.; Bilmes, G. M. The Photophysics of Some UV-MALDI Matrices Studied by Using Spectroscopic, Photoacoustic and Luminescence Techniques. *Chem. Phys. Lett.* **2006**, *426* (4–6), 334–340. https://doi.org/10.1016/j.cplett.2006.06.030.

(250) Stoeckli, M.; Staab, D.; Schweitzer, A. Compound and Metabolite Distribution Measured by MALDI Mass Spectrometric Imaging in Whole-Body Tissue Sections. *Int. J. Mass Spectrom.* **2007**, *260*, 195–202. https://doi.org/10.1016/j.ijms.2006.10.007.

(251) SUGIURA, Y.; SHIMMA, S.; SETOU, M. Thin Sectioning Improves the Peak Intensity and Signal-to-Noise Ratio in Direct Tissue Mass Spectrometry. *J. Mass Spectrom. Soc. Jpn.* **2006**, *54* (2), 45–48. https://doi.org/10.5702/massspec.54.45.

(252) Longuespée, R.; Kriegsmann, K.; Cremer, M.; Zgorzelski, C.; Casadonte, R.; Kazdal, D.; Kriegsmann, J.; Weichert, W.; Schwamborn, K.; Fresnais, M.; et al. In MALDI–Mass Spectrometry Imaging on Formalin-Fixed Paraffin-Embedded Tissue Specimen Section Thickness Significantly Influences m/z Peak Intensity. *PROTEOMICS – Clin. Appl.* **2019**, *13* (1), 1800074. https://doi.org/10.1002/prca.201800074.

(253) Prasanna, M. D.; Row, T. N. G. Weak Interactions Involving Organic Fluorine: Analysis of Structural Motifs in Flunazirine and Haloperidol. *J. Mol. Struct.* **2001**, *562* (1–3), 55–61. https://doi.org/10.1016/S0022-2860(00)00765-1.

(254) Dexter, A.; Race, A. M.; Steven, R. T.; Barnes, J. R.; Hulme, H.; Goodwin, R. J. A.; Styles, I. B.; Bunch, J. Two-Phase and Graph-Based Clustering Methods for Accurate and Efficient Segmentation of Large Mass Spectrometry Images. *Anal. Chem.* **2017**, *89* (21), 11293–11300. https://doi.org/10.1021/acs.analchem.7b01758.

(255) Klein, S.; Staring, M.; Murphy, K.; Viergever, M. A.; Pluim, J. Elastix: A Toolbox for Intensity-Based Medical Image Registration. *IEEE Trans. Med. Imaging* **2010**, *29* (1), 196–205. https://doi.org/10.1109/TMI.2009.2035616.

(256) Kompauer, M.; Heiles, S.; Spengler, B. Atmospheric Pressure MALDI Mass Spectrometry Imaging of Tissues and Cells at 1.4-Mm Lateral Resolution. *Nat. Methods* **2016**, No. November, 1–10. https://doi.org/10.1038/nmeth.4071.

(257) Schwab, M.; Bauer, R.; Zwiener, U. The Distribution of Normal Brain Water Content in Wistar Rats and Its Increase Due to Ischemia. *Brain Res.* **1997**, *749* (1), 82–87. https://doi.org/10.1016/S0006-8993(96)01165-1.

(258) Meyers, S. M.; Kolind, S. H.; MacKay, A. L. Simultaneous Measurement of Total Water Content and Myelin Water Fraction in Brain at 3 T Using a T2 Relaxation Based Method. *Magn. Reson. Imaging* **2017**, *37*, 187–194. https://doi.org/10.1016/J.MRI.2016.12.001.

(259) Kompauer, M.; Heiles, S.; Spengler, B. Autofocusing MALDI Mass Spectrometry Imaging of Tissue Sections and 3D Chemical Topography of Nonflat Surfaces. *Nat. Methods* **2017**, *14* (12), 1156–1158. https://doi.org/10.1038/nmeth.4433.

(260) Dufresne, M.; Thomas, A.; Breault-Turcot, J.; Masson, J.-F.; Chaurand, P. Silver-Assisted Laser Desorption Ionization For High Spatial Resolution Imaging Mass Spectrometry of Olefins from Thin Tissue Sections. *Anal. Chem.* **2013**, *85* (6), 3318–3324. https://doi.org/10.1021/ac3037415.

(261) Goodwin, R. J. A.; Pennington, S. R.; Pitt, A. R. Protein and Peptides in

Pictures: Imaging with MALDI Mass Spectrometry. *Proteomics* **2008**, *8* (18), 3785–3800. https://doi.org/10.1002/pmic.200800320.

(262) Goodwin, R. J. A. Sample Preparation for Mass Spectrometry Imaging: Small Mistakes Can Lead to Big Consequences. *J. Proteomics* **2012**, *75* (16), 4893–4911. https://doi.org/10.1016/j.jprot.2012.04.012.

(263) Ingrell, C. R.; Matthiesen, R.; Jensen, O. N. Sequence Handling by Sequence Analysis Toolbox v1.0. In *Mass Spectrometry Data Analysis in Proteomics*; Humana Press: New Jersey, 2007; pp 153–168. https://doi.org/10.1385/1-59745-275-0:153.

(264) Ellis, S. R.; Soltwisch, J.; Paine, M. R. L.; Dreisewerd, K.; Heeren, R. M. A. Laser Post-Ionisation Combined with a High Resolving Power Orbitrap Mass Spectrometer for Enhanced MALDI-MS Imaging of Lipids. *Chem. Commun.* **2017**, *53* (53), 7246–7249. https://doi.org/10.1039/c7cc02325a.

(265) Bilkey, J.; Tata, A.; McKee, T. D.; Porcari, A. M.; Bluemke, E.; Woolman, M.; Ventura, M.; Eberlin, M. N.; Zarrine-Afsar, A. Variations in the Abundance of Lipid Biomarker Ions in Mass Spectrometry Images Correlate to Tissue Density. *Anal. Chem.* **2016**, *88* (24), 12099–12107. https://doi.org/10.1021/acs.analchem.6b02767.

(266) Hecht, E. S.; Oberg, A. L.; Muddiman, D. C. Optimizing Mass Spectrometry Analyses: A Tailored Review on the Utility of Design of Experiments. *J. Am. Soc. Mass Spectrom.* **2016**, *27* (5), 767–785. https://doi.org/10.1007/s13361-016-1344-x.

(267) Passarelli, M. K.; Wang, J.; Mohammadi, A. S.; Trouillon, R.; Gilmore, I.; Ewing, A. G. Development of an Organic Lateral Resolution Test Device for Imaging Mass Spectrometry. *Anal. Chem.* **2014**, *86* (19), 9473–9480. https://doi.org/10.1021/ac501228x.